Dual use of artificial scaffold proteins for controlled magnetite synthesis and functionalisation for biomedical applications

By Lori A Somner
Supervisor Dr Sarah S Staniland

November 2019

A thesis submitted for the degree of Doctor of Philosophy

University of Sheffield
Faculty of Science
Chemistry Department

Abstract

Recently, bioengineered scaffold molecules have become an area of intense interest. The use of small, robust, monomeric proteins has become a viable alternative to much more complex and expensive antibodies. The protein scaffolds used by the Staniland group, and developed throughout this body of work, include: the coiled coil and a magnetite interacting Adhiron scaffold. Active loop sequences have been displayed on these protein scaffolds and the constructs have been shown to control the nucleation and growth of magnetic nanoparticle crystallization. The range of proteins introduced within this thesis produced a 'toolbox' to promote the synthesis of nanoparticles with favourable crystal morphologies. The structural limit to conformational changes keep the displayed region in the most active conformation. This thesis shows for the first time, how the protein scaffolds are utilised as attachment devices (for the attachment of dyes, antibodies and drug molecules) - making these proteins possible alternatives to antibody-drug conjugate systems and providing the basis for new diagnostic and therapeutic strategies.

Magnetotactic bacteria have become a model organism for iron biomineralisation since their discovery in the 1970's. A host of specialised proteins are involved in the production and regulation of the magnetosomes, and are responsible for synthesising high quality, uniform, magnetic nanoparticles under ambient conditions. Several key proteins have been identified from these bacteria and here have been shown to display activity in synthetic magnetite precipitation reactions, improving both the homogeneity and morphology of the crystals. However, these proteins are membrane spanning proteins meaning they have been difficult to produce and characterise. This research has identified regions and residues of importance for biomineralisation, by studying the hydrophilic loops that link the transmembrane helices. The use of both free peptides and constrained stem loop coiled coil scaffolds have been investigated. The active regions have been subjected to mutagenesis studies, for the purpose of identifying essential regions to maintain activity. This approach has generated novel biomimetic reagents for precision nanoparticle synthesis, as well as improving the inherent solubility issues of the full membrane protein. These artificial biomineralisation proteins exist as soluble, monomeric, antiparallel, coiled coil proteins, displaying active peptide regions as a hairpin loop. The coiled coil scaffold overcomes inherent solubility issues associated with membrane-spanning proteins, whilst retaining the activity of the wild-type species. Therefore, this study has developed an artificial membrane protein that expresses well, is versatile and retains activity regarding *in vitro* biomineralisation reactions.

Table of contents

Table of figures and tables

Abbreviations & definitions

- Aβ amyloid-beta
- AC alternating current
- AD Alzheimer's disease
- ADC antibody-drug conjugate
- AL active loop
- AMF alternating magnetic field
- AP alkaline phosphatase
- ATP adenosine triphosphate
- BCA bicinchoninic acid
- BSA bovine serum albumin
- CC coiled coil
- CD circular dichroism
- CFSE crystal field splitting energy
- CLSM confocal laser scanning micrscopy
- DLS dynamic light scattering
- DMF dimethyl formaldehyde
- d/ssDNA double/single stranded DNA
- DSC differential scanning calorimetry
- DSF differential scanning fluorimetry
- DTT dithiothreitol
- ECL enhanced chemiluminescense
- EDX energy dispersive X-ray
- ELISA enzyme linked immunosorbent assay
- ES-MS electrospray mass spectrometry
- FBS foetal bovine serum
- FITC fluorescein isothiocyanate
- GuHCl guanidine hydrochloric acid
- HRP horseradish peroxidase
- ICP induced coupled plama
- ILP intrinsic loss parameter
- ITC isothermal titration calorimetry
- MAM magnetosome associated membrane
- MMS magnetosome membrane specific
- MNP magnetic nanoparticle
- MRI magnetic resonance imaging
- MTB Magnetotactic bacteria
- MW molecular weight
- NHS N-hydroxysuccinimide
- Ni-NTA nickel nitrilotriacetic acid
- NIR near infrared
- NMR nuclear magnetic resonance
- NP nanoparticle
- PBS(T) phosphate buffer saline (tween)
- PCR polymerase chain reaction
- PEG polyethylene glycol
- PFA paraformaldehyde
- POFH partial oxidation of ferrous hydroxide
- Prp^c cellular prion protein
- RI refractive index
- RTCP room temperature co precipitation
- SA surface area

- SAR specific adsorption rate
- SAXS small angle X-ray scattering
- SDS-PAGE sulfo dodecyl sulfate polyacrylamide gel electrophoresis
- SEC-MALLS size exclusion chromatography-multi angle light scattering
- SEM scanning electron microscopy
- SPM superparamagnetic
- SWM Schwertmannite
- TCEP tris(2-carboxyethyl) phosphate
- TGA thermogravitational analysis
- UV ultra violet
- VR variable region
- VSM vibrating sample magnetometry
- XRD X-ray diffraction
- ySUMO yeast small ubiquitin modifier

Author Declarations & contributions

I declare that all work reported in this thesis is my own and all additional information and ideas are properly referenced throughout. Additional input and expertise are acknowledged below:

Chapter 3:

Dr Andrea Rawlings (Staniland group, University of Sheffield) and the *Bioscreening Technology Group* (BSTG, University of Leeds) began the initial development and phage display screening of the MIA scaffold of which the further work developed by me was heavily based.

Chapter 4:

All experimental work based on the copper chelating dye was based on the existing work of *Prof Antonio Colabufo and his group* (Biofordrug - SME, University of Bari, Italy). Initial planning and funding were aided by the Diagnostic and Drug Discovery Initiative for Alzheimer's Disease (D3i4AD).
Prof Steve Conlan and his respective group specialised in mammalian cell culture and the development of the RAGE antibody used in chapter 4. All experimental work using mammalian cells was performed by me, under their close supervision at Swansea University.
Prof Kerry Chester and her group provided expertise and the DNA plasmid for the work involving the scFv.

Chapter 5:

Dr Oleksandr Mykhaylyk and his phD student Tom Neal (University of Sheffield) were a great help when collecting the SAXS data for the CC scaffold. Although some samples were run by myself and Dr Andrea Rawlings, some were also run by Tom and Oleksandr, in addition to this much of the data analysis was performed by them.

Thank-you to all of the collaborators that have worked on this projected and contributed to the data in this thesis.

Acknowledgments

Firstly, I'd like to acknowledge the bodies that provided the funds to carry out this PhD. The University of Sheffield, chemistry departmental funding coming from the EPSRC made this project possible with the majority of funds coming from this source. Other smaller sources of money helped greatly in extra projects that aided the work for this thesis including: a RSC travel grant to visit Swansea University and learn techniques in mammalian cell culture; the Wellcome Trust for funding a summer student, along with the SURE scheme at the University of Sheffield; and the D3i4AD group for funding the work at a SME.

Most importantly, I'd like to thank my supervisor Dr Sarah Staniland. At the beginning of this process I was set on leaving Sheffield after finishing my MChem here, however, thanks to her endless enthusiasm for the world of bionanoscience she had soon convinced me that the project was worth sticking around for, and I'm really thankful she did. Sarah has been a great supervisor to have over the past four years, she is extremely approachable and always interested in the work you have done/are doing. She has endless new ideas to try out to keep the research interesting. With the support, enthusiasm and knowledge imparted on me by Sarah, I could not have asked for a better supervisor for this project. I'd also like to thank Dr Barbara Ciani for agreeing to be my independent supervisor for the past four years, even after putting up with me for the Masters projects.

A special thanks is reserved for Dr Andrea Rawlings. She has been an absolute rock in the lab, office and tea room since day one. Her knowledge of magnetic nanoparticle-based chemical biology is unparalleled, and she is always happy to share this knowledge with you (as long as you're using the right bins in the lab!). Thank-you to the rest of the Staniland group too (past and present). Thanks to Rosie, Chris, Zainab, Jenny, Scott, Pawel and Lukas and good luck to the new(ish) students starting out in the group. Thanks also to hard work of some of the undergraduate students, namely Vicky (SURE summer student) and Niall (master's student).

Departmental services and TEM in MBB at the University of Sheffield have been invaluable. Thank-you to Simon Thorpe, Sharon Spey and Neil Bramall for the samples you have run for me over the years. Thanks to Chris Hill and Svet Tzokov for all their help using the TEM.

Finally, I'd like to acknowledge my family for supporting me and helping me get through the highs and lows of life as a PhD student. Thank you to my Mum and Dad for always getting excited for me

when I mention any little achievements, even though you make it quite clear you have no idea what I'm talking about. Thanks to Sam for putting up with living 200 miles apart from me and not batting an eyelid when I said I was going to stay in Sheffield for another 4 years. Thanks to bub for kicking me throughout the writing of this thesis, reminding me that I have an impending deadline to meet.

Chapter 1: Introduction

1.1 Magnetism

1.1.1 A basic history of magnetism

Magnetism has been witnessed (yet not understood) for millennia - a science derived from a natural phenomenon that has become essential to the present population, underpinning many aspects of daily life. There is an ever-increasing reliance on electricity which is generated by the movement of conductors within a magnetic field and the world has become obsessed by 'smart' devices, such as mobile phones and magnetic strips on credit and debit cards, which contain magnetic components required for data storage. These are just a couple of examples, the list goes on and on: microwave ovens, computer disks, medical imaging etc.

These advances in technology are due to our better understanding of how magnetism works. It had been of interest to scientists for centuries, including the most famous of scientists such as Albert Einstein, but also scientists as far back in time as the Ancient Greeks. Magnetism has always been there. Paramagnets are common place in nature, coming from rocks containing magnetite which had the potential to become magnetised by extremely powerful electric currents. An example of these unbelievably strong currents are those currents generated by lightning strikes. The first major breakthrough in the utilisation of this naturally occurring force came from Zheng Gangliong in 1064 when his discovery lead to the first navigational compass. Gangliong realised that a small iron needle became magnetised when quenched from red-heat and once this magnetisation had been acquired the needles aligned themselves with the Earth's magnetic field.[1] This discovery was essential for explores such as Columbus to enable his crews to find new lands.

Another pivotal discovery in the history of magnetism came when Hans Christian Oested accidentally made the link between electricity and magnetism. He showed that when an electrical current travelled through a coil, it became equivalent to an applied magnetic field. This electrical current/magnetic field was able to magnetise the needle of a compass and caused a change its orientation in relation to the Earth's field. From this he coined the term electromagnetism. This finding was then built upon by Pierre Weiss' molecular field theory; detailing how iron can reversibly gain or lose magnetism by undergoing a phase transition.[1]

From the 1950s onwards, scientists had a better understanding of magnetism, helped by the advancement of fields including spectroscopy and diffraction. The molecular, electronic and so

magnetic structure of solid materials could now be characterised and analysed in much more detail than it ever could be before. It is this basic understanding that lead to huge advances across Earth, medicinal and material sciences.

1.1.2 Fundamental principles of bulk magnetism

The magnetisation of a sample is described as the magnetic dipole moment per unit volume of a material and it is measured in in amperes per meter (A m^{-1}).

$$M = {}^{m}/_{V}$$

Where M is the magnetisation, m is the magnetic moment and V is the volume of the material.[2] The field strength, or applied magnetic field is measured in A m^{-1} and it is also known as the imposed magnetic field.

1.1.2.1 Hard and soft magnets

The classification of a magnet as hard or soft is determined the width of the hysteresis loop exhibited upon magnetisation. The characterisation of hysteresis loops was carried out by James Ewing in 1881, he described these loops as a result of spontaneous magnetisation (M_s) of ferromagnetic materials. M_s is an intrinsic magnetic property of a material, it is reliant on the domains that exist within it. The plot below (figure 1) shows different stages of magnetisation of the material. Firstly, in the bottom left of the plot is where the sample is unmagnetised. An external magnetic field (H) is then applied and the material starts to become magnetised (M) as a result of the electronic domains within the sample starting to align with the field, until all the domains become aligned. At this point magnetic saturation is reached. When the applied field is removed, the material is then allowed to return to its unmagnetised state, the magnetisation remaining once the applied field is removed dictates the form of the hysteresis loop. A hard magnet has a characteristic broad hysteresis loop, with a square shape. This is due to a high magnetic remanence (M_r). M_r is an extrinsic property of the material, it relies on external properties of the material including its roughness and shape. Hard magnets are good, permanent magnets and are magnetised by applying $H \geq M_s$. They remain magnetised when H = 0. Soft magnets have a narrow loop and are so behave as temporary magnets. As H goes towards 0 they lose magnetisation. Different types of magnets are good for different applications.

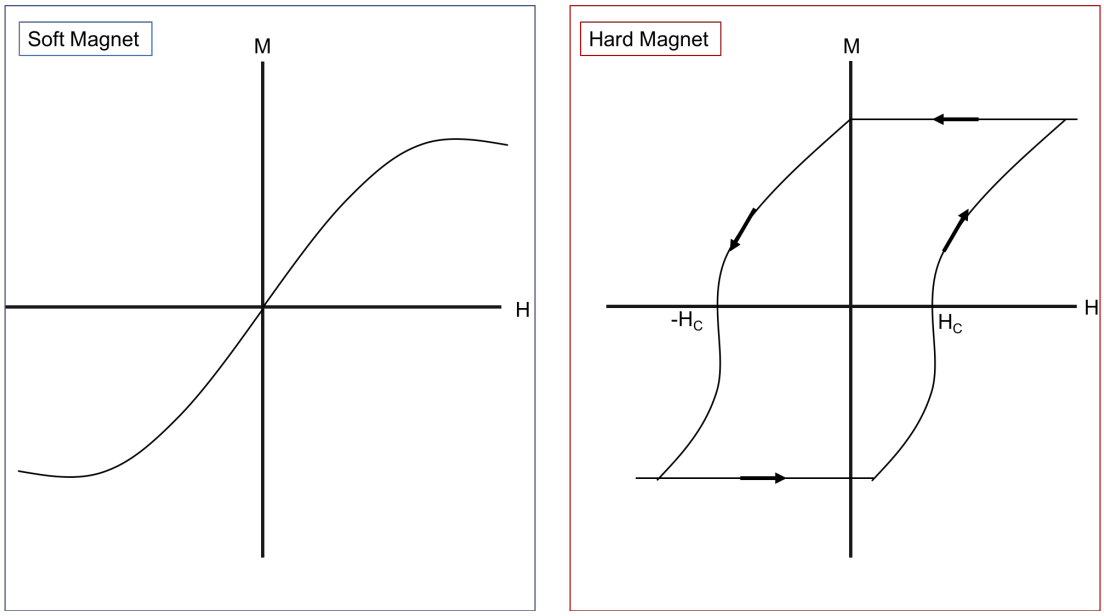

Figure 1 Diagrams showing examples of the hysteresis loops of soft (left, blue) and hard (right, red) magnets

Another point of note present observed on a hysteresis loop is the coercive field (H_c). The coercivity of a magnetic material quantifies the reverse field required to reduce M_r to zero. During this reverse process, M changes sign. H_c, like M_r, is an extrinsic property of the material. Iron and magnetite have a low coercivity meaning they do not require a substantial reverse field to return to ground state magnetisation - this is characteristic of soft magnets. Hard magnets such as cobalt and cobalt alloys have a high coercitivy and require a large coercive field to become unmagnetised.

Anisotropy is the directional dependence of magnetisation and therefore different properties result from the orientation of the field in different directions. Consequently, anisotropy lowers the coercivity in hard magnets, and increasing unwanted coercivity in soft magnets – making both types poorer magnets and less suitable for their applications. The anisotropy energy describes the energy barrier to movement reversal.[3] The energy barrier to movement reversal is not only dependent on temperature, it is also dependent on experiment time (τ_m). When $\tau << \tau m$ there is rapid flipping of the atomic moment in relation to the experimental time.

1.1.2.2 Ferro-, ferri, and anti-ferromagnetic materials

The electronic order of materials dictates their magnetic order. These characteristics are dependent on the magnetic moment or dipole moment of the species. All types of magnetism are derived from the pairing and orientation of electric spin, resulting in diamagnetic or paramagnetic electric properties. Simply, diamagnetic materials are compounds that have no unpaired electrons in their ground state. Main group elements tend to be diamagnetic. Paramagnetic materials, on the other

hand, do possess an unpaired electron in the ground state. Paramagnetic materials include the majority of the transition metals. The electron arrangements of these magnetic materials give rise to: ferromagnets, ferrimagnets and antiferromagnets. These types of materials exhibit magnetism (they have ordered magnetic moments) even in the absence of an applied field.

Materials that exhibit a parallel alignment of atomic magnetic moments are named ferromagnets, these materials are the most magnetic and include iron, nickel and cobalt. There is an irreversible and non-linear response to the M and H for ferromagnetic materials. In antiferromagnets the sub-lattices have atomic moments that are equal, but opposite, therefore there is no net magnetisation of the bulk material (figure 2). Although there is no resultant net magnetisation, the material can undergo a magnetic phase transition at the Néel temperature (T_N). Above this temperature antiferromagnetic materials become paramagnetic, this is because the thermal energy is large enough to overcome the magnetic ordering, resulting in random thermal motion of the electronic domains. Finally, ferrimagnets describe materials where the magnetic moments of the internal sub-lattices are not equal, resulting in unequal magnetisation of the electronic domains. As the magnetisation is not equal in opposite directions, there is a resultant net magnetisation of the bulk material (figure 2). This is a useful form of magnetic material which can be tailored for use in a wide variety of applications. Examples of these types of material include transition metal oxides, such as magnetite.

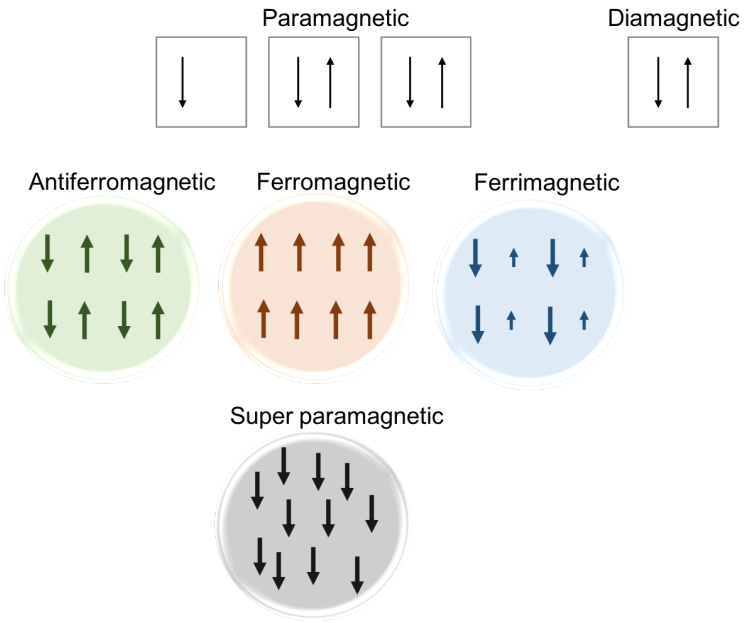

Figure 2 A scheme showing the different orders of magnetism: paramagnetic (with an unpaired electron), diamagnetic (no unpaired electrons); antiferromagnetic which shows no net magnetism; ferromagnetic, electron spins align and the material is magnetic; ferrimagnetic, where opposing spins are not of equal magnitude, showing net magnetism and superparamagnetic (SPM).

1.1.2.3 Paramagnetic and superparamagnetic (SPM) materials

There is another subclass of paramagnetic material: superparamagnetic (SPM) materials. At the point where the ferromagnetic particles become so small that thermal energy becomes larger than the volume of that particle the material is classed as SPM.[1]

$$K_u V \leq K_B T$$

Where K_u is the anisotropy constant, V is the volume of the superparamagnetic particle, K_B is the Boltzmann constant and T is temperature. For small particles (small V) the anisotropy energy is comparable to the thermal energy, resulting in superparamagnetism. At this point, the atomic moments of the particle fluctuate randomly, overcoming the electronic alignment and causing the magnetic susceptibility (χ) of the particle to follow the Curie law (with a large Curie constant (C)). The particle has localised electron spins within the sub-lattice. The electron spin can exist in one of two orientations: $+ {}^1/_2$ or $- {}^1/_2$ (up or down). Magnetite nanoparticles become superparamagnetic under 20 nm in diameter. The spontaneous magnetisation of a sample is a result of an alignment of the atomic magnetic moments of the domains. As can be seen from the equation above, this effect is temperature dependent. As heat is applied it causes random, thermal motion of magnetic dipoles, overcoming magnetism thermodynamically. As the temperature is increased, the thermal motion increases according to Boltzmann (k_BT), therefore magnetisation falls to zero. The Curie temperature (T_C) is reached at M_s=0. For ferromagnetic materials, below T_C, M(T) is reversible. When the temperature is above T_C, M(T) = 0, and the magnetic order of material is overcome resulting in the material becoming paramagnetic. The T_C of common magnetic materials can be seen in table 1 below.

Table 1 A table showing the values of spontaneous magnetisation (M_s) at room temperature and the Curie temperature (T_C) of ferromagnetic materials[1]

Material	M_s (kA m^{-1})	T_C (K)
Cobalt	1370	1388
Nickel	485	628
Iron	1720	1044
Magnetite	480	856

Once a material has become paramagnetic according to Curie law, there are still a few random thermal fluctuations of the magnetic moments of Bohr magnetons. For this reason, an applied field is able to induce alignment in some atomic magnetic moments, resulting in a small amount of magnetisation of the material. The strength of this magnetisation is dependent on the strength of

the applied field. This magnetic characteristic of the material is known as magnetic susceptibility (χ, dimensionless).

$$\chi = {}^{M}/_{H}$$

The response to H can be either paramagnetic or diamagnetic in nature. For paramagnets the M and H are orientated in the same direction; whereas for diamagnets they point in opposite directions. The χ of paramagnets follow Curie law:

$$\chi = {}^{C}/_{T}$$

Where C is the Curie constant (${}^{\mu_0 M}/_{B}$) and T is temperature. The ideal soft material has an χ which is infinitely large. Paramagnets have a χ in the range of 10^{-6} to 10^{-1}, whereas diamagnets have a range of 10^{-6} to 10^{-3}.[2]

1.1.3 Nanoscale magnetism

It is accepted that nanoscale (10^{-9} m) describes dimensions of 1 to 100 nm. These nanomaterials bridge the gap between classical materials and the quantum world - meaning they possess unique chemical, magnetic, electronic and optical characteristics which are fascinating both in theory and application. The surface area of these materials is greatly increased compared to bulk materials, making surface effects much more prominent. Nanomaterials can have one, two or three dimensions between 1 and 100 nm. Examples of each respectively include: thin films, nanowires and nanoparticles. The rest of this review and work relates to nanoparticles with all three dimensions on the nanoscale.

Magnetic nanoparticles (MNP) are interesting functional materials due to the fundamental difference in magnetic properties between nanoscale and bulk materials. The distance at which neighbouring electron spins retain collinearity is used to describe the dimensions of a magnetic domain. There are a number of these domains in bulk materials and each domain is confined within a domain wall. As materials enter the nanoscale, the number of domains is reduced, with single domain particles beginning to form when the dimensions of the particle are smaller than 100 nm.[4] As the single domain becomes smaller and reaches the SPM range, thermal fluctuations become powerful enough to cause random orientation of the atomic moments. This decrease in the number of magnetic domains is one reason for the difference between the magnetic properties of larger

microscale particles and smaller nanoparticles (NPs). The domains within bulk materials become orientated in the absence of an applied, in order to achieve a minimum in magnetostatic energy. This unfavourable thermodynamic property comes from competing long-range and short-range interactions within the material. When an external magnetic field is applied, it causes movement of the domain walls, enabling magnetisation of the particle. Eventually saturation magnetisation is achieved when the spins of all the domains are aligned with the field in a collinear arrangement.[4] As MNPs become smaller and single domain, there is collinearity of the magnetic dipoles, even in the absence of an applied field and according to the Stoner-Wohlfarth model, each of the spins rotate in unison upon the addition of the field.[5]

Nano-magnets approach the size, and so behaviour, of particles on an atomic scale (< 1 nm). At this size magnetism cannot be retained. NPs cross the boundary between atomic and bulk magnets - they are not small enough to be thermally excited over the energy barrier for spin-flip and reversal; however, unlike bulk magnets, the magnetic moments of the NP do exhibit spontaneous fluctuations around the energy minima. This effect is due to the instability of small NP when the energy barrier of reversal is comparable to thermal energy (k_BT). These spontaneous fluctuations result in the SPM properties, which in turn lead to the coercivity of the MNP approaching zero. Until this SPM cut off is reached, the coercivity of the MNP is significantly larger than that of the bulk material.[4]

1.2 Magnetite

1.2.1 Magnetite crystal structure

Magnetite (Fe_3O_4) is a useful material for biomedical applications. It is relatively biocompatible compared to other magnetic oxides (for example cobalt complexes) and is produced, naturally in the brain of humans.[6] The size, shape and composition of magnetite NPs can be controlled using a range of synthesis routes (to be discussed below), therefore the magnetic properties of the particle can be tuned to suit its application. Magnetite is used in preference to other iron oxides due to its superior magnetic properties. It has the highest magnetic saturation of all the naturally occurring iron oxides. Magnetite exhibits net magnetism in the range of 118 K to 850 K.[1, 7] Below 118 K the electrons within the magnetite lattice are no longer thermally delocalised and therefore prevent the movement required to generate a magnetic response. Above 856 K (T_C), thermal energy is able to overcome any long-range ordering within the lattice, causing a paramagnetic effect. The occurrence of these magnetic properties can be explained by examining the crystal structure of magnetite (figure 3).

Metal oxides often exist in the form of spinel or inverse-spinel crystal cubic structures.[8] Spinel crystals have the generic molecular formula: AB_2O_4, whereas for inverse spinel structures, the A ions and half of the B ions switch places, giving the formula: $B(AB)O_4$. For magnetite this is equivalent to $Fe^{3+}(Fe^{2+}Fe^{3+})O_4$. The (AB) cations occupy octahedral sites and the B ions occupy the tetrahedral sites. Fe_3O_4 has a reverse-spinel structure, justified by comparing the crystal field splitting energies (CFSE) of octahedral and tetrahedral, high spin iron (II) and (III). The high spin CFSE configuration is most likely to be adopted here as oxygen anions behave as weak-field ligands.

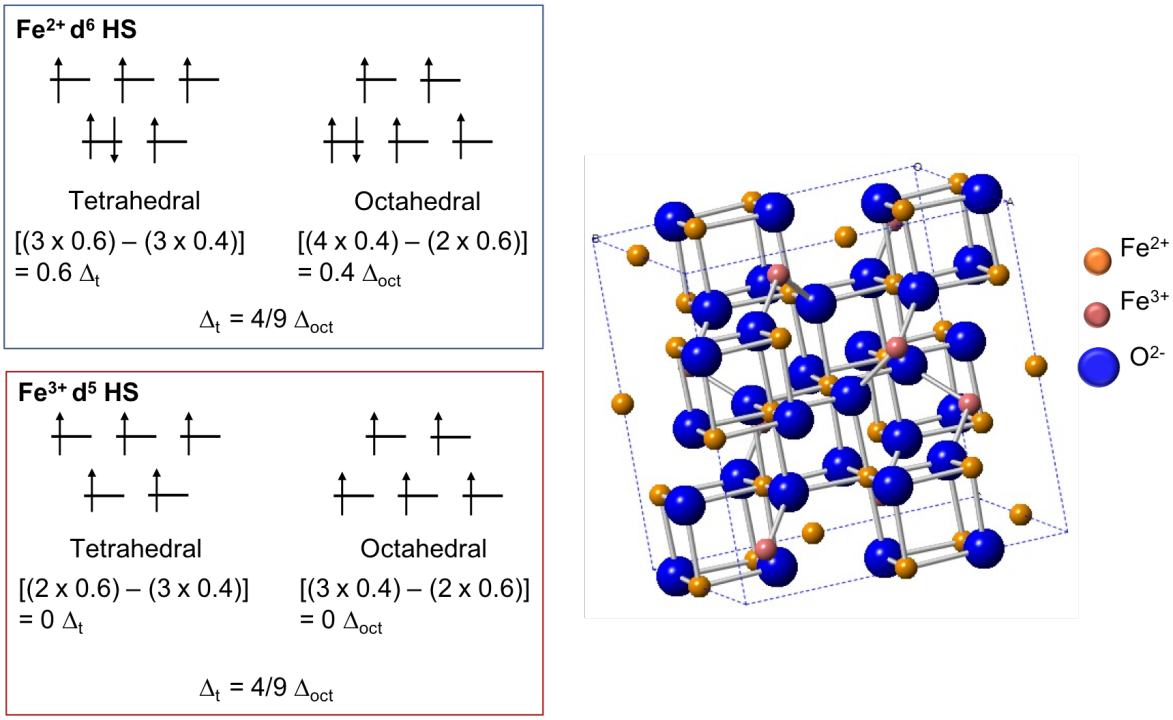

Figure 3 The reverse spinel crystal structure of magnetite. The oxygen (shown in blue) forms a close-packed, face-centred cubic lattice structure with the ferric ions (orange) occupying the octahedral holes and Fe(III) ions (pink) occupying the tetrahedral and remaining octahedral sites. To the left, the CFSE diagrams for Fe(II) and Fe(III). As the splitting energy for both tetrahedral and octahedral is equal to zero for Fe(III) – it shows no preference for either site, unlike Fe(II).

The CFSE diagram in figure 3 shows why ferric ions show no preference for either field, with the splitting energy for both octahedral and tetrahedral splitting equal to zero. Therefore, half of the ions will occupy tetrahedral sites, and the other half occupy octahedral sites. This is not the case for ferrous ions. These ions have a strong preference for an octahedral field and so all of the ions will occupy octahedral sites.

The spinel and CFSE structures also account for the ferrimagnetic properties exhibited by magnetite. All the spins within the octahedral sub-lattice are oriented in the same direction, this is also the case for all the spin-directions in the tetrahedral sub-lattice. The direction of the spin for tetrahedral sites is opposite to that of octahedral sites. Iron (III) occupies an equal number of tetrahedral and

octahedral holes and so these spins cancel. However, after these have cancelled, there are still the iron (II) spins to account for. Iron (II) has four unpaired electron spins that generate a net magnetic moment responsible for the ferrimagnetic nature of magnetite.[8]

1.3 Biomedical applications of magnetite nanoparticles

1.3.1 Magnetic nanoparticles for biomedical applications

One of the most promising applications of MNPs is their use in biomedicine. Some of the most research-intensive areas include: magnetic separation, targeted drug delivery[9], magnetic hyperthermia and magnetic resonance imaging (MRI)[10].[2, 11] Many considerations need to be addressed when designing MNPs for specific applications. One important consideration is the use of coatings. Coatings play various roles when increasing the specificity of the MNP to an application. Coatings can be used for stabilisation of the particle in solvent or serum; they can increase the biocompatibility of the particle when used in the body, preventing rejection and they can also be used for functionalisation and attachment to different surfaces.

1.3.2 Magnetic separation and cell labelling

For any biomedical application, the MNPs used must be monodisperse in terms of size, shape and surface effects. Physical properties alter the magnetic properties and therefore the ability of the particle to carry out the desired role. Cell labelling and magnetic separation are used to remove a biomolecule from its natural environment. There are a few ways in which this can be done. The biomolecule of interest can be tagged or labelled with a MNP;[2] this often requires functionalisation of the particle. Instead of binding the MNP to the surface of the biomolecule, it could be internalised. Internalisation is often achieved through endocytosis, this overcomes any issues with poor binding strength, however problems arise when a cell becomes over-loaded with particles. Increased MNP uptake can render the cell susceptible to apoptosis.[11] Once the particle is associated with the biomolecule or cell, the complex is separated using a fluid-based separation device.

Various types of separation work on different principles of separation. Separation can be as simple as applying and removing a permanent magnet from a sample tube. This system is simple and low-cost; however, it often results in the aggregation of the MNPs around the site of the magnet and therefore is only suited to single-use applications. More complicated systems rely on an increasingly complex magnetic gradient. Magnetisable beads or wires can be arranged within a column and then solvated (figure 4); tagged biomolecules are then passed through the column. A magnetic field is applied which captures the MNPs, and consequently the biomolecule, on the matrix. Following the capture, the applied field is removed, and the target molecules can be collected. This is faster than

separation using a permanent magnet due an increased surface area of the magnet, but it still has the problem associated with accumulation of MNPs. An additional method uses quadrupole magnetisation. A magnetic field is applied that radiates from the centre of the separation column.[2] This set-up reduces the agglomeration of the particles without compromising the speed of the process. For each of these devices, forces involved in the movement of the complexes needs to be considered. The force pulling the complex through the column must be large enough to overcome the hydrodynamic drag, yet small enough to have the advantages associated with increased surface area.

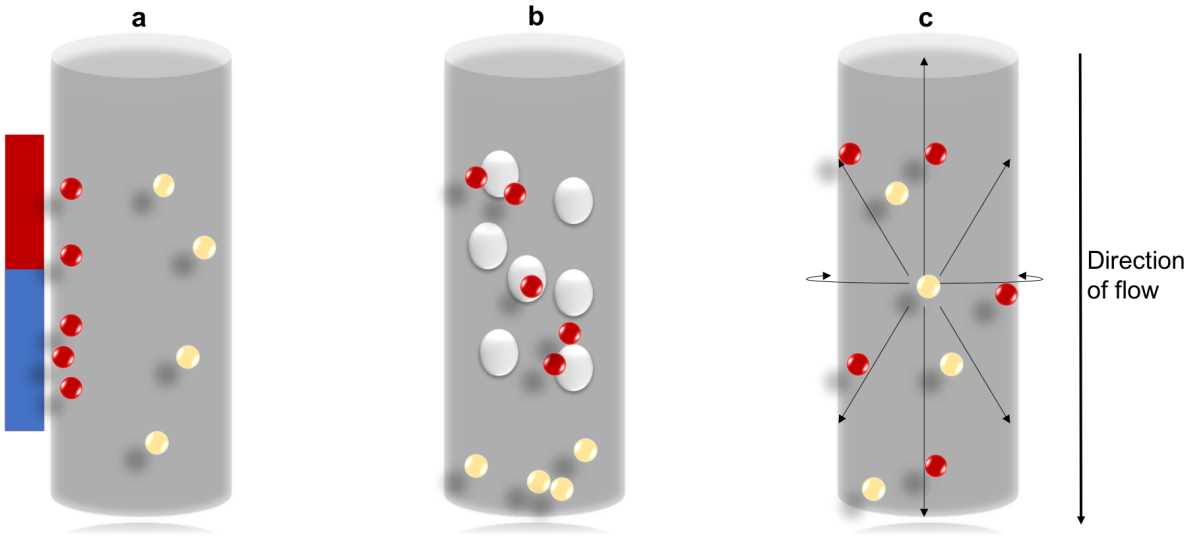

Figure 4 Methods of magnetic separation - a) simple application and removal of a permanent magnet, b) magnetised matrix and c) magnetic field radiating from the centre of the column. The red spheres are the tagged biomolecule, the yellow sphere are the solvent molecules and the white sphere are the magnetised beads.

Applications of tagging cells or biomolecules are vast. They can be used to separate out small numbers of target cells for analysis and counting. Research groups have prepared cubic iron oxide NPs, with a dimeter of less than 20 nm and coated them in lactoferrin or insulin. These NPs were then magnetically extracted and used to study the activity of fibroblasts. Their studies showed that the MNPs were internalised by the cells, causing cell disruption. When the protein was used to coat the particle, the MNPs remained stuck to the cell membrane, decreasing the cytotoxicity.[11] Another example of MNPs linked to specific cells is their attachment to neural cells. Iron oxide core-shell NPs have been shown to be effective in the manipulation of delicate neural cells in the brains of live rodents. The particles also show promise in their self-healing capabilities.[12]

MNPs have been used in enzyme linked immunosorbent assays (ELISAs). The particles can play one of two roles: they can bind to a solid support after conjugation to the biomolecule; or they serve as

the solid support themselves. An ELISA-based biosensor has been developed which can also aid magnetic separation. It utilises manganese ferrite nanoparticles that conjugate directly to PSMA – a monoclonal antibody.[13] Another use of MNPs attachment to antibodies is the ability for them to be used to target and bind specifically to receptors on the outside of specific cells. Examples of this include the attachment of iron oxide NPs to red blood cells and used for diagnosis of malaria[14]; targeting of cancer cells, such as lung cancer cells and the magnetic labelling of bacteria.[15]

1.3.3 Targeted drug delivery

Targeted drug delivery consists of magnetic materials that are directed by a magnetic gradient, towards a specific site. The concept is similar to that of magnetic separation; it requires a magnetic force to act upon a SPM MNP, causing the MNP to move in the direction of the applied magnetic field. Drugs used are often bound or encapsulated within a polymer matrix, however, the MNP can form a core with a biocompatible coating surrounding it. The core commonly consists of magnetite or maghemite. The cytotoxic drug within a biocompatible coating is usually injected into the bloodstream. Once it is the bloodstream a high-gradient magnetic field is used to concentrate the complex in the target region. Dr Munitta Muthana and her group in the oncology department at the University of Sheffield have shown MRI systems can be useful in directing macrophages to anatomic targets *in vivo*. Macrophages carrying an oncolytic virus were labelled with iron oxide NPs and directed around the bodies of mice using applied magnetic field gradient pulses. This study was pioneering in showing that MRI scanners are not only useful for imaging iron oxide particles, but are also capable of steering the NPs to target sites *in vivo*.[16]

Magnetic targeting of drug systems has obvious potential advantages over classical methods of drug delivery. Common place drug delivery, through intravenous or oral administration, have to be extremely stable, yet, only a small amount of the dose actually reaches the target region. For this reason, these drugs often have serious side-effects, for example the severe sickness that often accompanies chemotherapy. Not only would targeted drug delivery limit these side-effects, due to less interaction with non-targeted systems of the body, it would also lower the dose required and therefore the cost of drugs. The idea of targeted drug delivery was first proposed in the 1970s as a treatment for cancer.[17] Since this time, although the possibility looks extremely promising, optimising the system has been complex. There have only been a handful of systems that have made it to the clinical trial stage. The first of which was a study of fourteen patients, carried out by Lübbe.[18] It was found that ferrofluids were relatively 'well tolerated' by 'most' of the patients. The study was regarded as a success in directing the MNPs to the site, without associated organ toxicity.[2] Although there have not been many systems reaching the clinical trials stage, there have been a

number of academically promising examples. One drug that has had an intense amount of interest in the past decade is doxorubicin. It is an anti-cancer drug that has been incorporated into a number of magnetic targeting vehicles. The first example of a successful targeting experiment showed an increased uptake of doxorubicin by sarcoma tumours in the tails of rats. When a magnetic targeting system was adopted, total remission of the sarcoma was witnessed. When no targeting system was used, there was zero remission of the tumour.[19]

The next example is from Zhang *et al*. This group conjugated magnetite NPs to doxorubicin, which were then coated with poly ethylene glycol (PEG) and functionalised with a silica shell. The complex was internalised by MCF-7 cells through endocytosis. The uptake was increased further by attaching a target linker via the silica shell. A ligand targeting the folate receptor that is over expressed on the surface of MCF-7 and HeLa cells was found to increase internalisation.[20] Similarly Majeed *et al*. introduced monodisperse, water soluble magnetic iron oxide NPs, conjugated to doxorubicin. The efficacy of the complex was much higher than that for the drug alone. The group used DDT-PMAA polymer to help control the size and hydrophobicity of the system and the coating was also successful in increasing the stability and biocompatibility of the drug and the MNPs.[21]

There are a number of commonly used coatings. A couple of examples include PEG, dextran or silica. These coatings are important for controlling the biocompatibility and surface properties of the system. The size, surface properties and stability of the complex are all vital considerations for the design. The complex needs to be small enough so that it is capable of penetrating the thin capillaries and enter the tissue, however they must be large enough so that they are not rapidly removed from the circulatory system through renal clearance. For the targeting of most tissue, NP diameters are required to lie between 10 and 100 nm.[22] Particles above 200 nm are readily taken-up by the spleen, decreasing blood circulation times. Particles that do not possess a coating, bare NPs, are prone to agglomeration and in turn absorb plasma proteins. The absorption of these proteins produces hydrophobic surface properties and promote the incorporation of the NPs into the reticuloendothelial system of the liver. For most applications amphiphilic coatings are desirable, however, bare NPs can be useful for the targeting of the spleen, liver or gastro-intestinal tract.[11] Although agglomeration of the MNPs cause undesirable surface properties, agglomerates do better withstand the flow dynamics of the blood stream due to their larger size.

There are several reasons why more magnetic drug targeting trails have not taken place. There are a number of properties that must be present in parallel. There needs to be an effective way of

releasing the drug at the target site. The drug can be released from the carrier in different ways; it can be released by enzymatic activity, change in temperature or change in pH. This means that the required enzyme must be present at the site, or additional heating needs to be incorporated.[22] Even if the desired cleavage was established, the payload would no longer be controlled by the magnetic gradient. Another potential issue with the principle of magnetic drug delivery is that it is difficult to scale-up from animal models. Rodent to human studies required a much larger distance between the magnet and the target tissue, therefore it requires a much stronger magnetic gradient. Much more investigative efforts are required for the concept to be brought to the clinic.

1.3.4 Alternating current hyperthermia

Alternating current magnetic field (AMF) hyperthermia is a promising field of investigation for the non-invasive destruction of cancerous tissue. It has been studied for over 60 years and is getting closer and closer to becoming a viable clinical therapy.[23] The concept behind the therapy is that MNPs are concentrated at the tumour site. This is effective for topical tumours, whereas a fluid suspension of MNPs may be required, injected intravenously into the patient for treatment of deeper tissue. An external, oscillating magnetic field is localised around the site, causing the electrons in the MNPs (or the particles themselves to flip). This results in heating of the particle and therefore the surrounding tissue. The heat generated disrupts the cancer cells. The heating processes depends on the size of the MNPs used for the treatment. The oscillating field causes a slightly different mechanism of heating for particles that are larger, single domain particles, compared to smaller, SPM MNPs.[24] For larger particles, Néel rotations cause the heat rise due to rotation of the magnetic moment. This rotation causes flipping of the dipole moments of the MNP which produces thermal energy. Néel responses are expressed using the following equation relating to the power produced by ferro- or ferrimagnets (P_{FM}):

$$P_{FM} = \mu_0 f \oint H \, dM$$

Where $\mu_0 f$ is the field frequency and H dM differential describes the area of the hysteresis loop for the MNPs. The heating of SPM particles in an AMF is a response to Brownian rotation. Again, this is due to the rotation of the magnetic moment, however for SPM particles this causes the rotation of the whole particle. The heat is released due to the shear stress caused by the flipping particle. The principle follows the following equation:

$$P_{SPM} = \mu_0 \pi f \, \chi \, H^2$$

Where $\mu_0\pi f$ is the dependency on the applied frequency, χ is the magnetic susceptibility and H is the applied field strength. Common frequencies used for magnetic hyperthermia are between 50 kHz and 1 mHz. The frequency and AMF need to be high enough to induce sufficient heating, but low enough to be tolerated by the human body.

The heating capabilities of MNPs are often quantified using the specific absorption rate (SAR). This quantity can be described as the power produced per unit mass, or per unit mass of iron, with the mass of iron calculated using induced coupled plasma mass spectrometry (ICP-MS). However, recently there has been a move towards using the mass of the MNP, this gives a more accurate value of SAR due to the accountability of the oxygen within the sample. The mass is therefore determined by thermogravimetric analysis (TGA) instead.[24]

$$SAR\ (W\ kg^{-1}) = {}^{P\ (W)}\Big/_{m_{MNP}\ (kg)}$$

SAR is an extrinsic magnetic response property of the MNP; it is dependent on both the frequency applied and the applied field strength, as well as the size and roughness of the MNP. The intrinsic loss parameter (ILP) is becoming favoured in place of SAR, for the quantification of the power dissipated by the system. The variability in values of SAR is not only due to the frequency of field strength used; Wildeboer *et al* have suggested that the use of a non-adiabatic system is responsible for large discrepancies in values quoted in literature due to the heat transfer from the MNP to the surrounding.[25] SAR values currently used in the clinic give a good and valid indication of the heat propagation through tissue. Reasons for the inconsistency in SAR literature values arise from the fact that SAR values change depending on the form of the MNP, for example there are variations in values between powder form, suspensions and if the sample is analysed *in vivo*.

The shape of the MNP used for hyperthermia treatment is thought to have a substantial effect on the corresponding SAR value. Martinez-Boubeta *et al* produced and analysed atomic level, Monte Carlo comparative simulations of cubic and spherical iron oxide nanoparticles, with a diameter of 20 nm.[26] They found that nanocubes exhibit a larger anisotropy compared to the spherical particles. This increased anisotropy resulted in superior heat induction power of the cubic particles, they suggest that this may be in part due to increased aggregation into chains. The tendency to form chains is thought to be promoted by the cubic shape. The large anisotropy of the cubes is due to an increased surface area compared to similarly sized spheres.

$$SA_{cube} = 6a^2$$
$$SA_{sphere} = 4\pi r^2$$

Where a is the length of the cubic face and r is the radius of the sphere. If the 'radius' of the cube can be estimated as 0.5a, then for the same value of r, the cube will have the larger surface area. The increased surface area, and therefore anisotropy, results in a larger area occupying the hysteresis loop for nanocubes. An increased hysteresis loop indicated a large coercive field (H_C). In conclusion, cubic NPs are superior for AMF hyperthermia treatments compared to spherical nanoparticles of a similar size due to increased anisotropy and therefore SAR values.[27]

There are various occurrences within the human body that cause a decrease in SAR values, making it extremely difficult for magnetic hyperthermia to be optimised for clinical use as a therapy. For example, the adsorption of proteins to the surface of the MNPs result in decreasing SAR values. MNPs become covered in proteins when they enter the blood stream, resulting in the formation of a protein corona around the particle due to electrostatic interaction between the particle and the protein. These proteins cause problems for three reasons[24]:

1. The corona increases the hydrodynamic radius of the particle
2. It promotes agglomeration of the MNPs, increasing the hydrodynamic radius
3. The proteins act as markers, promoting the metabolism of the particles by the cell

Particle aggregation is also thought to be an important factor in this effect. As the particles are held in a closer proximity, there are more magnetic dipole interactions and so decrease in heating capabilities. Lartigue *et al* were able to show how cubic MNPs were processed by the cell and so indicated how the SAR values could differ during the process.[28] They found that upon uptake there was a dense area of MNPs held within the endosome, however the particles become more disperse and exposed again on passage to the lysosome.

There are other problems that prevent magnetic hyperthermia being more widely used. One of these reasons is that the exposure limit for humans is still unknown. The best estimate for the tolerance level is the Brezovich limit.[29] Brezovich suggested that the limit could be estimated by multiplying the applied field strength by the frequency. He therefore suggested a limit of 4.85×10^8 A $(m\ s)^{-1}$. This was found to be the limit when AMF hyperthermia was used to treat cancer of the thorax.

Although there are a number of hurdles to overcome, there are also a number of successful studies in the field. Connord *et al* developed a way to track cells using hyperthermia coupled with confocal microscopy.[30] Soft MNPs were internalised by samples of mammalian cells, concentrating the magnetic flux and homogenous field within the cell. This allowed them to observe magnetic hyperthermia of the cell and using confocal microscopy, track cell metabolism in real-time. Tietze *et al* have carried out hyperthermia using an AMF in experiments with rabbits.[31] In the study they used flat wire coils to produce the oscillating current with a frequency of 200 kHz and field strength of 6.76 A m^{-1}. Gneveckow *et al* developed this further by producing a human-sized prototype for AMF hyperthermia using a ferromagnetic core, in place of a flat coil, as an inductor.[32] In this study a frequency of 100 kHz and field strength of 18 kA m^{-1} was required. Finally, there have also been studies that have reached clinical trial. A company known as Mag force nanotechnologies AG, based in Berlin, Germany have developed Nanotherm® for the treatment of prostate, oesophageal and pancreatic cancers. The system uses iron oxide NPs which are injected directly into tumours. An external AMF is then used to cause a thermal response of the MNPs, resulting in the treatment of the surrounding cancerous tissue.

1.3.5 MRI

Magnetic resonance imaging (MRI) is a non-invasive, non-ionising, tool for imaging damaged tissue *in vivo*. MRI uses the magnetic moment of protons within the body to produce an output signal that is detected and used to produce an image. Although the magnetic moment of a proton is extremely small there are so many protons available in the form of water molecules, that the accumulative effect allows for a detectable signal. Only about one in a million proton spins are aligned in a 1.5 T field, however there are roughly 6.6 x10^{19} cm^{-3} protons in water, resulting in low sensitivity but sufficient detection. The problem, however, is that our bodies are full of water and so protons are everywhere, there are millions of protons present that can become excited. To overcome this, a contrast agent must be used. A magnetic contrast agent reduces the relaxation times T_1 and T_2. T_1 is the spin-lattice relaxation time, also known as the longitudinal recovery signal, accounting for loss of heat to the surrounding lattice. T_2 is the spin-spin relaxation time, also known as the dephasing signal, and is the measure of the time it takes for the signal to irreversibly decay, this decay occurs as excited nuclear spins in the xy plane interact with each other. T_2 relaxation results from a heterogeneous magnetic field and result in negative contrast, causing darkening on the imaged site.

MNPs have been the subject of intense research to occupy the role of next generation contrast agents. Currently, common contrast agents found in the clinic are paramagnetic, gadolinium-based molecules, but the achievable sensitivity is reaching its limits. MNPs, specifically SPM iron oxide,

have been used as MRI contrast agents, both academically and in the clinic. Iron oxides are often used because of their high magnetisation and therefore their ability to generate an extensive heterogeneous magnetic field gradient caused by the interaction between the electron spin of the contrast agent and the protons of the water molecules. The interaction increases the rate at which the protons drop out of phase with one another on removal of the radiofrequency. As this rate increases, the T_2 relaxation time is decreased, which in turn decreases the signal and causes a more intense negative contrast. MNPs are therefore classed as T_2, or negative, contrast agents whereas gadolinium (III) chelates are positive contrast agents due to the ability to increase the T_1 relaxation rate.

There are a few important factors that need to be considered when designing MRI contrast agents:

1. There needs to be sufficient contrast between the region of interest and the surrounding tissue, therefore any contrast agent needs to be taken up by the site preferentially.
2. The contrast agents must be biocompatible and not cause an adverse immune response upon uptake
3. The metabolism of the contrast agent must be slow enough that the contrast agent is able to remain at the site long enough for an image to be taken.

One example of the use of iron oxide NPs is in MRI imaging of the liver.[2] Preferential uptake of the MNPs in the liver is partially due to diameters of 30 nm collecting more readily in the liver whereas sizes below this are not. This shows the importance of size control over the NP. More recently, the role of MRI has been investigated to assist therapeutic strategies involving MNPs. The NPs can act as more than just diagnostic contrast agents. The external magnetic field applied by the MRI can be used to localise the MNPs to a specific area of the body, using a field gradient. As with targeted drug delivery, if this targeting is possible many nasty side effects of alternative therapeutics may be overcome. There have also be developments in multimodal imaging. Multimodal imaging is the use of two or more methods of imaging simultaneously, utilising the advantages of the methods, while cancelling out the disadvantages. One example of this is the use of magnetic resonance and optical imaging in parallel. MRI allows for good spatial resolution (dependent on the field strength), and exceptional penetration, however it often results in poor sensitivity. Whereas, optical imaging is very sensitive, but has poor spatial resolution.[33] This combination of imaging techniques requires an iron oxide contrast agent, conjugated to a fluorophore. The fluorophores used tend to have excitation and emission wavelengths in the near infra-red (NIR) due to the enhanced tissue penetration compared to visible or ultraviolet (UV) radiation.[33]

Another example of the use of iron oxide NPs as contrast agents comes from the use of 'smart' MNPs that are activated at the targeted site. This concept targets biomolecules that are in close proximity to the site of interest. Gallo *et al* used 6 nm iron oxide particles, activated by click-chemistry upon exposure to metalloproteases, which were overexpressed at the tumour site.[34] The activation resulted in the self-assembly of the MNPs, increasing the T_2 signal (decreasing the T_2 relaxation time), increasing the local magnetic susceptibility due to aggregation. When the contrast agent was injected intravenously into mice, a 14 % decrease in T_2 relaxation was witnessed after four hours, increasing to 25 % when injected directly into the tumour. These values were compared to the negligible change in the T_2 of the control.

For T_2 contrast agents, the iron oxide used it almost always magnetite, maghemite or hematite and the relaxation response of these iron oxides are dependent on their size, geometry and composition. For example, the saturation magnetisation decreases with size, therefore decreasing the contrast of T_2 and enhancing T_1 relaxation, due to a shift towards paramagnetic behaviour. Another example is changing the composition of the MNP, such as doping the iron oxide with cobalt or platinum causes an increase in the magnetic saturation, increasing the T_2 effect. The problem with using the dopants however, is that they are often much more toxic than the relatively biocompatible iron oxide. Spherical MNPs have an enhanced T_2 contrast compared to cubic MNPs, due to a larger radius of a sphere for the same volume. For this reason, it has long been accepted that the best T_2 values are expected for spherical particles (30-300 nm). However, Lee *et al* found that this is not necessarily the case. They discovered that nanocubes with a diameter of 22 nm provided similar T_2 relaxation times to spheres of 30 nm. The group showed that the hydrodynamic radius of iron oxide NPs with a diameter of 22 nm is 44 nm, this size is where the particle is in a static dephasing regime. The static dephasing regime is the point at which the fastest T_2 relaxation is observed. This phase is dependent of the magnetisation of the particle and the gyromagnetic radius.

As could be expected from the number of promising academic applications of MNPs in MRI, there have been a number of iron oxide reagents that have become clinically available. A couple of examples of these include: Resovist (Bayer Schering), and Ferumoxytol (AMAG Pharma).[35] Resovist is used as an MRI contrast agent in Japan, it was found to perform better clinically than existing gadolinium-based molecules for the imaging of the liver in respect to the most commonly used clinical field strengths. Ferumoxytol is used as a treatment for anaemia, as well as an MRI contrast

agent. It was found to be superior in the diagnosis of myocardial inflammation when compared to gadolinium-based agents.[36]

In summary research into iron oxide NPs for biomedical applications has taken off in recent years, with a number of candidates entering clinical trials. However, there is still the need to develop and improve on current targeting techniques and identify appropriate synthetic routes for the production of the MNPs.

1.4 Problems with current magnetite synthesis

1.4.1 High temperature and pressure

The synthesis of magnetite MNPs is a complex task. The conditions in which the reaction proceeds need to be considered, as does the yield, the degree of monodispersity and the scalability of the reaction for industrial purposes. There are a vast number of chemical routes that result in the successful synthesis of magnetite NPs. The production of spheres, cubes and hexagons have become common place within the literature associated with this area of materials science.[20, 37] The ability to control the formation of magnetite NPs has led to a breakthrough in their use as biomedical agents. SPM MNPs are of interest for a range of biomedical applications, however it is really important that the size and shape of the particles can be tailored and controlled as their magnetic properties are highly dependent on these factors. The literature shows that this control is now becoming possible. However, there are common flaws arising in many of these synthetic routes; namely the use of high pressures; high temperatures and expensive organic solvents. With climate change and global warming at the forefront of many scientist's minds, it is becoming essential to steer away from these methods, towards a more environmentally friendly, more 'green' process. Some currently used methods utilising high temperature and pressures for the production of different shaped and sized MNPs are discussed below.

1.4.1.1 Sonochemical synthesis

Well-defined magnetite nanorods have been synthesised using sonochemistry. Sonochemical synthesis involves the application of powerful ultrasound radiation with a frequency of 20 kHz to 10 MHz. This high frequency radiation causes the formation of cavities within the reaction mixture. Following the formation, these cavities/bubbles begin to increase in size upon the diffusion of solute vapour into the bubble. Once they reach a critical size, they collapse, resulting in a chemical reaction and formation of chemical bonds. It is understood that there is an immense and rapid temperature increase that occurs at the point of collapse, with temperatures reaching in excess of 5000 K.[38] This

temperature, however, only lasts for around 1 ns, therefore there is super-fast cooling of the system. This cooling interrupts the crystallinity and breaks bonds. Kumar *et al* have demonstrated the synthesis of magnetite nanorods using sonochemical oxidation of aqueous iron (II) acetate, in the presence of a β-cyclodextrin templating agent.[39]

1.4.1.2 Thermal decomposition and solvothermal synthesis

Thermal decomposition has been used to synthesise both spherical and cubic magnetite NPs, in a range of sizes. Protocols using thermal decomposition often lead to monodisperse products and exhibit excellent size control. The technique uses high temperature decomposition of iron-based organic precursors in organic solvents, with the addition of surfactant molecules. Common precursors include $Fe(Cup)_3$, $Fe(CO)_5$ and $Fe(acac)_3$.[10] It is possible to have a high level of control over the reaction and it is well understood how the reaction time, temperature, ratio of reactants, solvent, precursors and seed addition can alter the morphology and composition of the product. Park *et al* synthesised spherical magnetite nanoparticles of 4, 8 and 11 nm by thermal decomposition of an iron-oleate precursor.[40] The precursor was synthesised from $Fe(CO)_5$ and oleic acid, heated to 100 °C. An oxidant was added to ensure good crystallinity of the product. In this case the oxidation step used trimethylamine N-oxide, others use residual oxygen from subsequent aeration. The reaction was heated to 300 °C to yield the desired product. The group were also successful in controlling the size of the magnetite crystals. They suggest that using an initial step to produce the precursor results in NPs between 4 and 11 nm (dependent on ratio of $Fe(CO)_5$ and acid). Larger particles can be produced by producing the precursor *in-situ* (13 nm), or using a higher boiling point solvent, with a higher boiling point giving a larger particle diameter.[40]

Nano-cubes of magnetite have been produced using high temperature thermal decomposition. Cho *et al* used ferrous acetyl acetate in the presence of a surfactant and 4-biphenylcarboxylic acid, in benzyl ether solvent.[41] The reaction was heated to 200 °C for three hours and then the temperature was slowly raised to 280 °C for a further hour, in an anoxic environment. This protocol produced cubes with sizes between 11 and 26 nm, with the size dependent on the concentration of the iron acetyl acetate, volume of benzyl ether and the reflux time. Once the cubes were made, they were washed in acetone and suspended in hexane.[41] As with many techniques that require high temperature and volatile solvents, thermal decomposition is not suitable for industrial applications and there are inherent issues regarding safety when scaling up these reactions. Also, the precursors such as $Fe(CO)_5$ are toxic and expensive organometallics.

Octahedral magnetite can be synthesised using solvothermal synthesis. This synthesis route uses an organic solvent as the reaction media and the reaction proceeds in a steel reactor or autoclave at high temperature and pressures. Temperatures used are in excess of 200 °C and pressures as high as 2000 psi. The first step of the reaction involves the hydrolysis and oxidation of ferrous salts, into ferrous hydroxide. The second step is neutralisation of mixed metal hydroxides. The NP size is tightly controlled through both the nucleation and growth stages of crystallisation, with these stages being dependent on temperature. A higher temperature results in faster nucleation and supressed growth and so forms smaller crystals.[10] Ooi *et al* have produced octahedral magnetite using the solvothermal synthesis method.[42] They used an $FeCl_3$ precursor in ethylene glycol, with the addition of organic surfactants and a sodium acetate steric stabiliser. Using this route, they were able to produce octagons with a diameter of around 90 nm. Using this process, they were able to provide a better understanding of the importance of amine groups in the organic surfactants. It is known that amine functional groups play an important role in the anisotropic growth of magnetite crystals. It is thought that these groups accelerate growth rates, whilst simultaneously acting as a reducing agent and surfactant when used at high temperatures. It is likely that the amines adsorb onto the surface of the forming magnetite, exerting influence on the direction of facet growth, altering the surface energies for magnetite. With this understanding, Ooi *et al* were able to alter the reaction in order to produce spherical magnetite in addition to octahedral.[42] Spherical particles were produced when the concentration of amine was decreased. This led to a different type of competition for the adsorption sites on the magnetite nuclei, generating a homogenous surfactant/solvent environment, resulting in isotropic coverage of the nuclei and therefore spherical growth. Although this is a useful insight into the dynamics of the reaction, it is unfortunate that high temperatures and organic solvents are required to ensure a dynamic chemical environment, enabling the efficient adsorption and desorption from the magnetite surface.

1.4.1.3 Supercritical fluid synthesis

Magnetic hexagonal nanoplatlets of magnetite have been synthesised by Li *et al*, utilising supercritical fluid synthesis.[43] In supercritical fluid synthesis, supercritical carbon dioxide can be used as a solvent. It is used for its low surface tension and viscosity. The group used thermal decomposition of a ferrocene precursor to produce reduced iron. The iron was then oxidised using supercritical carbon dioxide. The reaction was conducted in a quartz boat containing ferrocene. The boat was positioned in a high-pressure reaction chamber, which was charged with the carbon dioxide and heated to an extremely high temperature (750 °C). This example highlights the range of options of magnetite synthesis pathways if harsh conditions were not a factor.

1.4.2 Room temperature co precipitation (RTCP)

There is a good reason for the use of harsh conditions in the synthesis of magnetite nanoparticles – these conditions often offer a much higher degree of control over the formation of the desired products. It is often easier to control the size, shape and composition of the inorganic crystals when you have access to high temperature, high pressure and/or the use of organic solvents. One simple and efficient way to produce magnetite NPs is through room temperature co-precipitation (RTCP). This technique is one of the most widely adopted pathways in the literature due to its simplicity, yield and cost. The problem with the RTCP route however is the poor control over the morphology of the particles. This lack of control is the result of the crystal growth phase being almost entirely dependent on kinetic factors. The process involves a rapid nucleation phase, followed by a slow crystal growth phase, these phases have a tendency to occur simultaneously, leading to poor control over the process and therefore a mixture of products. The reaction proceeds under aqueous, anoxic conditions, at room temperature and pressure, with complete precipitation occurring around pH 8. It is essential to keep the reaction and products under an inert, non-oxidising environment as magnetite is extremely susceptible to oxidation, resulting in the formation of maghemite, this is not ideal due to the reduced magnetism of maghemite compared to magnetite. Oxidation from iron (II) to iron (III) is caused by the migration of cations through the iron oxide lattice. It is this cation migration that results in vacant octahedral sites and lower magnetic saturation. To ensure the desired iron oxide is formed in a RTCP, control of proton and electron transfer is required. Slight adjustments in redox potential (E_h) and/or pH can have a dramatic effect on the iron oxide formed. This can be seen in the E_h-pH Pourbaix diagram below (figure 5). The defined areas on the diagram represent the range in which each mineral is stable.

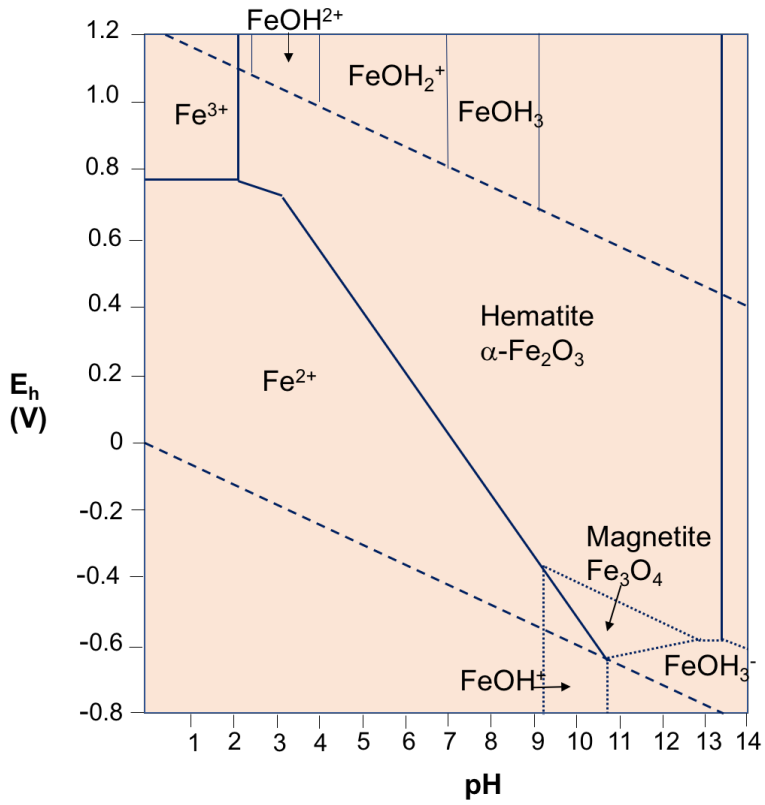

Figure 5 Eh vs pH Pourbaix diagram for magnetite formation. The diagram shows the effect of oxidation, reduction, hydrolysis and dehydration on iron oxide formation. Taken from Tekeno et al.[44, 45] The diagram shows that magnetite is formed at high pH (9-13) under reducing conditions (-0.3 - -0.6 V)..

During RTCP, an aqueous suspension of ferric and ferrous salts is added to a reaction vessel. As the reaction proceeds, a base is added dropwise, at a constant rate, pushing the reaction towards the synthesis of the magnetite product.[10] The system is kept under anoxic conditions. The reaction scheme for this route can be seen below:

$$Fe^{2+} + 2Fe^{3+} + 8OH^- \rightarrow Fe_3O_4 + 4H_2O$$

The nature and abundance of different iron-based compounds formed during the RTCP is dependent on two factors: X and R. The ferric molar fraction (X) is the molar ratio of iron (III) compared to the total iron:[46]

$$X = {[Fe^{3+}]}/{[Fe]_{tot}}$$

For example, if ${[Fe^{3+}]}/{[Fe^{2+}]}$ was in a ratio of 1:2, X would be equal to 0.33. The hydration rate (R) is described as the molar ratio of base compared to total iron content:[46]

$$R = {[NaOH]}/{[Fe]_{tot}}$$

Mass balance diagrams have been constructed to depict the dependence of the reaction on these factors (see figure 6). These diagrams also show the different phases the occur during the formation of magnetite from the mixture of ferric and ferrous salts. One common iron-based product that forms along this route is green rust, however this only occurs in the presence of sulphite ions. The three main stages of the reaction, leading up to magnetite formation are as follows:[46, 47]

1. The precipitation of ferric basic salts, for the formation of goethite:

$$Fe^{3+} + 3OH^- \rightarrow FeOOH + 2H_2O$$

2. Fe^{2+} and SO^{4-} are absorbed onto the FeO_2H surface, for the formation of green rust (GR) at the solution/solution interface:

$$4Fe^{2+} + 2Fe^{3+} + 12OH^- + SO_4 \rightarrow Fe_4^{2+}\, Fe_2^{3+}\, (OH)_{12}\, SO_4$$

3. Under anoxic conditions, green rust plus ferrous hydroxide is transformed into magnetite:

$$Fe^{2+} + 2Fe^{3+} + 8OH^- \rightarrow Fe^{2+}Fe_2^{3+}O_4 + 4H_2O$$

The reaction can then proceed further, forming the ferric hydroxide schwertmannite (SWM).

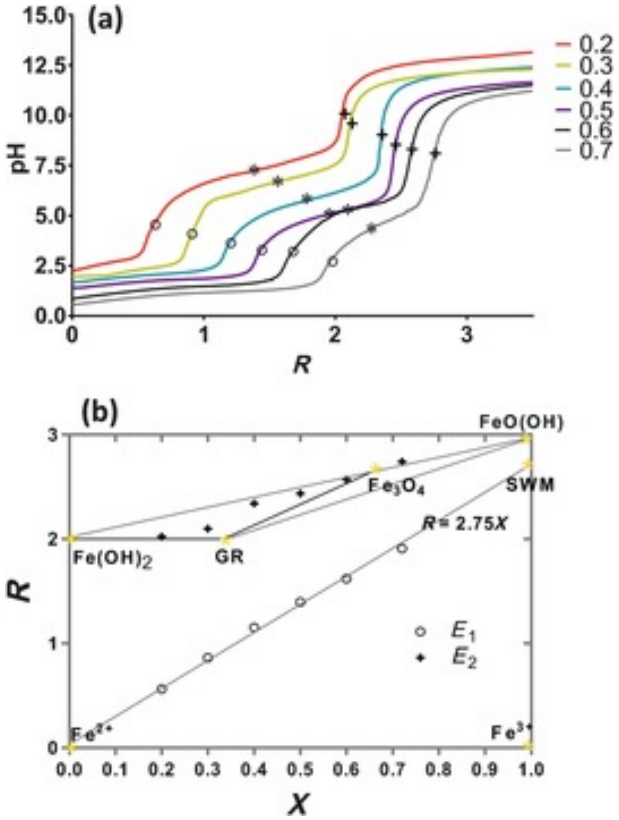

Figure 6 Shows the equivalence points between the pH titration and mass-balance diagram constructed by A Rawlings et al. A is the results from the pH titration at varying values of x (seen in the key to the right of the plot) at a rate of 0.05 R min^{-1}. B is the mass-balance diagram showing the occurrence and dependence of the iron-based products in the RTCP reaction.[47]

The equivalence points on a pH titration and mass-balance diagram can be compared to better understand the phases reached during the RTCP. There are three plateau regions that can been seen in figure 6, linking two sloping regions on the plot. The first equivalence point lies in the middle of the first slope region on the pH titration and this correlates to R = 2.75X on the mass-balance diagram, indicating the formation of SWM. The second equivalence point lies in the middle of the second sloping region of the pH titration plot. This corresponds to the formation of magnetite, depending on the value of X.[47] When X = 0.67, magnetite is produced, this is expected due to the formula of magnetite: $Fe^{3+}(Fe^{2+}Fe^{3+})O_4$.

However, even with the information available from the mass-balance diagram and equivalence points, it is still not trivial to produce pure magnetite with a monodisperse morphology. Varying levels of oxidation are required to reach the formation points of different iron oxides and the formation of magnetite often requires an aging process for complete conversion, especially at low vales of X.[47] It is important not to over-shoot the length of time for the aging process, as over aging causes oxidation and the formation of maghemite. It is therefore a delicate process where there is a thin line between magnetite formation and other iron oxide formations, which often results in less than desirable control over the NP composition. These diagrams also do not take away the fact that the crystal nucleation and growth stages occur simultaneously, making it difficult to control the morphology of the NP.

One of the most promising co-precipitation reactions for the synthesis of magnetite with a well-defined morphology is the RTCP protocol using ammonia diffusion to gradually increase the pH. Lenders *et al* show that the reaction kinetics of the reaction can be controlled using a two-step protocol, rather than direct co-precipitation.[48] The first step involves producing a ferrihydrite precursor from ferrous salts. This step occurs at a low pH. The second step increases the pH of the reaction through diffusion of ammonia, resulting in the slow conversion of the ferrihydrite into the magnetite product. The crystallisation kinetics of the precipitation is controlled by the rate of ammonia diffusion and the concentration of iron used.

Now that the problems with current routes to magnetite synthesis have been introduced, there can be a discussion of possible solutions that may overcome these issues. These solutions incorporate the use of ambient temperatures and pressures, synthesis routes that reduce costs and the use of organic solvents and precursors, yet they are methods that generate well-defined, reproducible MNPs that can be tailored to various applications.

1.4.3 Biomineralisation of inorganic crystals

Biomineralisation describes the process by which organisms precipitate minerals in the form of inorganic crystals. These inorganic crystals include iron oxides and sulfates, calcium phosphates and carbonates and silicates; however, this list is my no means exhaustive and there are many other examples of biomineralised crystals that could be drawn upon. The exquisite control exhibited by these organisms has intrigued chemists, physicists and engineers alike, who have tried to mimic the structure and properties of these minerals *in vitro*. The process of mineralising these crystals can be conducted for one of two reasons. Firstly, the mineral can be of use by the organism and play a vital role, for example it may play a role in magnetotaxis, mechanical support or avian navigation and be designed and created specifically for this purpose.[49, 50] On the other hand, it may be produced as a by-product to ensure non-toxic effects and removal of unwanted products of various biochemical reactions, such as microbial respiration.[51]

Over sixty different types of minerals are known to be produced in this way, with examples from each kingdom. The most abundant biogenic mineral formed in nature is calcium chlorides, specifically calcite, which is found in skeletons and shells. Sea urchins use calcium carbonate deposits for protection and maintenance of their structure.[52] It is also used as a gravity sensor in both marine and land animals. The problem with calcium carbonate, however, is that it is a very brittle material and therefore not suited to contributing towards protection and strength of organisms. This physical property of the mineral is aided by the inclusion of a range of proteins that are present within the crystal layers. These proteins are essential for preventing cracking of the mineral.[52] Coccolithophores, such as haptophytic algae, biomineralise an extracellular covering of scales. These scales can consist of calcium carbonate or silica, with those made up of calcium carbonate drastically contributing to the percentage of calcium carbonate biomineralised globally.[53] The precipitation of the inorganic minerals is aided by long-chain polyamines and polypeptides such as actin, which regulate silica morphology. Langer *et al* found that coccolithophores that had been treated with an inhibitor of actin polymerisation resulted in major malformation of the organism. These results indicate the importance of actin in the formation of scales.[54] This proves that biomineralisation of inorganic crystals does not only occur in larger animals and marine life, it is just as common in species of algae and bacteria. In each case, no matter how large or complex the species, the process of biomineralisation relies heavily on the function of specific biomineralisation proteins. The study of these proteins by interdisciplinary scientists and engineers has become an intense area of research, yielding promising results for mimicking biomineralisation *in vitro*. One well studied group of biomineralising organisms is magnetotactic bacteria.

1.4.4 Magnetotactic bacteria

Precipitation of magnetite by living organisms is thought to be the most ancient form of biomineralisation and today it occurs in a wide-range of species, ranging from the production in the human brain, to the formation of chains in magnetotactic bacterium.[6] The majority of the literature states that magnetotatic bacteria (MTB) was discovered by Blakemore in the 1970s.[55] He was observing bacteria present in marine samples from the USA when he noticed that some of the bacteria in the sample would group at one edge of the water droplet. At first Blakemore assumed this was a phototactic response of the bacteria, trying to move towards or away from the light source in the lab. However, he soon realised this was not the case, and in fact they would move in the vicinity of external magnets. The response was termed magnetotaxis. Blakemore was able to characterise the bacteria as gram negative and showed that they each had flagella to aid mobility and iron-rich compartments within their cytoplasm which were responsible for their magnetotactic response. Blakemore likened this characteristic to the needle of a compass. The bacteria contained chains of nano-magnets with a dipole moment strong enough to orient themselves parallel to the Earth's magnetic field lines. Although it is still true that Blakemore independently discovered these bacteria and was able to compare the iron-containing chains to a compass to aid navigation, he was not in fact the first scientist to document magnetotactic bacteria. Bellini, an Italian scientist, actually described the bacteria in his Master's thesis written in 1963.[56] This publication was only released in Italian at the time and therefore was not well circulated within the scientific community. Bellini also failed to introduce a convincing argument for magnetotaxis.

Generally, MTB, such as the *Magnetospirillum magneticum* AMB-1, are found in close proximity to the oxic-anoxic interface. This interface is a transition zone generated by the opposing oxygen gradients between the aquatic surface and the bottom sediment. This region tends to be microaerobic. It is thought that the existence of the oxygen gradient and the need for the MTB to occupy an environment with a low and specific oxygen content led to the evolution of chemotaxis, specifically, magnetotaxis. Magnetotaxis is the passive alignment of the magnetosomes along the geomagnetic field lines. The flagella of the bacteria are then responsible for movement along these lines, propelling the MTB up and down. This machinery reduces the search area for the optimum growth conditions for the bacteria. Instead of searching in three dimensions, they only have to search in one dimension – up and down. MTB can be bipolar or unipolar and are thought to be either north-seeking or south-seeking. North-seeking MTB have a tendency to swim downwards in the northern hemisphere and south-seeking cells swim downwards in the south hemisphere.[57] This directs navigation to microaerobic conditions. Due to the use of magnetotaxis in conjunction with

aerotaxis, the phenomenon witnessed in MTB has been more accurately termed 'magneto-aerotaxis'.

Since the discovery of MTB and magnetotaxis, the concept that the magnetosome evolved for this sole purpose has faced scrutiny. This speculation grew further when MTB were found to reside at the equator, here there are no vertical components adding to the geomagnetic field vector, therefore there is no advantage for the MTB in terms of magneto-aerotaxis. One fact, that helps to preserve the idea however, is that south-seeking and north-seeking cells are found in roughly equal concentrations at the equator. Adding to this, although north-seeking cells make up the majority of MTB within the waters of the northern hemisphere and south-seeking the southern hemisphere, there is also a minority culture of the opposite cells, again showing no advantage for these few cells. Some MTB also appear to have more magnetosomes than necessary for magnetotaxis, therefore other suggestions have arisen for the role of magnetosomes within the MTB. These suggestions include iron storage, removal of toxic molecules and a source of power to the cell.[57, 58] Kopp & Kirschvink hypothesised that redox changes leading to the transition of magnetite to maghemite could be substantial enough to generate energy and act as a 'magnetosome battery'.[59] This battery could explain how magnetosomes are useful when present in excess or in MTB at the equator.

It is clear that although current literature is able to provide a great degree of speculation in order to determine the ultimate purpose of the magnetosome, there are still parts of this puzzle that don't quite fit. Magnetosomes do not form in aerobic conditions and so are incapable of aiding MTB in the search for optimum oxygen levels when needed the most. Arguments based on the removal of toxic species would appear to make sense, but then why do MTB scavenge? These are the types of questions that are yet to be answered.

The distribution of MTB is immensely widespread – they are found across the globe, in almost all aquatic environments, including sediments of marine, freshwater and brackish water. They are also found across the phylogenetic tree such as *Cocci, Vibrio* and *Spirilla*.[60] Each species of MTB biomineralise magnetite or greigite (Fe_3S_4) within unique organelles known as magnetosomes. These magnetosomes are usually between 50-70 nm and consist of a lipid bilayer membrane, enveloping the single magnetic domain crystal. The magnetosomes arrange themselves in to chains within the cytoplasm of the bacteria. The formation of chains, parallel to the long axis of the cell, is the most magnetically efficient arrangement, maximising the magnetic dipole moment of the cell.[57] Although this characteristic and the presence of flagella is conserved among the MTB, there are also a number

of differences between species. Although all exhibit exquisite control over the synthesis of inorganic crystals within their core, the morphology of these nanocrystals differs greatly between different types of MTB. For example, all alphaproteobacteria synthesise cuboctahedral crystals, whereas others produce cuboidal, spherical or even bullet-shaped minerals. Relatively recently, even extremophiles have been identified. Lefèvre *et al* suggested the presence of thermophilic MTB in hot springs in Nevada and alkaliphilic MTB in hypersaline, alkaline lakes in California.[61, 62] It is these unique properties of the magnetosome, their high purity, uniform morphology and synthesis under ambient conditions that make them promising choices for future biomedical and biotechnological applications. Some MTB are capable of a phototactic response, responding negatively to white light, therefore directing them deeper into the aquatic environment, to lower oxygen concentrations.[57]

1.4.4.1 Magnetosomes as a source of MNPs

There are numerous issues surrounding the use of magnetosomes themselves as potential sources of MNPs. Although they do show extremely promising properties, it would be almost impossible to scale their production to an industrial scale. There are also problems surrounding the sterilisation and presence of endotoxins. Issues such as long cell-dividing times and sensitivity to light, temperature, redox and oxygen gradients and media constituents make it difficult and time-consuming to culture even the smallest amount of MTB in the laboratory.[57] A more promising alternative would be to mimic the process of biomineralisation *in vitro*. For this to be a viable option, a much deeper understanding of the steps and proteins involved needs to be established.

1.4.5 Magnetosome membrane specific proteins

Five main steps are required for the generation of magnetosomes and synthesis of magnetite crystals.[58] The first step is membrane invagination and biogenesis, this is a prerequisite for magnetite synthesis as the formation of compartments within the cell provides an optimal chemical environment for biomineralisation, whilst protecting the MTB from possibly toxic by-products such as oxygen radicals and iron cations. The ability to form magnetosomes from invagination of the cytoplasmic membrane requires a host of proteins that enable the bending and breaking of the lipid bilayer through the process of lowering the energy barrier of exposing hydrophobic groups to the aqueous conditions within the cell. The second step is protein sorting. It has been proven that the proteins that occupy spaces in and on the magnetosome membrane (magnetosome associated membrane – MAM and magnetosome membrane specific – MMS proteins) differ from proteins of the cytoplasmic membrane. These MMS and MAM proteins are ONLY present in the magnetosome. Therefore, a process must be adopted, following the invagination of the cytoplasmic membrane, to recruit and sort proteins into the magnetosome. The third step is formation of chains. The separated

compartments are grouped and held together to form chains. It is these chains that are capable of functioning as a compass needle, orientating the MTB along magnetic field lines. Specific proteins and filaments are essential to this step, evident from many gene knock-out studies, of which a couple will discussed. It is not until step four that biomineralisation occurs. It is during this step that iron needs to be transported into the cell and then into the magnetosome, initiating crystal nucleation and growth. There are various biomineralisation proteins that are essential here, many of which are thought to control the size and morphology of the forming crystal. The final step is crystal maturation.[58] The deletion of a number of genes has been proven to alter the morphology of the resultant nano-crystals produced. These effects range from minor misshaping, to the complete lack of magnetite NP synthesis. The magnetosome membrane proteins involved in each step will be discussed in more detail below.

A large number of magnetosome proteins are encoded by gene clusters that sit within a magnetosome island on the genome. The presence of a genetic island such as this, is most commonly associated with pathogens.[58] The magnetosome island of AMB-1 encodes roughly one hundred proteins and like other MTB, it plays a vital role in all the steps leading to magnetite biomineralisation.[63] Because this group of genes is present in a wide-range of MTB, it is likely that magnetosome biogenesis was only introduced once during evolution, likely during the period where the Earth had a microaerobic environment and the MTB required ancient forms of respiration.[58]

Murat *et al* used multiple deletions of gene clusters within the magnetosome gene island to identify which genes appear to be involved in membrane biogenesis is AMB-1.[64] As mentioned above, the majority of the magnetosome proteins are not present in the cytoplasmic membrane and so a protein-sorting stage is essential to recruit and distribute the necessary proteins. One of the most prominent proteins involved in protein sorting is MamE. MamE is a protease enzyme which contains a number of heme-binding domains. It is likely to function as another marker protein, providing a platform for the recruitment of a number of other magnetosome proteins, including MamM, MamN and MamO. Upon deletion of *mamE* by Murat *et al*, the localisation of all the other magnetosome proteins was dramatically impaired, indicating the essential nature of the protein sorting abilities.[64] There were also no magnetite crystals mineralised, however, empty magnetosome membranes were still visible – this was also true for the deletions of *mamO*, *mamN* and *mamM* but these deletions did not alter the localisation of the magnetosome proteins as was the case with *mamE*.[64]

A separate group of proteins is required for chain formation in MTB. In AMB-1, the chains of magnetosome membranes are established prior to the initiation of biomineralisation (this is not the case for all types of MTB). An important gene encoding proteins for this process is *mamK*, it is vital as it encodes proteins required for the generation of actin-like fibres which are thought to aid chain assembly. Komeili *et al* suggested that MamK is associated with a key gene cluster, mamAB, and may be involved in the formation of a structural protein scaffold for the assembly and organisation of the magnetosome chain.[65] The group were also able to show that the deletion of mamK gave mutants that contained magnetosomes localised in a random fashion, with no obvious chain formation. A similar, but not so substantial effect is witnessed following the deletion of *mamJ,* a gene directly upstream from *mamK*. Scheffel *et al* observed bent magnetosome chains in MTB with *mamJ* removed.[66] The group proposed that this is due to the co-function of MamJ and MamK, with MamJ aiding interactions between MamK and the magnetosomes.[58, 66]

Following the production of magnetosome membranes, and their alignment into chains, iron must be transported into the vesicles in order to initiate biomineralisation. The mechanism of iron transport is still largely unknown, and it is thought that maybe the process is fairly generic in comparison to other systems utilised by other organisms for the transport of metal cations. It has been known for a number of years that AMB-1 use siderophores. Siderophores are small, iron-chelating molecules which function to sequester iron from the surrounding environment and bind and transfer ferric iron across the cell membrane.[67] Although these molecules are likely to have a role in magnetite biomineralisation, this role is unlikely to be in iron transport. Calugay *et al* showed that siderophores in AMB-1 are not functional until later in the mineralisation process when iron levels are depleted in the surrounding environment.[68] One magnetosome membrane protein that may be utilised in iron transport is MamA, which exhibits activity in active transport of iron when expressed in *E.coli*.[58] A further insight as to why iron transport is not more transparent in MTB is that the biomineralisation of magnetite may be initiated outside of the magnetosome, followed by the transport of magnetite precursors into the organelle. This was suggested following Mössbauer spectroscopy performed by Frankel *et al*.[69] These findings are still debated.

The involvement of magnetosome membrane proteins in iron transport and the mechanism for the initiation of biomineralisation is still unclear. Therefore, the process and proteins required for crystal maturation and control are at the forefront of research due to its possibility to unlock a completely novel toolbox for the *in vitro* synthesis of magnetite nanoparticles. There have been a number of deletion studies that have been found some effect on the resultant inorganic crystal. These effects

range in how drastically the magnetosomes differ from the wild-type. For example, deletion of the *mms6* gene cluster (containing *mms6* and *mmsF*), *mamC*, *mamD*, *mamG*, *mamR*, *mamS* or *mamT* causes a reduction in the size of the mature crystal; whereas deletion of *mmsF, mamR*, *mamS* or *mamT* results in major deformities in the crystal morphology, size or shape.[64, 70] It is the apparent functionality of some of these proteins *in vivo*, that has led to further investigations of their capabilities in magnetite synthesis *in vitro*.

One protein studied using *in vitro* synthesis reactions is Mms6. Mms6 is a small protein that tightly associates with the forming magnetite crystal and as well as aiding the control of biomineralisation *in vivo*. Deletions of *mms6* produced crystals with a lower aspect ratio and smaller size compared to wild-type particles, it also resulted in unusual, high energy morphologies and crystal facets such as the unstable (100) face of magnetite.[71] The properties and characteristics of Mms6 were reported by Arakaki *et al*, in addition to other tightly bound proteins: Mms5, Mms7 and Mms13.[72] The *mms6* gene encodes for a protein of 12-15 kDa, however proteins extracted from MTB were substantially truncated, with sizes around half of that expected. Other intriguing characteristics include the overall negative charge of the truncated protein, concentrated at the acidic C-terminus. This is unusual when compared to other biomineralisation proteins which tend to have regions of positive charge. It has been hypothesised that this charged nature promotes the binding and concentration of iron ions.[47] Mms6 also contains a glycine-leucine repeat motif common in self-assembling structural proteins, such as silk fibroin. This motif is thought to promote the self-assembly of Mms6 to form protein rafts in the membrane.[73] The negative residues are hydrophilic and lie on the outside of the protein raft, these residues have been observed to bind metal cations such as iron (III), calcium (II) and magnesium (II), with some degree of specificity as they do not appear to bind zinc (II), nickel (II) or copper (II).[72] Functioning as an iron binding agent strengthens the idea that Mms6 is required to promote nucleation of the magnetite crystal. The N-terminal is hydrophobic and sits on the inside of the proteasome.[47]

When added to RTCP Mms6 showed some degree of control over the size and morphology of the particles synthesised. The particles had a narrow size distribution, around 21 nm in diameter and a cuboidal appearance when observed under the transmission electron microscope (TEM). In addition to this the sample had much higher purity in terms of magnetite compared to other RTCP reactions where other iron oxide contaminants are common.[72] A reduced size distribution of MNPs were also observed on the addition of Mms6 to POFH reactions, however in this case there appeared to be two species of particles forming, one group similar to particles synthesised in the control reaction

and one group similar to the particles produced by RTCP in the presence of Mms6. There the process is thought to be dependent on the ratio of iron to Mms6 *in vitro*.[74] These findings were a huge step forward in mimicking biomineralisation *in vitro*. Another biomineralisation protein, Mms13, was also isolated alongside Mms6 however it was found to be highly insoluble and so little has been done with this wild-type protein *in vitro*.

Finally, another magnetosome protein with promising activity *in vitro* is MmsF. MmsF is a transmembrane, biomineralisation protein, consisting of three transmembrane helices with a flexible loop region located on the inside of the magnetosome, linking helices two and three. Murat *et al* identified the major regulatory role of MmsF *in vivo*.[75] The researchers were able to show this through sequential deletion experiments involving an 8-gene region named R3, this region contained the *mms6* gene cluster and *mmsF* gene. Upon deletion of the entire region, the crystals synthesised by the MTB were extremely misshapen and reduced in size. It was the consequential deletions that indicated that this effect was primary due to *mmsF*. In this work, they also demonstrated that magnetite nucleation was largely unaffected by MmsF, however crystal growth was inhibited.[75]

The findings by Murat *et al* indicate the essential function of MmsF in magnetite crystal growth within the magnetosome. This led to the investigation of MmsF activity *in vitro*. Rawlings *et al* studied the protein behaviour and concluded MmsF self-assembled into water-soluble proteasomes, similar to the response observed for Mms6, although Mms6 does not form a micelle.[76] The addition of MmsF was found to be responsible for the improved quality of magnetite NPs synthesised by RTCP. The particles had a narrower size distribution, and larger average diameter compared to control synthesis. The particles also appeared to display a much more defined, homogeneous morphology.[76] The improvement of these properties consequently resulted in improved magnetic properties of the MNPs, for example a great increase in the saturation magnetisation of the particles.[76] There is still a lack of knowledge and understanding surrounding the activity and mechanisms of the magnetosome proteins, with their use *in vitro* only arising in the last five to ten years. However, research into these proteins continues to develop at a rapid pace. These proteins offer an alternative to high temperature, high pressure magnetite synthesis reactions, that often rely on the presence of toxic, organic solvents are precursors. Mimicking processes witnessed in nature opens the door to green methods of synthesis that compete with the control possible with harsher routes. The problem with taking inspiration from biomineralisation proteins however, is that they are often transmembrane proteins that are inherently insoluble, difficult to extract and difficult to work with.

1.5 Biopanning

Novel peptide sequences that possess biomineralisation capabilities can be identified using biocombinatorial approaches. One approach analyses sequences expressed naturally by an organism and investigates the binding of said protein to a material of interest. A different approach can be used to identify artificial protein or peptide sequences that have a high affinity for a target material, or specific facet. Displaying of artificial sequences is more common than using sequences expressed naturally as it is often difficult to pin-point a biological function to a single protein, and even when this is possible it is difficult to locate and study the single protein due to the similarity between various proteins.[77] Both of these methodologies: development of naturally occurring binding proteins and the development of artificial binding proteins, can utilise phage display. The idea of phage display was introduced more than thirty years ago by the scientist George Smith. Since then other similar techniques have been developed, including: cell-surface display, yeast display, ribosome display, epitope mapping and receptor-ligand identification.[78] For phage display specifically, interesting peptides, proteins or antibody fragments are inserted into a phagemid vector or into the phage genome, basic models of the technique allow for a simple 'fishing' action being adopted that allows the interaction between a phage and single target to be confirmed. Today, with more sophisticated methods adopted and high-throughput synthesis of clone libraries, millions, if not billions of different ligands can be screened in only a few days.

The most widely used method of phage display is the filamentous phage method, where a bacteriophage virus, such as M13 or Fd, that is able to infect and replicate within *E. coli,* is used. DNA encoding millions of peptide sequences are batch cloned into phagemid vectors, generating fusions to genes which encode for specific coat proteins. Two common bacteriophage coat proteins involved in forming fusions are pIII and pVIII. Coat protein pIII is the minor coat protein and is present in five copies at the tip of the phage filament, with the peptide sequence fusing to pIII N-terminus. The other protein, pVIII is termed the major coat protein due to 2500 copies present. The fusion of the ligand to a coat protein ensures that the sequence is displayed on the surface of the virus, enabling binding between the ligand and a target material. The target material is immobilised, and the bacteriophages are washed over the material. Any ligands that do not bind are washed away in subsequent washing steps. There are a number of methods for immobilisation and capture. Magnetic materials are beneficial as the particles can be magnetically extracted with ease, however if the binding material is an antigen or other macromolecule additional steps are required. One example used is biotinylation of the target molecule and then using streptavidin coated beads or column for the capture and separation of the molecules.[77] Once the material, with the ligands bound, has been captured, the bacteriophages need to be eluted from the surface of the target and

amplified. Elution is often carried out using sonication or pH changes, the eluted phage is used to infect bacteria for identification and amplification ready for another round of binding and washing – termed biopanning (figure 7).[77] Several biopanning rounds are conducted to ensure specific binding with a high affinity for binding between the partners. The final stage is DNA sequencing to identify which peptides or proteins were most successful in binding to the target.

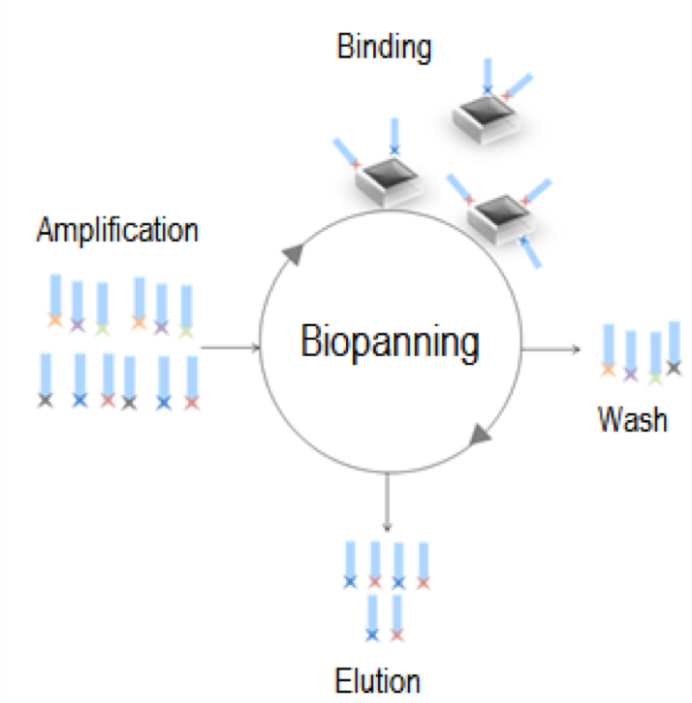

Figure 7 The basic stages in biopanning. The blue rods represent a phage support with the coloured ends representing various peptide sequences. Firstly, the phage are bound to the target molecule (i.e. [100] plane of magnetite). Any non-bound ligands are washed away, before those that have bound strongly and specifically are eluted (i.e. using varying pH washes). Finally, those ligands that have been eluted are amplified using the lysogenic nature of the phage in E.coli cells.

Peptide binding to inorganic materials has been a promising area of research in materials science for applications in nanotechnology and biomedicine. One recent example of the use of phage display and biopanning to identify new peptide binding partners for inorganic minerals is the work by Rothenstein *et al*, investigating twelve amino acid-long peptides interacting with zinc oxide surfaces – zinc oxide is known to be useful semiconductor.[79] The group were specifically interested in the interaction with the zinc surface termination (0001) and the corresponding oxygen surface termination point. A library containing roughly 2.7 billion peptides was displayed on the pIII coat protein of the bacteriophage M13, the phage was allowed to bind, and any unsuccessful binders were washed away before amplification and DNA sequencing of promising peptides. To study the binding in more depth Rotenstein and the group used nuclear magnetic resonance (NMR) spectroscopy and were able to show that polar interactions of ionic components play an important

role in binding, not only the formation of salt bridges that are vital for specific binding. The specificity and strength of binding was found to be dependent on many different types of non-covalent bond: ionic interactions, hydrogen bonds, dipole interactions, Van der Waals forces, as well as hydrophobic effects. In conclusion, sequences enriched with histidine residues bound well to the zinc and oxygen terminated surfaces and as expected for oxygen-termination acidic residues were depleted. Interestingly, lysine and aspartic acid were both enriched for zinc-termination – as these residues have opposite charges it is another indication that the interaction cannot only be charge dependent, if this was the case it would be expected that one residue would be significantly enriched for zinc-termination while the other would be not be enriched at all.[79]

As suggested above, phage display is not only used to screen artificial peptide sequences, but also to investigate interactions of naturally occurring proteins or peptides and the interaction with specific minerals faces. For example Baumgartner *et al* did not use phage display for the direct assessment of peptide sequences, but instead to identify novel *in vivo* biomineralisation proteins, without the need for mutagenesis experiments.[80] A biocombinatorial approach, utilising a homology search and synthetic mineralisation reaction was successful in identifying biomineralisation proteins, naturally occurring in MTB, that influence nucleation of magnetite *in vitro*. From the results it was concluded that *in vivo*, nucleation required positively charged residues on a protein, interacting with negatively charged atoms on the crystal surface, therefore negatively charged groups on the proteins are likely to inhibit nucleation, but may become vital in crystal growth stages.[80] Thermodynamically, this makes sense as a repulsive charge interaction between two negatively charged surfaces is energetically unfavourable, leading to higher surface tension and nucleation inhibition. Kinetically, however, the interaction between iron ions and the protein is much faster than the interaction with iron oxide and so this stage occurs to trap an amorphous precursor state.

These interactions began to give an insight into the activity of MamJ *in vivo.* Baumagrtner *et al* suggested that MamJ binds ferric and ferrous ions, inhibiting magnetite nucleation and promoting the formation of amorphous precursors. Although this paper introduces some interesting and novel methodology, further analysis and explanation of the conclusions drawn could be beneficial. For example, it is possible that the function of MamJ is over exaggerated as the protein does not sit in close proximity to the site of nucleation in the magnetosome and so it is hard to visualise how the affects concluded here could be possible. In addition to this it is unclear how positively charged groups can aid crystal nucleation as the nucleation state of magnetite involves cationic iron species and there are no crystal surfaces available at this point. This work does however indicate the

importance and vast applicability of phage display as a technique and demonstrates how this technique can be used in conjunction with MTB.

1.6 Mimicking naturally occurring proteins using protein scaffolds

The previous sections have given an overview of the types of naturally occurring proteins that show promise for the improvement of magnetite synthesis. Methods of identifying these proteins and protein sequences, using phage display has also been discussed (section 1.5). Using these in wild-type form can prove to be problematic due to poor expression in *E. coli*, low solubility, the need for extensive purification and therefore inevitably low yields. Therefore, it is important to consider the use of protein scaffolds. These scaffolds are discussed below.

1.6.1 Principles for the design of a peptide displaying scaffold

For decades antibodies have been the most widely used binding proteins in biotechnology and for biomedical applications. This is largely due to the unrivalled affinity and specificity they have shown in binding target antigens. For the first time, this is being challenged by antibody alternatives. Recently, intense research has been conducted into developing novel alternatives to antibodies, retaining their useful characteristics and improving on their less than desirable properties such as their large and complex, multimeric nature and the requirement for expensive mammalian cell cultures for production. A wide variety of artificial scaffold proteins have been developed in the last twenty-five years. Peptide displaying scaffold is a generic term for an engineered protein with the ability to display a desired peptide sequence, although these scaffolds do not necessarily possess any specificity, the peptides displayed are often designed to bind a target molecule with similar or higher specificity and affinity than an antibody. A protein scaffold designed to be an artificial antibody must meet some extensive criteria. They should be: small, preferably under two hundred amino acids long; water soluble; robust in terms of thermal stability, thermodynamic stability and ability to withstand a range of pH; the synthesis should be able to be scaled for industrial production; single domain with high expression levels in *E. coli*, therefore making the production much cheaper then antibodies which removes the need for animal models. Most proteins that have been engineered for this function also lack cysteine in their primary sequence, this is for two principle reasons: the first reason is that this ensures rapid and specific protein folding in the cytoplasm of *E. coli* as it is not dependent of the formation of disulphide bridges; the second is that a single cysteine may be introduced as required for site-directed attachment of dyes, drugs or antibodies. Below are a few examples of artificial antibody alternatives that have shown real promise in the laboratory, with some even undergoing clinical trials as therapies and diagnostics for different diseases.

1.6.2 Affibodies

Affibodies (see figure 8 below) are scaffold proteins consisting of a triple alpha-helical bundle, developed by Nord *et al* over twenty years ago.[81] The scaffold was generated using a combinatorial library of alpha-helical immunoglobulin binding *Staphylococcal* proteins, enabling the formation of a consensus sequence for the structure, therefore exhibiting the most favourable chemical and biophysical properties. This method yielded a novel protein that was small (around 6.5 kDa), monomeric, thermally and chemically stable and generally robust and was therefore a real possibility to use in place of antibodies for targeted binding proteins. Since the development of affibodies, a large number of binding loops have been identified and incorporated into the scaffold. The scaffold protein itself is based on the Z-domain of *Staphylococcal* protein A, a 58 amino acid domain that rapidly self-folds. Incorporated into this single domain is a 13-residue variable region (VR) to form libraries of millions/billions of different sequences, where the variable binding region is displayed as a flexible hairpin loop. Phage display was used for the identification of specific sequences. Mutant Z-domain genes were inserted into a phagemid vector and libraries containing millions or billions of peptide sequences were generated and screened. These sequences were biopanned against a range of different target molecules including (but not limited to): DNA polymerase, insulin and transferrin. Successful binders were then expressed and amplified in *E. coli*. The resulting affibodies showed a high affinity for the binding targets, with dissociation constants on the pico-molar to micro-molar scale.[81]

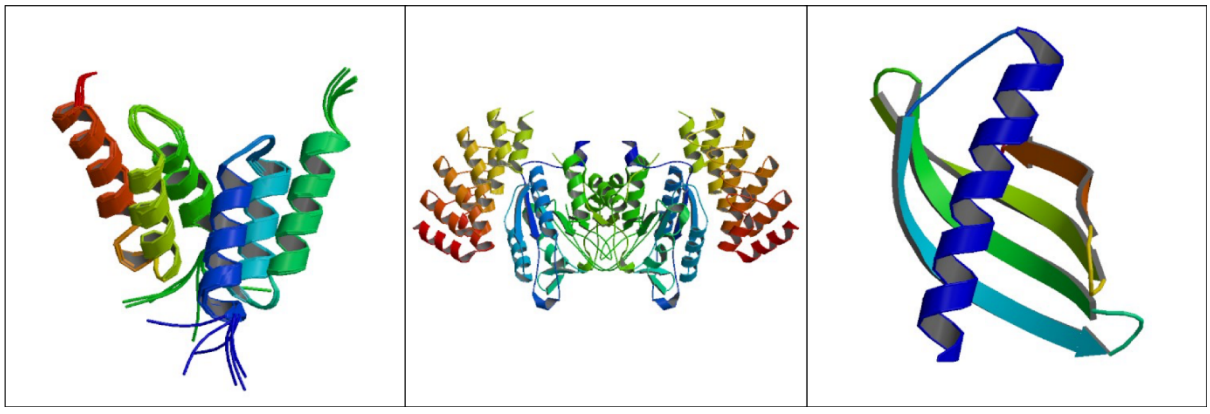

Figure 8 From left to right: Affibody (PBD: 1H0T)[82]; DARPin (PDB: 4JB8)[83]; Adhiron (PDB: 4N6T)[84] Each are examples of well used peptide displaying scaffold proteins.

Usefully, the affibody peptide displaying scaffold was designed to contain no cysteine residues within the structure, as discussed above, which enabled the protein to be mutated to contain a single thiol group and therefore introduce site-specific binding of molecules such as fluorescent probes, through a thiol-based interaction. An example of this came from Lundberg *et al*, where

affibodies, designed to bind to the human epidermal growth factor receptor (HER2), were coupled to the fluorescent tag, Oregon green 488, through a C-terminal cysteine residue.[85] This complex was then used to successfully track expression levels of HER2 in cancerous cells with the aid of flow cytometry and confocal microscopy.[85]

There has also been heightened interest in designing and generating new capturing agents for use in affinity chromatography. The use in protein purification and binding studies meant that this was an interesting new field of application for affibodies. In the early 2000s Nord *et al* were able to show specific targeting of taq polymerases and apolipoprotein A-1M using affibodies as capture agents in affinity chromatography.[86] These proteins were well suited for this function due to their compatible biophysical properties and robust nature.

In addition to the applications of affibodies in imaging and protein purification, they have also proven to be useful in biomedicine, with examples of this scaffold even reaching clinical trials in Europe.[87] Radio-labelling of affibodies has been on interest, with early research involving non-specific labelling of the scaffold, these methods included non-specific iodination and the attachment of radioactive groups through interaction with the primary amine groups of lysine residues on the protein.[87] However, specific-labelling appeared much more desirable and the attachment moved towards the use of a single cysteine residue, incorporated into the scaffold, with functional groups coupled using thiol chemistry. The affibody ABY-025 reached clinical trials in Germany in 2008 and through the substitution of a few amino acids residues within the affibody scaffold, the thermal stability and hydrophobicity were both increased substantially, whilst retaining the function of the protein both *in vivo* and *in vitro.* The specific affibody was HER2-specific and coupled to maleimido-DOTA via a single cysteine residue. The complex has shown great promise, with no toxicity witnessed in rat or monkey subjects when used in treatment of metastatic breast cancer.[88]

1.6.3 DARPins

Designed Ankyrin repeat proteins (DARpins) are monomeric, single domain scaffold proteins that show real promise as alternatives for antibodies. The repeat units consist of thirty-three residues, with tight, regular packing. For each repeat (of which there tends to be four, five or six per scaffold) a β-turn is directly proceeded by two right handed, antiparallel α-helices. The rapid folding of the full protein is driven thermodynamically, generating an energetically favourable hydrophobic core and a large, solvent-accessible, hydrophilic surface. Ankyrin proteins are a common class of binding proteins found in nature. Examples from this class of proteins include ANK2 and ANK3, these proteins were identified in human brain and neuron cells and play a role in the distribution of

membrane proteins such as the Na^+/Ca^{2+} exchanger.[89, 90] ANK3 is also believed to play a role in bipolar disorders.[91] Exploiting the high number of naturally occurring proteins of this type, and the use a consensus design, enabled Plückthun and his group at the University of Zürich to establish the Ankyrin sequence with the highest stability and most favourable biophysical properties.[92] Thousands of Ankyrin protein sequences were aligned. This followed the idea that the most conserved residues and regions would have each evolved due to their useful characteristics. During the design of the scaffold the residues proline, glycine and cysteine were avoided. Proline and glycine disrupt α-helical secondary structure. Within the designed scaffold, six variable positions per repeat unit were incorporated. These variable loop regions sat between the α-helix in each repeat. It is this accessible region that is available for binding a specific target molecule.

Phage display and ribosomal display were used to identify peptide sequences that could be inserted into the VRs on the DARPin and binding with high affinity and specificity to a desired target.[92] During the phage display sequence, the DARPin was fused to the pIII coat protein of the bacteriophage and expressed in *E. coli*. The proteins were highly soluble and underwent rapid folding in *E. coli*, making them extremely easy to study. The complexes identified and generated were found to have affinities in the region of pico-molar (k_D) for their targets. These DARPin scaffolds have been proven to have a wide range of applications, especially within biomedicine. Examples include their use as real-time sensors for protein conformations;[93] the use as crystallisation chaperones; they are able to induce apoptosis in tumours by interrupting the signalling cascade.[92] Good safety and efficacy levels in treatment of macular degenerative diseases has propelled these scaffolds into phase I/II clinical trials.

The first DARPin scaffold to reach clinical trials was named MP0112.[94] It acted as a vascular endothelial growth factor and was used to treat wet age-related macular degeneration – a disease of the eye caused by excessive swelling of the blood vessels under the retina. The DARPin drug was administered via intravitreal injections and was documented to be safe and well tolerated by the patient, with the potential to be used for treatment of a range of retinal diseases in the future.[94] Another DARPin that is currently undergoing phase I/II trials is termed MP0250.[95] This complex is being used to treat cancerous neoplasms in patients that have a life expectancy of over three months. The current trials investigate the effects of the drug in the human body, studying how it is altered in physiological conditions and also how it is removed from the body. Molecular Partners AG, who have generated the drug and carried out the trials are analysing the safety, tolerability and drug levels in the blood to identify whether this could be a viable cancer treatment in the future.

There are also on-going investigations into DARPins as a form of cancer therapy which have not yet reached clinical trial, but none-the-less appear to show promising results. An example is HER2-specific DARPins which have shown strong, cytotoxic effects on tumours that over-express HER2.[96] The scaffold proteins were found to cause a reduction in movement of the HER2 molecules in relation to the cell membrane, in-turn leading to the loss of phosphorylation and therefore a major interruption in the signalling process. The cell surface receptors were bent in the presence of the DARPins which caused the specific kinases to be unable to bind and interact, inhibiting the signalling process and resulting in cell-specific apoptosis without the use of a toxin.[96] Destruction of cancerous cells, without the need for a toxin that would also result in nasty side-effects is an important break-through in the field of oncology.

1.6.4 Adhirons

The Adhiron is a monomeric, thermally and thermodynamically stable, peptide displaying scaffold consisting of ninety-two amino acids. Due to codon optimisation during the design process, it benefits from high expression levels in *E. coli*.[84] As with the previous scaffold proteins described above, the exceptional stability was introduced into this artificial protein using the consensus sequence design concept.[97] The Adhiron was produced using the consensus sequence of plant phytocystatins - small proteins that are found in rice and corn; they play a role in the inhibition of cysteine proteases.[98] Fifty-seven homologous sequences were aligned, yielding a protein containing two variable loop regions, displayed on the surface, ready for binding to a target. Nine interchangeable amino acids were mutated and screened against different target molecules in order to determine the molecular recognition abilities and to test stability. During the design of the Adhiron, a heat enrichment step was also added to ensure the scaffold displayed the highest possible thermal stability (T_M in excess of 101 °C).[84] Tiede *et al* were able to determine the crystal structure of the protein using X-ray crystallography.[84] The structure consisted of a four-strand beta-sheet centre with a central alpha-helix. The relative size was around 12 kDa.

Following the introduction of random loop regions a phage display library was compiled containing approximately 1.3×10^{10} variants and as with most, if not all libraries, there was no bias towards any amino acid (other than no cysteine residues had been added for reasons described previously).[84] The lack of bias was important to ensure any specificity found in binding does not come from an original bias. For phage display the Adhiron was fused to the pIII-coat protein of the bacteriophage and screened against yeast-SUMO (small ubiquitin-like modifier). Interestingly, twenty-two distinct Adhirons bound strongly and specifically to yeast-SUMO (and did not appear to bind human-SUMO).

The strength of these interactions was on the low nano-molar scale and confirmed using phage-ELISA (enzyme-linked immunosorbent assay).[84] The common occurrence of proline and glycine residues between amino acids two and five gave Tiede *et al* reason to believe that some structural aspect could play a role in binding.[84] Other target molecules were also successfully screened by the group, including: fibroblast growth factor (FGF1) and platelet endothelial cell adhesion molecule (PECAM-1;CD31). Both of which showed similar levels of affinity and specificity to SUMO-binding Adhirons.[84] This initial phage display research was later followed by a further investigation into SUMO binding. Hughes *et al* incorporated peptide sequences into the Adhiron scaffold that were able to efficiently function in the isolation of naturally occurring binding proteins that have a major role in inhibiting SUMO-dependent protein-protein interactions, both in cells and synthetically.[99] These findings may help aid the regulation of a number of cellular processes as SUMOylation is an essential posttranslational reaction which hugely affects numerous biochemical pathways.[99]

1.6.5 Other peptide displaying scaffolds

Although the engineered protein scaffolds discussed above are some of the most extensively used, showing great promise in their respective fields, there have been over one hundred similar artificial scaffold proteins designed and published, each with their own unique functions. Table 2 below introduces some of these.

Table 2 Examples of protein display scaffolds and their properties

Scaffold	Year developed	Size	Secondary structure	Model structure	Target	Affinity (k_D)
Repebodies[100]	2012	29 kDa	Repeat β-strand-turn-α helix in horseshoe-shape fold	Lymphocyte receptors	Interleukin-6	nM
Anticalins[101]	2000	66 kDa	β-barrel made of 8 antiparallel β-sheets	Libocalin	Digoxigenin	nM
Fibronectins[102]	1998	25 kDa	β-sandwich	Immunoglobulin domains	Ubiquitin	μM-nM
Kunitz domains[103]	2006	7 kDa	2 antiparallel β-sheets with 1 or 2 α helix	Kunitz-type protease inhibitors	Kallikrein	pM
RAD[104]	2017	28 kDa	Antiparallel β-shets linking 2 α helix	Globular ATPase domain of *Pyrococcus furiosus*	CK2α kinase	nM
Armadillo repeat proteins [105]	2012	31.5 kDa	3 α-helix	Armadillo	Neurotensin	μM
Fynamer[106]	2014	7 kDa	β-sandwich	SH3 domain of human Fyn tyrosine kinase	Proinflammatory cytokine interleukin-17A	pM
Centyrin[107]	2014	10-20 kDa	β-sheet	Fn3 domains of hTenascin C	Hepatoctye growth receptor factor	nM-pM

1.7 Aims

The introduction to this work has identified numerous obstacles to the synthesis of MNPs for use as biomedical agents. Well-defined and controlled magnetic properties are required for NP in therapies and diagnostics and these magnetic properties are heavily dependent of the chemical and physical properties of the particle. Size, shape, morphology and composition all affect the magnetic response of the MNP. It is for this reason all of these properties need to be tightly controlled during synthesis. Current synthetic methods for the production of magnetite NPs rely on high temperatures and pressures and often require the addition of expensive and toxic organic solvents. With the scientific world pushing towards more environmentally acceptable routes, these conditions must be addressed. RTCP reactions were introduced as an alternative route of synthesis to avoid the use of these conditions. However, although the NP products can be altered slightly in these reactions by changing the iron (III) to iron (II) ratios, the reaction time and the base used, particles produced by alternative methods still remain vastly superior.

The use of protein additives, for example proteins found in MTB has been discussed. Although it is clear that these biomineralisation proteins help control the production of magnetite nanoparticle *in vivo*, their activity *in vitro* is not well understood. In addition to this, the proteins are often difficult to work with. They are transmembrane proteins which inherently exhibit poor solubility in aqueous solutions, therefore resulting in poor yields and extensive purification process to enable them to be studied *in vitro*. It is for this reason the use of protein displaying scaffolds has been investigated.

The aim of my project is to synthesise well-defined, monodisperse magnetite NPs under ambient conditions and in an aqueous media. The formation of these particles will be controlled by the addition of water soluble protein additives. These proteins consist of active peptide sequences displayed on different protein scaffolds with the peptides being developed artificially and as a natural mimic (inspired by MTB). It is also my aim to provide a better understanding of how and why these proteins behave in this way and what makes them capable of controlling the synthesis. In addition to this, methods of functionalisation for the conjugation of therapeutic and diagnostic agents will be investigated with the aim to provide simple attachment using a variety of different methods.

Chapter 3 will introduce the Adhiron scaffold and its development into a magnetite interacting protein. It will show for the first time how this protein is capable of controlling the production of magnetite nanoparticles *in vitro*, preferentially promoting the formation of the cubic [100] face of magnetite. Chapter 4 will then provide conjugation routes for the attachment to the magnetite surface and how these conjugates can subsequently be used in biomedical applications. The novel uptake of the MNP-antibody conjugates into cancer cell lines will also be discussed. A new scaffold, termed the coiled coil will then be introduced in chapter 5. The design and the development will be analysed before proving it can be used to control magnetite synthesis by displaying important loops that mimic biomineralisation proteins found in MTB. Mutagenesis studies alongside the study of known homologs will aim to provide an insight into the mechanism of action of biomineralisation proteins *in vitro*.

Chapter 2: Materials & methods

2.1 Sterilisation by autoclaving

The autoclave sterilises equipment and solutions by subjecting them to high temperatures and pressures. The most common cycle is heating the contents to 121 °C for 15 minutes. A vacuum pump removes trapped air before sterilisation begins.

2.2 Molecular cloning

2.2.1 Oligonucleotide primer design

Primers were designed to amplify desired sequences of DNA. They were also used to generate sticky-ends at the termini of these sequences, needed for restriction enzyme digest and sticky-end ligation. The primers are specific for the DNA sequence of interest with the sense primer having a sequence complementary to the start of the reverse strand (3'-5') and the antisense primers have a sequence that is the reverse compliment to the end of the forward DNA strand (5'-3').

Oligonucleotide primers were designed using the PrimerX server. The primers were designed based on optimum primer length, guanine/cytosine (GC) content and melting temperature. These characteristics were calculated using Oligo Cal[108]. To ensure high specificity the primer length was designed between 18 and 30 base pairs, and the primer annealing temperature was specified between 52°C and 72°C. Above this temperature there is a higher probability that secondary annealing may occur. The melting temperature is described as the temperature at which half of the double stranded DNA becomes single stranded and is dependent on the amount of hydrogen bonding between strands. The total GC base pair content was therefore set between 40% and 60%. The termini of the primers generally featured a GC sequence to act as a clamp, promoting specific binding. The primers were the synthesised from Eurofins at 0.01-0.05 µM, in salt-free, lyophilised aliquots.

2.2.2 Polymerase chain reaction (PCR)

The polymerase chain reaction (PCR) uses a specifically designed pair of primers and a thermally stable DNA polymerase to produce copies of a specific DNA sequence. The polymerase extends the primers in the 5'-3' direction using a DNA template, amplifying a region of DNA in an exponential manner.[109]

The reagents are shown in table 3. The buffer maintains optimal conditions for the polymerase activity. Plasmids, gene strings or previously amplified DNA fragments were used as the template DNA. The primers flank the start and end of the desired DNA sequence. These primers were then

extended during the reaction utilising the polymerase and deoxyribose nucleic acid triphosphate (dNTP) building blocks. The magnesium from $MgSO_4$ acts as a cofactor for the enzyme - although the magnesium is not consumed in the reaction, the reaction cannot proceed in its absence.

Table 3 Novagen KOD Hot Start DNA Polymerase Protocol detailing the reaction components

Component	Volume (µL)	Final Concentration
10X Buffer for KOD Hot Start DNA Polymerase	5	1X
25 mM $MgSO_4$	3	1.5 mM
dNTPs (2 mM each)	5	0.2 mM
Water	32.5	MilliQ
Sense (5') Primer (10 µM)	1.5	0.3 µM
Anti-sense (3') Primer (10 µM)	1.5	0.3 µM
Template DNA (20 ng μL^{-1})	0.5	0.2 mM
KOD Hot Start DNA Polymerase (1 U/µL)	1	0.02 U μL^{-1}
Total Reaction volume	50	

Three steps were cycled during the reaction: i) denaturation of the double stranded DNA template, ii) annealing of the primers to the single stranded template, and iii) elongation of the primers using DNA polymerase (figure 9). The extension time is dependent on the length of target product. These steps were repeated several times. A final extension step was required before the reaction reached completion.

Table 4 Novagen KOD Hot Start DNA Polymerase Protocol detailing the steps of the reaction

Step	Time (s)	Temperature (°C)
Polymerase Activation	120	95
Denaturation	20	95
Annealing	10	55
Elongation	10 sec per kilobase.	70
Repeat steps 2-4	x34	
Final Extension	40	70
Hold	∞	4

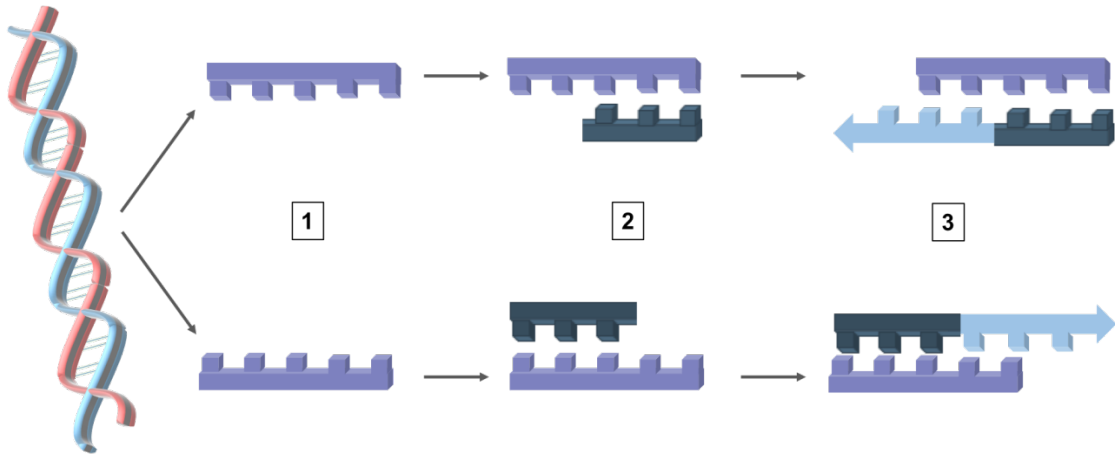

Figure 9 shows a schematic of the polymerase chain reaction. Step 1 is where denaturation of the dsDNA occurs, followed by step 2 where the dNTPs anneal to the ssDNA in a complimentary manner. Step 3 shows the elongation of the DNA.

2.2.3 Agarose gel electrophoresis

DNA gel electrophoresis allows for analytical separation of nucleic acid species.[110] It is used to analyse the size and purity of DNA samples. Due to the inherent negative charge of the phosphate backbone of DNA at neutral pH, fragments are pulled through the agarose gel from the negatively charged anode to the positively charged cathode upon the application of an electric field. The speed at which the fragments travel through the gel is directly proportional to the mass-to-charge ratio – meaning that larger fragments move more slowly and subsequently do not travel as far down the gel. A DNA ladder is used as a marker to determine the molecular weight of the sample. To achieve suitable resolution, the percentage of agarose can be adjusted.[109] The DNA is visualised using a fluorescent dye such as SYBR safe which intercalates DNA, producing a fluorescent signal upon binding, visible when illuminated with UV radiation.

For a 1% agarose gel, agarose (500 mg) was added to tris-acetate EDTA buffer (TAE) (50 mL, appendix 1.1) and heated until the agarose had dissolved completely. SYBR safe stain (5 μL, 10000X

concentrate in DMSO, Invitrogen) was added, and the mixture poured into a mould. A comb was placed in the setting gel to generate wells. After 20 minutes the gel was submerged in TAE buffer in an electrophoresis tray (BIORAD) and loaded with sample (6 μL, consisting of 5 μL DNA and 1 μL 6x mass ruler loading dye, ThermoScientific). Mass ruler mix (5 μL, 103 ng μL^{-1}, ThermoScientific) was loaded in a separate well. The gel was electrophoresed (200 V, 20 mins) before visualising using a trans-illuminator (BIORAD), irradiating the bound SYBR safe with UV light. Images were captured and saved.

2.2.4 PCR purification

A clean-up removed any unreacted starting materials including: primers, dNTPs and salts from PCR products. This was performed using the ThermoScientific GeneJet PCR Purification Kit. The kit utilises a spin column containing a silica-based membrane. The kit is highly efficient with DNA recovery rates close to 100% for sequences between 25 base pairs (bp) and 20 kbp. The kit was used according to the manufacturer's protocol. The concentration of eluted DNA was measured by absorbance at 260 nm.

2.2.5 Restriction enzyme digestion

Restriction endonucleases were used to cleave specific DNA sequences known as recognition sequences. Recognition sequences are often incorporated into primers used during PCR amplification. Restriction enzymes cut the sequence to produce single strand overhangs (sticky ends), which allow the fragment to bind to similarly digested fragments. As the name suggests, these overhangs are then stuck to complimentary overhangs during ligation.[111] The type II restriction endonuclease *Dpn*1 recognises and cuts methylated DNA. The pPR-IBA1 plasmid (appendix 2.1) was engineered to produce proteins with a C-terminal Step-II tag. It is ampicillin resistant and contains Bsa1 restriction sites.

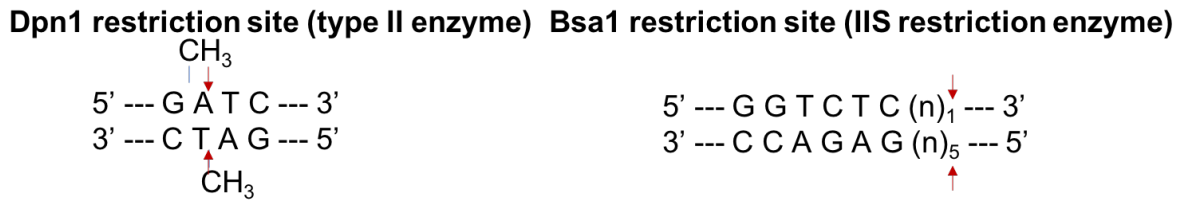

Figure 10 The left shows a methylated DNA fragment with Dpn1 restriction site (red arrows). The right shows the Bsa1 restriction site.

Purified dsDNA was mixed with CutSmart buffer (5 μL, NEB). Following this the restriction enzyme of choice (Bsa1, Nhe1, Not1, or DpnI) was added (1 μL of each). The reaction mixture was made up to a final volume of 50 μL using ultra-pure water and incubated (37 °C, 1 hour). The reaction could also be completed at room temperature overnight. The enzymes were heat inactivated following the completion of the reaction.

2.2.6 DNA Ligation

The insert DNA was then ready to be incorporated into the digested vector to produce a recombinant plasmid.[111] DNA ligase catalyses the formation of phosphodiester bonds between the vector and insert. Digested vector (100 ng) was added to digested PCR product (typically 25 ng). T4 DNA ligase reaction buffer was added (1 μL, 10 x buffer, NEB. T4 DNA ligase, 0.5 μL, NEB) was added and the reaction mixture made up to 10 μL using ultrapure water. The ligation reaction was then incubated (16 °C, overnight) as suggest by the manufacturer instructions. Alternatively, a ligation master mix was used for rapid ligation. The Instant Sticky-end Ligase Master Mix from NEB was used. It is a 2 x T4 DNA ligase mix, ready-to-use. The mixture contains the reaction buffer and enables rapid ligation of cohesive-end (2-4 bp) substrates. For a 10 μL reaction of digested DNA, Instant Sticky-end Ligase Master Mix (10 μL) was added. The 10 μL mixture contained 1800 cohesive end units of T4 DNA ligase. The recombinant plasmids were then ready to be used in the cellular transformation of competent *E. coli* cells.

2.2.7 Preparation of chemically competent cells

Competent cells were produced using a treatment of calcium or rubidium chloride salts. This makes the membrane permeable to plasmid DNA, promoting the attachment of the DNA to the cell membrane. Two types of chemically competent cells were required: XL10-Gold® and BL21(DE3). The respective transformation efficiencies were: >5 x 10^9 cfu μg^{-1} DNA and >1 x 10^8 cfu μg^{-1} DNA. XL10-Gold® cells were engineered to transform large DNA molecules with high efficiency and limit degradation, this is due to the presence of Hte phenotype and deficiency in endonucleases. The BL21(DE3) cells carry the λ-DE3 lysogen and are suited for uses with bacteriophage T7 promoter-based systems including pPR and pET vectors. All flasks and tubes were sterilised using the autoclave before use. Stocks of competent cells (10 μL) were incubated in LB media (5 mL, appendix 1.5) overnight (37 °C). This was then added to a flask of LB (500 mL) containing the required antibiotic and grown to an OD_{595} of 0.5 (37 °C, around 3 hours). The flasks were cooled on ice (15 minutes) before being subjected to centrifugation (10 minutes, 4000 rpm). The supernatant was discarded, the pellet was re-suspended in transformation buffer 1 (TfbI) (30 mL, appendix 1.6) and placed on

ice (15 minutes). The suspension was subjected to further centrifugation (5 minutes, 4000 rpm), and the supernatant discarded. The pellet was re-suspended, this time in TbfII buffer (6 mL, appendix 1.7). The cells were kept chilled during aliquoting, and then immediately placed in the -80 °C freezer.

2.2.8 Transformation of competent *E. coli* cells

Cellular transformation is the uptake of foreign genetic material by the competent cell. Once the cells had been made competent the DNA is encapsulated within the cell using a heat shock method. For each transformation reaction, chemically competent cells (XL10 Gold, BL21 (DE3)) were removed from the -80 °C freezer and thawed on ice. After 10 minutes the desired plasmid was added to the cells (1-5 μL). This was then heated (42 °C, 30 seconds) before incubating on ice for a further 2 minutes. LB media was added (300 μL, appendix 1.5) and the cells allowed to recover (37 °C, 1 hour, with shaking). After incubation, the transformed cells (150 μL) were applied to LB agar plates containing antibiotic (carbenicillin and chloramphenicol were used for recombinant DNA containing pPR-IBA1 vector; 50 μg mL^{-1} and 34 μg mL^{-1} respective working concentrations). The plates were incubated at 37 °C overnight.

2.2.9 Preparation of pPR-IBA1 vector

The pPR-IBA1 plasmid encodes a C-terminal Strep-II tag. It contains genes conferring antibiotic resistance for ampicillin (carbenicillin). There are also a number of available restriction sites including Bsa1 in the multiple cloning region. For the preparation of pPR-IBA1 vector, plasmid (2 μL) was introduced into XL10 Gold cells. A culture of the cells was grown overnight (37°C, shaking) before pelleting by centrifugation and isolating the plasmid from the cell pellet via mini prep. Purified pPR-IBA1 vector (50 μL) was linearized by digestion using Bsa1 (1 μL) in CutSmart buffer (5 μL, 10x, NEB). The mixture was incubated (37 °C, 1 hour) and heated to inactivate the enzyme (80 °C, 20 minutes). A PCR purification protocol removed any residual buffer and impurities. Alkaline phosphatase (AP, 1 μL) and the supplied compatible buffer (5 μL, NEB) were added and the mixture incubated (37 °C, 1 hour followed by 70 °C, 5 minutes). This was proceeded by a final PCR purification step. The 50 μL sample of vector was analysed by 1 % agarose gel. The digested vector was excised from the gel and purified according to the Qiagen gel extraction kit instructions.

2.2.10 Colony PCR

The cloning success was assessed using colony PCR. PCR products were analysed using agarose gel electrophoresis. If the insert was present a band of the expected size would appear on the gel. Plasmids found to contain the insert were sent for DNA sequencing. Colonies were picked from the

LB agar plate using a sterile pipette tip (3-6 colonies per plate) and re-suspended in a 1.5 mL micro-centrifuge tube containing ultrapure water (100 μL). For the screening of six colonies, GoTaq Green Master Mix (70 μL, Promega), autoclaved ultrapure water (56 μL) and the forward primer and reverse primers designed for the amplification of the desired DNA insert (3.5 μL) were mixed together in a 1.5 mL micro-centrifuge tube. The mixture was evenly split into six PCR tubes. To each of the tubes a different cell suspension (1 μL) was added. Thermo-cycling conditions specified by the manufacturer were used, and the completed reaction loaded directly on a 1% agarose gel for electrophoresis. Positive colonies were grown overnight at 37°C with shaking in 5 ml of LB with appropriate antibiotics, before purification of the plasmid via mini prep.

2.2.11 Overnight cultures and miniprep

The ThermoScientific GeneJet Plasmid Miniprep kit uses silica-based spin columns to recover high copy plasmid DNA. Individual colonies were taken from an LB agar plates using a sterile pipette tip, added to LB media (5 mL), containing appropriate antibiotics and incubated (37 °C, overnight). The *E. coli* cell culture was subjected to centrifugation to produce a cell pellet. The miniprep kit was used according to the manufacturer's instructions. The purified DNA was analysed by DNA sequencing. Before miniprep purification, glycerol stocks of the cells could be generated. Glycerol helps to stabilise frozen bacteria by preventing damage to the cell membrane. After the *E. coli* overnight grow-ups, a small sample of the culture (500 μL) was added to a sterile 1.5 mL micro-centrifuge tube. Glycerol was then added to the tube (500 μL, 50%). The samples were stored at -80 °C until needed. When required a sterile pipette tip was used to scrape cells from the surface of the stock. The pipette tip was then used to streak the cells onto a LB agar plate containing appropriate antibiotics. The colonies that grew on the plate could then be used to continue the overnight growth and purification.

2.2.12 DNA sequencing

To determine the exact sequence on the engineered construct, purified DNA was analysed using chain termination DNA sequencing. Di-deoxynucleotide triphosphates were used to terminate the DNA sequence in chain termination (Sanger) DNA sequencing.[112] These molecules lack a 3'-OH group and so are unable to form the required phosphodiester bonds. The di-deoxynucleotide triphosphates are fluorescently labelled (they can also be radioactively labelled) enabling detection in automated sequencing machines. A different coloured fluorophore is used for each of the nucleotide bases. A polyacrylamide gel is then used to separate the fluorescent bands and the DNA is detected. The protocol was carried out by Genewiz and required 15 μL of sample at 100 ng μL^{-1}.

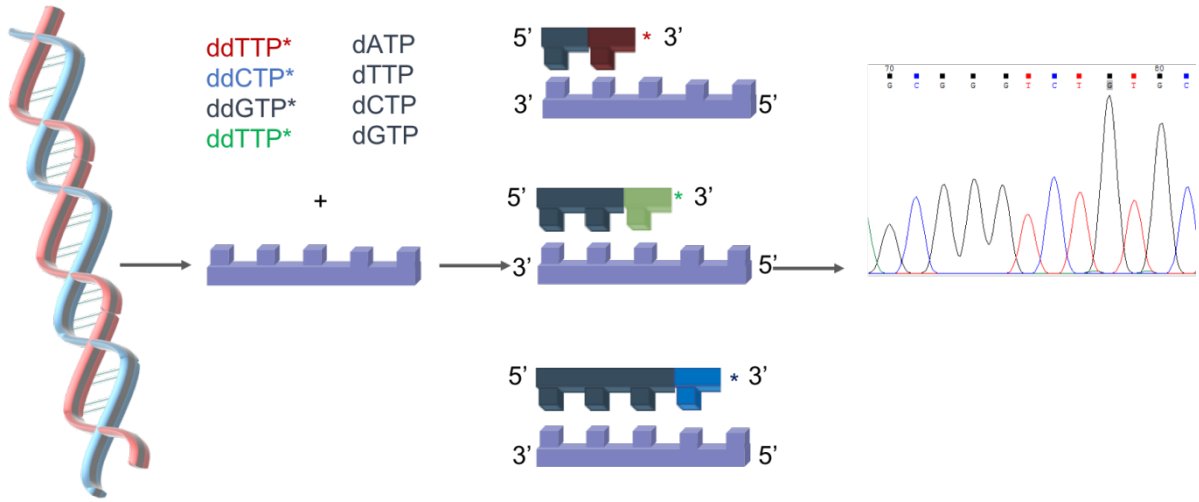

Figure 11 Schematic showing the basic process of Sanger DNA sequencing. The process uses fluorescent dideoxygenated NTPs to visalise the DNA sequence. The ddNTPs terminate the chain and are visualised as a fluorescently coloured band on an electrophoresis gel. The results are then depicted as coloured peaks on a graph (shown as the final stage in the figure).

2.3 Site directed mutagenesis

2.3.1 Design of mutagenic primers

In vitro site-directed mutagenesis introduced a mutation to a fragment of DNA. This could be a deletion, insertion or an alteration of one or several amino acid residues. The QuikChange technique is a simple, convenient technique that utilises miniprep plasmid DNA. The supercoiled, double-stranded pPR-IBA1 vector was used alongside an insert containing the genetic code for the desired product and two complementary oligonucleotide mutagenic primers. When designing the primers, the site of mutation within the original template DNA was identified. Both primers were then designed to incorporate this mutation whilst being largely complimentary to opposite strands of the parental vector. The primers were generally between 25 and 45 bases in length, with 10-15 bases either side of the mutated site to ensure successful binding and a T_m around 78-80 °C for high specificity resulting in a successful reaction and product. In every other sense the design of mutagenic oligonucleotide primers is identical to the design of other primers required for PCRs.

2.3.2 The mutagenesis reaction & Dpn1 treatment

The reaction requires three steps: synthesis of the mutant strand; digestion of the template with Dpn1; transformation. During the reaction, the mutagenic primers are extended resulting in a mutated plasmid containing nicks in the sequence. These nicks are regenerated by the cell during transformation. The Dpn1 digest is required to remove residual parental plasmid DNA[113].

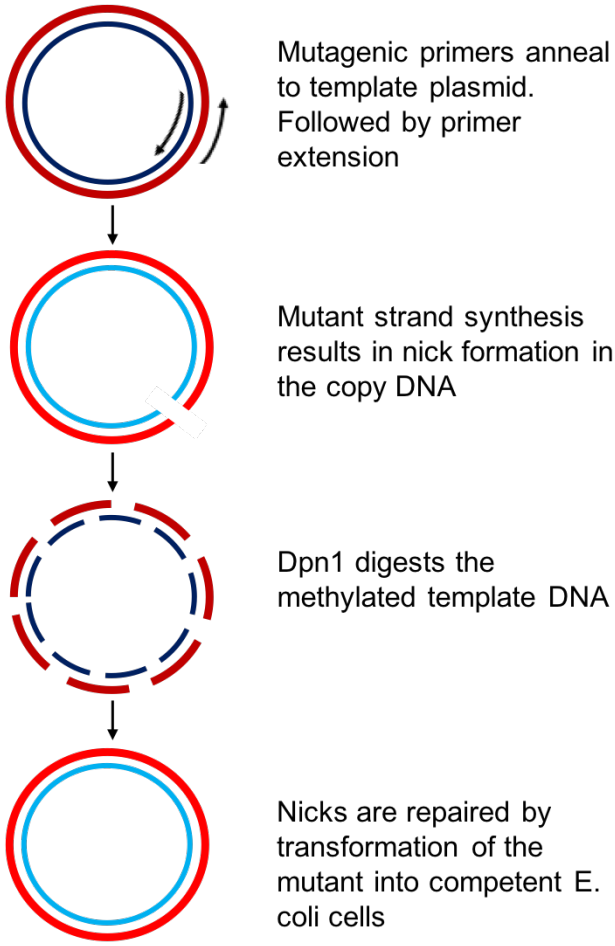

Figure 12 A Schematic showing the process of QuikChange site directed mutagenesis. The process is used to mutate a DNA sequence using carefully designed mutagenic primers which are complimentary to the template plasmid either side of the region to be mutated.

The reaction components (table 5) were mixed together, placed in the BIORAD T100 Thermal Cycler and subjected to temperature cycling detailed (table 6). Following the temperature cycling step, the template was degraded by Dpn1 digestion. Dpn1 (1 μL, NEB) and cut smart buffer (5 μL, NEB) were added to each mutagenesis reaction before incubation (37 °C, 1 hour). The reaction samples were then heated to inactivate the enzyme (80 °C, 20 minutes). The products were used to transform XL10 Gold cells and two resulting colonies selected for culturing and miniprep before analysis by DNA sequencing.

Table 5 The contents of the site directed mutagenesis reaction

Component	Volume (µL)	Final Concentration
10X Buffer for KOD Hot Start DNA Polymerase	5	1X
25 mM $MgSO_4$	3	1.5 mM
dNTPs (2 mM each)	5	0.2 mM
Water	32	MilliQ
Sense (5') IBA1 Cysteine Primer (10 µM)	1.5	0.3 µM
Anti-sense (3') IBA1 Cysteine Primer (10 µM)	1.5	0.3 µM
Template DNA (20 ng μL^{-1})	1	0.2 mM
KOD Hot Start DNA Polymerase (1 U/µL)	1	0.02 U μL^{-1}
Total Reaction Volume	50	

Table 6 Thermal cycling steps during site direct mutagenesis

Step	Time (s)	Temperature (°C)
Polymerase Activation	120	95
Denaturation	50	95
Annealing	50	55
Elongation	780	68
Repeat steps 2-4	X16	
Final Extension	420	68
Hold	∞	4

2.4 Protein expression

2.4.1 Culture growth and harvesting

Colonies of BL21(DE3) cells harbouring the plasmid of interest where picked from an LB agar plate using a sterile cell scraper or pipette tip. These colonies were then incubated in LB medium (5 mL) and the required antibiotic (carbenicillin and chloramphenicol, 10 µL, 50 mg mL^{-1} and 34 mg mL^{-1} respectively). The cultures were grown whilst shaking (7 hours, 37 °C, 180 rpm). 2 L fluted conical flasks containing appropriate medium (400 mL) were sterilised in the autoclave before being left to

cool. The required antibiotic, carbenicillin and chloramphenicol (800 μL, 50 mg mL^{-1} and 34 mg mL^{-1} respectively) were added. The cultures were added to the flasks (1 mL) and subjected to shaking (37 °C, 180 rpm). Cells were harvested by centrifugation (20 minutes, 3200 rpm). The resultant cell pellet was transferred to a clean 50 mL Falcon tube and re-suspended in 1 x phosphate buffer saline (PBS, appendix 1.10, 20% w/v) by pipetting up and down and vortexing. Once completely suspended the cells were lysed by sonication (10x cycles of 5 seconds on/20 seconds off, 70 % amplitude), releasing the contents of the cell in to the PBS solution. A further round of centrifugation was required to separate the insoluble proteins and membranes from the soluble protein. For proteins that were less soluble and therefore found in the insoluble fraction, the insoluble pellet was suspended in guanidine hydrochloric acid (GuHCl) (8 M, 20 % w/v) using pipetting and vortexing and sonicated (5 seconds on, 20 seconds off, 10 cycles, 70 % amplitude). Centrifugation removed remaining cell debris (30 minutes, 12000 rpm) and the lysate was recovered.

2.4.2 Auto induction induced expression

Auto induction is dependent on the proportions of glucose and lactose present in the reaction media.[114] Glucose prevents the uptake of the lactose by the cell as it is the preferred energy source, and so is metabolised in preference to lactose. The ratio of lactose to glucose in the commercially available auto induction growth medium is optimised. This ensured the cells were receiving sufficient energy from the glucose enabling replication and a high expression efficiently; but low enough amounts to ensure complete metabolisation of glucose, enabling lactose to be metabolised and protein expression to occur. Glycerol often replaces glucose in auto induction media as it does not ferment to acetic acid. Auto induced cultures are grown to saturation and yields are often higher than those resulting from IPTG induction.[115] Terrific broth (TB) or Super broth (SB) auto induction media including trace elements (Formedium) was used for culture growth, suspended in ultrapure water (400 mL) in a 2 L fluted flask. A sponge stopper was added to the top and autoclaved. The cell culture was added to the flask along with the antibiotics before incubation (48 hours, 37 °C, 180 rpm).

2.4.3 IPTG induced expression

Isopropyl β-D-1-thiogalactopyranoside (IPTG) can be used for the expression of proteins that are under the control of the lac operon. IPTG is an allolactose mimic. Unlike lactose, IPTG contains sulphur bonds and cannot be metabolised by the cell and so the concentration is not depleted during the course of the reaction.

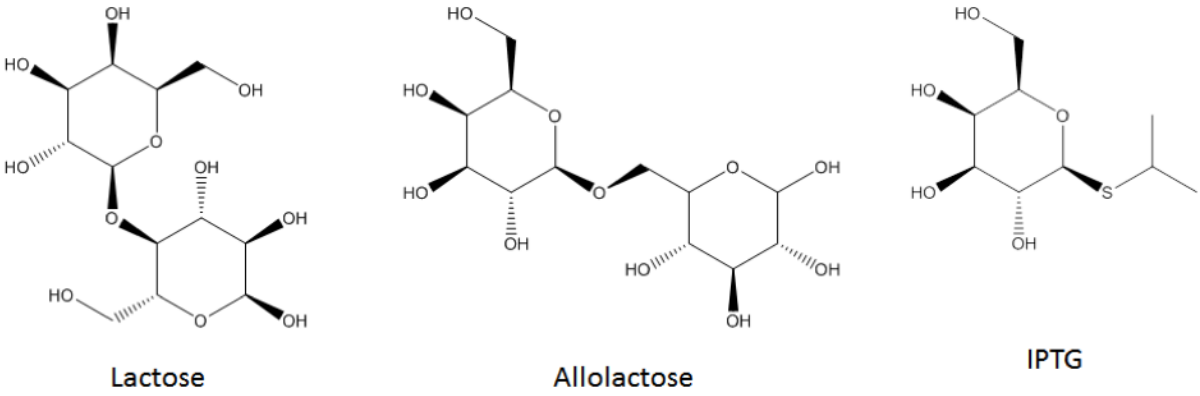

Figure 13 The chemical structures of lactose, the lactose metabolite: allolactose and IPTG: an allolactose mimic

The overnight cultures (50 µL) were added to LB medium (5 mL) containing carbenicillin and chloramphenicol (10 µL, 50 mg mL^{-1} and 34 mg mL^{-1} respectively) and shaken (37 °C, 4 hours). The optical density was monitored using UV-Vis spectroscopy until the optical density reached 0.8, at this point the cultures were induced. IPTG was added to the cultures (50 µL, 1 M) and left overnight (30 °C). The following day the cultures were harvested by centrifugation (3000 rpm, 15 minutes). At this point the cell pellets could be frozen.

2.4.4 Expression trials

Optimisation of the expression conditions was required to ensure the maximum possible efficiency of expression and therefore the highest possible yield of protein. The optimisation steps trialled various growth times, temperatures, media and induction methods. The media contained varying nutrient concentrations, and the induction methods used were auto induction and IPTG induction.

2.5 Protein purification

2.5.1 Affinity chromatography

Proteins and tags can bind specifically to other molecules and this can be exploited in the purification of proteins. The sample containing the desired protein is passed through a column. The proteins become attached to the matrix through the specific interaction between the tag and the stationary phase; whereas the contaminants flow through the column. The column is washed to remove any residual impurities. The proteins are then eluted using a specific elution buffer which can displace the protein from the support. The Strep-II tag is a synthetic eight amino acid peptide (Trp-Ser-His-Pro-Gln-Phe-Glu-Lys) that has been designed for the purpose of protein purification.[116] It has a high affinity for streptactin (a truncated form of streptavidin) which has an extremely high affinity for biotin. D-desthiobiotin can be used for the elution of the protein as it competes for binding pockets on the streptactin support.

The streptactin column was regenerated using ultrapure water (5 mL), sodium hydroxide (3 mL, 0.5 M), ultrapure water (5 mL) and finally 1 x PBS (5 mL). The lysate was added to the top of the column and allowed to run through. The flow-through was collected in Falcon tubes. The column was washed with PBS (5 mL) and the protein was eluted in a buffer containing d-desthiobiotin in PBS (1.125 mg mL^{-1}). Each elution was in 0.5 mL of buffer until the fractions no longer contained protein. The fractions containing protein were then combined. The streptactin column was stored in 20 % ethanol at 5 °C.

Proteins that contain a polyhistidine tag (his_6) can be purified using a nickel resin column.[117, 118] Nickel nitrilotriacetic acid (Ni-NTA) is used in the nickel resin column to attach the nickel to the solid support; this ligand leaves a free binding site on the nickel for the his_6 tag to bind.
Ni-NTA (1 mL) was added to a 1.5 mL micro-centrifuge tube. The solution was spun in the centrifuge (1-minute, 2000 rpm) and the supernatant discarded. Denaturation buffer (1 mL, appendix 1.11) was added and centrifuged again, these steps were then repeated. This was then added to the protein lysate and incubated whilst shaking (30 minutes). The supernatant was then discarded. The resin containing the protein was re-suspended in denaturation buffer (1 mL). The column was then washed with refolding buffer (10 mL, appendix 1.13) and with buffers of decreasing denaturant concentration (named buffer A to D, appendix 1.13). The washes were collected in 50 mL Falcon tubes. The protein was eluted with an elution buffer (500 µL fractions, appendix 1.14) until all the protein had been eluted. The Ni-NTA resin can be stripped and recharged with other metal ions. The flexibility of the metal charge on the resin can also make it a useful technique for the qualitative study of metal-protein binding.

Heparin is a naturally occurring sugar-containing molecule with a high negative charge density; it is this likeness to DNA that enables heparin affinity chromatography to be used to displace bound DNA molecules from the protein. Elution of the protein proceeds via increased salt concentration in the elution buffer. The use of a heparin column for the purification of DNA-binding proteins is therefore a cross between affinity and ion-exchange chromatography. The column is recovered with washes of NaOH (5 mL, 1.5 M) and PBS (5 mL, 0.5%). The protein sample was loaded onto the column and allowed to flow through. The flow-through was collected. Subsequently the column was washed with increasing salt concentrations (0.1 M, 0.3 M, 0.5 M, 0.7 M, 1.5 M, 2 M, 5 mL each) until the protein had been eluted.

The eluted fractions from the affinity chromatography techniques were analysed using sodium dodecyl sulfate polyacrylamide gel electrophoresis (SDS-PAGE) to locate the protein. Fractions containing the desired protein were combined.

The columns used for these purification techniques could be in the form of Hi-trap columns (GE Healthcare) and therefore run automatically under the desired program using an ÄKTA purification system.

2.5.2 Size exclusion chromatography

Size exclusion chromatography separates proteins based on the difference in size between the molecules. The technique is also referred to as 'gel filtration'. The separation based on size enables the removal of any impurities and provides an estimate of the protein molecular weight (MW). It can be utilised to determine the whether a protein is assuming a monomeric structure or a higher order oligomer. The sample is filtered through beads stacked within the column. Small species are retained on the column longer than larger species due to their uptake within the pores of the beads. Larger species are not able to access the pores of the beads and so are eluted earlier.

The Superdex 200 10/300 GL column, with the ÄKTA system was used for the separation of the protein samples. The column was equilibrated with filtered, degassed PBS (the storage buffer of the protein samples). The sample was then injected into the system before the column was washed with PBS (1.2 column volumes). The eluted fractions were collected in a deep 96-well plate with fraction volumes of 500 μL. Fractions that indicated a strong UV absorbance at a wavelength of 280 nm, indicating the presence of protein, were retained and analysed using SDS-PAGE.

2.5.3 Reduction of protein disulphide bridges

Breaking sulfur-sulfur bonds within a protein requires a reduction reaction and therefore a reducing agent. There are a range of commercially available reducing agents including: tris(2-carboxyethyl) phosphine (TCEP), dithiothreitol (DTT); and 2-mercaptoethylamine (2-MEA), also known as cysteamine. TCEP is often the reducing agent of choice as it is powerful, odourless and undergoes irreversible reduction. A 10X molar excess of TCEP was added to the protein sample containing disulphide crosslinks. A 200 mM stock of TCEP was made (57 mg mL^{-1} in ultrapure water). The protein sample containing the appropriate amount of TCEP was left to react (overnight, room temperature, shaking). The success of the reaction was analysed using non-reducing SDS-PAGE.

2.5.4 Protein storage

Following expression and purification, proteins were stored at -80 °C in a suitable buffer until required for analysis. Buffers with high salt concentrations, denaturants or imidazole present after purification were exchanged using dialysis. Dialysis can be used for the reduction of unwanted small molecules such as salts or dyes from a purified protein sample. The method works based on the different diffusion rates of the molecules through a semi permeable membrane. Diffusion of molecules from a solution with a high concentration of molecules moves towards the solution where the molecules exist at a lower concentration according to Le Chatelier's principle. A specific membrane is selected ensuring the pore size does not allow the protein to leach into the surrounding dialysis buffer, containing it within the membrane with the newly exchanged buffer. The dialysis snakeskin tubing or dialysis cassette (ThermoScientific) was prepared according to the supplier instructions. The purified protein sample was then inserted. The cassette/tubing was secured to prevent leaking and placed into dialysis buffer (often 2 L of ultrapure water or 2 L of 1 x PBS). The system was stirred overnight (4 °C). Once complete, the concentration of the protein was measured using absorbance at 280 nm.

2.6 Protein characterisation

2.6.1 UV-Vis Spectroscopy to determine protein concentration

The energy required for the n to π* and π to π* transition in biological molecules lie within the UV-Vis spectrum. The main chromophores within these molecules are the nucleotide bases in DNA (absorbing at 258 nm) and the tryptophan and tyrosine residues in protein (absorbing at 280 nm and 274 nm respectively). The Beer-Lambert law is used to calculate the concentration of the sample[27]:

$$C = A/\varepsilon_{\lambda} l$$

A is the absorption (dimensionless), ε_{λ} is the molecular extinction coefficient at a given wavelength (M^{-1} cm^{-1}), C is the concentration of the protein (mol L^{-1}) and l is the path length (cm). The molecular extinction coefficient for proteins can be estimated by accounting for the number of tryptophan and tyrosine residues within the molecule:

$$\varepsilon 280 = n\,Tyr \times 1280 + n\,Trp \times 5690$$

The NanoDrop 2000 ™ (Thermo Scientific) is an ultraviolet and visible (UV-Vis) spectrophotometer which measures the concentration and purity of nucleic acid and protein samples. The absorption

coefficient is required for an accurate calculation of protein concentration. The value can be estimated using the online Protparam tool[119]. For protein samples, a baseline absorbance measurement at 280 nm and 260 nm of buffer alone was measured (2 µL) before measuring the absorbance of the protein sample. For DNA, the absorption at 260 nm was measured. Another method of calculating the protein concentration is using an assay based on bicinchoninic acid (BCA). BCA allows for the colorimetric quantification of protein concentration. It requires the reduction of Cu(II) into Cu(I) in an alkaline medium. The detection of Cu(I) by BCA consequently results in the colour change from yellow to purple. The intensity of the purple colour is directly proportional to the amount of protein present. The purple colour is produced by the chelation of two BCA molecules with a single Cu(I) ion and can be measured by absorbance at 562 nm. This absorbance reading can be compared to a standard absorbance curve of known concentrations of a control protein (BSA for example) in order to calculate the protein concentration of the sample. The BCA kit was used according to the manufacturers protocol (ThermoScientific).

2.6.2 SDS-PAGE

SDS-PAGE is a form of gel electrophoresis and works on similar principles to agarose gel electrophoresis although the gel is produced using polyacrylamide in the place of agarose. The gel is made up of two layers, a resolving bottom layer and a stacking top layer. SDS-PAGE separates proteins based on their size-to-charge ratio which is usually proportional to their relative molecular mass. To ensure this is the case, SDS is an anionic detergent used to denature and linearize proteins; it also distributes a uniform negative charge (SO_4^{2-}). To ensure complete unfolding the protein samples are boiled in the presence of β-mercaptoethanol, or similar reducing agent. This disrupts any disulphide bridges and produces an even charge distribution over the protein allowing separation based on size. Molecular weight markers are analysed alongside the protein fractions; this is a mixture of proteins with known molecular masses. The distance an unknown protein moves through the polyacrylamide gel can then be compared to the marker and used to reliably estimate the molecular mass.

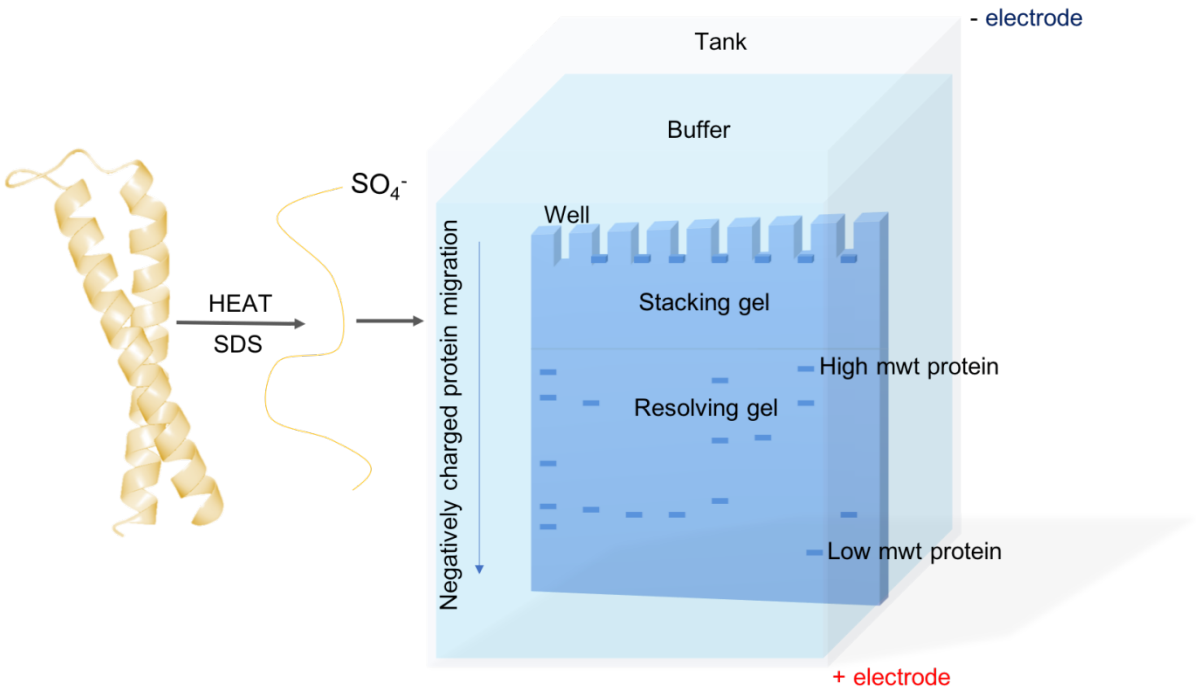

Figure 14 SDS-PAGE schematic showing the denaturation of proteins using SDS. A protein is denatured using heating and binding of SDS. The linearised and negatively charged protein is then loaded onto a polyacrylamide gel alongside a ladder of known mass. The proteins are separated by size.

A protein sample (10 μL) was added to a loading dye containing 2x β-mecaptoethanol (10 μL) and boiled (90 °C, 5 minutes). The samples were then loaded into the wells of a precast gel and the gel electrophoresed (200 V, 25 minutes). The gel was then stained using instant blue stain (expedeon) and left to shake (30 minutes) before being de-stained with water. The gel could then be imaged using a ChemiDoc gel imager (BioRad).

2.6.3 Blot protocol

Western blot is used for detecting and identifying proteins. Protein samples are separated using electrophoresis (such as SDS-PAGE) and the protein bands are transferred onto a nitrocellulose membrane. The process uses a method of electro-blotting where the protein gel is placed between sheets of nitrocellulose and blotting paper then subjected to an electrical current. The applied current runs at 90° to the gel, resulting in transfer of the proteins from the gel onto the membrane. The blot is then submerged in a blocking buffer in order to block the remaining hydrophobic sites of the sheet. The blot is incubated with a primary antibody which will bind to specific protein tags; it is then incubated with a secondary antibody which will bind to the primary antibody (if required). Enhanced chemiluminescence (ECL) is used as a method of detection. When hydrogen peroxide and luminol are present, horseradish peroxidase (HRP) oxidises luminol. The light emission as a result of

the reaction can then be detected. Antibodies used were often conjugated to HRP and the detection reagents provided luminol and hydrogen peroxide.

The gel, nitrocellulose membrane and blotting sheets were soaked in 1 x Towbin blotting transfer buffer (1-hour, room temperature, appendix 1.19). The sheets were then stacked in the order of: blotting paper, nitrocellulose membrane, gel, blotting paper (bottom to top), and the proteins transferred using a Transblot turbo(BioRad) for 30 minutes. The nitrocellulose membrane was then blocked with 3% BSA in PBS (1-hour, room temperature). The primary antibody was added and incubated (40 minutes, room temperature, concentration used was that suggested by the supplier). The solution was discarded, and the membrane washed with PBS (3x 10 mins, room temperature, 25 mL). If a secondary antibody was required, it was added at this point and the washing steps repeated. The blot was then visualised using ECL and visualised using a ChemiDoc imaging system (BioRad).

A dot blot is similar to western blot in that it is also used in the detection of proteins using a nitrocellulose membrane, primary and secondary antibodies and similar visualisation methods. It differs to western blotting in that it does not require an electrophoresis step. Pelleted cells were re-suspended, incubated and lysed used sonication (5 seconds on, 20 seconds off, 10x, 70% amplitude). The protein sample (25 μL) was incubated in dot blot buffer (75 μL, 30 minutes, room temperature, appendix 1.20). A drop of sample (3 μL) was applied to the nitrocellulose membrane (blotting paper was placed underneath) in an ordered arrangement. The blotting paper was then removed, and the nitrocellulose was blocked using 3% BSA in PBS containing tween (PBST) (1-hour, room temperature). The appropriate antibody was then introduced (40 minutes, room temperature using the concentrations suggested by the supplier). The blot was washed three times with PBST (25 mL, room temperature, each wash was incubated for 10 minutes). The blot was visualised using ECL and imaged using the ChemiDoc system.

2.6.4 Electrospray mass spectrometry (ES-MS)

Mass spectrometry (MS) was used to determine the molecular mass of the proteins. Electron spray ionisation (ESI) MS is an analytical technique that converts the sample into gaseous ions which are separated and detected using the mass to charge ratio (m/z) of the species.[27] In ES-MS ionisation is achieved by spraying the protein solution into an electrical field; a soft ionisation method that produces small droplets allowing intact proteins and DNA to be analysed. The ionised samples travel down a pressure and potential gradient towards the analyser. Before reaching the analyser the kinetic and thermodynamic barrier at the surface of the droplet is reduced and ions are ejected into

the gaseous phase for analysis and detection. Depending on the m/z of the sample, the ions hit the detector at different times (figure 15). As the ions hit the detector a signal is measured and sent to a computer for visualisation. 50 µL of 1 mg mL^{-1} protein, in ultrapure water was used. All protein samples were analysed using the Agilent Technologies 6530 Accurate Mass Time of Flight Mass spectrometer in the chemistry department at the university of Sheffield

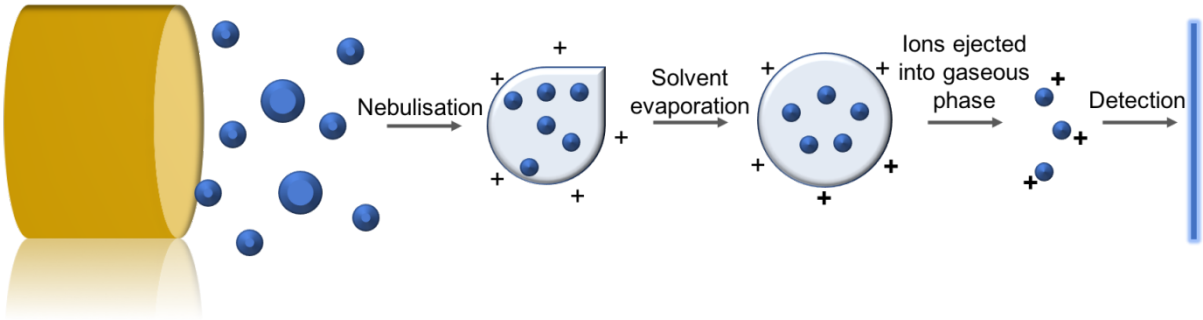

Figure 15 A schematic showing the processes involved in ES-MS. The blue spheres indicate the pathway taken by the analyte as they are transformed from solid molecules into gaseous ions

2.6.5 Secondary structure analysis using circular dichroism

Proteins have a chiral backbone and absorb UV radiation; this allows them to be analysed using circular dichroism (CD). CD measures the difference in absorption between left and right handed circularly polarised radiation. The CD of proteins occurs at low UV, between 190 nm and 260 nm. Characteristic peaks of the protein secondary structure are analysed. An α-helical secondary structure can be identified by three characteristic peaks: a negative peak at 208 nm or 209 nm which is result of the π-π* transition; another negative peak at 222 nm as a result of the n-π* transition; and a positive peak at 192 nm due to the π-π* transition. Other secondary structures exhibit different characteristic peaks. The Dichroweb server is a useful tool to evaluate the secondary structure predicted by CD.[120]

Protein samples (0.1-0.2 mg mL^{-1}) were prepared in ultrapure water. The volumes used filled a 2 mm path length UV-quartz cuvette to 75% of the maximum volume (around 700 µL). The absorbance of the protein was measured between 260 nm and 190 nm, at increments of 1 nm. The scan was then repeated. The CD spectra could also be measured whilst increasing or decreasing the temperature of the protein sample in standard increments.

2.6.6 Determination of protein T_m

The temperature ramp during CD is able to give an indication of the melting temperature (T_m) of the protein. Other methods for calculating this value include differential scanning calorimetry (DSC) and differential scanning fluorimetry (DSF).[121] DSC can be used to directly measure the T_m and enthalpy of a thermally induced protein transition. The melting temperature is the temperature at which the protein is 50% denatured/unfolded. At the T_m the change in Gibbs free energy is zero and the change in enthalpy is equal to the temperature multiplied by the change in entropy. As the heater raises the temperature of the DSC cells at a steady rate, the temperature difference between the reference and sample cell is monitored (ΔT_1), along with the temperature difference between the cells and the adiabatic jacket (ΔT_2). Both the jacket and the cells are equipped with a feedback mechanism.[122] Protein samples were diluted to concentration of 0.3 mg mL^{-1} to 6 mg mL^{-1} in PBS (750 µL). The temperature was ramped from 10 °C to 100 °C and back down again at a rate of 90°C hr^{-1} on heating and 60°C hr^{-1} on cooling. The temperature ramp was repeated 20 times.

DSF can also be used to determine the melting temperature of a protein. When the proteins are heated they begin to unfold which presents their hydrophobic core to the surrounding solution.[121] Sypro orange is a fluorescent dye which binds the hydrophobic residues producing a fluorescent signal. The sample therefore becomes fluorescent upon denaturation. The technique can be carried out in a real time PCR machine enabling different concentrations and samples to be measured simultaneously. Advantageously, only small amounts of proteins are required compared to DSC. Protein samples (5 µM to 100 µM, 25 µL to 50 µL) were analysed in a 96-well plate. The samples were run using a variety of buffer systems including NaCl (2M), ultrapure water and 1 x PBS. 71 cycles were run for each sample using a real time PCR machine with a 1 °C temperature ramp each cycle. The temperature was therefore increased from 25 °C to 95 °C with the temperature being held for between 1 and 10 minutes during each cycle.

2.6.7 SEC-MALLS

Size exclusion chromatography (SEC) is a method that separates macromolecules by their size. The scattering of light caused by the radiation travelling through a sample is detected. The protein has a different refractive index (IR) to the surrounding solution leading to extra light scattering. The change in the light scattering angle is dependent on the concentration and the molecular mass of the protein, this enables the molecular mass of an unknown protein to be estimated.
A protein sample in ultrapure water (120 µL, 1 mg mL^{-1}) was sent to the biology department at the University of York and analysed by Dr. A. Leech using a Wyatt Dawn HELEOS-II 18-angle light

scattering detector and Wyatt Optilab rEX refractive index monitor linked to a Shimadzu HPLC system comprising LC-20AD pump, SIL-20A Autosampler and SPD20A UV/Vis detector.

2.6.8 Structure analysis using SAXS

Small angle X-ray scattering (SAXS) can be used to determine the size and a crude three-dimensional shape of a molecule, for example whether it forms of disks, spheres or rods. This method of characterisation is suitable for a broad range of particle sizes making it useful for the study of macromolecules. It works by bombarding a sample with a monochromatic X-ray beam. Upon the beam hitting solid matter, the X-rays are scattered and picked up by a detector. These measurements are taken in close proximity to the primary beam – giving it the name 'small angle' X-ray scattering. This small angle enables measurements of a wide range of sample sizes, with high resolution. The scattering data obtained can then be used to calculate parameters including the pair-distance distribution (P(r)) and the radius of gyration of the scattering objects (R_s). The pair-distribution is used to calculate the size of the protein.

A protein sample (around 3 mg mL^{-1}, 400 μL) was inserted into a clean capillary tube and inserted into the sample chamber. A detection camera length of 1 m was used. The sample was exposed to the X-ray beam and the scattering was detected. Following completion of the process the data collected was analysed using GNOM[123] by Dr Oleksandr Mykhaylyk, which produced a smooth plot of the experimental data. The plots generated could then be fit against existing known models to help determine the size and shape of the protein. A PBS blank and protein of known size and shape (lysozyme, 10 mg mL^{-1}) were also analysed as a control.

2.7 Magnetite nanoparticle synthesis

2.7.1 Room temperature biomineralisation

Magnetite precipitation reactions require the presence of a base such as NaOH, NH_3 or tetramethylammonium hydroxide (TEAOH). The room temperature co-precipitation (RTCP) reaction was performed at varying ratios of iron (II) to total iron however the total iron concentration was kept constant at 50 mM. The chemical equation of the reaction can be seen below.[10] The counter ion can be sulphate or chloride.

$$Fe^{2+} + 2Fe^{3+} + 8OH^- \rightarrow 2\beta FeO_2H + Fe^{2+} + 2H_2O + 2OH^- \rightarrow Fe_3O_4 + 4H_2O$$

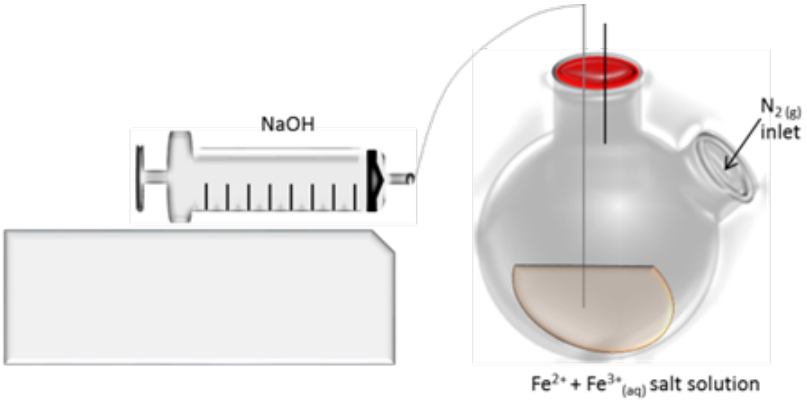

Figure 16 A schematic of the RTCP reaction indicating the addition of NaOH to the reaction vessel containing a solution of iron salts. Addition of the base requires a syringe and pump driver. The reaction must be kept under an inert atmosphere to prevent oxidation of the magnetite product. A reverse RTCP reaction pumps in the iron salt solution into a base such as NaOH.

An example reaction uses $FeSO_4.7H_2O$ (106.35 mg, 35 mM) and $Fe_2(SO_4)_3$ (47.75 mg, 15 mM) in a round bottom flask dissolved in ultrapure, degassed water (10 mL). NaOH (4 mL, 0.5 M) was added at a rate of 20 µL min^{-1} using a precision syringe pump driver (Harvard instruments). The reaction was kept under an inert nitrogen atmosphere. The reaction was also performed in the presence of protein. When the addition of protein was required it was added at different stages of the reaction at various volumes and concentrations to determine optimal conditions. The reaction could also be performed in the opposite way, producing smaller NPs when compared to the forward reaction.[124] For this reaction a mixture of iron salts was added dropwise to a basic solution.

A further variation of the RTCP used a microfluidic system. This set-up produced MNPs at a very fast rate, preventing oxidation of the reagents and so a higher ratio of Fe(II) to total iron concentration could be used; reaching the stoichiometric ratio of magnetite (0.6). $Fe_2(SO_4)_3$ (178.711 mg) and $FeSO_4$ (111.22 mg) was dissolved in degassed, ultrapure water (24 mL). This iron solution was pumped into the microfluidic chamber at a constant rate, while NaOH (0.5 M) was pumped in through another inlet, also at a constant rate. The reaction product was then collected as they were ejected from the device.

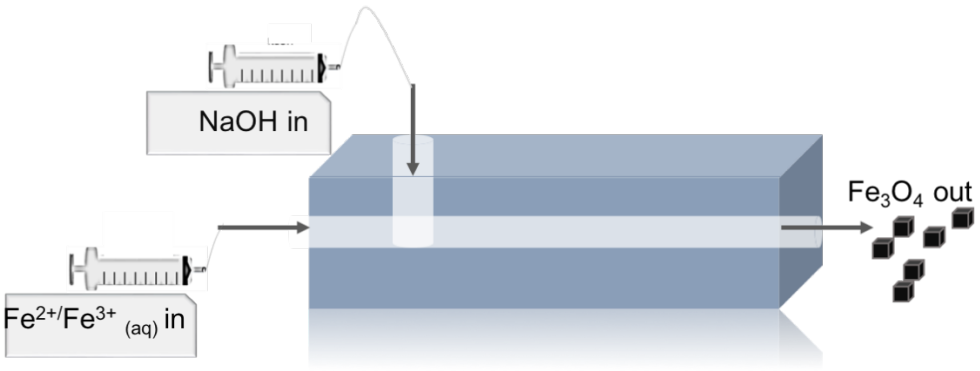

Figure 17 Schematic showing the set up for the reaction using the microfluidics device. A base such as NaOH and an iron salt solution containing both ferric and ferrous ions are pumped at a steady pace onto tube of the device. The reactants interact and form magnetite within the device before it is eluted from the other end.

2.7.2 Ammonium diffusion

Ammonium diffusion is another room temperature precipitation method, however in this case the base is ammonia and the total volume of the base is present at the beginning of the reaction diffuses over time into the iron salts. $FeCl_2$ (6 mg, 1 mM) and $FeCl_3$ (16 mg 2 mM) were added to a glass vial containing NH_3 (600 µL, 2 % vol) and degassed, ultrapure water (29.4 mL). The reaction was kept under vacuum (24 hours).

2.7.3 Partial oxidation of ferrous hydroxide

In contrast to the other magnetite synthesis methods trialled, the partial oxidation of ferrous hydroxide (POFH) requires increased temperatures; however, these temperatures are still significantly lower than temperatures used in thermal decomposition synthesis routes. During the reaction, ferrous iron was heated to 80 °C for a sustained period of time in the presence of KOH. This produced the ferrous hydroxide required for the reaction. The ferrous hydroxide could then undergo partial oxidation, using KNO_3. The chemical equation for this reaction can be seen below.[125]

$$3\,Fe^{2+} + 6OH^- \rightarrow 3Fe(OH)_2$$
$$2\,Fe(OH)_2 + NO_3^- + H_2O \rightarrow 2Fe(OH)_3 + NO_2^-$$
$$Fe(OH)_2 + 2Fe(OH)_3 \rightarrow Fe_3O_4 + 4H_2O$$

$FeSO_4.7H_2O$ (0.5 M, 350 mg in 2.5 mL of degassed ultrapure water) was added to a 100 mL round bottom flask, KOH was then added (1M, 154 mg in 2.75 mL of degassed ultrapure water) and stirred using a Teflon coated magnetic flea. The round bottom flask and its contents were heated (80 °C).

KNO_3 was added to the reaction in a dropwise manner (0.5 M, 1.01 g in 20 mL of degassed ultrapure water, 4 mL min^{-1}). The reaction was kept under an inert nitrogen atmosphere. After the reaction had reached completion (4 hours), the product was left to cool (room temperature).

2.7.4 Nanoparticle clean-up and storage

Magnetite NPs are highly susceptible to oxidation, reducing the magnetisation of the crystals and therefore decreasing their usefulness for many applications. It is for this reason a swift and thorough clean-up is required. It is also why the storage conditions of the NPs is an important consideration. The washing and storage should be under non-oxidising conditions.

The resulting magnetite crystals were transferred to a clean, deoxygenated glass vial and washed several times with nitrogen sparged ultrapure water (5 mL) using magnetic separation of the NPs. The particles were washed with ethanol (2 mL) and the solvent removed using magnetic extraction. The particles were placed under vacuum in a vacuum desiccator until completely dry (around 24 hours). When the magnetite was required for further analysis the particles could be re-suspended and sonicated in a buffer of choice (often water).

2.8 Nanoparticle characterisation

2.8.1 Determination of the iron content using ICP-MS

Inductively coupled plasma mass spectrometry (ICP-MS) combines the high temperature technique of ICP with MS as a powerful detection technique. The ICP converts the atoms within the sample into ions. This is done using the ionisation of argon within the chamber, causing collisions and producing plasma. The sample is applied using a nebuliser. The elements of the sample are then transformed into gaseous atoms which are then ionised. These ions are then detected using MS after filtration through a quadrupole mass filter.[126] The detected elements are then analysed. The instruments can accurately calculate elemental concentrations down to parts per billion or even parts per trillion (ppb/ppt).

A known mass of magnetite NPs was transferred into a clean glass vial and dissolved in aqua regia (1 mL, 1:3 molar ratio of concentrated HNO_3: HCl). The strong acid was added to the vessel using a glass pipette and the volumes used were calculated by measuring the mass added. The samples sometimes required sonication using a sonic bath (30 minutes) to ensure complete dissolution. Once fully dissolved ultrapure water was added (9 mL) to dilute the acid. ICP-MS was used to analyse the samples alongside a blank solution (1 mL aqua regia, 9 mL water). The iron content was analysed using an Agilent technologies spectrometer ICP-MS HP4500. Optical emission lines specific to iron

were identified using comparison to lines of known elemental standards. The total iron concentration could then be calculated by using a calibration curve.

2.8.2 Determination of composition using powder-XRD

Determination of the structure of an ordered crystal is made possible using X-ray diffraction (XRD). The Bragg equation is used to calculate the distance between specific lattice planes[127]:

$$n\lambda = 2dSin\theta$$

Where d is the distance between the lattice planes, λ is the wavelength of the incident X-rays, n is an integer and θ is the angle between the beam and the lattice plane. The interaction of the X-rays with matter causes acceleration of electrons which emit a quantum of radiation. This emission is dependent on the incident radiation. The displacement of the incident rays compared to the displacement of the reflected rays gives rise to constructive and destructive interference which correlates to the crystal structure. Minerals such as magnetite have specific lattice spacing and so characteristic values are identified and can be used to confirm the sample as magnetite. However, the lattice spacing of other iron oxide species having similar crystal structures (for example maghemite) mean that in practice it can be difficult to rule out the presence of these other materials. MNPs were magnetically separated from the solvent and washed with ethanol (1 mL) magnetically separated and dried under vacuum (1 hour). The powder was then analysed by the X-ray characterisation team using an in-house diffractometer. Data was collected by rotating the sample between 20° and 80°.

2.8.3 Size determination using DLS

Dynamic light scattering (DLS) was used to analyse NP size distribution. It picks up on the random changes in intensity of scattered light within a NP suspension. Inside the suspension the particles undergo random Brownian motion, in-turn causing either constructive or destructive interference.[128] The calculation of the hydrodynamic radius based on Brownian motion is described using the Stokes-Einstein equation, see below.

$$D_h = {K_B T}/{3\pi\eta D_t}$$

Where D_h is the hydrodynamic radius of the particle; K_B is the Boltzmann constant; T is temperature; η is the dynamic viscosity of the surrounding solvent and D_t is the translational diffusion coefficient – the value calculated by DLS. D_t is measured via the illumination of the cell containing the NPs using a

laser. This light from the laser is scattered and it is this scattered light that is detected. Detection can occur by one of two detectors; either a detector at 90 ° or one at 173°. In this case the detector was positioned at 173°. Smaller particles produce increased fluctuations due to faster motion and therefore there is slower motion of larger particles resulting in fewer fluctuations. For monodisperse samples signal interpretation uses an auto-correction function, this function is described as the exponential decay as a function of delay time.

Magnetite NPs were diluted in water (1 mg 100 mL^{-1}, 1 mL) before transfer into a clean, plastic cuvette for analysis. The cuvette was inserted into the Brookhaven ZetaPALS DLS machine and the system was allowed to warm up (to 25 °C). The sample was then held at this temperature during the scans (x10). These scans were used to calculate the distribution of hydrodynamic radii of the NPs. The results were then plotted and interpreted using Microsoft Excel and GraphPad Prism.

2.8.4 Size and shape determination using TEM

Electron microscopy is used for visualisation when a greater resolution is required than that possible by optical microscopy. A transmission electron microscopy (TEM) image is produced from electrons that form a beam which is passed through the specimen and detected. A high voltage is passed between an anode and cathode causing a tungsten filament to emit electrons, these electrons pass through a hole in the anode to form the beam. The beam is then passed through a number of electromagnetic lenses until it reaches the specimen. Electrons that are transmitted through the sample are detected by a camera. Dense areas of material do not allow electron transmission and so appear as dark spots on the image – showing the size and shape of the MNPs within a sample.[129] Magnetite is a dense material and therefore does not require any additional staining. The NPs were suspended in deoxygenated ultrapure water (5 mL), the suspension was dried onto glow discharged, carbon-coated TEM grids (10 µL). The TEM was performed on a FEI Tecnai G2 Spirit microscope at 80 kV with a camera attached. Multiple images were taken from each grid. Particle size was calculated using the measuring tool in ImageJ.[130]

2.8.5 Analysis of the magnetic properties using VSM

A vibrating sample magnetometer (VSM) uses a method of induction to analyse the magnetisation of a given material. Electromagnetic induction induces a voltage. A resultant change in the magnetic flux is then used to determine the magnetisation of the sample. The process requires vibration of a magnetic sample, with the direction of vibration perpendicular to an applied field. Once magnetised, the magnetic moment of the sample generates an alternating magnetic field, which in-turn generates an electric field. The electric field is detected using a set of coils located in close proximity

to the sample. The strength of the electric field detected is directly proportional to the magnetic moment generated by the sample upon magnetisation. NPs were magnetically separated from the solvent, washed with ethanol (1 mL), magnetically separated and dried under vacuum (1 hour). A precisely calculated mass of the MNPs was placed in a gelatine capsule. The gelatine capsule was then attached to a carbon rod and loaded into the VSM (Oxford instruments MagLab VSM, Leeds university). The samples were vibrated at 55 Hz in a field range of -10 to 10 kOe at room temperature. The saturation magnetisation and coercivity could then be calculated.

2.8.6 Analysis of the magnetic properties using magnetic susceptibility measurements

The magnetic susceptibility (χ) of a material describes how responsive it is to an applied magnetic field and is related to the magnetisation (M) and magnetic field strength (H) by the equation below.[2]

$$\chi = {}^{M}/_{H}$$

The magnetic susceptibility is measured in units of centimetre second gram (cgs), this is the SI unit when the magnetic field is current generated. The Bartington MS2G alternating current susceptitometer, single frequency sample sensor MS3 meter and BartSoft analysis software were used to obtain the data. Firstly, a blank micro-centrifuge tube was inserted into the sample holder and measured at a frequency of 1.3 kHz, followed by ultrapure water and finally a known mass of MNPs. Each sample was analysed in triplicate.

2.9 Protein binding

2.9.1 Protein binding to MNPs during RTCP reactions

Protein additives were used during RTCP reaction to aid the control of the size, shape and morphology of the MNPs. The addition of these macromolecules often resulted in improved monodispersity of the product and evident preference for the synthesis of specific crystal facets. An example involves the addition of the protein of interest (50 μg suspended in ultrapure water to the RTCP reaction) at the start of the reaction.

2.9.2 Protein detection by ELISA

An enzyme-linked immunosorbent assay (ELISA) is used to measure the binding capability of a biomolecule, resulting in a colour change. In the first step, a primary antibody is bound to the molecule, usually a protein (figure 18). A secondary antibody may then also be required. An enzyme is conjugated to the antibody and on addition of substrate, a reaction resulting in the colour change is catalysed. Antibodies are most commonly labelled with either AP, or HRP, both of these enzymes

produce a colorimetric response with certain reagents. If only a primary antibody conjugated to the enzyme is required, this is termed a 'direct ELISA'. If a secondary antibody is conjugated to the enzyme and is required, this is known as an 'indirect ELISA'.[109] For this work, when a direct ELISA was used, the antibody was conjugated to HRP. The substrate for HRP is 3, 3', 5, 5'-tetramethylbenzidine (TMB), which has an A_{max} of 370 nm - 652 nm, upon catalysis it is oxidised by oxygen radials produced by the hydrolysis of hydrogen peroxide, produced by HRP – this causes the solution to turn from yellow to blue. TMB has a detection limit of around 60 pg mL^{-1}; it is used at a dilution ratio of 1:1000. This substrate is provided alongside hydrogen peroxide in the TMB substrate kit (Bio Rad). For indirect ELISAs, an AP conjugated antibody was used. A substrate for AP is 5-bromo-4-chloro-3-indolyl phosphate (BCIP) which is found in the BluePhos® microwell substrate kit (Sera Care). BCIP has an A_{max} of 595-650 nm, a detection limit of around 100 ng mL^{-1}, and it has a working dilution ratio of 1:5000.

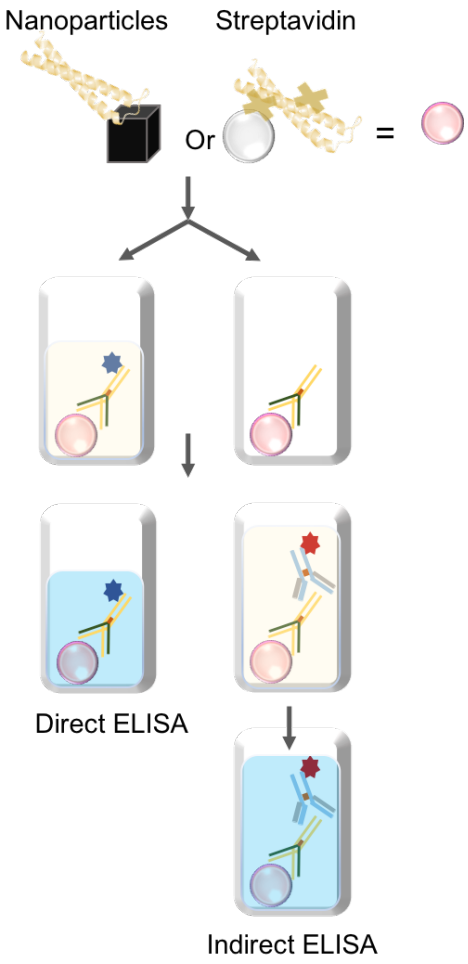

Figure 18 A schematic showing the different between a direct and indirect ELISA. It also shows how the stationary phase could be MNPs or streptavidin beads. The protein is shown as a yellow coiled coil, the MNPs are black cubes, the streptavidin beads are white spheres, while the pink spheres indicate the use of either MNPs or streptavidin. A direct ELISA uses a tagged primary antibody,whereas an indirect ELISA requires a primary antibody to bind to the species of interest, followed by a complimentary secondary antibody that binds the primary antibody and is tagged with a detection reagent.

NPs were added to 1.5 ml micro-centrifuge tubes (50 µL, 10 mg mL^{-1}) with duplicates prepared. 2x blocking buffer (ThermoScientific) in PBST was added to each tube (300 µL). Protein was then added (1 µg) and the reaction mixed (1-hour, room temperature). The particles were magnetically separated and washed three times (300 µL blocking buffer). Primary antibody was added (at the working ratio according to the manufacturer's instructions, in blocking buffer and PBST). The reaction was then mixed (1-hour, room temperature). The particles were magnetically separated and washed a further three times. If required, a secondary antibody was added (at the working ratio according to the manufacturer's instructions in blocking-PBST) and mixed (1-hour, room temperature). The particles were magnetically separated, washed then transferred to new tubes and the liquid removed. Detection reagent was added (150 µL) and incubated (15 minutes, room temperature). The particles were magnetically separated, and the absorbance was recorded on the FLUOstar Omega microplate reader (BMG LABTECH). ELISAs were also carried out using streptavidin stationary phase in the place of MNPs.

2.9.3 Binding affinity determination using ITC

Isothermal titration calorimetry (ITC) is a technique used to study biomolecular interactions and determine the binding constant (K_D), enthalpy (ΔH) and entropy (ΔS) of the reaction. Binding interactions are either intrinsically exothermic or endothermic and therefore will either increase or decrease the temperature of the surrounding solvent. This change in temperature is measurable by ITC. The ITC consists of two adiabatic cells: one reference cell and one sample cell. These cells are kept at exactly the same temperature while a ligand is gradually titrated into the sample cell. The energy required to keep the cells at the same temperature during this process is recorded and this energy is directly proportional to amount and strength of binding. As the protein becomes more saturated, there is a decrease in binding of the ligand, resulting in smaller energy requirements. This continues to occur until a level of saturation has been reached and no further change in temperature is observed. An isotherm can then be plot, showing the integrated area of the peaks measured, versus the molar ratio.[131]

The reaction was performed at a constant temperature (25 °C), using the TA instruments Nano ITC, in a variety of buffers and with varying protein and NP concentrations. The reference cell was filled with ultrapure water. The protein samples (400 µL) were titrated, using the injection needle, into the sample cell containing a suspension of MNPs. The protein was added in a course of 20 injections (2 µL per injection, addition over 4000 seconds). The sample chamber was under constant mechanical stirring (400 rpm) to prevent the MNPs from aggregating. The heat required to maintain the constant temperature of the sample cell was measured.

2.9.4 Fluorescent labelling of protein

Sulfhydryl-reactive dyes such as DyLight 650 Maleimide are able to react with free thiol groups at neutral pH resulting in the formation of thioether bonds. The free thiol group comes from a terminal cysteine residue. For the proteins used in this work, the single cysteine residue was introduced using site directed mutagenesis. Purified, cysteine tagged protein (0.4 mg) was added to reducing buffer (150 µL, appendix 1.21) containing DTT (10 µL, 1 M) and incubated (90 minutes, 37 °C). The sample was then cooled to room temperature and applied through a PD MiniTrap desalting column equilibrated with conjugation buffer (appendix 1.22) according to the manufacturer's instructions (GE Healthcare Life Sciences). After the protein had entered the stationary phase of the column, protein fractions were collected (500 µL) with the addition of conjugation buffer. Fractions containing protein were combined. DyLight 650 Maleimide (Thermo Scientific, 200 µg in DMF, 20 µL) was added and mixed well. The reaction was then allowed to proceed (overnight, room temperature). Non-reacted dye was removed by dialysis. The degree of labelling was determined by measuring the absorbance at 280 nm and 652 nm.

2.9.5 Peptide-nanoparticle binding assay

A peptide carrying a fluorescent tag, fluorescein isothiocyanate (FITC), was used to assess the binding ability of the peptide to MNPs. Fluorescein derivatives are convenient reagents for the study of biological molecules due to their high absorbance, useful quantum yields and water solubility. The maximum excitation and emission wavelengths of FITC are 490/525 nm respectively, it therefore lies in the green region of the visible spectrum. FITC-tagged peptide (1 µL, 1 mg mL^{-1}) was prepared in PBST (200 µL). This mixture was then added to magnetite NPs in PBST (200 µL, 1 mg mL^{-1}) in order to determine the peptide binding ability. The solution was incubated in the dark (overnight, 4 °C) as light could cause quenching of the fluorescent signal. The following day the samples were added to a black 96-well plate (100 µL per well) and the fluorescent signal was measured and recorded using the Omega FLUOstar microplate reader.

2.9.6 Protein biotinylation

Biotinylation is the process of covalently attaching biotin to proteins for biochemical assays, protein purification, and the linkage of other molecules via streptavidin. Streptavidin is a protein purified from *Strepomyces avidinii* and its interaction with biotin is thought to be one of the strongest non-covalent interactions to occur in nature. Each biotin molecule has four binding sites for streptavidin. Biotin molecules were added to the proteins using two different routes: primary amine biotinylation and enzymatic biotinylation. The EZ-Link® NHS-Biotin reagents kit from ThermoScientific was used to label proteins using primary amine biotinylation. The amount of biotin reagent required for the

reaction was calculated according to the manufacturer's instructions. This calculation used the appropriate molar ratio of biotin to protein. For most reactions in this work a 20-fold molar excess of biotin was used. The biotin reagent was incubated (room temperature, 30 minutes) and the protein was prepared in PBS (1 mg mL^{-1}). The biotin reagent was suspended in dimethyl formaldehyde (DMF) (10 mM, 2 mg in 590 μL of solvent). At this point the previously calculated volume of mixture was added to the protein. The reaction was incubated on ice (2 hours). Finally, the excess biotin reagent was removed using dialysis into buffer and the product was analysed using MS and SDS-PAGE. Avi-tagged protein in the presence of BirA was used for enzymatic biotinylation.[132] The BirA enzyme (0.3 μM) was added to purified Avi-tagged protein (0.3 mM), biotin (4 μM) and ATP (5 mM). The mixture was incubated at room temperature for 14 hours. The success of the reaction was analysed using MS and SDS-PAGE.

2.9.7 Protein linker chemistry for antibody attachment

The linkers used in this work were based on sulfo-succinimidyl 4-[N-maleimidomethyl] cyclohexane-1-carboxylate (sulfo SMCC). Sulfo SMCC is a water-soluble heterobifunctional cross-linker that contains maleimide and an N-hydroxysuccinimide (NHS) ester functionality. These groups enable covalent attachment to proteins through reactions with sulfhydryl (cysteine) and primary amine (lysine) groups by the formation of thioether and amide bonds respectively. There is a cyclohexane ring linking the two terminal functional groups and the presence of this ring increases the stability of the maleimide group, decreasing the rate of hydrolysis.

The protein sample required to link to the antibody was prepared in water (10 μL, 0.5 mg mL^{-1}) in a 1.5 mL micro-centrifuge tube. The concentration of primary amine groups available in the protein was used to determine the appropriate amount of cross-linker to add to the solution. A 50-fold molar excess of sulfo-SMCC was required and therefore added to the tube (40 μL, 4.8 mg mL^{-1}). The mixture was incubated (1-hour, room temperature). The antibody was then added (2.5 μL, 1 mg mL^{-1}) and the mixture was left to react (overnight, 4 °C, whilst shaking). Unreacted cross-linker was then removed using dialysis into PBS. The complex was then analysed using MS and ELISA on MNPs.

2.10 Cell culture and biomedical techniques

2.10.1 Cell Passaging

Cell passaging is also known as cell sub-culturing or cell splitting. The process involves the removal of used media and the transfer of cells from one flask to a new, sterile flask, followed by the addition of fresh, nutrient rich media. Cell passaging ensures the healthy growth of cells and the propagation of the cell strain, leading to higher possible passage numbers. Human ovarian cancer cells (SKOV-3)

were cultured (37 °C, 5% CO_2) in McCoy's 5A (IV) medium, supplemented with 10% foetal bovine serum (FBS, filtered), penicillin (100 000 units L^{-1}) and streptomycin (100 mg L^{-1}). The media was warmed (37 °C for 15 minutes) before starting. When splitting cells, the existing media was discarded. The T75 flask was washed with PBS (4 mL, warmed to 37 °C). The PBS was discarded, and Trypsin was added to the flask (2 mL, 37 °C) to detach the cells before incubating (37 °C, 5% CO_2 for 5 minutes). After 5 minutes, PBS was added (5 mL). The contents of the flask were re-suspended and transferred to a centrifuge tube before the cells were pelleted (1000 rpm, 5 minutes). Media was then added to new T75 flasks (10 mL). The supernatant was discarded and inoculated after centrifugation and the cell pellet was re-suspended in media (8 mL). The cell suspension (1 mL) was then added to the T75 flask. The flask was incubated again (37 °C, 5% CO_2). The media in the flask was replaced every two days and cells were split once 85% confluency was reached (around 72 hours).

2.10.2 Studying nanoparticle uptake with SEM

Scanning electron microscopy (SEM) uses a beam of high energy electrons to produce a signal. As the beam hits the specimen, electron-sample interactions cause the dissipation and deceleration of the electrons (figure 19). The electrons that consequently escape from the sample are termed 'secondary electrons'. The signals produced by the secondary electrons are used to determine the morphology and size of the material within the sample. As with TEM, the electrons that make up the beam have a much smaller wavelength than visible light and therefore SEM has a much higher resolution than optical microscopy. Also, as with other types of electron microscopy, the system is kept under vacuum to prevent attenuation of the electrons. A high voltage is passed between an anode and cathode causing a tungsten filament to emit electrons, these electrons pass through a hole in the anode to form the beam. The path of these primary electrons is controlled using various lenses within the chamber.[129]

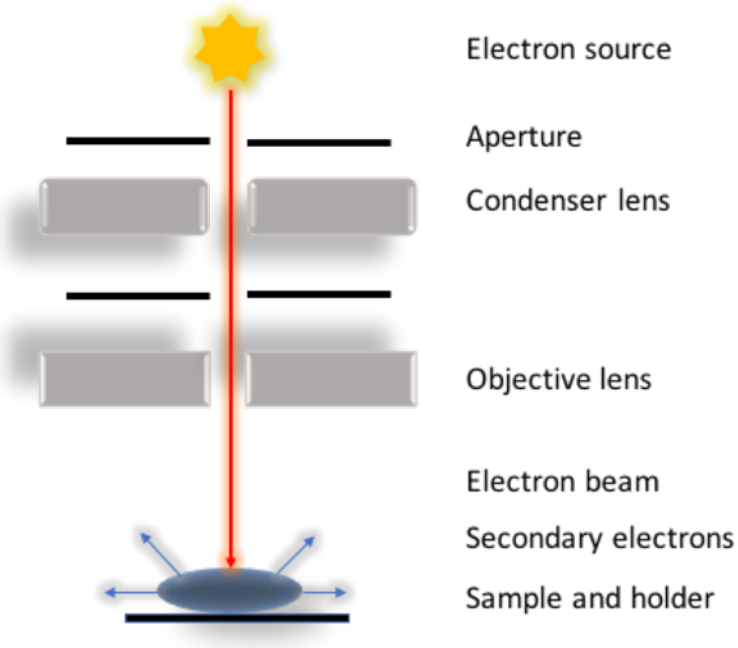

Figure 19 Diagram showing the components of a scanning electron microscope. The microscope uses a beam of electrons that are focuses using a range of lenses, shown in this figure. The beam then hits the sample and the secondary electrons that are emitted from the sample are measured to produce an image.

Silicon wafers (chips) were used to mount the cells. The silicon chips were sterilised before use. They were initially washed with ethanol (70%, 500 μL) and sonicated (15 minutes, in a sonic bath, high power). The chip was then washed with isopropanol (500 μL) and then water (500 μL) before being placed under UV-light (15 minutes). SKOV-3 cells were trypsinised at 70% confluency and reseeded on the silicon wafers, then placed in the 6-well plate. The cells were left to grow (24 hours, 37 °C, 5% CO_2), after which the cells were treated with NPs (50 μg mL^{-1} and 100 μg mL^{-1}; with and without RAGE antibody attached) and cells incubated under the same conditions for a further 48 hours. The cells containing the NPs were fixed on the silicon wafer using glutaraldehyde (3% in PBS) and then washed three times (PBS, 1 mL). The cells were dehydrated using a series of ethanol washes: 30% for 20 minutes; 50% for 10 minutes; 60% for 10 minutes; 70% for 10 minutes; 80% for 10 minutes; 90% for 10 minutes; 95% for 10 minutes; 100% for 20 minutes. The samples were then left to dry at room temperature for 1 hour. Images were acquired using the Hitachi S4800 scanning electron microscope with energy dispersive x-ray spectroscopy (EDX) capabilities for composition mapping.

2.10.3 Studying nanoparticle uptake with In-Cell analysis

The In-Cell analyser 2000 is a rapid, high-throughput method of imaging fluorescently tagged dead or living cells and produces confocal-like images. Confocal microscopy can image cells in 3D, whereas the In-Cell analyser is only capable of 2D image production. SKOV-3 cells were seeded in a 12-well plate (50, 000 cells per well) and incubated in growth medium (24 hours, 37 °C, 5% CO_2). The cells

were treated with FITC-tagged magnetite NPs (varying concentration, with and without conjugated antibody) for 24 hours, 37 °C, 5% CO_2. The medium was removed, and the wells were washed with PBS (2x 1 mL). Paraformaldehyde (PFA) was added to fix the cells (4% in PBS, 500 μL) and the plate was left to shake (4 °C, 20 minutes). The wells were washed again with PBS (2x 1 mL) before a DAPI stain was added to the cells (4 μM, 500 μL). The cells were left to shake (4 °C, 20 minutes). PBS was added to each well for the reading (1mL). The fluorescence of the DAPI and FITC stains were detected using the In-Cell Analyser 2000. 42 random fields per well were scanned, at a magnification of 20X.

2.10.4 Studying nanoparticle uptake with confocal microscopy

Unlike conventional wide-field optical microscopy, confocal eliminated interference caused by fluorescent signals emitted away from the site of interest. A laser is focused from a focal point of one lens, onto a single spot of another lens, and is scanned across the sample. The laser provides a beam with a wavelength equal to the excitation wavelength of the fluorophore attached to the sample. The laser is reflected, hitting two mirrors allowing the light to scan across the sample. The light emitted by the specimen is scanned and focused back to the focal point where it is detected. The computer then builds an image of the observed points of the scan. Standard glass coverslips (24 x 24 mm) were cleaned in the same way as the silicon chips for SEM analysis. The SKOV-3 cells were seeded on coverslips and prepared/fixed in the same way as InCell analysis. The coverslips housing the fixed, treated cells were mounted on to poly-L-lysine-coated glass slides using cell mounting media. The slides were allowed to dry (1-hour, room temperature). The cells were visualised using the Zeiss LSM 710 confocal microscope with a magnification of 20 and 40X. The FITC and DAPI were detected using the appropriate filters and laser. The confocal system uses a Zeiss AXIO Observer Z1 inverted microscope stand with transmitted light (HAL), illuminator HXP 120C and laser illumination sources.

2.10.5 Cell cytotoxicity determination using Real-Time Glo

The RealTime-Glo™ MT cell viability assay allows monitoring of the cell metabolism in a single well, over a period of 72-96 hours. The reaction relies on the non-lytic nature of the reagents supplied in the kit. The assay is used to measure the reducing potential of any viable cells present in the well. The enzyme luciferase and the MT cell viability substrate is added to the cells. The viability substrate diffuses into the cell and is reduced to form the luciferase substrate. Only living cells which have the ability to metabolise the substrate are detected. Detection relies on light produced by the reduction. The output was measured using the Omega FLUOstar microplate reader. Unlike other cytotoxicity assays, this reaction is ATP independent.

The Promega RealTime-Glo™ MT Cell Viability Assay was used to monitor cell viability of a single sample, continually, for 96 hours. SKOV-3 cells were harvested and plated for a final cell density of 500 cells per well in a white, opaque-wall 96-well tissue-culture plate. The cells were incubated for 24 hours (37 °C, 5 % CO_2) before being treated with magnetite NPs. Immediately after treatment with the NPs the MT cell viability substrate and the NanoLuc© enzyme (obtained from the kit and incubated at 37 °C prior to use) were added to the cell suspension for a final dilution of 1 in 500. The luminescence of the wells was then measured using the FLUOstar Omega multi-mode plate reader by BMG labtech, using a 1 second integration time per well. Reader Control Software and MARS data analysis, (BMG labtech) were used.

2.10.6 Cell cytotoxicity of 3D models

The CellTiter-Glo 3D cell viability assay is used to measure the viability of cells that make up microtissue spheroids. The reagents were engineered to penetrate the 3D spheroids and cause lysis. The assay measures the ATP dependence of the cells and the reagents produce a luminescent readout which can be measured using the Omega microplate reader. The spheroids used were comprised of SKOV-3 cells. Pre-grown SKOV-3 spheroids were visualised under an optical microscope and then transferred into a black 96-well tissue-culture plate, using PBS (100 μL) to detach the spheroids from the initial plate. The 3D spheroids were immediately treated with a magnetite NP solution, suspended in cell growth media. The cells were incubated for 48 hours (37 °C, 5 % CO_2). The CellTiter-Glo® 3D reagent was thawed (4 °C overnight) and equilibrated to room temperature. The CellTiter-Glo® 3D reagent was then added to the wells in a 1:1 mixture, matching the volume of cell solution. The contents were incubated at room temperature for 25 minutes following an initial 5 minute mix. Finally, luminescence was recorded using a BMG labtech FLUOstar Omega with an integration time of 1 second per well. Data was analysed using MARS and Reader Control Software by BMG labtech.

2.10.7 Magnetic hyperthermia

In magnetic hyperthermia an alternating current (AC) magnetic field is applied to the MNPs, resulting in particle heating. It is the characteristics of the magnetic hysteresis loop associated with the ferromagnetic or ferrimagnetic nature of the NPs that enable magnetically induced heating. The equation for the amount of heat generated by the particles can be seen below[25]:

$$P_{FM} = \mu_0 f \oint H \, dM$$

This equation gives the heat produced per unit volume where: μ_0 is the permeability of free space; f is the frequency (optimum between 0.05 – 1.2 mHz); H is the magnetic field strength; M is the magnetisation. A magnetherm (used for the analysis of the magnetically induced heating) contains a coil that has a current flowing around it. The flow of this current generates a magnetic field. The sample was placed in the coil at zero voltage, and once the temperature of the sample was stable, the voltage was increased. The change in temperature of the sample was recorded using a fibre optic temperature probe and plotted against time. The ILP and SAR values were then calculated.[25]

$$SAR = {}^{P}/_{m}$$

$$ILP = {}^{SAR}/_{f\ H^2}$$

Once the current was flowing and the voltage was increased (15.1 V), the previously sonicated sample (15 mg in water) was exposed to the magnetic field. Temperature data was collected for approximately 20 minutes. Control samples containing only buffer were also analysed.

Chapter 3: Magnetite Interacting Adhirons (MIAs)

3.1 Introduction to the dual use of MIAs

This chapter will introduce an Adhiron; an artificial peptide displaying scaffold. An explanation of the development of the protein will be provided; alongside a description of its evolution into a useful tool to aid the synthesis of monodisperse MNPs. The proposed dual functionality of the MIA scaffold stems from the idea that it is not only used to help control crystal nucleation and growth during synthesis - it is also capable of behaving as an attachment device to adhere drugs, dyes and antibodies to the surface of the magnetite particles.

3.1.1 The development of the Adhiron scaffold

In recent years there has been an increase in research power focused on identifying alternatives to antibody scaffolds. Monoclonal antibodies have shown promise in molecular recognition, diagnostic and therapeutic applications, with over 240 candidates under clinical development.[133] However, artificial protein scaffolds are advantageous for a number of reasons. Their production is both ethically and economically favourable as animal models and mammalian cell cultures are not required (unlike for the production of antibody-based products). Alternative protein scaffolds are also much simpler; most are monomeric and less than 200 amino acids in length with chemical and physical properties that can be tailored to suit the desired function. The low MW protein reduces possible steric barriers to binding which has previously been witnessed during monoclonal antibody use. Often the protein sequence intentionally lacks cysteine residues, decreasing complex folding and disulphide formation during protein production and post-translational modifications. Interestingly, cysteine residues may be incorporated later in development for site-specific attachment. This move away from antibody-based peptide displaying scaffolds was the initial motivation for the design and development of the Adhiron scaffold.

The early research and development into the Adhiron was conducted by Dr Darren Tomlinson, Prof Michael McPherson and their respective groups at the University of Leeds. This work was published in the Oxford Journal 'Protein Engineering, Design and Selection' in 2014.[84] These groups were members of the Bioscreening Technology Group (BSTG), providing an interactive service for characterisation of protein function and binding. The primary objective was to identify a highly

stable, small, monomeric protein that expressed well in bacterial systems such as *E. coli*. The focus soon narrowed in on the use of plant phytocystatin sequences as a template for the scaffold. An average size of around 100 residues and the presence of two hairpin loops within the protein structure indicated a promising starting point. It was essential that the protein was extremely stable, thermally and chemically, as changing or inserting various peptide loops into a scaffold can dramatically decrease the protein stability. To achieve maximum stability of the scaffold, a consensus sequence was derived. A tBLASTN[134] search of the Genbank database was performed using several cystatin protein sequences and the coding sequences resulting from the search were aligned using MUTALIN[135] – generating a consensus sequence. This step was an essential one in the design of the scaffold; a consensus sequence maximises the stability of the sequence by incorporating only the residues that are most highly conserved across the range of sequences analysed. It relies on the theory that the most common residues have been evolutionary advantageous, leading to greater overall stability. With the identification of the most stable sequence, an Adhiron consisting of 95 amino acids was carried forward. The N-terminus was set before the first β-strand and the C-terminus was set after the final β-strand (with four β-sheets in total). To enable the most efficient expression in *E. coli* the consensus gene sequence for the Adhiron scaffold was then codon optimised. The optimised Adhiron consensus sequence was cloned into a pBSTG1 phagemid vector, between Nhe1 and Not1 restriction sites. This provided a DsbA signal peptide at the N-terminus, the Adhiron sequence, a His-tag, TAG stop codon and truncated gene III of bacteriophage M13 at the C-terminal.

A new phagemid vector was successfully generated; the stable Adhiron sequence had been fused with a bacteriophage gene required for phage display and rounds of biopanning (Section 1.5) producing a library of 1.3×10^{10} clones. Synthesis of the clones used splice overlap extension PCR[136]. This variant of the polymerase chain reaction is widely used in chemical biology to insert mutations into gene sequences and to splice smaller DNA fragments into larger DNA sequences. Firstly, two shorter DNA sequences are amplified and purified. A linker between the two fragments can then be introduced using two overlapping internal primers (or alternatively a specifically designed linker primer). The vectors containing the genes of the Adhiron library were expressed in *E. coli*, following electroporation of competent cells. The Adhiron was cloned and purified using the His-tag. The protein was then biotinylated using a EZ-link NHS-SS-Biotin kit from Pierce. Western blot was used to confirm expression of the Adhiron-pIII fusion. An anti-pIII antibody gave a positive result indicating the successful fusion. The high stability was confirmed using DSC which showed a very attractive melting temperature of 101 °C. This high thermal stability opened up a range of possible

applications for the protein. Importantly, it was showed that the protein could be stored for longer lengths of time at ambient temperatures and would be stable for a range of purification techniques. Purification would not need to be rushed or carried out at low temperatures.

Structure determination of the new artificial scaffold was successfully achieved, and a crystal structure identified. These crystallisation trials were set up according to the protocol described by Walter *et al*.[137] The 95-residue, full length Adhiron gave rod-like crystals that were around 25 μm across. The crystal structure was consistent with the CD data collected: a high β-sheet ratio. The structure consists of four anti-parallel β-sheets and a single, central α-helix (figure 20). This structure is characteristic of the conserved cystatin fold. It is this highly structured arrangement that gives rise to the high stability and T_m witnessed for the Adhiron and cystatin structures. Two variable regions (VR) can be seen in the crystal structure, these insertion sites are located between β-sheets 1 and 2 and between β-sheets 3 and 4. The positions of these loops are also consistent with the loops in other phytocystatins, for example in the rice phytocystatin OC-1 which also has a known crystal structure.[138]

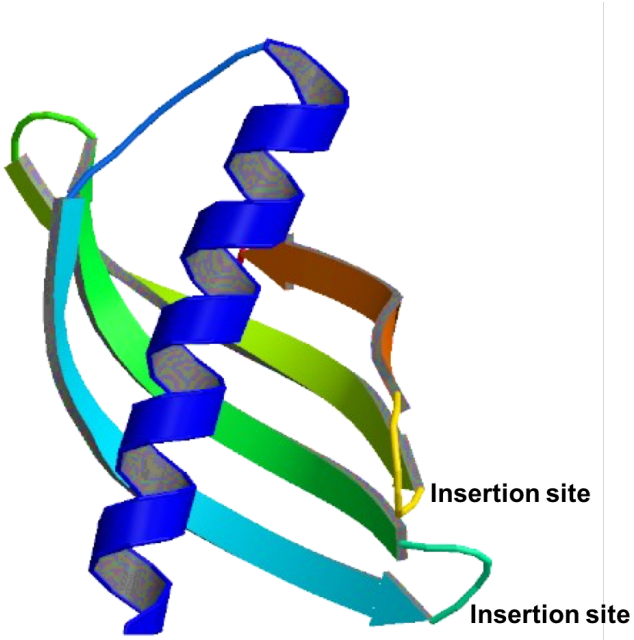

Figure 20 The Adhiron crystal structure (PDB: 4N6T). The image shows the four β-sheets and single α-helix, characteristic of the phytocystatin fold. Two variable loop regions, marked 'insertion site' can be seen in yellow and aqua. VR1 is located between β-sheets 1 and 2 and VR2 between β-sheets 3 and 4.

With the primary purpose of the development of this novel peptide displaying scaffold protein being to act as a useful alternative to antibodies, it was essential to determine its effectiveness in

molecular recognition. Thus, the Adhiron was screened against yeast small ubiquitin modifier (ySUMO). This study incorporated known SUMO binding sequences into the variable loop regions of the scaffold. Phage display and subsequent biopanning rounds showed similar SUMO-binding affinities to the previously developed DARPin scaffold. Indicating a promising target binding ability of the new Adhiron.

BSTG were successful in testing the Adhiron against a range of other molecules, with over 100 targets and sequences studied and a number of specific sequences displayed as variable loop regions within the Adhiron identified. The need and success of these types of scaffold rely on their ability to hold a peptide sequence in position, preventing conformational freedom, providing stronger and more specific binding. BSTG worked to characterise proteins and use the data to better understand the interactions which form between biomolecules and target ligands. This understanding aids the preliminary identification of potential diagnostic biomarkers and therapeutic targets. Further research is currently being conducted to explore the possibility of using the Adhiron for diagnostics, therapies, imaging and drug delivery. The properties match those required to generate an alternative protein scaffold, for example small, monomeric and highly stable – however these properties are yet to be tested in a clinical setting. The proteins have however been developed commercially. BSTG formed a close collaboration with Avacta Life Sciences to further the develop the Adhiron, which is now known commercially as an affimer.

3.1.2 Phage display for the production of MIAs

Phage display is an *in vitro* screening technique used to identify new binding partners for existing proteins or molecular recognition complexes (section 1.5). Target ligands can be other proteins or peptides, small molecules or inorganic compounds and minerals. The protein of interest is fused to a truncated phage, such as pIII, and this bacteriophage is then used to infect bacterial cultures to amplify any sequences found to be successful in binding. Subsequent rounds of biopanning are conducted to ensure only the strongest and most specific sequences are analysed further. This Adhiron scaffold protein has been subjected to rounds of phage display and biopanning for the identification of novel binding partners. Initial binding partners were identified by BSTG, in collaboration with the Staniland group, led by Dr Andrea Rawlings.[84] This work has been developed further by me, for this thesis, with improved synthesis of MNPs at the forefront of the research.

The interest in MNPs for magnetic separation, clean-up and biomedical applications has been growing at an incredible rate over the past decade or so, with one of the most promising materials emerging being magnetite (Fe_3O_4). Applications such as therapeutics and diagnostics rely on highly

uniform NPs in terms of composition, size, shape and therefore magnetic properties and biocompatibility; currently the only reliable syntheses for magnetite require high temperature, high pressures and the use of expensive organic solvents, all of which are environmentally destructive methods of synthesis.[10] For this reason, biological additives for *in vitro* mineral synthesis have become a highly desirable alternative, allowing chemical reactions to proceed under ambient temperatures and pressures, in aqueous conditions. The new, stable, well-expressing Adhiron peptide displaying scaffold was deemed an interesting candidate to be explored for displaying peptide sequences for the development of a novel molecular recognition agent for specific facets of magnetite. It was the first time that this scaffold had been screened against mineral targets. It was hypothesised that if it binds to the [100] facet, it will promote the formation of that face and thus the crystal favour a cubic morphology following a synthesis reaction.

A phage display library of Adhiron clones was screened with the scaffold displaying two variable loop regions, each containing nine random amino acids. Cysteine was not included in the library. The VRs were selected *in situ* based on their affinity to bind the [100] face of cubic magnetite. Selected proteins formed the basis of a collection of Adhiron proteins named magnetite interacting Adhirons (MIAs). The Adhiron library was generated using codon optimised semi-trinucleotide cassette synthesis and over 1.3×10^{10} clones were present and fused to the truncated pIII minor coat protein of M13 bacteriophage.[139] These protein fusions were incubated with cubic magnetite NPs in the presence of blocking buffer. The blocking was required due to the high charge density on the magnetite surface which had the potential to lead to the formation of a large number of weak, non-specific interactions in the absence of the buffer. The particles were washed, and the binding partners were eluted using increasing pH washes. The eluted proteins, alongside the MNPs, were used to infect *E. coli* cells. It was important to also analyse the apparently bare MNPs as it is possible that proteins may have been bound so strongly that they were not removed during the elution stage, however no proteins were located in this fraction. The phage display procedure was repeated for a total of three cycles to ensure sufficient enrichment of the protein pool (a representation of the protocol can be seen in figure 21). Each round resulted in increased enrichment. A total of 72 MIAs were selected for further analysis.

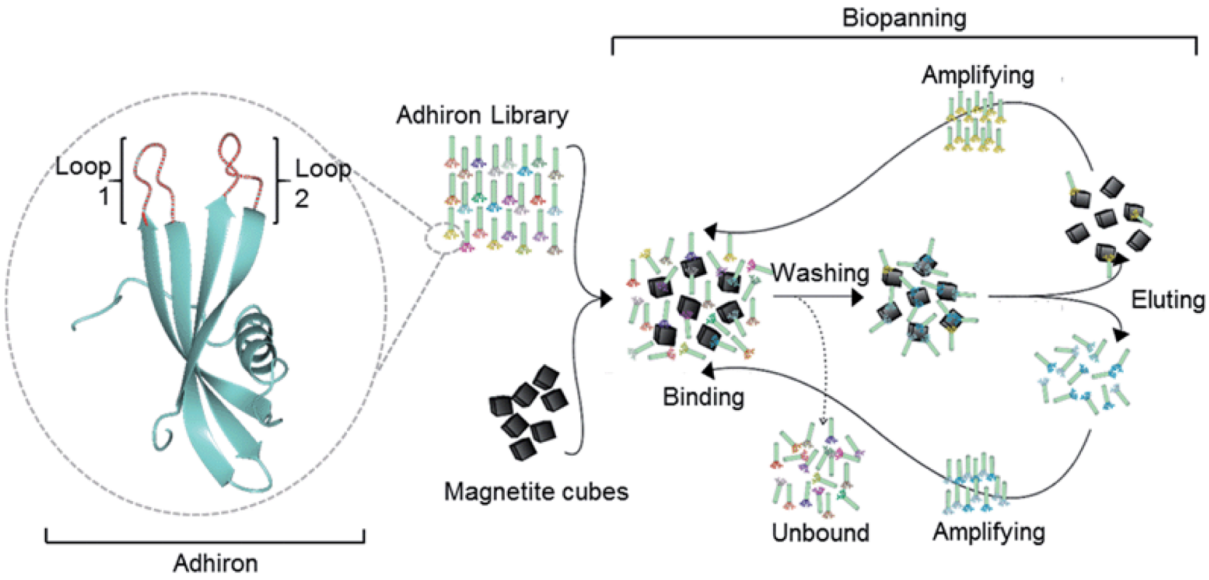

Figure 21 Adhiron in rounds of biopanning. The green cylinders represent the Adhiron scaffold and the various of coloured tips indicate different peptide sequences displayed on the Adhiron. Image produced by Dr Andrea Rawlings, University of Sheffield.[139]

Analysis of the peptide sequences that appeared to bind strongly and specifically to the [100] face of magnetite was performed using phage ELISA with an AP phage and showed a strong preference for basic residues, particularly lysine. Alongside the binding sequences, the M13 phage was also analysed using a phage ELISA and showed no specific binding to the magnetite NPs, as expected. Molecular dynamic simulations backed-up these findings as the simulations indicated the lowest energy of absorption for the binding of lysine to the magnetite surface. The interaction between the VRs of the MIA and the [100] magnetite face were simulated at Leeds University by Dr Darren Tomlinson, Prof Michael McPherson and their respective groups, these simulations have since been published.[84] The simulations used DL_POLY classic code to provide a better understanding of how specific amino acids were able to interact with the surface atoms of magnetite with the single residues being brought towards the surface to calculate the associated adsorption energy (in water). These simulations suggested that lysine residues were able to interact strongly through the formation of hydrogen bonds between its sidechain and the mineral surface. Hydrogen bonds were also shown to form between the peptide carbonyl and the [100] surface. For glutamic acid, only the oxygen atom present in its side chain was shown to be available for binding (figure 22). For this reason, the lysine was suggested to have the most negative adsorption energy (-52 kJ mol^{-1}), whereas glutamic acid was found to have one of the least favourable adsorption energies (-3 kJ mol^{-1}). These simulations were found to match the data supplied for the frequency of these residues appearing in successful MIAs. Lysine residues account for 24% of the amino acids in the VRs whereas the frequency is decreased to 3% for glutamic acid and remained low for other acidic groups. Again,

suggesting the importance of basic residues (particularly lysine) for binding the magnetite [100] facet.

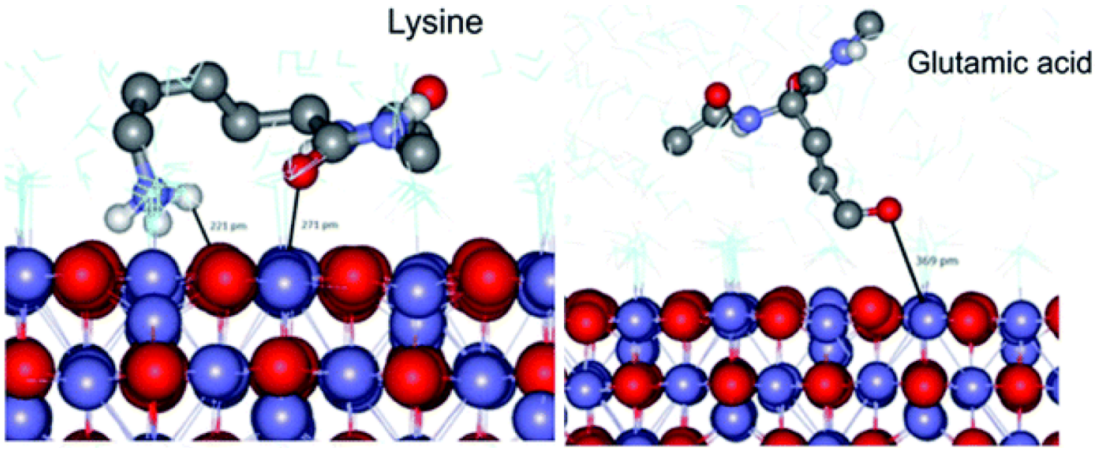

Figure 22 Image taken from 'Phage display selected magnetite interacting Adhirons for shape controlled NP synthesis'.[84] The schematic depicts a molecular dynamics simulation of how the acidic (i.e. glutamic acid) and basic residues (i.e. lysine) of a MIA VR may adsorb onto the [100] magnetite surface. Hydrogen atoms that would bind to carbon are not shown.

The specific binding of the MIAs to MNPs will be discussed in more detail later in this chapter.

Although this chapter and work concentrates on the use of the Adhiron scaffold to display sequences for the binding of magnetite NPs only, the general approach has the potential to be used for the production of an extensive toolkit of additives to aid material synthesis. This material synthesis could extend beyond magnetite and iron oxides; alternatives to the Adhiron acting as the protein scaffold could also be investigated.

3.1.3 Aims

- To complete molecular cloning, protein expression and protein production of a number of MIA proteins
- To characterise the proteins
- Addition of the MIAs to RTCP reactions to control the size and shape of the resulting MNPs
- Characterise MNPs produced in the presence of absence of MIA proteins and peptides.

3.2 Molecular cloning strategies used in MIA production

The initial phage display studies were successful in finding a number of peptide loops, displayed on the Adhiron scaffold protein, that were able to target the [100] magnetite facet. A handful of these proteins were then taken forward to access the specificity in their binding capabilities away from the

phage display set-up. The first stage was to discover optimum cloning and protein production conditions. PCR was used to amplify the chosen peptide sequences displayed on the Adhiron. Specific forward and reverse primers were designed to anneal and therefore amplify the DNA sequences in the presence of dNTPs and polymerase; these primers contained Bsa1 restriction sites required for sticky-end ligation.

DNA sequences for further analysis were not chosen at random. Each of the successful binding partners were found to possess different and interesting properties, for example some displayed peptide sequences at both VR 1 and 2, whereas others (of which their numbers were enhanced in the phage display study) displayed only a single variable loop. Another important factor from the previous study appeared to be the number of basic residues within the loops. Many binders were enriched with basic residues, however some successful binders contained very few, or even no basic amino acids within the variable loops. Adhirons labelled A3, D1, E8, G4, G9 and H4 were studied. The sequences of the variable loops and a summary of the basic properties can be seen in table 7 below:

Table 7 Showing the properties of the MIAs used in for this project. Column one is identifies the protein code, columns two and three show the sequences of the variable regions of the scaffold, followed by whether there are one of these regions displayed. Column five indicates whether the variable regions are lysine rich or poor (1-2 lysine residues is described as lysine poor, 2-3 is medium and more 4+ is categorised as lysine rich). The final column shows the protein isoelectric point.

Adhiron	Sequence VR2	Sequence VR1	Loops displayed	Lys rich/medium/poor	Protein PI
A3	-	HNHKSKKSK	1	Rich	10.5
D1	-	DHFRKGYHH	1	Poor (His rich)	8.6
E8	-	AHMYTKAQT	1	Poor	8.6
G4	-	QRAQSVSKK	1	Medium	11.2
G9	YKKNDLSQI	NYKKRQKKK	2	Rich	10.7
H4	PKKSKIELK	QKFVPKSTN	2	Rich	10.0
Control	DWWEAGVFM	WNEINYMFD	2	Poor	5.5

Both of the sequences displaying two loops were rich in basic residues, this was not missed when deciding upon the sequences to study. All sequences displaying both VRs that were found to bind strongly to the magnetite were rich in lysine, therefore indicating that although binding may be favourable for species displaying a single loop (possibly due to the sterics of the binding process), species displaying both loops could also bind favourably if the steric interactions could be overcome with an increased number of basic residues available for stronger or more competitive binding.

PCR was used to produce amplified DNA of the expected MW for the fragments of interest. Each fragment was around 400 bp in length and contained the desired restriction sites and a PelB leader sequence to enable protein expression in the periplasm, if required. Figure 23 shows an example of a 1 % agarose electrophoresis gel of a successful PCR reaction. All PCR fragments were visualised using gel electrophoresis to access the success of the reaction and the product formed.

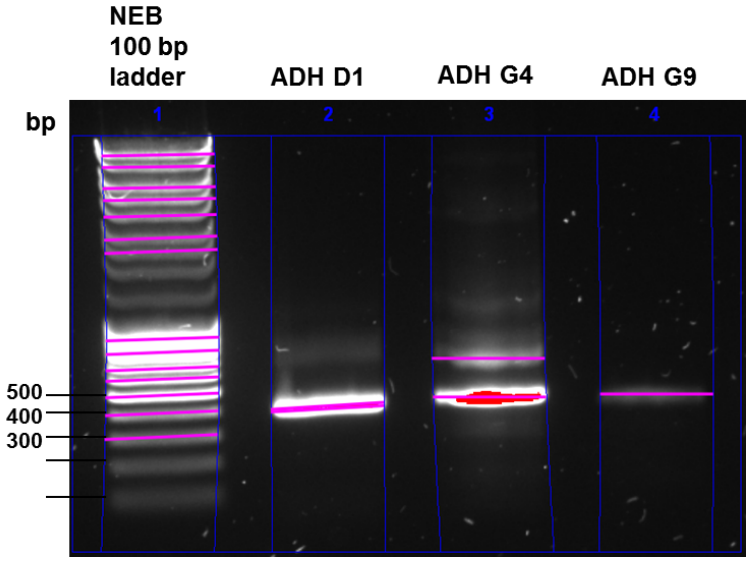

Figure 23 An example of an agarose electrophoresis gel showing the successful amplification of MIA DNA fragments using PCR. The DNA fragments are all around 400 bp. The first lane contains 5 µL of NEB 100 base pair ladder, the next three lanes contain proteins ADH D1, ADH G4 and ADH G9 respectively, mixed with loading dye. Significant bands are highlighted in pink.

The PCR fragments were cleaned and prepared for restriction digestion. The Bsa1 sites were digested using the Bsa1 enzyme in the appropriate buffer system, Dpn1 was also added to destroy any remaining template DNA. Both enzymes were compatible in CutSmart buffer (NEB). The digest produced single strand DNA overhangs that were available to bind complimentary sticky-ends of another piece of DNA. This method allowed the ligation of the MIA DNA fragments into a chosen DNA plasmid. pPR-IBA1 was the chosen vector system for this work. A vector map can be viewed in the appendix (2.1). This vector was chosen to:

- Ensure efficient transformation in competent *E. coli* cells by means of T7 promoter-based expression.
- Aid cell growth and prevent contamination due to the inherent Ampicillin/ Carbenicillin based resistance.
- Fuse a C-terminal Strep-II tag to the insert allowing affinity-based purification of the recombinant protein.

The pPR-IBA1 vector was subject to restriction digest and gel extraction to produce a clean vector with complementary sticky ends to the digested MIA sequences. The two DNA fragments were mixed together in the appropriate buffer system, with the addition of DNA ligase. The reaction was incubated until the fragments had ligated and the DNA insert had successfully been incorporated into the plasmid, forming circular, supercoiled DNA. Agarose gel electrophoresis was used to track the reaction. Although the DNA insert was small compared to the vector, the reaction could still be accessed on the gel as the circular, supercoiled DNA moves more easily through the gel matrix compared to linear DNA and so travelled further down the gel in the allotted time. It was difficult however to determine whether the supercoiled DNA contained the DNA insert or whether it was empty vector. The pPR-IBA1 vector was analysed on a gel after digestion and before ligation to ensure that all the vector had been digested, therefore there should be no substantial amount of circular vector remaining at the start of the ligation process. Also, the Bsa1 restriction enzyme cuts at a different point to the recognition sequence which should prevent the vector (or insert, if large enough) ligating to itself, re-circularising.

The recombinant plasmid was then transformed using chemically competent *E. coli* cells. At this stage XL10 Gold cells enabled good expression levels. The cells were spread on LB agar plates containing the desired antibiotic and the plates were incubated to allow cells to grow. Useable amounts of colonies grew on the plates (usually around 50). At this stage however it should not be assumed that all the colonies contained the correct DNA insert, therefore colony PCR was used to test a number of them before preparing them for further sequencing. Colony PCR amplifies the DNA sequence contained within the *E. coli* colony using primers complimentary to the insert DNA. The colonies picked for colony PCR almost always contained the desired insert, an example of the agarose gel used to analyse the reaction can be seen below. The fragments here were amplified with primers specific to the D1 insert and when comparing the fragments to the DNA ladder, the size appears around 400 bps – consistent with that expected of the DNA insert. The agarose gel was run for each of the inserts and yielded similar results. When occasionally a colony did not contain the desired insert, there would be no band present for the amplification of that DNA on the gel, this is due unsuccessful binding of the primers, leading to an unsuccessful PCR reaction. These colonies were removed from further analysis.

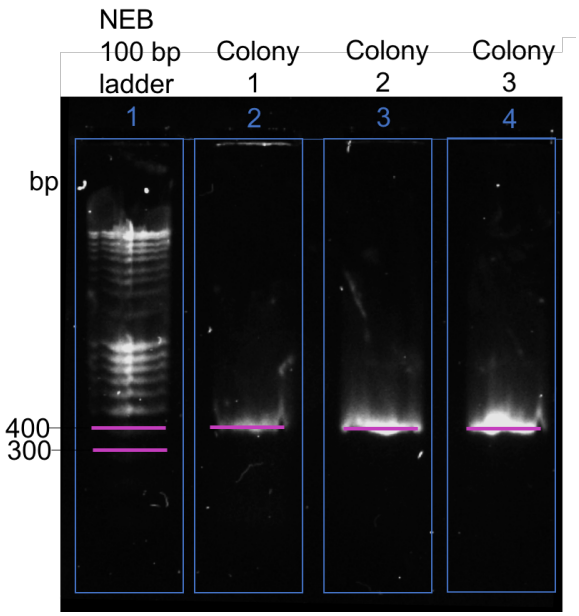

Figure 24 An example of an agarose electrophoresis gel showing the successful colony PCR products containing MIA DNA fragments. The DNA fragments are all around 400 bp. The first lane contains 5 µL of NEB 100 base pair ladder, the next three lanes contain proteins samples of three different colonies, picked for LB agar plates, mixed with loading dye. Significant bands are highlighted in pink.

Colony PCR could only be used as an indication that the correct insert was present in the *E. coli* colony, it could not determine any point mutations or single insertions or deletions to the sequence. Therefore, following a further transformation round of the colonies appearing promising from the colony PCR results, the DNA sequences could be analysed in more detail. The recombinant DNA was transformed, this time into BL21 (DE3) chemically competent *E. coli* cells, the resulting colonies were then grown in a nutrient rich medium, before the culture was spun down to produce the *E. coli* pellet containing the DNA. The DNA was sent for Sanger sequencing read from the T7 promoter region. The sequences for each of the Adhirons (A3, D1, E8, G4, G9 and H4) came back as expected. The VR sequences displayed on the Adhiron scaffold can be found table 7. Upon identification of the correct DNA sequences, the recombinant DNA could be used for protein expression.

Overall, the cloning of the MIA species worked well, with few errors or complications. Basic PCR reactions with temperatures and times tailored to the length of the DNA fragment and the annealing temperature of the designed primers appeared to work with little optimisation required. Ligation of the plasmid and DNA insert also worked well, with the standard 1:3 molar ratio of vector to insert yielding good results from the start. Also, expression in XL10 gold chemically competent *E. coli* cells gave a good number of successful colonies. The relative ease, with minimal optimisation of the MIA molecular cloning strategy already begins to indicate the desirability of the MIA scaffold as an alternative to antibodies and as an additive for synthetic NP reactions.

3.3 Optimisation of protein production

Following the successful cloning of the MIA DNA, the next step was to produce protein. MIA protein production would require optimisation of protein expression and protein purification routes. Expression levels were considered first. Two expression routes were compared: expression using auto induction and expression using IPTG. Both routes yielded similar amounts of soluble protein, the auto induction method was slightly simpler and so this route was studied in more depth. A dot blot technique was used to compare the amount of total and soluble protein produced under different expression conditions. Four different auto induction medias were prepared and compared, with varying nutritional content. These mediums were: LB, 2 x YT, TB and SB. Two incubation temperatures were used: 25 °C and 37 °C and each of these conditions were measure at 0, 12, 24, 36, 48 and 60 hours in order to track the protein expression as a function of time.

Cultures of *E. coli* containing known sequences of the MIA DNA were grown in LB media. Samples of these cultures were then added to various autoinduction mediums containing the desired antibiotics before incubation at the temperatures being tested. At each time point a sample of the autoinduction reaction was taken and spun to pellet the cells. For the dot blot technique to work the *E. coli* cells producing the MIA protein first needed to be lysed. Originally, this was done using a cell lysis solution named 'Bug Buster' containing Triton X-100 surfactant, lysozyme enzyme and benzonase® endonuclease. However, this gave poor results indicating that lysis had been unsuccessful. This may have been due to the degradation of one or more of the buffer components. An alternative to the lysis solution was to use sonication to lyse the cells and release the DNA. Sonication as a form of lysis appeared to work well. The lysed cell pellets were resuspended in dot blot buffer and a sample of this mixture was taken to add to the nitrocellulose membrane, this would provide the intensity of the total amount of protein produced. Following this, the remaining sample was subjected to centrifugation to remove the insoluble debris and leave the soluble protein fraction in the supernatant. When added to the membrane, the intensity would correspond to the amount of soluble protein. The results from the dot blot can be seen below in figures 25 and 26.

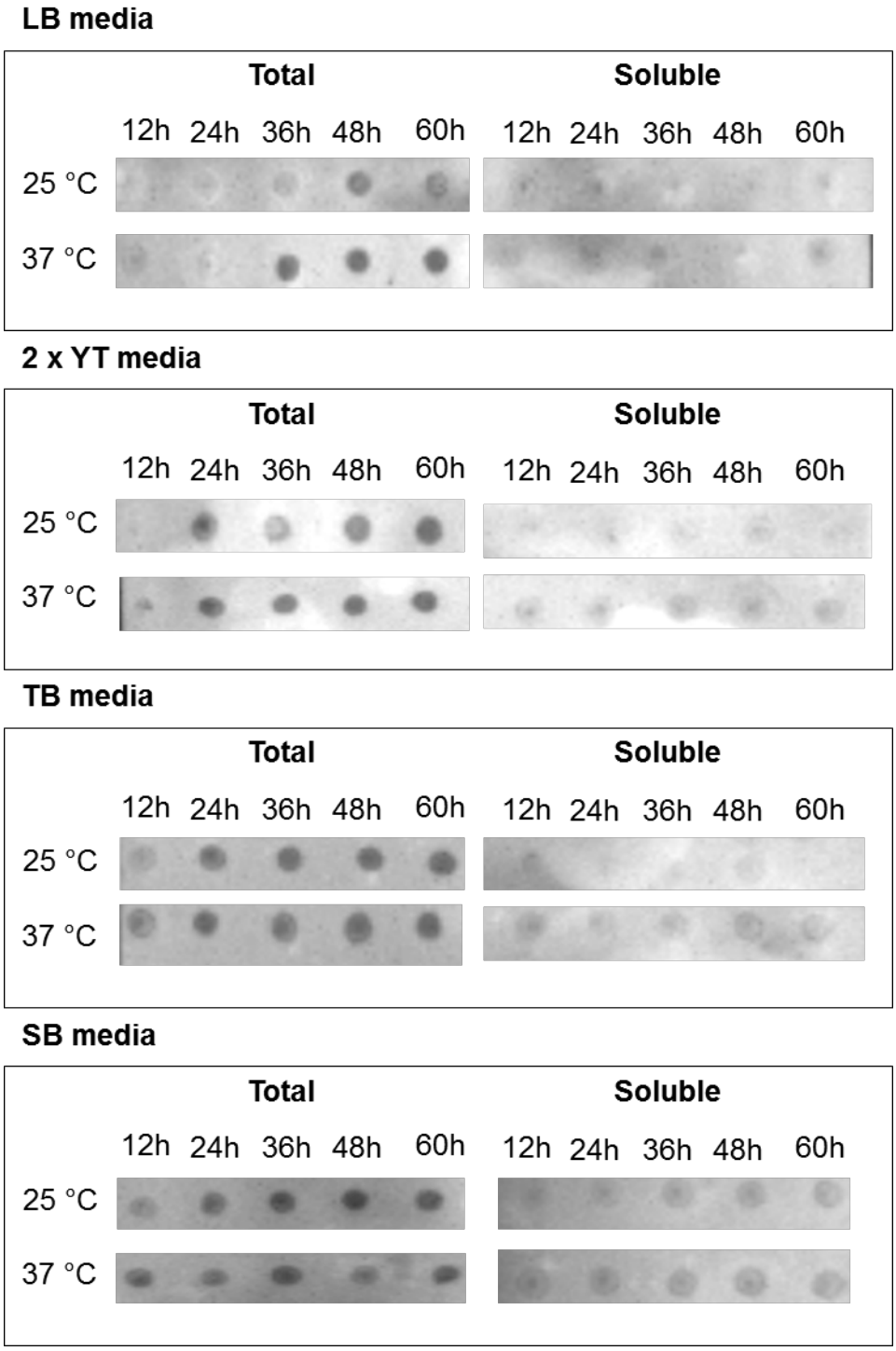

Figure 25 The initial dot blot results for the expression trial for the MIAs. Four mediums and two temperatures were compared to determine which combination would yield the maximum production of soluble protein. The left column indicates the intensity of the dot blot for the total amount of protein (soluble + insoluble) and the right side of the figure shows the intensity of the soluble fraction. From top to bottom, the boxes show the results for protein expressed in: LB, 2 x YT, TB and SB media at both 25 and 37 °C.

When comparing the total amount of protein produced in each of the conditions from figure 25 above, it is reasonable to suggest that there is no significant difference in the expression levels, with only short timescales in LB media indicating a lower protein intensity on the dot blot. This is not the

case for the important soluble fractions. Further analysis of the soluble fractions can be seen in figure 26. The plot shows the average of two independent repeats, each consisting of three technical repeats. The blot intensity has been normalised for comparison between the two independent repeats. Maximum binding intensity was made equal to 1 and no binding equal to 0. This plot indicated a significant difference between the use of an SB autoinduction medium compared to the other medias. The plot also indicates that optimum soluble protein production in SB media occurs at 37 °C between 36 and 48 hours. After 48 hours, the expression levels begin to drop as the *E. coli* levels increase to levels that are no longer sustainable at those conditions; oxygen is being used up resulting in levels lower than necessary to keep the cells replicating and therefore killing some cells.

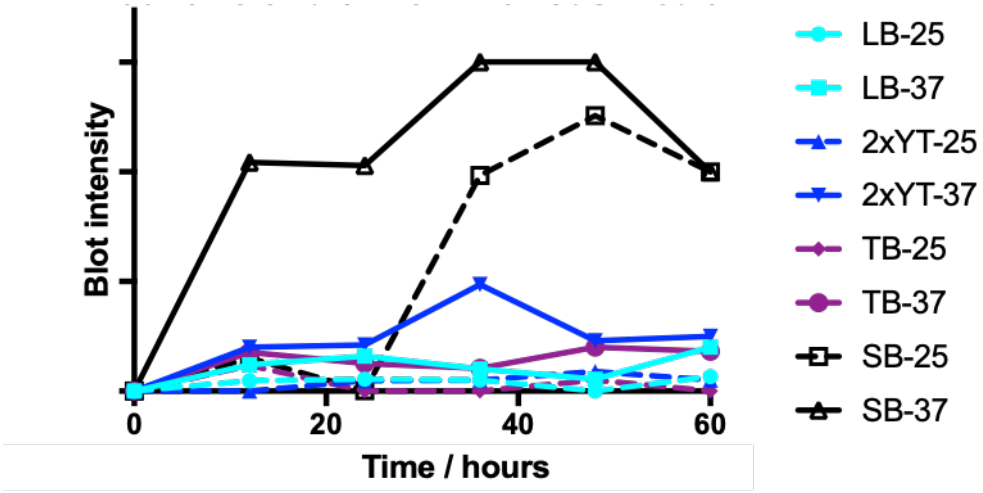

Figure 26 A plot showing the relative blot intensities for the soluble protein fractions of the MIA expression trial at 25 ℃ and 37 ℃ in various media (labelled in the key on the right side of the graph over a period of 60 hours). The aqua coloured lines indicate protein production in LB media, blue is 2 x YT, purple TB and black SB media. The squares show expression at 25 ℃ and the triangles at 37 ℃.

High expression levels for SB medium at 37 °C was not a surprise. The SB autoinduction medium is more nutrient rich than the LB and 2 x YT media. Higher temperatures often result in faster bacterial replication times therefore it makes sense that the expression levels would be higher at 37 °C compared to 25 °C. The results from the expression trial suggested protein expression should be conducted in SB autoinduction media, incubated at 37 °C for between 36 and 48 hours for optimum soluble protein yields. Therefore, all the work past this point involving MIA protein expression uses these conditions with the protein harvested after 40 hours of incubation.

With the protein expression optimised, the protein purification protocol could be considered. The MIA proteins had a Strep-II tag fused to the C-terminus which was readily available for purification purposes. It was also known that the MIA scaffold itself was extremely stable, making it desirable for

the range of applications the protein had been designed to do. This high stability enabled purification to be carried out at room temperature instead requiring a cold room (at 4 °C). This stability gave an uncomplicated start to planning the purification.

Following protein expression using autoinduction, sonication was used to lyse the cells and release the MIA protein, present in the supernatant. Purification via a Strep-Tactin column could be performed on the bench-top in a reusable column packed with Strep-Tactin beads or alternatively it could be carried out on the ÄKTA using the HiTrap™ affinity column, StrepTrap HP (GE Healthcare). An example of an SDS-PAGE gel showing the fractions collected from the bench-top column can be seen below in figure 27. The first lane on the gel contains the page ruler, used to estimate the molecular weight of the protein samples, lane two contains the supernatant flow-through. As the supernatant is added to the column the Strep-II tagged protein binds to the Strep-Tactin beads, resulting in those proteins being retained on the stationary phase. All other components should not bind the stationary phase and therefore pass through the column unhindered. The resulting elution is labelled flow-through in figure 27. The column was then washed to remove any unbound components (lane 3, figure 27). Finally, the bound Strep-II MIA was eluted from the column using an elution buffer containing d-desthiobiotin, which competes for binding and dislodges the Strep-II tag from the Strep-Tactin. Clean MIA protein should be eluted; lanes 4 and 5 seen on figure 27 confirm this. The protein bands in lanes 4 and 5 are around 12 kDa, the size expected on monomeric MIA proteins. The lanes look clear of any other protein.

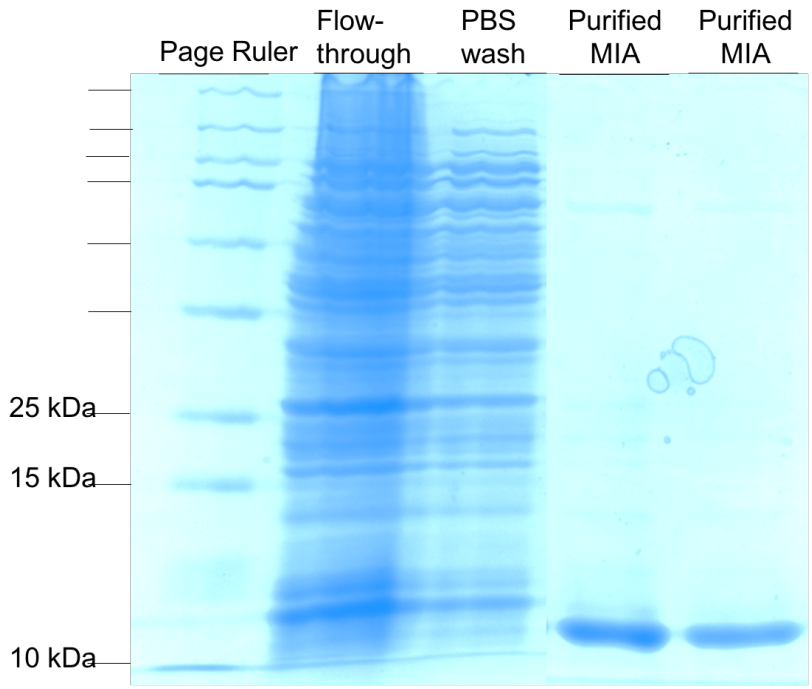

Figure 27 An example of an SDS PAGE gel showing the size and purity of the Streptactin purified MIA (D4), using bench-top purification methods. Lane one contains the page ruler, lane 2 is the intial flow-through of the lysate through the column, lane 3 is the elution from the column following a PBS and lanes 4 & 5 are the purfied MIA, eluted using D-desthiobiotin.

The apparently clean MIA protein was then dialysed into the desired buffer overnight. This buffer was often water or PBS as no additives were required for increased stability during storage. The MIA is known to be extremely stable at a range of pH and temperatures. Again, an advantage of its use. The dialysis stage ensured the removal of d-desthiobiotin from the sample which could alter concentration measurements when using UV-Vis spectrometry. The NanoDrop 2000 was often used to measure the concentration, with absorbance readings taken at 280 nm (the wavelength at which proteins yield maximum absorbance) and 260 nm (the wavelength at which DNA yields maximum absorbance). When this reading was first taken for each of the MIA proteins (A3, D1, E8, G4, G9 and H4) the ratio of the peak intensity at 260 nm and 280 nm was significantly above 1. This indicated that there was a much higher amount of DNA present in the sample than protein. However, the SDS-PAGE run using the protein elution from the affinity purification step indicated that a high concentration of protein was being produced. This was the same from each of the MIA samples. One explanation for the high proportion of DNA could have been that the MIA proteins were binding DNA. To determine whether DNA was binding the protein, a heparin column was aquired. Again, this column could be run on the bench or on the ÄKTA.

The heparin purification column uses a mixture of ion-exchange and affinity chromatography. The heparin within the column binds preferentially to the MIA, displacing the bound DNA. The protein is then eluted using a buffer system increasing in ionic strength, therefore a buffer increasing in NaCl concentration was used. A salt concentration of between 500 and 700 mM was required for protein elution from the column. An SDS-PAGE gel was used to track the elution of the protein from the column. After dialysis, the 260/280nm reading was measured again. The 260/280nm reading was significantly reduced (as can be seen in table 8 below). This confirmed DNA was bound to the protein but had been removed. This binding may be due to the high proportion of basic residues, including lysine of the VRs of the MIAs. It has been shown that DNA binds favourably to polylysine and it may be a similar effect being witnessed here.[140, 141] This makes sense as attractive interactions form between the negatively charged phosphate backbone of the DNA and the positively charged amine groups of the lysine sidechains.

Table 8 Ratio of absorbance at 260 nm/280 nm before and after purification of the protein using a heparin column. The readings indicate DNA binding to MIA E.8

MIA	Concentration before heparin (mg mL^{-1})	260/280 before heparin	Concentration after heparin (mg mL^{-1})	260/280 after heparin
E8	0.5	2.12	0.09	0.38

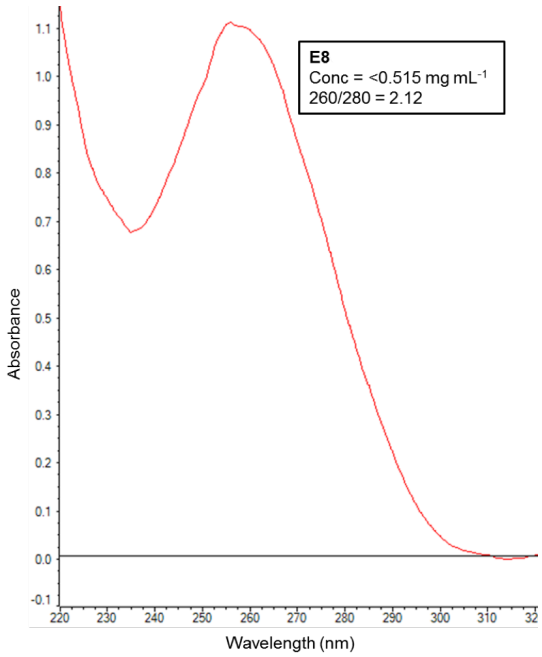

An additional purification step and therefore a decreased yield of purified MIA product was the first downfall the MIA use as a simple, well-expressing protein scaffold for displaying magnetite interacting peptides. When the StrepTrap HP column and HiTrap Heparin HP columns were used in conjunction with the ÄKTA, the purification process could be followed more closely, and the plots of the process are shown in figure 28 below.

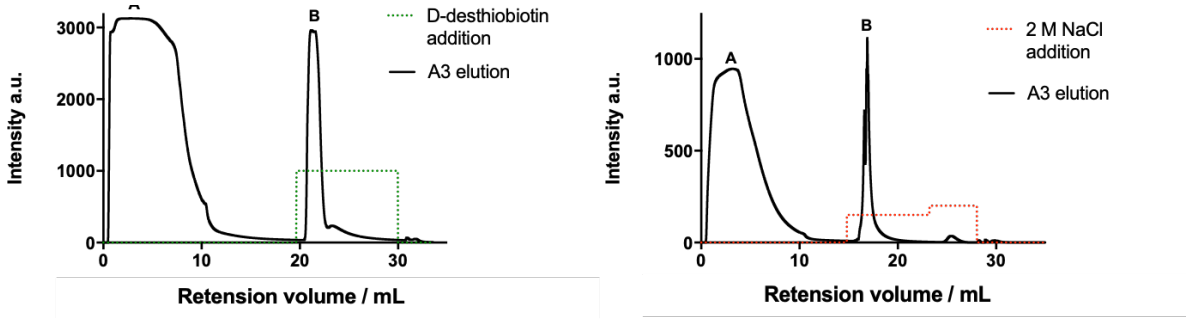

Figure 28 Plots showing the two-step ÄKTA purification of MIA A3. The plot of the left shows Step one which used the StrepTrap HP column for the initial purification of MIA A3 and on the right is step two which used a HiTrap Heparin HP column to remove any DNA bound to MIA A3. The intensity is measured at 280 nm. The green dotted line indicated the timng of the addition of the elutant D-desthiobiotin and the red dotted line the addition of 2 M NaCl. The solid black lines indicate the elution of MIA A3 from the column(s).

Figure 28 shows that the protein product is extremely clean with a single elution peak from each column. It also indicated that when the ÄKTA was used for the purification of the MIA proteins, the amount of protein lost during heparin-based purification was reduced considerably when compared to the same purification performed on the bench-top. However, a decrease in yield of any magnitude is not desirable, neither is the need for a lengthier purification process. The need to remove this DNA was considered.

The logical binding position of the DNA would be the VRs due to the cationic residues located there. Also, initial studies reviewing the Adhiron as a possible peptide displaying scaffold do not indicate any problems arising from DNA binding. Therefore, it is likely that DNA binding would affect the activity of the MIA as the DNA may block the magnetite binding sites, reducing binding strength and specificity. One way to overcome this problem was to identify whether any of the MIAs found to bind magnetite in the initial phage display binding study would bind magnetite in preference to DNA. This would mean that mixing the species would be enough to displace the bound DNA, resulting in successful magnetite NP binding. Protein pellets from 46 MIAs were generated and the *E. coli* cells were lysed to release the desired proteins. Addition of magnetite NPs directly to the cell lysate ensured that cellular DNA was still present in the solution and therefore available for binding to the MIAs.

An ELISA was used to determine the capability and strength of protein binding to the MNPs. The primary antibody recognised and bound the Strep-II tag of the proteins, the secondary antibody contained an AP fusion for a characteristic colour change on the addition of the Blue-Phos detection reagent. A darker blue or purple colour change indicated strong binding whereas a yellow colour indicated unsuccessful binding. A dot blot was carried out in unison to check that each MIA protein had been expressed to a similar degree and therefore the MNP binding was not simply due to the amount of protein present in the reaction. The results from these experiments are shown in figure 29. A control Adhiron was added to well A1 in the ELISA and can be seen as the dot on the top left in the dot blot. The control Adhiron displays a peptide sequence that does not bind magnetite. A further control was added to the ELISA in well D1, containing only the detection reagent and buffer to ensure any colour change witnessed was not an artefact of the detection reagent itself. Both of these controls appeared yellow in the ELISA, indicating no binding.

Adhiron	Intensity	Loops	Previous intensity	K content	Ranking	Blot intensity	Ranking
E1	0.0465	2 loop	low	rich	33	130492.933	27
C3	0.0524	2 loop	high	rich	32	270193.063	10
C8	0.0561	2 loop	low	poor	31	98445.4706	29
C7	0.0591	2 loop	low	rich	30	178892.733	17
A3	**0.6415**	**1 loop**	**high**	**rich**	**4**	62268.6944	**31**
G4	**0.7357**	**1 loop**	**highest**	**med**	**3**	1998834.56	2
G1	0.7372	1 loop	low	med	2	252477.556	11
E8	**0.8284**	**1 loop**	**high**	**poor**	**1**	180966.344	16

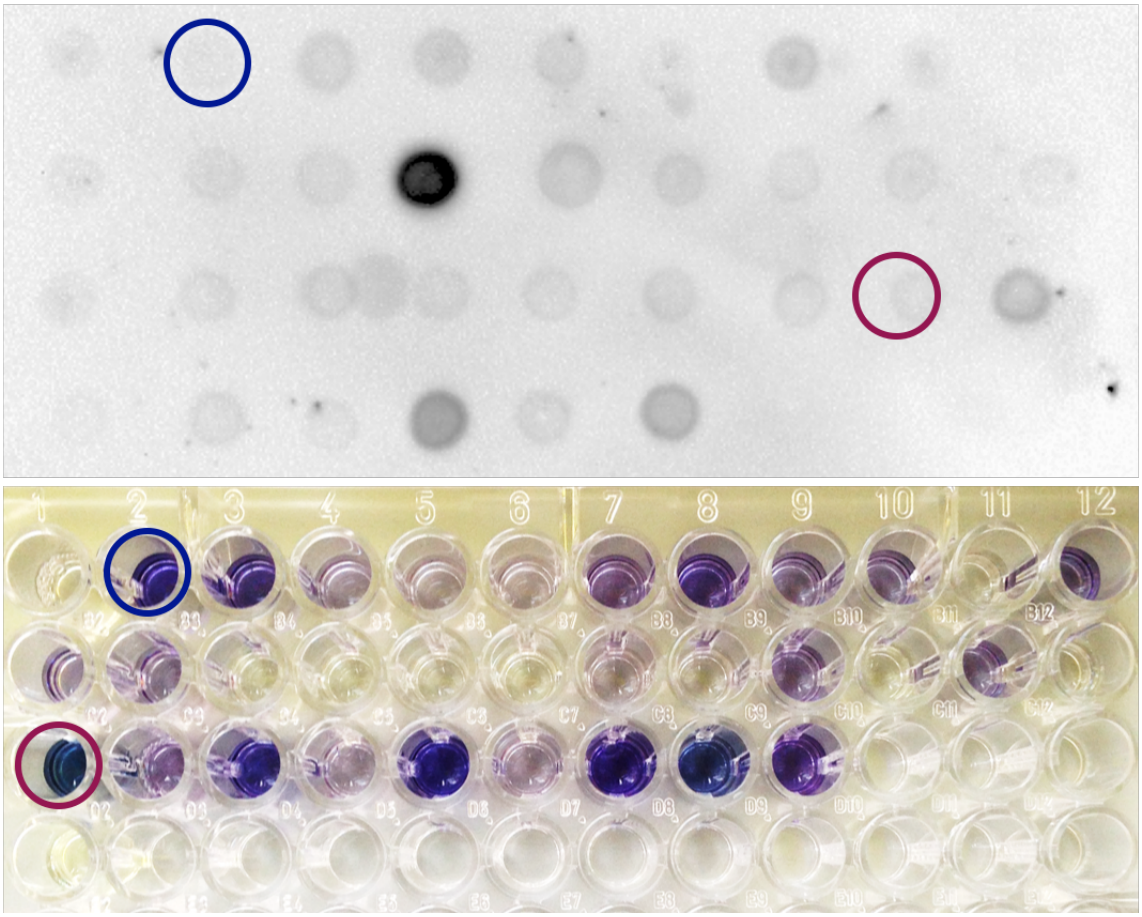

Figure 29 From top to bottom, a table showing the 4 best (green) and worst (orange) binders to magnetite when DNA is assumed bound to the VRs of the MIA. Middle is a dot blot on nitrocellulose showing the protein intensity used in the study. The spot corresponding to MIA A3 is circled in blue and E8 in purple. Finally, an image of the ELISA used to measure the binding strength of the MIA to magnetite when bound to DNA. A3 is circled in blue and E8 in purple

From the table above (figure 28), it can be seen that each of the top 4 binding MIAs, able to displace bound DNA, contained only a single VR. The opposite is true from the MIAs where the NPs were unable to displace the DNA, showing no or little binding to the MNPs. Therefore, it can be concluded that the number of loops is extremely important in magnetite binding capabilities and ability to displace any bound DNA molecules. It is not clear whether the DNA can bind more strongly if both loops are displayed or if the steric clash upon MNP binding to MIAs containing 2 VRs is just too great that it is unfavourable for the MNPs to replace the bound DNA. Another interesting observation is

that it appears that the concentration of basic lysine residues within the VRs does not appear to have a significant effect on whether the MNPs bind in preference to DNA molecules. With one of the top four binders being lysine rich, another lysine poor and the remaining two neither rich or poor. The four worst magnetite binders contained three lysine rich MIAs and one lysine poor.

Two of the most promising MNP binders were taken forward from this stage on. These MIAs had been considered from the start of the project and were A3 and E8. These were picked from the other top binders as they gave a combination of both lysine rich and lysine poor loops, therefore the effects of this could be monitored in further analysis. Both of the MIAs gave previously high readings for MNP binding intensity before the experiment was repeated, therefore these results were reproducible and reliable. Finally, both showed moderate blot intensities, therefore they appear to express well in *E. coli,* but the high binding intensity was not solely reliant on a higher yield of protein compared to the other MIAs tested. Alternatively, G1 was not chosen as it previously gave a low intensity reading in binding studies, suggesting that the results were not as reproducible and G4 had one of the highest intensities on the dot blot and therefore it could not be concluded with confidence that the high binding was due to strong specific binding of MNPs dictated by the peptide sequence displayed, or if in fact it was a bias result due to the higher than average protein yield.

With the data showing that MIAs A3 and E8 were able to bind MNPs in preference to DNA, the need for the extra heparin step during purification was eradicated, resulting in a simple, one-step purification process of soluble protein which gave a good yield of the desired MIAs.

3.4 MIA characterisation

Molecular cloning and protein production was optimised for generating good yields of the MIAs. The proteins could be synthesised systematically and reliably using the conditions detailed above. Further characterisation of the proteins was conducted to access their properties and ensure the correct proteins had been produced and did display the structure and stability expected for the Adhiron scaffold.

The MIAs were expressed and purified. A small sample of the purified protein was used for western blot analysis. The protein was linearised and run on an SDS-PAGE gel to separate species present in the mixture by MW. The contents of the gel were then transferred onto a nitrocellulose membrane, before the Strep-II tag fused to the C-terminus of the MIAs was detected using a HRP-conjugated

antibody system. A photometric assay was used to amplify the HRP signal, catalysing the conversion of the chemiluminescent substrate for protein detection. It was this photo-emission that was visualised. A signal would only be visible is the Strep-II tag was present for the primary antibody to bind to and the only Strep-II tagged proteins should be the MIAs. Therefore, if a signal was present at the correct MW, it could be accurately assumed that the protein was the protein of interest.

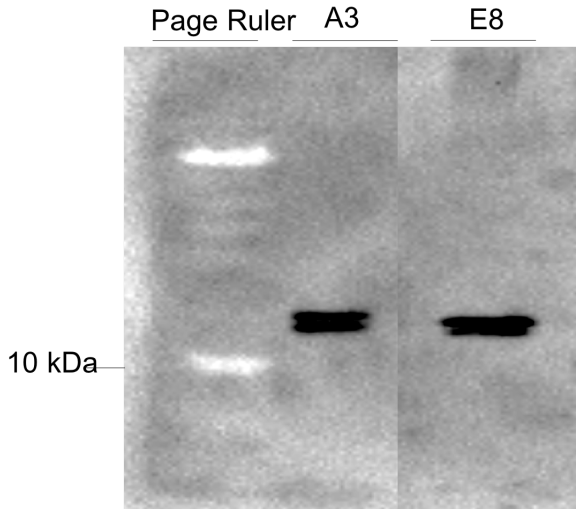

Figure 30 Western blot analysis of MIAs A3 (lane 2) and E8 (lane 3). The page ruler is visible in lane . Both MIAs are roughly at 12 kDa when compared to the ladder.

Figure 30 shows two bands present on the western blot membrane, both around 12 kDa in size – the size expected for the MIAs. The band for A3 is shown in the middle lane, the band for E8 in the right-side lane and the page ruler can just about be made out in the left lane. This blot suggests that the desired proteins had been produced and the samples look clean with no fragmentation of the proteins visible. It also shows that the Strep-II tag remains conjugated to the MIA throughout the expression and purification stages.

After the initial protein characterisation data showed that the proteins produced were likely to be the desired MIAs, the exact mass of the proteins was analysed. A more precise indication of the MWs was obtained using MS, which worked by giving the mass to charge ratio of the species. ES-MS was used for this data analysis, resulting in a single positive charge on the species and therefore the m/z value of the molecular ion peak (M^+) obtained from the spectrum would be equal to the MW of the protein. The MS for MIAs A3 and E8 are shown in figure 31. The attached table shows the expected M^+, the calculated M^+ and indicated any other major peaks observed.

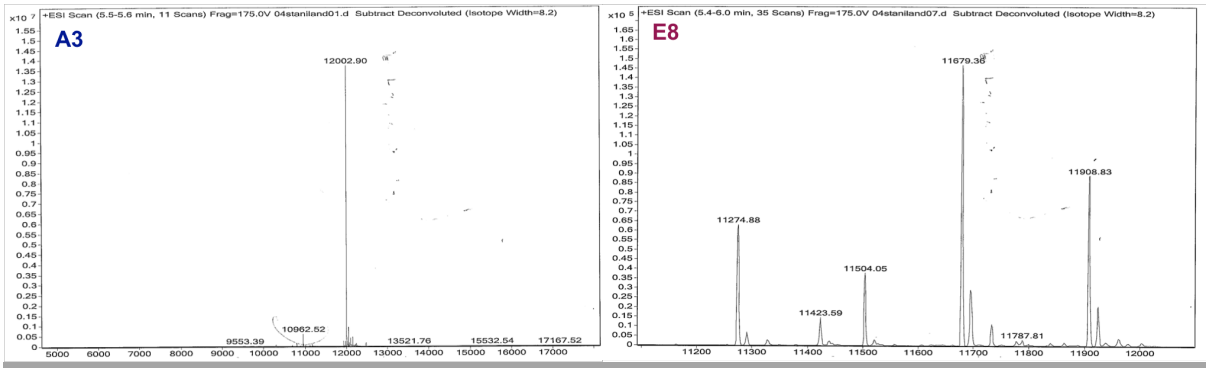

MIA	Expected M^+	Calculated M^+	Major Peaks
A3	12002.68	12002.90	12002.90
E8	11908.62	11908.83	11908.83, 11679.36, 11274.88

Figure 31 m/z from ESI-MS for MIAs A3 (left) and E8 (right) show the molecular ion peak (M+) expected for each protein. Fragmentation is visible in E8 sample with multiple major ion peaks

The expected M^+ for each of the proteins was calculated using the ExPASy Compute pI/Mw online tool.[142] The predicted m/z for A3 was 12002.68 and for E8 was 11908.62, these values were a good match (within error) to the m/z of the M^+ calculated for A3 and E8 using MS, these values were: 12002.90 and 11908.83 for A3 and E8 respectively. These values are consistent with the protein lacking the N-terminal methionine. The matching values indicated with even more certainty that the proteins produced were the desired MIAs.

MS could also be used to indicate the purity and stability of the of the proteins. A clean spectrum with a single major peak would indicate a pure and stable structure, however, a spectrum containing a variety of other major peaks would suggest the presence of contaminants within the protein solution, or fragmentation or degradation of the protein product. It can be seen in figure 31 that there is only one major peak at the predicted MW for the protein, therefore the A3 sample was pure and complete. It also showed that the protein was monomeric as when the mass spectrometer scanned to the m/z expected for dimers or trimers, there were no peaks present (this matched data shown in the SDS-PAGE and western blot analysis).

The purity was not as high for the E8 sample, with three major peaks present in its spectrum (one being the predicted peak). The M^+ peak was consistent with that expected for the MIA, however there is a larger peak at 11679.36 suggesting some degree of fragmentation, however it is not clear what the fragment with a molecular weight of 229.47 g mol^{-1} could be – one possible explanation is biotinylation, expected at 226.1 g mol^{-1}. An alternative to this could be that there was a small mutation in the primary structure of MIA E8, resulting in the addition peak. If a mutation was the cause it is unlikely that it was present in the active VR of the MIA as the binding analysis suggests strong magnetite binding, consistent with repeats performed, including with the initial phage

conjugated MIA. Also, sequence analysis from the molecular cloning stages confirmed the corrected DNA sequence, with no mutations. In case of a mutation elsewhere in the protein scaffold, secondary structure analysis was performed to ensure there was no alteration in the structure.

The secondary structure of the MIA proteins was investigated using CD. Different protein secondary structures give characteristic peaks and troughs as a result of varying interactions with circularly polarised light. The absorbance of the protein was measured between 260 nm and 190 nm, before conversion to give the molar elipticity of the protein (which takes into account the number of residues and the molecular weight of the protein). The most intense response occurs for α-helical structures present in the sample, however there is only a single α-helix present in the predicted MIA spectrum, which is surrounded by four β-sheets and regions of random loops, therefore the characteristic dips at 208 nm and 222 nm corresponding to α-helical content should not be intense. The baseline corrected CD spectra for MIAs A3 and E8 in water is shown in figure 32.

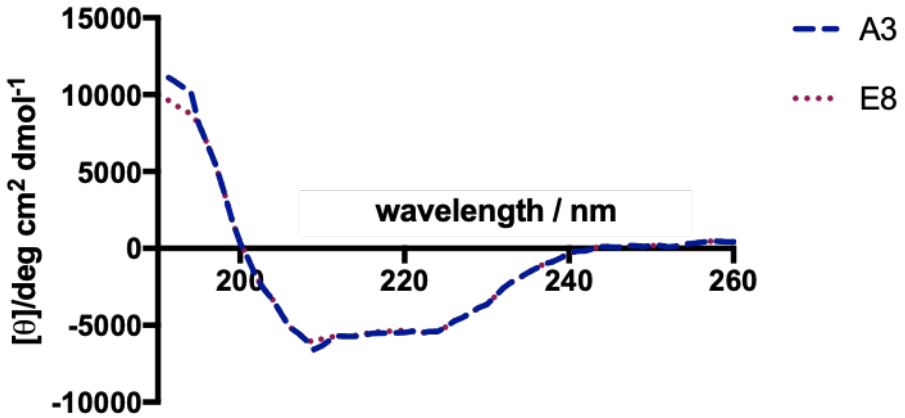

Figure 32 Secondary structure analysis of MIAs A3 and E8 at room temperature using CD from 260 nm to 190 nm. 1 nm intervals, repeated in triplicate. Water base-line has been subtracted. Blue dotted line for MIA A3 and purple for E8. Protein concentration was 0.2 mg mL^{-1} in ultrapure water.

The CD for each of the MIAs revealed a high β-sheet content compared to α-helix or random coil – as predicted, with the centre of the broad negative peak sitting around 218 nm (π-π* electron transition) and then a positive peak below 200 nm (n-π* electron transition). This is shown in figure 32 above. The main aim of the CD analysis, in addition to a prediction of the type of secondary structure present, was to determine if the spectra for MIAs A3 and E8 were similar and so it would be reasonable to suggest that a similar secondary structure was adopted by the two proteins and no mutations responsible for any structural change were present. As can be seen in the CD spectra in figure 32, the data collected for A3 and E8 are almost identical, with the curves lying almost entirely on top of each other. The main difference is the slightly more positive peak for A3 compared to E8 as

the wavelength of the circularly polarised light reaches 190 nm. Below 200 nm other molecules such as water begin to absorb, making it difficult to analyse data points collected below this point, therefore this small difference in the protein spectra is not seen as significant and the proteins are highly likely to have adopted the same structure.

Characterisation of the MIA structures was investigated further. Gel filtration was performed in the hope to confirm the formation of a monomeric protein structure, previously predicted for these proteins. Before any sample analysis was done, the column was calibrated giving a calibration curve (figure 33) of a straight-line plot with a useful R-value of 0.992. The MIAs were dialysed into a low salt, 1 x PBS buffer before the addition to a Superdex gel filtration column.

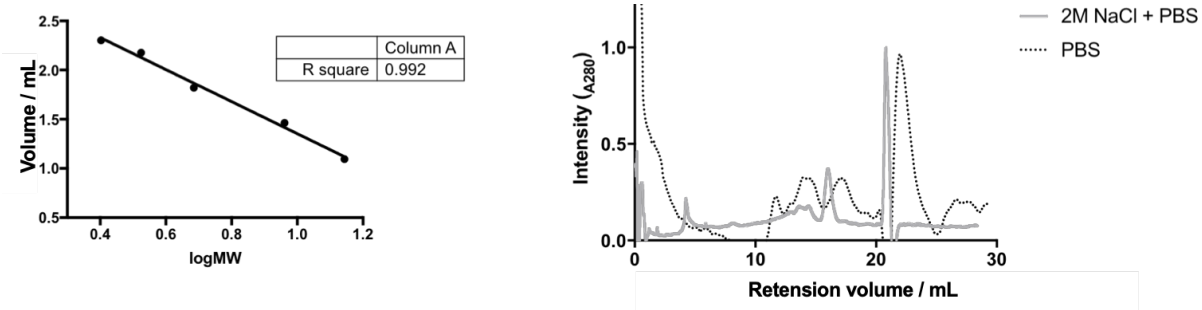

Figure 33 Results from the gel filtration of MIA A3. The calibration curve for the Supderdex Sepharose GL200 column is shown on the left. The elution plot of A3 is on the right. Varying concentrations of salt were tested to see the effect on the retention volume. Low salt (PBS) is displayed using the black dotted line and high salt (2 M NaCl) is displayed using the solid grey line.

The initial run of A3 through the column in PBS buffer gave an undesirable trace. The major elution peak was witnessed at 21.5 mL, after consulting the calibration sheet, this suggested a molecular weight of 2.44 kDa for the protein, around 10 kDa smaller than the actual molecular weight for MIA A3. Due to the charged and 'sticky' VR of the MIA it is likely that the protein was sticking to the stationary phase of the column, giving a higher retention volume than should have been seen. A running buffer with an increased salt content was tested with the aim to reduce the non-specific interactions between the column and the MIA and give a more accurate retention volume. As can be seen in figure 33, the buffer change did have some effect in reducing the retention volume of the protein, with the volume decreasing from 21.5 mL to 20.2 mL – suggesting there was binding occurring between the protein and the column. However, this decreased volume still had a much lower than expected MW of 4.38 kDa. It was clear that gel filtration would not be an accurate method of confirming the formation of the monomeric MIA protein due to the non-uniform flow rate of the sticky sequence through the column. The same protocol was used to test E8 with the same problems arising.

In summary, the size and structure data for MIAs A3 and E8 show a good match to the predicted results for the proteins. The data suggests that the two proteins fold to give similar products in terms of size and secondary structure. They appear to form monomeric species with a high degree of β-sheet structure compared to α-helix and random coil. The proteins also appear to remain fused to the Strep-II tag, with no obvious fragmentation or degradation following the protein expression and purification steps used in the protein production and storage in aqueous buffers including water and PBS.

3.5 MIAs as additives in biomineralisation reactions

Three commonly used methods for the synthesis of magnetite MNPs were assessed to determine which would be most suitable for this project. Ideally, the method could be conducted at room temperature and pressure, to produce a high yield of product, in the shortest possible time. The methods are outlined below and explain why only the RTCP reaction was used for magnetite NP synthesis with MIA additives.

3.5.1 POFHK reaction

The POFHK reaction is a widely used route for the synthesis of MNPs. The reaction uses moderately high temperatures (around 80 °C) for around four hours and requires an inert atmosphere when used to produce magnetite. Magnetite MNPs were synthesised using this reaction before being analysed using TEM. The resultant particles had a relatively large size distribution, however exhibited a high degree of control over the shape of the NPs produced. A TEM image taken of the particles following the POFHK reaction, along with the grainsize analysis can be seen in figure 34. The diameter of roughly 100 particles was measured and the values were plot and analysed using GraphPad Prism. A Gaussian distribution curve was fit to the data to indicate the mean particle size and the extent of the distribution.

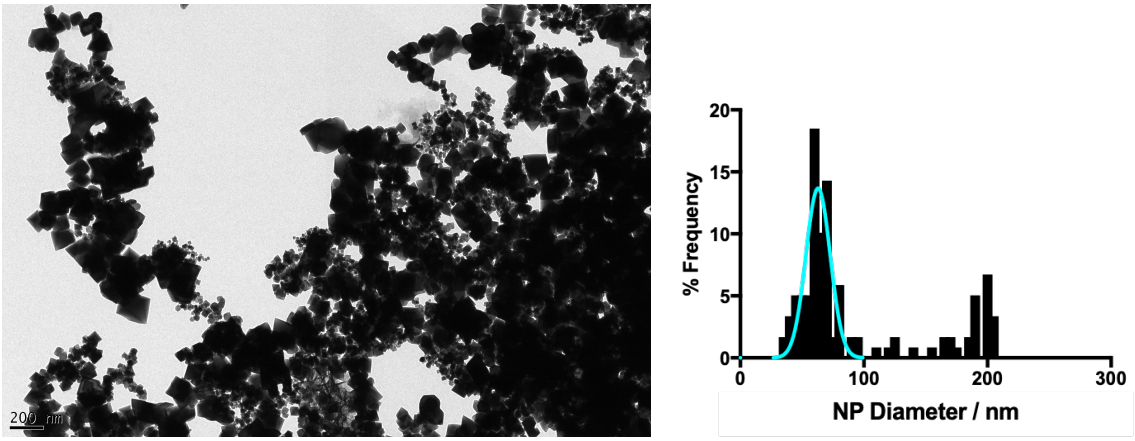

Figure 34 Image on the left is a TEM image of magnetite NPs synthesised using the POFHK reaction. Sample was loaded on to a copper-coated grid and analysed on the Technai microscope. The plot on the right shows the grainsize analysis of the NPs synthesised using the POFHK reaction by calculating the frequency distribution of the NP sizes. Two major species in terms of size can be witnessed on the frequency distribution plot. .

The average NP diameter is 64 nm; however, the Gaussian curve is not a good fit as there are two major species produced in the reaction (shown in figure 34). The highest number of particles fit into the 64 nm $\pm$ 31 nm, however there are also a number of particles that fit between 202 nm $\pm$ 10 nm. Giving rise to the large size distribution of the particles synthesised in this way. Although the shape control observed using this reaction pathway appears to be a good starting pointing of magnetite NP synthesis for biomedical applications, there are also a number of disadvantages to using this method. These disadvantages are namely the poor size control and the increased temperatures required. One of the aims of this project was to develop an environmentally friendly route to magnetite synthesis and the temperature pay out does not compensate for the quality of NPs produced in this reaction. For this reason, the POFHK reaction was not taken any further in this project.

3.5.2 Ammonia diffusion reaction

An alternative to the POFHK reaction was the ammonium diffusion reaction, a synthesis route that uses ammonia as a base to precipitate magnetite NPs. The reaction can be run at room temperature, under an inert atmosphere. Magnetite NPs were synthesised using this reaction and the particles produced were analysed using TEM (figure 35).

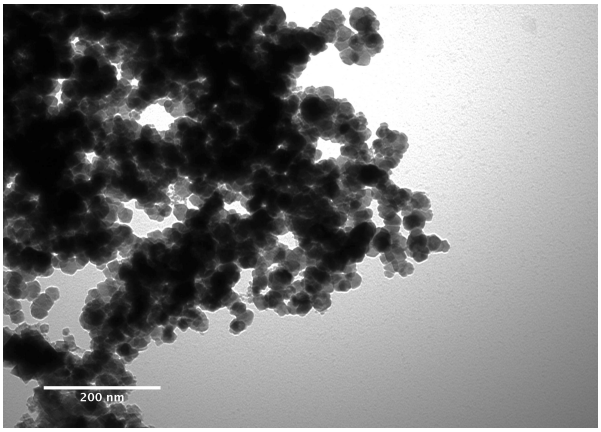

Figure 35 A representative TEM image, captured on the technai of magnetite NPs synthesised using an ammonia precipitation reaction and loaded on to copper coated grids. From the TEM images the quality of the particles do not appear to be as superior as using a POFHK reaction and the reaction time was much longer.

This synthetic route appeared to be a possible alternative to synthesis using the POFHK reaction. However, when compared to the POFHK reaction there was a significant difference in the reaction time. The POFHK reaction was incubated at 80 °C for 4 hours, allowing the reaction to run to completion. On the other hand, the ammonia diffusion reaction required over 24 hours to reach completion, a clear disadvantage of this reaction pathway. Therefore, an alternative reaction pathway was identified, that would incorporate the reaction time of the POFHK reaction and the ambient conditions from the ammonia diffusion reaction. Focus turned to the RTCP.

3.5.3 Optimisation of RTCP reactions

The RTCP reaction is a synthetic route which produces MNPs in ambient conditions (room temperature and pressure), under an inert atmosphere. The method leads to a high yield of NPs in just a few hours.

Magnetite NPs were synthesised using the RTCP and the particles were analysed using TEM. After imaging the particles in this way, grainsize and shape analysis could be performed. Grainsize analysis was acquired my measuring the largest diameter of around 100 NPs using ImageJ software. These measurements were then plot using GraphPad Prism and analysed to give the frequency distribution. Once the frequency distribution had been calculated a Gaussian curve was fit to the data to determine the average NP diameter and the range of sizes present in the sample. The TEM image of the control particles in figure 36 gives an indication of the quality of the NPs synthesised in this way. The particles consist of a wide variety of different sizes and shapes and as expected when using the RTCP for the synthesis of magnetic NPs, there is poor control over the product. It is unlikely that the needle shaped particles produced by the RTCP are magnetite. The reaction product is likely a mixture of a variety of iron oxides. The linear, needle-shaped products are likely to be an iron oxide

that is capable of forming, linear, elongated, acicular particles such as maghemite or goethite (γ-Fe_2O_3, α-FeO(OH) respectively).

At this stage, the MIA proteins could be introduced, and their activity tested. The MIAs had previously been shown to preferentially bind the [100] facet of magnetite and therefore it was expected that when these proteins were introduced to the RTCP, they would bind to this face of the magnetite as the crystal was forming, promoting the formation of cubic shaped magnetite NPs.

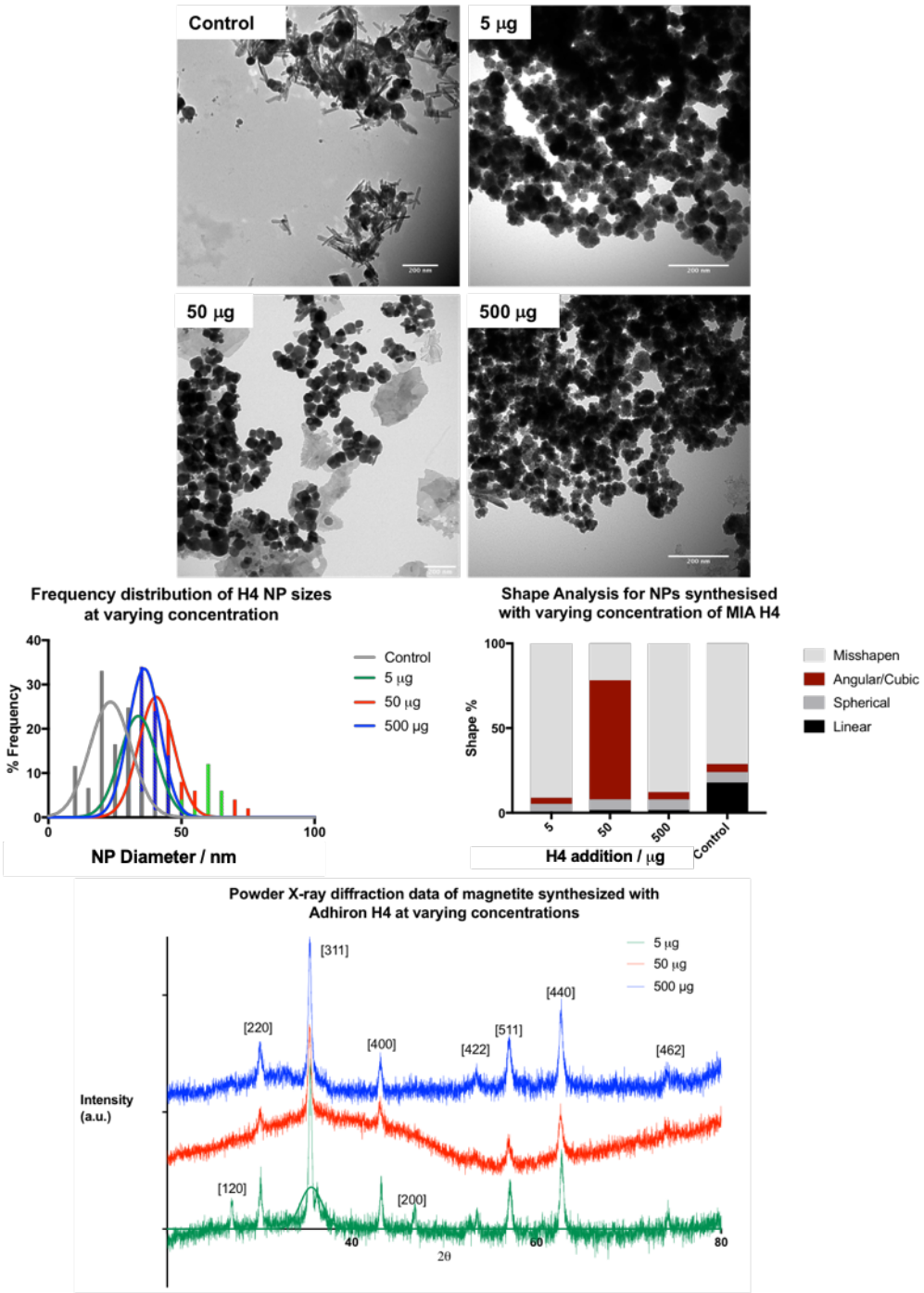

Figure 36 Analysis of MNPs synthesised in the presence of varying concentration of MIA H4. From top, to bottom: TEM images captured on the technai microscope of magnetite NPs, loaded on to copper coated grids. Particles produced with 0, 5, 50 and 500 µg of MIA H4 additive are shown. The most clean and angular particles can be identified in the TEM image for 50 µg additionBelow the TEM images are the frequency distribution of the particles from the images, left (grey is control, blue 5, red 50 and green 500 µg of additive) and shape analysis for NPs produced with varying additive concentration. At the bottom is the powder XRD data for NPs synthesised with varying concentration of MIA H4 additive. The data was collected between 20 and 80 °. Each of these further analysis also show the 50 µg addition to be superior to the others.

The use of the initial MIAs were chosen for the optimisation of the biomineralisation process using MIA additives because of their strong binding signal in previous studies by Dr Andrea Rawlings. Figure 36 shows the NP characterisation resulting from the RTCP reaction proceeding with a MIA H4 additive. A rough calculation (appendix 3.1) showed that 1 mg of magnetite NPs with an average

diameter of around 30 nm would require 1.5 μg of MIA to equate to theoretical total coverage. As the average RTCP reaction produces around 70 mg of product, you would therefore expect the optimum addition of protein to be roughly 100 μg. The calculation when used to assess MIA required for the RTCP may be an over-estimation however, as under the reaction conditions it was not yet clear whether the protein would remain bound for the duration of the synthesis or whether they would be in an equilibrium between the bound and unbound state. It is for this reason a MIA concentration of 50 μg per 10 mL reaction volume was predicted to be optimum. Concentrations of 5 and 500 μg were also analysed as outer boundary concentration conditions.

Magnetite NPs were synthesised using the RTCP method with the addition of 5, 50 and 500 μg of the MIA H4. The NP products were initially visualised using TEM and the images can be seen in figure 36. For increased accuracy and precision grainsize analysis was performed on the NPs by measuring the longest length of around 100 particles, again using the ImageJ measurement tool. The plots for the size analysis for the particles synthesised in the presence of 5, 50 and 500 μg of H4 is shown in figure 36. The average NP diameter did not vary significantly between the three samples. On the addition of 5 μg of H4 the particle size was found to be 34 nm $\pm$ 22 nm, when 50 μg of H4 was added the size was 42 nm $\pm$ 18 nm and for the addition of 500 μg the size was 37 nm $\pm$ 20 nm.

The composition of the magnetite crystals formed in these RTCP was analysed using powder XRD. The crystallographic data obtained could help determine whether the major product was magnetite or another iron oxide. XRD was obtained between 20 and 80° and the position of the peaks from the base-line corrected data was then converted into d-spacing which gave the inter-atomic distances within the crystals. These values calculated were then compared to literature values corresponding to the know facets of magnetite. The peaks labelled XRD peaks can be seen in figure 36. The most common and identifiable d-spacing, specific to magnetite can be found in table 9. These spacing are characteristic of the type of crystal and therefore the values vary between different iron oxides.

Table 9 showing the d-spacing and corresponding Miller indices for magnetite which a comparison to the d-spacing and facets calculated for NPs synthesised in the presence of MIA H4. D-spacing calculated from the measured 2θ using the equation $n\lambda = 2dSin\theta$

Miller Indices	d-spacing	5 μg H4	5 μg H4	500 μg H4
[220]	2.966	2.97	2.97	2.97
[311]	2.530	2.53	2.53	2.53
[400]	2.096	2.09	2.10	2.10
[422]	1.712	1.71	1.71	1.71
[511]	1.614	1.61	1.61	1.62
[440]	1.483	1.48	1.48	1.48

From the XRD plot and the comparison to the literature values for d-spacing in magnetite it can be confirmed that the NPs produced in all three reactions consist mainly of magnetite. Although magnetite is likely the major product, it is difficult to conclude for certain as the d-spacing of maghemite is extremely similar to that of magnetite, therefore it is difficult to distinguish between the two. Maghemite has a much lower magnetisation compared to magnetite and if maghemite was the major product this would be flagged up in any magnetic characterisation of the particles later on. There is also little difference in the crystallographic spectrum between the three samples, therefore the amount of protein added does not appear to have a significant effect on the type of crystal produced.

The major difference between the three reactions can be seen in the shape analysis of the NP products. A good indication of the shapes can be obtained from the TEM images (figure 36). Analysis of the shape was not an arbitrary task, it was difficult to be able to group the NP shapes and morphologies and present this in a way that would accurately represent the particles. ImageJ was used to measure the aspect ratios of roughly 100 particles from each of the reactions, the shape by eye was also accounted for. The particles were then grouped into four classes: Misshapen; angular/cubic; spherical; linear. NPs were classified as misshapen if the aspect ratio was calculated to be between 0.25 and 0.75 and did not appear to exhibit any vertices equal to 90°. Angular or cubic NPs were found to have an aspect ratio of close to 1 (>0.75) and also appear to have corners equivalent or close to 90°. The sides of the particles also appeared straight when examined by eye. Spherical NPs also had an aspect ratio of close to 1, however these particles did not have any obvious vertices and the sides were curved. Finally, NPs were classified as linear if the aspect ratio was close to 0 (<0.25), giving them a needle- or rod-like appearance.

Most particles in the control reaction, and the reactions containing 5 or 500 μg of MIA were misshapen, therefore there was poor control over the shape of the NPs during synthesis. This was not the case when 50 μg of MIA was added to the 10 mL reaction volume, in these conditions the major shape of the NPs witnessed was cubic. Indicating that shape control was at its optimum at the predicted 50 μg per 10 mL reaction volume. Below this concentration it is unlikely that there is enough protein present to bind to the forming crystals, with the dilute mixture interactions between the crystal and MIA would be uncommon. Above this concentration the MIA may start to act as a contaminant, changing the surface properties of the forming crystals, resulting in poorer quality products. This is shown in the TEM images of the particles synthesised with 500 μg of protein. They show a rough, uneven surface, suggesting that the reaction pathway is sensitive to changes in conditions and the increased organic content may push the dynamic equilibrium of the reaction towards the production of other types of iron oxides, such as maghemite. The increased organic content results in a change in redox potential of the system. The formation of magnetite is extremely sensitive to oxidation; therefore, the final product can be easily altered. Maghemite would be an obvious product as it would be difficult to tell this apart from magnetite when analysing the powder XRD patterns of the two products. However, other possible products could include amorphous iron oxides, which would be XRD invisible.

From this point forward RTCP were run with the addition of 50 μg of MIA to the 10 mL reaction volume. This concentration gave the shape control expected from the MIA whereas higher and lower concentrations of MIA were not able to match this effect.

3.5.4 Particle characterisation

On completion of the optimisation of the RTCP with MIA additives, particles were synthesised with the aim to characterise and understand their properties, specifically magnetic properties and to assess their use as potential biomedical agents. MIAs A3 and E8 were focused on as additives in RTCP.

Magnetite NPs synthesised using RTCP with A3 and E8 additives were visualised using TEM. The images from the TEM are shown in figure 37. The size and shape of the NPs synthesised in this way were analysed to obtain the NP size and distribution, and a Gaussian curve fit. A plot of this is also shown in figure 37. The average size of the particles synthesised in the presence of A3 was 33 nm $\pm$ 16 nm and for E8 the average NP diameter was calculated to be 37 nm $\pm$ 17 nm. This gave both

samples a relatively narrow size distribution with no other clusters of sizes present. The shape of the particles is similar in both cases and like for H4 the major product is cubic shaped crystals.

As in the optimisation studies with MIA H4, powder XRD was used to analyse NPs from A3 and E8 reactions. The major product of the RTCP with MIA additives was magnetite. The data did indicate the formation of magnetite with peaks at 2θ equal to (°): 30.11, 35.37, 43.10, 53.55, 57.06, 62.61, 74.35 (shown in figure 37). Table 10 below shows that these peaks correspond to d-spacing that is a good fit for magnetite.

Table 10 Showing the d-spacing calculated from the XRD peaks of NPs synthesised with A3 or E8 additives

A3/E8 XRD peak (°)	Calculated d-spacing (Å)	d-spacing in magnetite (Å)	Magnetite facet
30.11	2.97	2.966	[220]
35.37	2.54	2.530	[311]
43.10	2.10	2.096	[220]
53.55	1.71	1.712	[422]
57.06	1.61	1.614	[511]
62.61	1.48	1.483	[440]
74.35	1.28	1.279	[462]

The data fits well to the d-spacing expected for magnetite and so strongly suggests that the majority of the crystals formed in a RTCP with the addition of MIA A3 or E8 are magnetite. It also suggests that the crystals are somewhat resistant to oxidation or hydrolysis which would result in the conversion of magnetite to other forms of iron oxide.

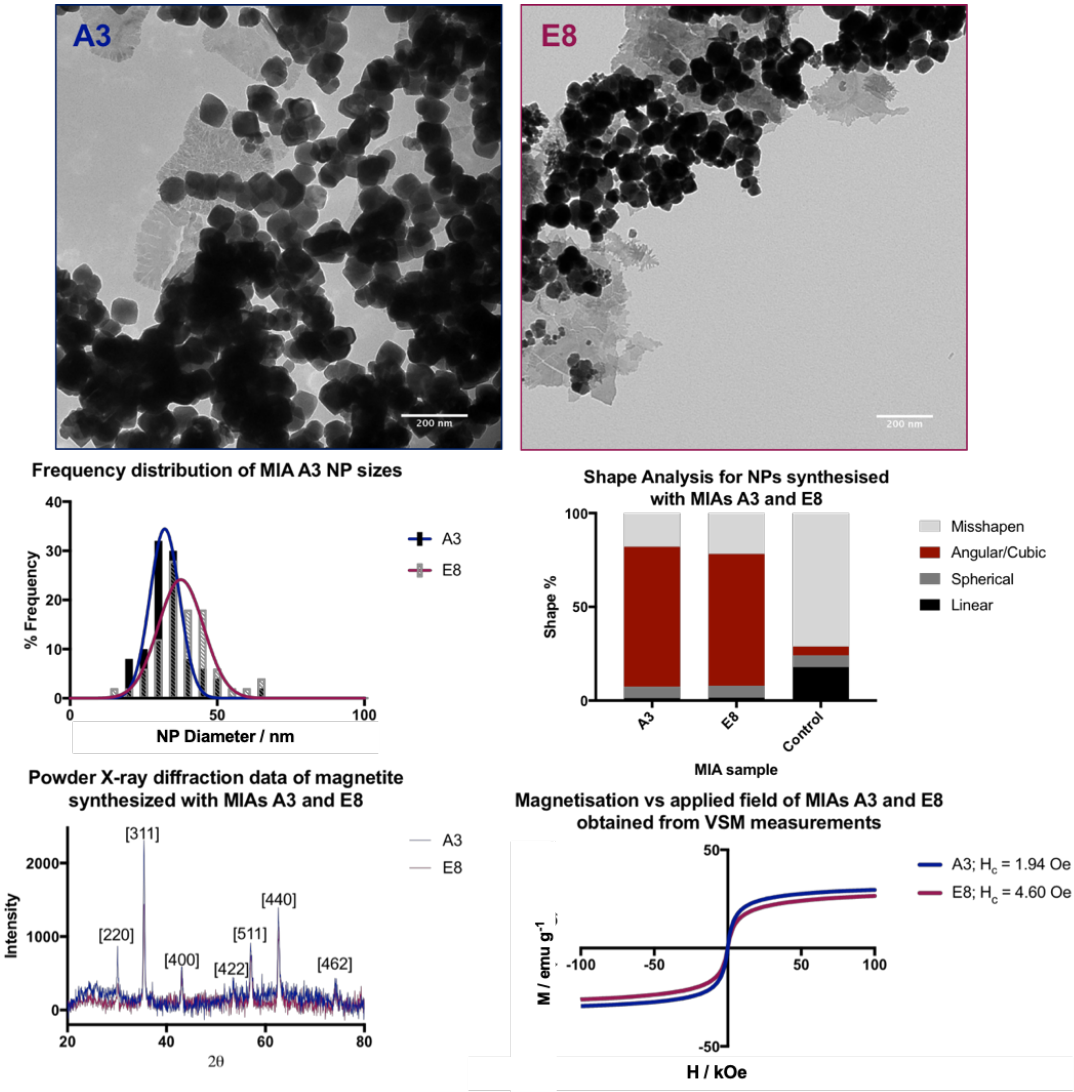

Figure 37 Analysis of NPs synthesised in the presence of MIAs A3 and E8. At the top is the TEM images of particles produced with the addition of MIA A3 (left) and E8 (right) to the RTCP reaction. Images were collected on the Technai microscope on copper coated carbon grids. The middle left is a plot of the frequency distribution of particle sizes when synthesised in the presence of MIA A3 (blue) and E8 (purple), produced on GraphPad Prism. Middle right indicates the size distribution of the NPs. Bottom left is powder XRD data for the NPs. Data was collected between 20 and 80 °. Bottom right is magnetisation data of the MNPs. Data was collected using VSM. Each of the analysis shown here show comparable results for particles using MIAs A3 and E8.

The data analysed so far suggests that the addition of MIAs to a simple RTCP results in improved control over the reaction pathway and products. The addition of these additives appears to drastically narrow the size distribution of the particles compared to a RTCP carried out in the absence of such proteins. When used at the optimum concentration they also have a significant effect on the shape of the crystals generated. Increased control gives the vast majority of particles the desired cubic morphology. Results from powder XRD analysis suggest that the main product of the reaction is magnetite with the d-spacing matching those expected for the main magnetite facets, however it is often difficult to differentiate between magnetite and maghemite using XRD alone as

the d-spacing is very similar. Magnetite is the much more magnetic species and it would be expected that if the sample was magnetite it would show a response to an applied magnetic field.

VSM at room temperature was used to analyse the magnetic response of the NPs synthesised in the RTCP with A3 and E8. If the crystals consisted of magnetite a response to the application of the magnetic should be evident. Also, as the NPs are relatively uniform in shape, size and composition a uniform magnetic response would be expected. This is vital for the MNPs use in almost any application, especially applications for clinical therapies or diagnostics.

The majority of the NPs synthesised in this way have a diameter which lies between 30 and 40 nm. This size means that the NPs sit on the boundary between SPM and single domain MNPs. Magnetite particles below 80-90 nm, with an aspect ratio close to 1 are classed as single domain and those below 20-30 nm are SPM. The VSM plot in figure 37 shows the effect on the particle magnetisation on the addition of an applied magnetic field. Analysis of the data shows the magnetic saturation and the coercivity (H_c) of the NPs. The values were extremely similar for particles synthesised with A3 and those synthesised with E8. The hysteresis loop for each sample is very narrow and barely visible, indicated by the low H_c values (1.94 and 4.60 Oe for A3 and E8 particles respectively). This can be a favourable trait for a number of applications as the particles do not retain their magnetisation when the external field is removed, and thermal fluctuations provide enough energy to 'flip' the magnetic moment. The saturation magnetisation is the point where an increase in external field no longer has an effect of the magnetisation of the NP. The saturation magnetisation was calculated for identical but masses of MIA A3 and E8 and as expected, there was little difference between the two samples studied. The values calculated for particles produced in the presence of A3 and E8 respectively were: 28.71 and 26.20 emu.

It is clear from the data presented that the addition of the MIAs to the RTCP has a significant effect on the resultant crystal formation. Although molecular dynamic models indicate the favourable binding of lysine residues to the magnetite surface, the mechanism of how the proteins generate this effect is not well understood. The binding and possible interactions between the residues of the MIA VRs and the [100] facet of magnetite was considered. The MIA constructs appear to have a higher affinity for [100] faces of magnetite and therefore promote the formation of cubic particles. Reactions involving MIAs at high temperatures do not see this same preference for cubic morphology, this is likely due to denaturation of the MIA protein, causing a loss of conformational integrity of the VR.[139] This suggested that the structure of the VR of the MIA was highly important for

the activity observed. Another important aspect for functional activity, as suggested earlier is the presence of basic, positively charged residues, including lysine. However, having studied MIA proteins containing varying number of lysine residues, although there is a strong binding preference for lysine rich sequences, there is not a linear correlation between the number of lysine/basic residues and binding strength. Therefore, it appears that the position and local topology of the positive charges are important. Further, in-depth magnetite binding analysis of the whole MIA binder pool is required to ensure a complete understanding of the mechanism adopted in magnetite cube formation.

3.6 Binding of the Adhiron to magnetite NPs

Binding strength between MIAs and magnetite NPs was analysed using an ELISA. A blocking buffer was added to prevent the formation of weak, non-specific interactions. A simple wash stage was possible by utilising the magnetic properties of the MNPs, allowing the particles to be magnetically separated from the reaction mixture. The primary antibody was chosen due to its ability to bind the Strep-II purification tag at the C-terminus of the MIA protein. A secondary recognition antibody, tagged with AP was then used for the detection of the protein. If the protein remained bound a solution of BluePhos detection reagent would turn from yellow to blue/purple. This colour change was detected using UV-Vis spectroscopy and measuring the absorbance of the sample at 600 nm. A system utilising alkaline phosphatase (AP) was used in place of a HRP-based system as there are examples in the literature suggesting that free radicals produced by magnetite NPs produce a colorimetric response, even in the absence of bound protein.

Before the binding ELISA, it was important to determine whether A3 remained bound after the RTCP. Although this was unlikely due to the pH of the reaction exceeding pH 9, this had not been tested and could not be confirmed. At high pH the basic residues in the VRs lose their charge and become neutral. As the basic nature of the amino acids is thought to play some role in binding, the extent of binding was predicted to be reduced. The 30 nm NPs (NPs synthesised with A3) were analysed in the ELISA. No further MIA was added to these particles and so if the protein had not remained bound after the reaction, there should be no colour change upon the addition of the detection reagent. This was the case. The solution remained yellow/colourless and the absorption at 600 nm was 0 (see figure 39). This reading indicates that any colour change during the ELISA following the addition of the MIA was due solely to the know amount of protein added at that stage.

The binding of MIAs A3 and E8 to magnetite NPs synthesised using the RTCP was assessed. Pre-synthesised NPs with an average diameter of 5 nm and 30 nm were used to determine whether the size of the NP used had an effect of the binding strength. Magnetite NPs with a diameter of around 5 nm were synthesised using a reverse RTCP reaction. In this reaction, a mixture of ferrous and ferric salts was added dropwise to a solution of sodium hydroxide. The rapid formation of the magnetite crystals results in the generation of smaller NPs (shown in figure 38). The average diameter of the NPs produced using the reverse RTCP were 5.58 nm $\pm$ 3.13. The Gaussian curve fit to the frequency distribution data for the NP size shows a narrow size distribution.

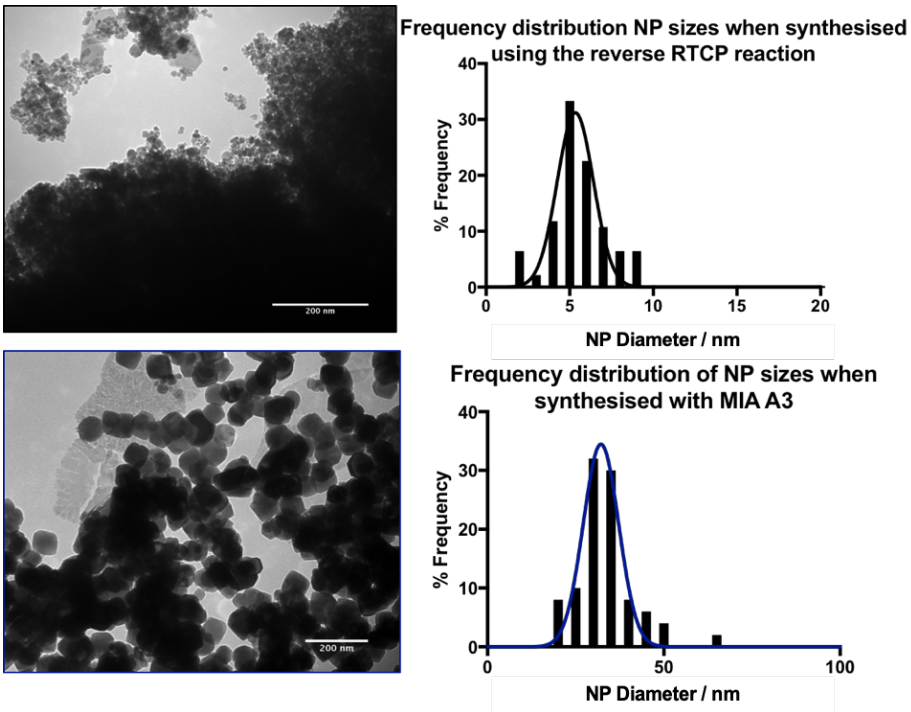

Figure 38 TEM images and grainsize analysis for the synthesis of magnetite NPs with an average diameter of 5 nm (reverse RTCP) and 30 nm (RTCP with A3 additive. Top images show data collected for MNPs synthesised using the reverse RTCP method – producing particles in the range of 5 nm in diameter. Top left is a TEM of these particles. The image was collected using the Technai microscope with the particles dried on to copper coated carbon grids. Top right is a plot of the distribution of particle sizes, produced using graphpad prism. The bottom images show dat for particles synthesised using standard RTCP protocol – producing MNPs with a diameter of around 30 nm. Bottom left is a TEM of these particles, showing a 200 nm scale bar and bottom right is the size distribution plot for these particles.

Magnetite NPs with a size of roughly 30 nm were synthesised using the forward (normal) RTCP with the addition of MIA A3. The TEM images and grainsize analysis is shown in figure 38. The average particle diameter was found to be 32.56 nm $\pm$ 15.69 nm. The Gaussian curve fit to the frequency distribution data for these NPs shows a narrow size distribution, expected for NPs synthesised with MIA additives.

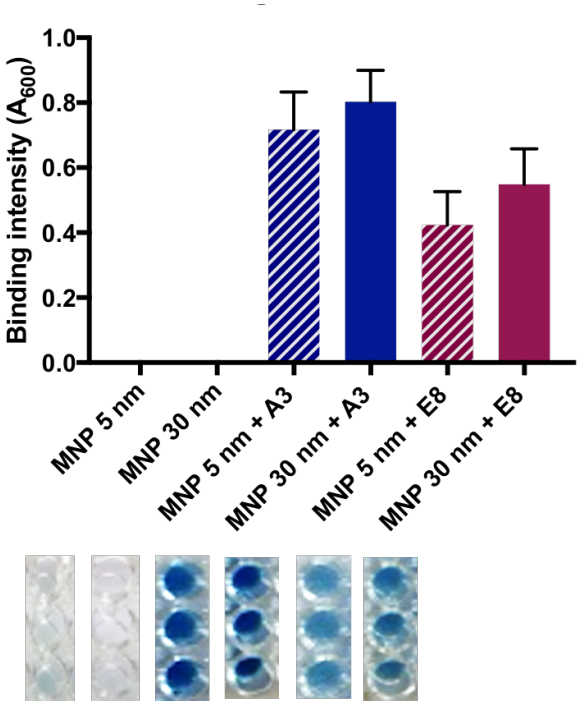

Figure 39 ELISA data for the binding of MIAs A3 and E8 to magnetite NPs measuring an average of 5 nm and 30 nm The plot displays the binding of MIAs A3 (blue) and E8 (purple) to MNPs with an average diameter of 5 nm (striped bars) and 30 nm (solid bars). The binding intensities measured for the 5 nm and 30 nm particles did not differ significantly, with the readings being within the associated error of each other. There was a slight difference in the binding intensities of A3 and E8, with A3 appearing to bind slightly more favourably. The control showed no binding

The binding intensities measured for the 5 nm and 30 nm particles did not differ significantly, with the readings being within the associated error of each other (see figure 39). There was a slight difference in the binding intensities of A3 and E8, with A3 appearing to bind slightly more favourably to the MNPs than E8, however both proteins showed a promising degree of binding, indicating a strong, specific interaction with the mineral. The control samples, to which no protein was added, showed no binding (A_{600} = 0).

3.6.1 Assessing the specificity of the MIA – magnetite interaction

Interactions with zinc oxide performed by Dr Andrea Rawlings, University of Sheffield[84]

To determine whether the MIAs were able to distinguish between metal oxide minerals an ELISA assay was performed. The binding capability of the MIA to equal amounts of zinc oxide and magnetite was compared. A primary antibody was picked that would recognise and bind to the Strep-II tag present at the C-terminus of the MIA; a secondary antibody was then employed for the detection of the MIA. The detection reagent turned from yellow to blue in the presence of the MIA (and therefore secondary antibody) and this colour change was recorded by measure the absorbance of the samples at 600 nm (see figure 40).

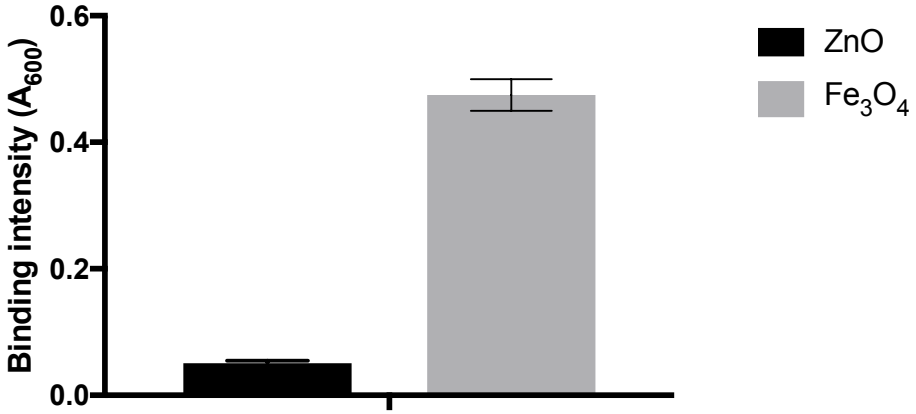

Figure 40 A plot to show the binding intensity of MIAs to ZnO (black) and magnetite (grey) NPs to indicate specificity of binding absorbance for the magnetite sample was significantly higher than for the zinc oxide NPs, suggesting preferential binding

The measured absorbance for the magnetite sample was significantly higher than for the zinc oxide sample, suggesting stronger, preferential binding to the magnetite and therefore showing the MIA exhibits good specificity to the target mineral. The ELISA was also carried out with a control MIA – an Adhiron scaffold that displays a peptide that does not bind magnetite. These samples did not change colour upon addition of the detection reagent and therefore no binding occurred in for either mineral.

3.6.2 Investigating peptide binding to magnetite NPs

MIA binding to magnetite NPs has been well established through this work, it has been shown that the MIAs bind strongly and specifically to the magnetite NPs. It has yet to be confirmed whether this binding ability is dependent on the presence of the Adhiron scaffold, or if this binding effect could be established with the same sequence of the loop as a free peptide in solution. Many previous studies suggest that a scaffold protein is essential, the peptides are confined to a single orientation, preventing conformational freedom and therefore aiding specific binding. This theory was tested using a pull-down experiment with peptides of the A3 and E8 loops, along with VR2 of the control MIA. The peptides were fluorescently tagged via a FITC fusion. The fluorescence could then be traced throughout the binding reaction. Two parameters were measured: the decrease in fluorescence of the peptide solution, following the addition to MNPs; and secondly, the increased fluorescence of the MNPs. It was thought initially that the photo-fluorescent properties of the MNPs may interfere with the readings, however this did not appear to be the case.

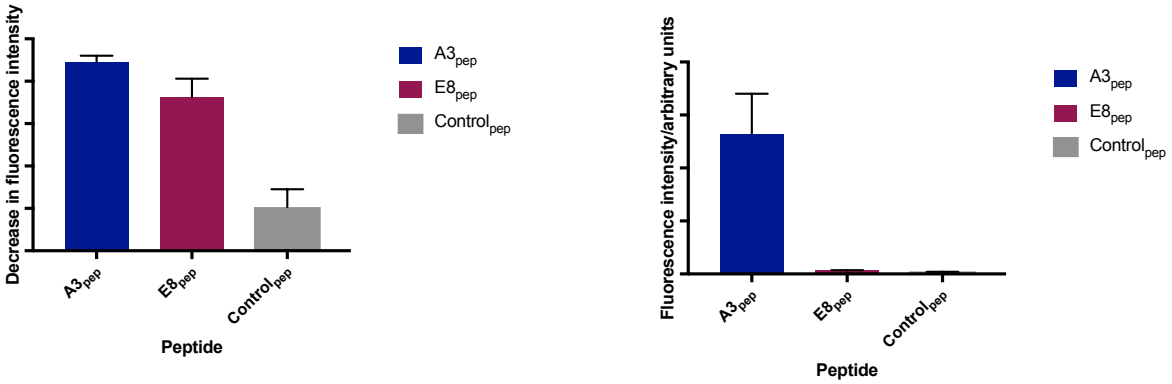

Figure 41 The plot on the left shows the level of decrease in the fluorescence of the FITC-tagged peptide solution and the plot on the right shows the increase in fluorescence of the MNPs after peptide binding, following 24 hours incubation with FITC-tagged peptides. Fluorescence was measured at Em/Ex of the FITC fluorophore.

As expected the fluorescence intensity of the peptide solution decreased least for the control peptide (figure 41). To measure this parameter the peptide solutions were magnetically removed from the MNPs. Although the decrease in fluorescence is not zero, this low value suggests that there is no significant binding to the MNPs; A small decrease in fluorescence can be attributed to a natural decay of the fluorescent signal, for example during sample preparation the plate would not have been kept in complete darkness, leading to photo-degradation. For the other two peptides, there appears to be some binding to the MNPs with the strongest binding witnessed for $A3_{pep}$.

The data measured for the fluorescence of the peptide solutions for $A3_{pep}$ and $Control_{pep}$ appear to match the results obtained for the fluorescence of the MNPs. There was a significant increase in fluorescence signal of the MNPs that had been left to bind at $A3_{pep}$ for 24 hours, in dark conditions, indicating strong binding between the free peptide and the MNPs. This positive result also confirms that the magnetite NPs do not quench the fluorescent signal of the FITC to any significant degree. The control peptide did not show any indication of binding to the MNPs in the 24 hours allowed for interaction as the fluorescent signal of the MNPs did not increase. This control also shows that the FITC-tag does not bind the MNPs and the particles do not give an unwanted fluorescent signal.

However, the data from the peptide solution and the MNPs did not appear to match for $E8_{pep}$. This experiment was repeated for reliability and reproducibility; however, the same problem arose each time. When measuring the decrease in the fluorescence of the peptide solution, after being extracted from the NPs, there was a clear decrease in the reading, suggesting that the peptide had bound to the NPs and therefore been retained when the MNPs were magnetically extracted. On the other hand, when the fluorescence of the MNPs that had been mixed with $E8_{pep}$ was measured, there was no obvious increase in fluorescent signal, suggesting no binding. It is therefore difficult to

draw any conclusions for the $E8_{pep}$ interactions with magnetite NPs. It may be that only weak binding is occurring so in a new equilibrium the bound peptide becomes detached.

The activity of MIA peptides as additives in RTCP was also investigated to determine whether they were able to control the shape of the particles in the same way as the MIAs. RTCP reactions were carried out with each of the peptide additives. The reaction products were analysed using TEM. Grainsize and shape analysis was collected as before. This data can be found in figure 42 below.

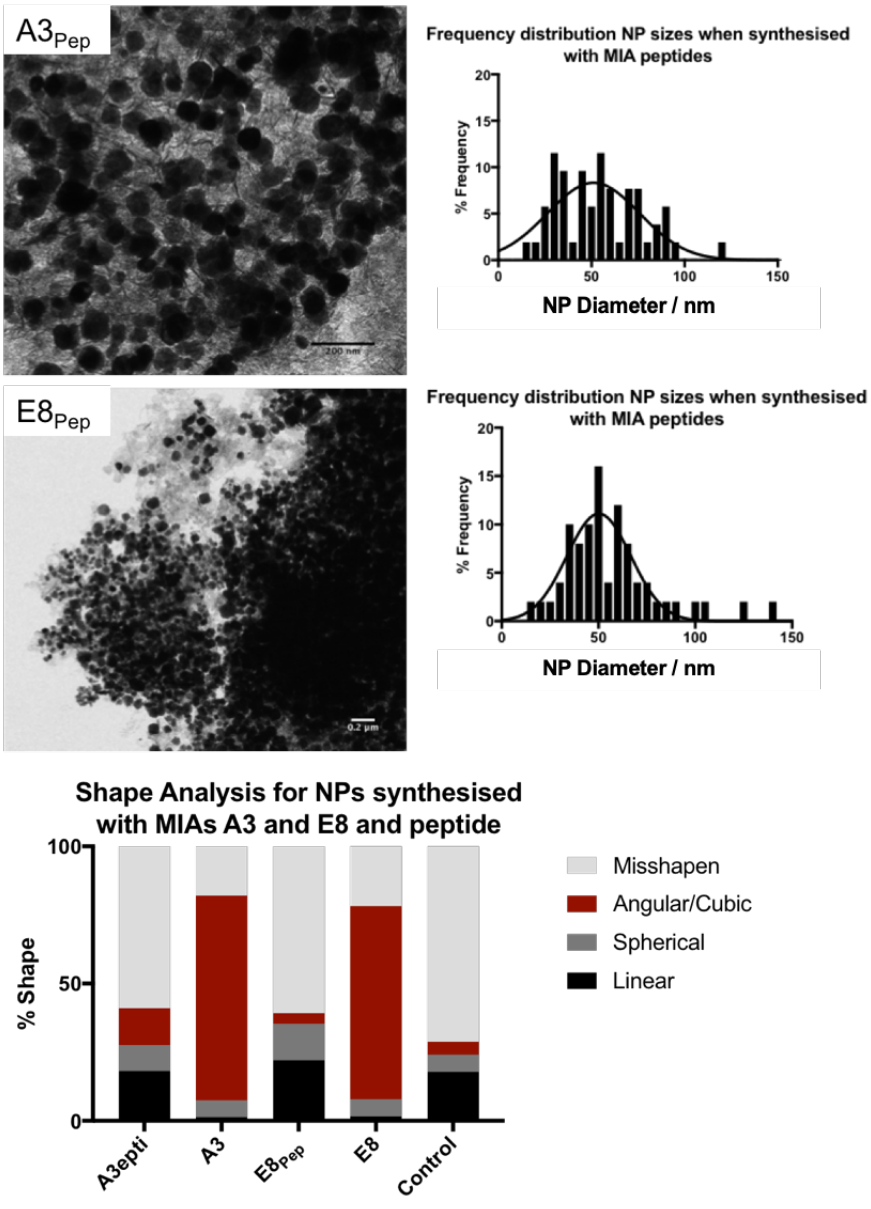

Figure 42 TEM images captured using the Technai microscope, imaging MNPs on carbon-coated copper grids. Here the particles are not as clean or angular as previous;y witnessed. Grainsize analysis in the for of the frequency distribution plots can be seen along side the TEM images for particles synthesised in the presence of A3pep (top) and E8pep (middle). Shape analysis can been seen at the bottom of the figure for magnetite NPs synthesised in the presence of flexible MIA peptides A3pep and E8pep. This analysis can be compared to NPs synthesised with the complete MIA scaffold

The images from the TEM show the reaction products looking 'messy'. A number of different species of iron oxides are visible including needles and platelets. Magnetite does not form these structures and so the composition of the iron oxide is likely to be maghemite, goethite or hematite. The range of different particles is emphasised when studying the grainsize and shape data. The NPs produced in the presence of peptide gives a much broader range of sizes with species ranging from <20 nm to >130 nm. The shape analysis shows a significant rise in the proportion of rod-like and misshapen NPs compared to MNPs synthesised in the presence of the MIAs; there is also a drastic decrease in the proportion of NPs forming an angular or cubic shape.

3.7 Chapter summary

This chapter has shown the successful cloning strategy adopted in the production of the MIAs and provided the expression and purification conditions for the optimisation of protein production. The MIAs produced appear to adopt a monomeric structure, with a high β-sheet content and high stability. The addition of these proteins to RTCP reactions aids the control of the NPs synthesised, especially in terms of shape, with a cubic morphology being preferentially adopted with the addition of these additives. Particle analysis following peptide addition to the RTCP showed that the Adhiron scaffold is essential to this effect. All of the results collected here suggest that the MIAs would be useful agents in the replacement of monoclonal antibodies for a range of biomedical applications due to their high stability, ease of production and strong binding capabilities.

The particles generated with the flexible peptides appear to be much more similar in nature to the control NPs synthesised using the RTCP method without the addition of any protein. Therefore, it was proposed that the peptides are not capable of controlling the crystal formation or ultimate shape of the particles in the same way as the MIA proteins have been shown to do. A more rigid system, such as the Adhiron protein scaffold is required to hold the peptides in the favourable conformation ensuring strong interactions between the peptide sequence and the forming crystals and increased specificity of binding. The binding process is much more energetically favourable when the peptide loops are already constrained as the loss of entropy is much more severe for the binding of the free and flexible peptide. However, it should be noted that some peptide sequences can bind to the MNP but cannot control the synthesis. The MNP can template the flexible peptide, however, only rigid proteins, such as the MIA are able to template particle shape.

Chapter 4: Attachment to MNPs via MIAs for biomedical applications

4.1 Introduction into attachment to MNPs for biomedical applications

Magnetite NPs have recently arisen as a promising agent in a range of biomedical applications. The low toxicity of iron oxides, along with the SPM nature of magnetite NPs, promises uses for diagnostics including MRI and treatments such as magnetic hyperthermia and targeted drug delivery. There are numerous publications detailing synthesis methods for magnetite NPs.[10, 143, 144] Often methods for the synthesis of uniform, well-defined particles involve high temperature, high pressure conditions and the addition of organic solvents. The NPs that give rise to the results found in this chapter were synthesised using more environmentally friendly and less hazardous syntheses. Reverse RTCP methods were used (unless stated otherwise). This technique produced monodisperse particles with the size of the nanocrystal is in the range of 5-15 nm, resulting in SPM properties.

As explained in the previous chapters, one type of additive used in the synthesis of magnetite NPs is MIA proteins, due to their ability to bind strongly and specifically to the [100] facet of magnetite. The proteins themselves have the potential to be dual use; not only do they control the morphology of magnetite NPs, they could also be utilised as attachment linker groups to attach the NPs to other moieties such as drugs, dyes and antibodies. They also function as a biocompatible coating for the particles. This chapter presents how the MIA proteins have been realised as a successful linker between MNPs and antibodies, antibody fragments and fluorescent dyes using a variety of attachment methods.

4.1.1 Aims

- To successfully attach fluorescent dyes to the MNPs
- To successfully attach therapeutically relevant antibodies to MNPs.
- To analyse the level of uptake and cytotoxicity in cell lines containing varying expression levels of the target antigen and to use 3D ‘spheroid’ models to model this uptake and cytotoxicity.
- To identify the effect of AC hyperthermia on these systems in order to act as proof of concept data for the future of MIA functionalised MNPs as therapies and theragnostics.

4.2 MIA biotinylation for attachment

Biotinylation is the process of covalently attaching biotin to a protein. It can be used for attachment of other molecules to a protein through the biotin-avidin or biotin-streptavidin interaction, but also for labelling, detection and purification methods. This interaction is highly specific and one of the strongest known non-covalent interactions to form with a K*a* of 10^{15} M^{-1}. Biotinylation is a useful method of labelling and attachment for proteins and other macromolecules due to the rapid bond formation between biotin and avidin. In addition to this, once the biotin moiety has been attached, it is insensitive to experimental conditions such as pH, temperature or solvent. Also, due to the small size of biotin (244 g mol^{-1}) there is minimal interference with the activity or folding of the larger protein.

Two different biotinylation methods were tested for this project. Firstly, chemical methods of biotinylation were analysed. Chemical biotinyaltion uses *in vitro* methods and can offer greater flexibility in the type of biotin-labelling required; for example, there are a range of biotinylation reagents that target a host of different functional groups. Attachment via primary amine groups, such as the side chains of lysine, is the most widely used and well established chemical attachment method. This method was utilised here. An alternative to chemical methods is enzymatic biotinylation. Enzymatic biotinylation is performed using the co-expression of the bacterial biotin ligase, BirA and the protein of interest, modified with a specific tag signalling the site of biotinyaltion. An AviTag was the signalling peptide used. Although there is limited flexibility for *in vivo* biotinylation approaches, it does enable a more specific and more uniform route to biotinylating proteins.

4.2.1 *In vitro* biotinylation

A chemical biotinylation method was adopted to biotin-label MIA A3. The *in vitro* reaction used the ThermoScientific EZ-link™ Sulfo-NHS-Biotin kit to label each of the primary amine groups of the lysine side chains and N-terminus with a biotin moiety. The reagent was water soluble and produced a non-cleavable, covalent interaction between the biotin and amine, forming an amide bond. Optimisation of the biotinylation reaction compared two reaction conditions: the MIA in a 20-fold excess and in a 50-fold excess. The success of the reactions was then analysed using MS. If the biotinylation reaction was not successful only a peak at M^+=12003 should be present, this was observed when the MIA was used in a 50-fold excess, indicating the reaction had not been successful. For conditions using the 20-fold excess of MIA, the chemical biotinylation reaction appeared to be a success based on the MS data. Multiple peaks were observed, each being a good fit

to expected m/z peaks for varying numbers of bound biotin. An example of the spectra is shown in figure 43. Multiple independent repeats were analysed (whenever a new batch of protein was synthesised or biotinylated) each yielding almost identical spectra.

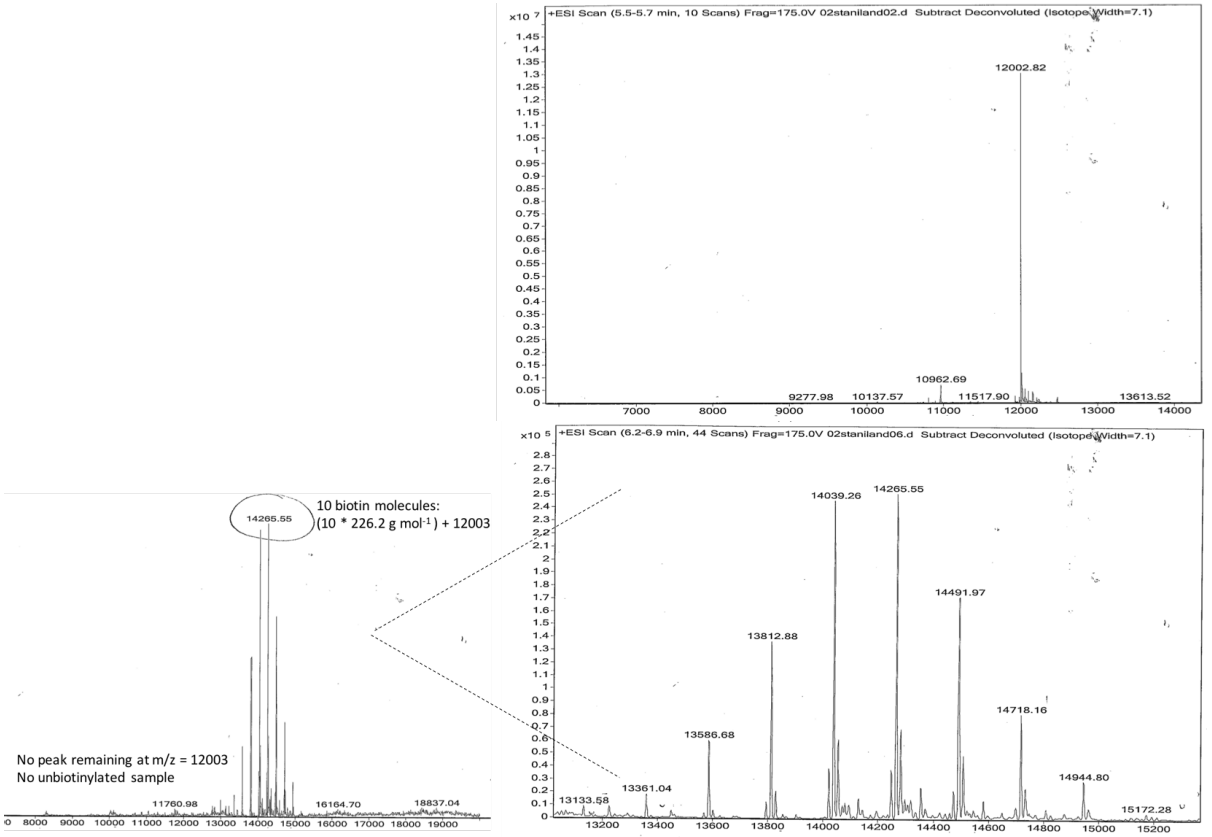

Number of biotin molecules	Expected m/z	Observed m/z	Sample %
0	12003	12003	0
1	12229	-	0
2	12455	-	0
3	12681	-	0
4	12908	-	0
5	13134	13134	0.8
6	13360	13361	1.5
7	13586	13586	5.6
8	13813	13813	13.1
9	14039	14039	24.3
10	14265	14265	24.8
11	14491	14492	16.8
12	14717	14718	7.9
13	14944	14944	3.7
14	15170	15172	0.5
15	15397	-	0

Figure 43 Mass spectrometry data for MIA A3 before and after chemical biotinylation. 50 µL of 1 mg/mL MIA A3 diluted in ultrapure water. The table displays the expected and observed m/z peaks for each degree of biotinylation assuming a single charge on the protein fragment (0-15 Lys residues biotin-labelled); 5-14 of the 'available' residues are biotinylated, with an average of ten biotin molecules per protein

The total number of lysine residues in MIA A3 is 15, there is also a primary amine group present at the N-terminus of the protein. It can be seen from the MS data that five to fourteen of the available residues are biotinylated, with the average being ten biotin molecules per protein (24.8 % of the protein sample contains 10 biotin groups). The proportion of the sample containing more or less than ten decreases the further away the number of biotin gets from ten. These percentages were calculated by measuring the intensities of the peaks. This shows that the biotinylation reaction for MIA A3 at a 20-fold excess was a successful, with no peak observed for the unlabelled sample at m/z = 12003.

The positions of the most and least accessible lysine sites for biotin-labelling were estimated using the Adhiron PDB file and Swiss PDB viewer (figure 44).[84, 145] Two or three (Lys 71, 73 & 74) of the lysine side chains are classed as hidden and largely inaccessible, this explains why full biotinylation of the protein is not achieved, with 13-labelled sites being the maximum observed for MIA A3. Two of the most accessible sites (Lys 50 & 51) flank the VR, thought to be responsible for magnetite binding. This had the possibility of reducing the binding capacity of the construct.

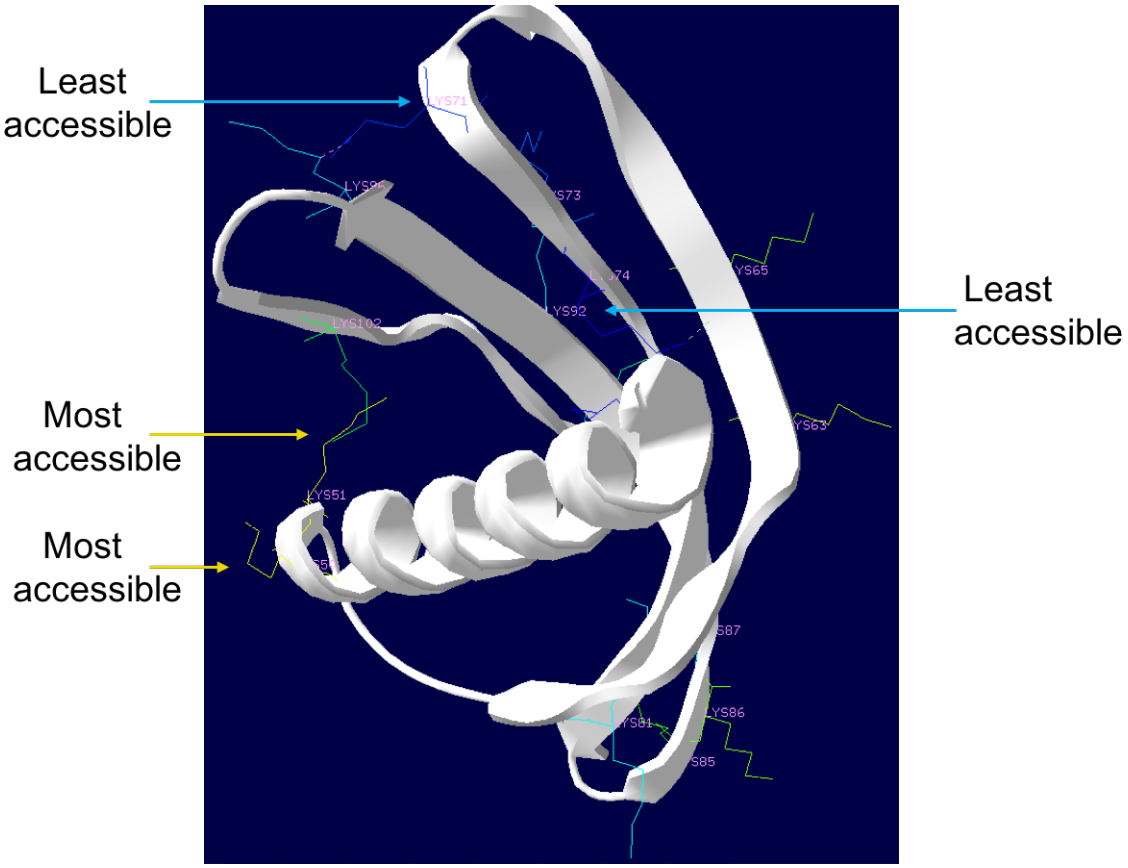

Figure 44 Protein model of MIA A3 showing the most (yellow) and least (blue) accessible site for biotin-labelling The positions of the most and least accessible lysine sites for biotin-labelling were estimated using the Adhiron PDB file and Swiss PDB viewer

After confirming the biotin attachment using MS, the secondary structure of the unbiotinylated and biotinylated samples was analysed. The CD spectrum was run between 260 nm and 190 nm. The response of the protein to circularly polarised light was measured and the molar elipticity was plot using GraphPad prism. The spectrum is shown in figure 45. This was a single repeat and could be validated further by repeating the CD analysis on more samples of biotinylated MIA. There is little difference between the spectra of the two samples and calculations for the percent of helical content for the samples suggest an identical proportion of α-helical folding. The proteins contain a low total amount α-helical secondary structure (14 %), this matches the predicted structure which contains mainly β-sheet secondary structure.

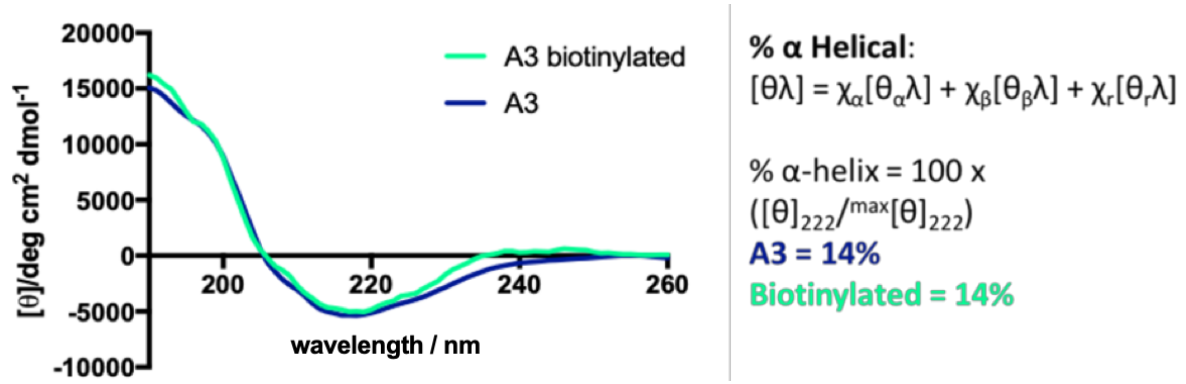

Figure 45 CD data comparing the secondary structure of MIA A3 before and after biotinyaltion to determine whether the biotin tag affects the secondary structure of the protein. CD spectrum was run between 260 nm and 190 nm with a protein concentration of 0.2 mg/mL diluted in ultrapure water

MS analysis had shown that the MIA protein had been labelled with biotin, however as suggested previously the extent of biotinylation was not specific or uniform in nature as a differing numbers of lysine sites were biotinylated. The binding of the biotinylated protein ($A3_{biotin}$) was analysed using an ELISA. An initial ELISA was performed to ensure that the biotin moieties were present and available to bind to streptavidin. A second ELISA was performed to determine whether biotinylation of the MIA would affect the binding ability of the protein to MNPs. The results from these ELISAs are shown in figure 46. The initial ELISA was performed on streptavidin plates, using a HRP-conjugated antibody for detection. This antibody recognised and specifically bound to the Strep-II tag at the C-terminus of the protein. A detection reagent containing the HRP-substrate was added at the end of this reaction. During the ELISA, an additional washing step was introduced for some of the samples, this involved washing the wells with a d-desthiobiotin solution to ensure that binding between the Strep-II tag and the streptavidin plates did not interfere with the readings. The wash did not appear necessary, with similar binding intensities observed for samples that had and had not received this

additional step. Therefore, it was unlikely the tag bound to streptavidin in the presence of a blocking buffer. Analysis of the ELISA data suggested strong binding between the biotinylated MIA and streptavidin plates and little binding for the unlabelled sample, as predicted. Again, confirming the success of the biotin-labelling experiment and suggesting that the biotin groups added were available for binding and attachment. Figure 46 below indicates the results from three independent repeats, consisting of two technical. The results were normalised between the independent repeats for ease of comparison. Images of the wells from the two technical repeats of a single independent repeat are shown alongside the figure.

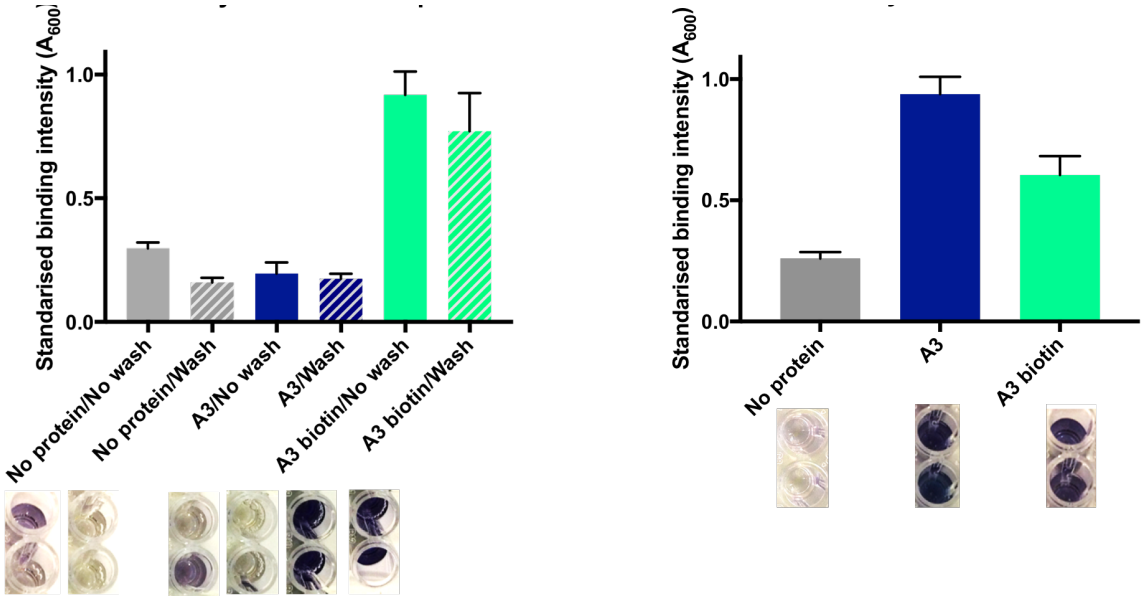

Figure 46 ELISA binding intensity data for assays performed on streptavidin plates (left) and on magnetite NPs (right). Wash denotes a d-desthiobiotin wash. Proteins were in 1 x PBS buffer. A blue colour in the plate wells indicates a strong binding interaction, whereas a colourless or yellow colour indicated little or no binding of the ligand in that well. Results were standardised to enable a better comparison between the results from the streptavidin plates and the MNPs. The results were standardised to give the maximum binding intensity as 1 and no binding as 0.

The second ELISA was performed on magnetite NPs to test the ability of the biotinylated sample to interact with the MNPs. An AP-conjugated antibody was used for the ELISA to prevent any side reactions between the magnetite NPs and HRP-substrate. Again, the primary antibody targeted the Strep-II tag fused to the MIA. The measured binding intensities are shown in figure 46. MIA A3 showed strong binding to the MNPs as previously observed. Although some binding to the MNPs was apparent for the $A3_{biotin}$ species (compared to the binding intensity measured in the no protein negative control) there was a significant decrease in the binding capacity compared to the non-biotin-labelled protein. The binding intensity for $A3_{biotin}$ was roughly halved compared to unlabelled A3. This reduction in binding is likely due to biotin groups bound to the lysine residues in or near the active loop region of the MIA. Although individual biotin groups are small, there are multiple lysine residues available in this region which results in multiple biotin groups attaching. This accumulative

effect is likely responsible for blocking the binding sequence on the protein, preventing binding to the MNP.

The reduced binding ability of $A3_{biotin}$ compared to A3 was a major disadvantage of this method for protein attachment and was therefore not taken any further in this project. Attachment of the MIAs to MNPs before performing the chemical biotinylation reaction was investigated, however binding studies suggested either a low degree of labelling or no biotin labels present. This order of reaction also prevented the protein being characterised using MS to determine the degree of labelling, leading to more time-intensive analysis. Incomplete biotinyaltion of MIAs bound to MNP may result from blocked lysine sites by the MNPs and other MIAs in close proximity. Also, the inclusion of magnetite NPs resulted in a change in reaction conditions which may not have been compatible with the chemical biotinylation kit used. Biotinylation reagents are commercially available that target a variety of specific groups, however the same problem is likely to arise with a number of different amino acids present in the binding region of the MIAs. For this reason, enzymatic biotinyaltion was investigated as an alternative. The enzymatic labelling reaction is much more specific, allowing control over the position and number of labelling sites.

4.2.2 *Enzymatic* biotinylation

Enzymatic biotinyaltion was used as a targeted, site-specific method of biotinylation of the MIA protein. An AviTag was fused to the terminus of MIA E8, with the tag acting as a recognition site for site-specific biotin-labelling. The aim was to attach a single biotin molecule to the protein, away from the MNP binding site.

A Gene String was designed and ordered from ThermoScientific to generate the fusion between the MIA and the AviTag (MIA_{Avi}). The design included a His_6-tag at the N-terminus, for protein purification purposes. The tag was proceeded by a TEV cleavage site that would allow enzymatic cleavage of the tag if necessary. As the His_6-tag is known to bind with strong affinity to nickel resin, and also with moderate affinity to other transition metal ions, it may become necessary to remove the tag if it was found to bind to the MNPs. The MIA DNA sequence was flanked by Not1 and Nhe1 restriction sites, this ensured that the MIA could be ligated in and out, generating a plasmid for the tagging of any protein. Finally, the AviTag was encoded at the C-terminus of the protein, followed by a TAA stop codon, to prevent expression of the Strep-II tag when using the pPR-IBA1 plasmid. The full sequence design is shown in figure 47, with colour coding for identification of the specific DNA sequence. Once designed the sequence was codon optimised for expression in *E. coli* and the sequence was checked for unwanted restriction sites using the NEB cutter 2.0 software. No

unwanted internal sites were identified. Primers were designed to provide Bsa1 restriction sites to the Gene String sequence, required for restriction digest and ligation into the pPR-IBA1 vector.

His-Tag:

GSSHHHHHH

TEV (cleavable site using protease):

ENLYFQG

ADHE8:
ATGVRAVPGNENSLEIEELARFAVDEHNKKENALLEFVRVVKAKEQAH
MYTKAQTTMYYLTLEAKDGGKKKLYEAKVWVKRELQEFKPVGDAAAA

Avi-Tag:

GLNDIFEAQKIEWHE

DNA sequence:

GGTAGCAGCCACCACCACCACCACCACGAAAACCTGTACTTCCAGG
GTGCTAGCGCTACCGGAGTACGGGCTGTGCCGGGTAATGAAAATTC
GCTGGAAATCGAAGAGCTGGCGCGCTTCGCCGTAGATGAACACAAC
AAGAAGGAAAATGCGTTGCTTGAGTTCGTCCGTGTGGTTAAAGCGA
AGGAACAAGCGCACATGTACACCAAAGCGCAGACCACCATGTATTAT
TTGACCCTGGAGGCGAAAGATGGCGGTAAAAAGAAACTGTATGAA
GCGAAAGTGTGGGTGAAACGCGAACTGCAAGAATTTAAACCAGTTG
GTGATGCGGCAGCCGCAGCGGCCGCGTGCGGTCTGAACGACATCTT
CGAAGCGCAGAAAATCGAATGGCACGAATAA

Figure 47 Design of the Gene String for the Avi-tagged MIA (codon optimised) As shown, the construct contains a His-purification tag, a site for protease cleavage and the MIA E8 protein sequence. This is followed by an Avi-tag C terminal, available for enzymatic biotinylation

The PCR for the amplification of the Gene String was optimised using a gradient PCR (figure 48). At lower annealing temperatures, agarose gel electrophoresis showed multiple bands as multiple PCR products were produced. As the temperature was increased to 65 °C the band at the expected MW for the complex became more intense, suggesting this was the optimum temperature to use for PCR amplification. The Gene String was amplified successfully before undergoing restriction digestion using Bsa1, this produced the sticky ends required for ligation into the pPR-IBA1 plasmid.

Following the ligation of the insert into the vector, the plasmid was inserted into competent *E. coli* cells, which produced colonies on treated LB agar plates. A number of individual colonies were picked at random for colony PCR allowing visualisation of the successful uptake of the plasmid by the colony. Primers specific to the MIA sequence were used. All colonies tested resulted in a band on the agarose gel at the expected MW (around 500 bp, see figure 48). A couple of the successful colonies were grown overnight in an antibiotic-containing LB medium before pelleting and purifying the cells for sequencing. A positive sequence was obtained for MIA_{Avi}.

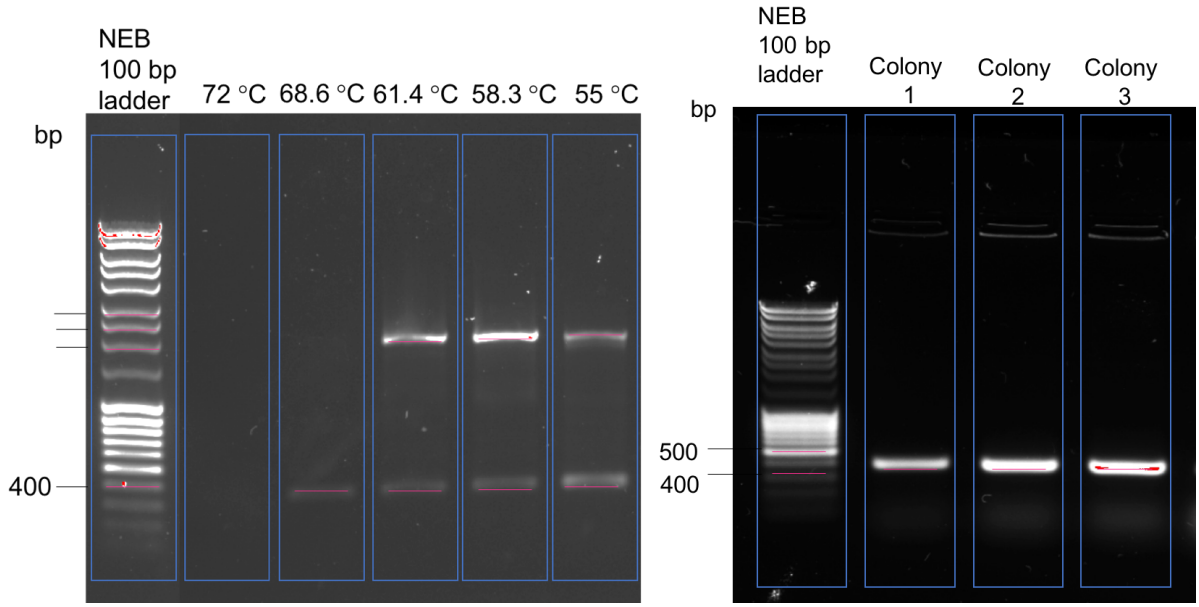

Figure 48 Gradient PCR to determine optimum annealing temperature of amplification of MIA_{Avi}.(left). Annealing temperatures of 55 ℃ – 72 ℃ were analysed. At lower annealing temperatures the agarose gel electrophoresis showed multiple PCR products were produced. Above to 68 ℃ the band at the expected MW for the complex became more intense. Agarose gel electrophoresis of the colony PCR, testing 3 colonies for uptake of MIA_{Avi} (right). All colonies tested resulted in a band on the agarose gel at the expected MW at 500 bp.

The MIA_{Avi} protein was expressed using SB auto induction media with incubation for 40 hours (protein production protocol established in chapter 3). The N-terminal His_6-tag was utilised for protein purification to yield a pure MIA_{Avi} protein product. The purified protein was analysed using SDS-PAGE and MS (figure 49). The predicted MW of the protein was 14256 Da, therefore the band just below 15 kDa on the gel suggests the correct protein product as does the single intense M^+ peak with m/z = 14256 on the MS. With the MIA successfully fused to the AviTag, the BirA enzyme was produced.

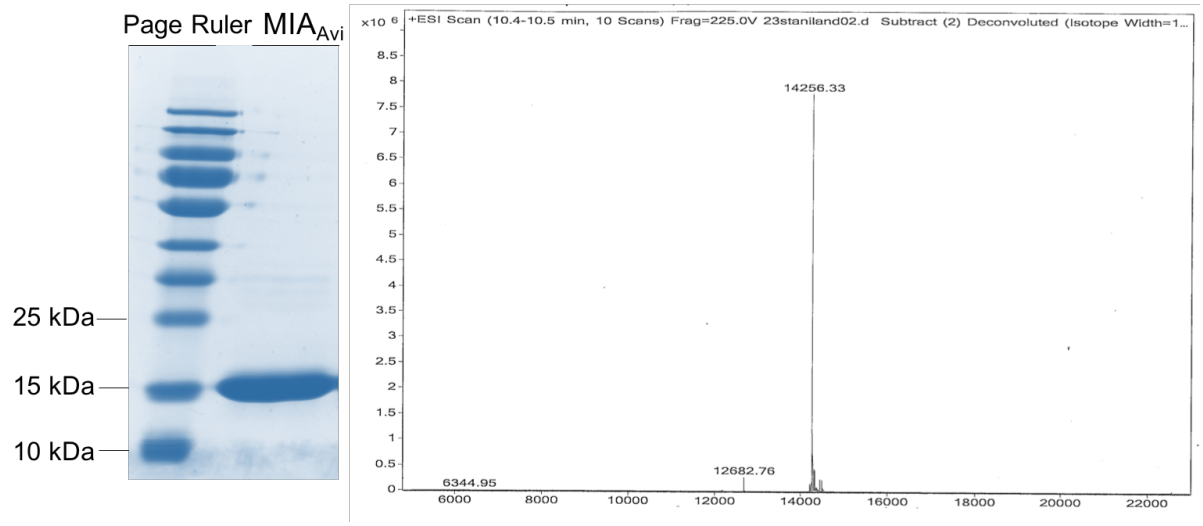

Figure 49 Protein analysis of MIA$_{Avi}$. SDS-PAGE band (left) at around 15 kDa was the expected band position for the Avi-tagged MIA. The m/z peak at predicted position for the correct molecular weight on the ES-MS plot (right). MIA-Avi was diluted to 1 mg/mL in ultrapure water for MS analysis.

The BirA plasmid was received from Zainab Taher and Pawel Lysyganicz – members of the Staniland group at the University of Sheffield. The plasmid was transformed into chemically competent *E. coli* cells and grown overnight on LB agar plates containing kanamycin antibiotic. The colonies were picked the following day and grown in LB media containing antibiotic, before addition to SB auto induction media containing antibiotic. The cultures were incubated at 18 °C for 24 hours for the optimum protein yield. After 24 hours incubation, the cells were pelleted and lysed. The soluble protein was purified using Ni-NTA affinity purification which was possible due to the His_6-tag fusion on the BirA protein. The purified protein was analysed using SDS-PAGE and MS. The gel and MS data suggest that the correct BirA complex had been produced (figure 50). Bands on the gel around 55 kDa and 37 kDa match the predicted MW of the thioredoxin-tagged and untagged BirA enzyme respectively. BirA enzyme is only 37 kDa, there is a thioredoxin tag fused to the protein, increasing the molecular weight to 54 kDa. The single M^+ peak on the mass spectrum with m/z = 54010 corresponds to the predicted MW of the protein.

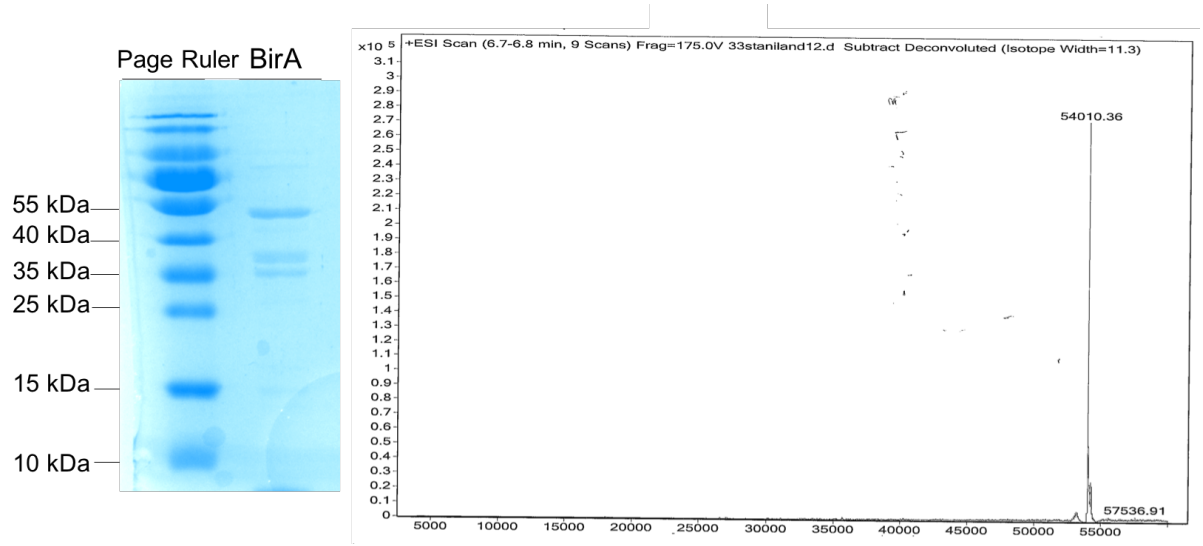

Figure 50 Protein analysis for BirA enzyme after purification. SDS-PAGE (left). Bands at 55 kDa and 37 kDa match the predicted MW of the thioredoxin-tagged and untagged BirA enzyme respectively and ES-MS (right) indicate the product is the expected molecular weight. A 50 mL sample of BirA was diluted to 1 mg/mL in 1 x PBS for MS analysis.

With the production of BirA and MIA_{Avi} confirmed using SDS-PAGE and MS, the enzyme was used to catalyse the biotinylation of the MIA at the AviTag site. The two proteins were expressed using the methods detailed above, however before cell lysis, the protein pellets were mixed together and incubated with additional biotin and ATP. The cells were then lysed using sonication, before a further incubation step with additional biotin and ATP, allowing the enzyme and tagged protein to react using biochemicals released from the *E. coli* cells, required for catalysis to proceed. The protein product was purified using affinity chromatography and the His_6 purification tag and the purified protein analysed using MS. The MS data was analysed before and after the enzymatic biotinylation process and the spectra are shown in figure 51 below.

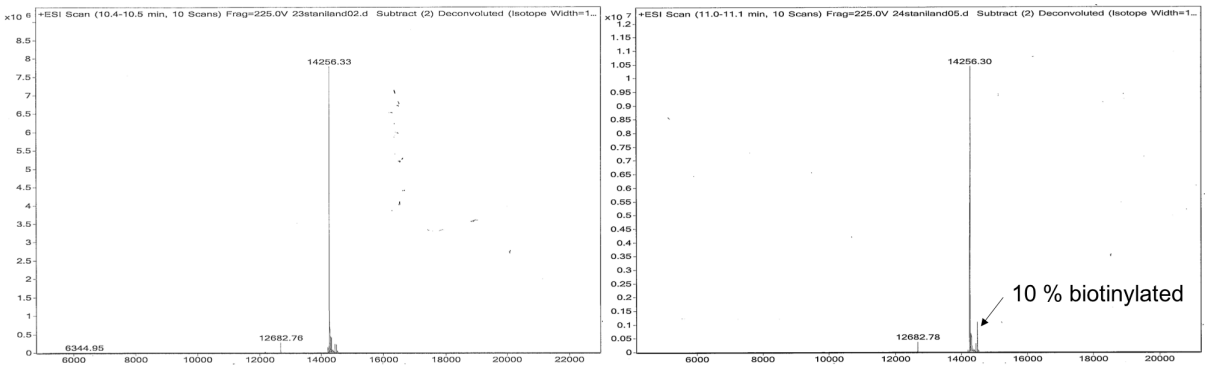

Figure 51 MS of MIA_{Avi} (50 µL, 1 mg/mL in ultrapure water) before (left) and after (right) enzymatic biotinyaltion with BirA. The presence of a new peak at m/z = 14482 indicates a small proportion of the sample is biotinylated

Analysis of the mass spectra indicates that a small amount of the protein sample had been biotinylated, compared to the sample that had not been incubated with BirA. The percentage of successful product, calculated using the peak intensities, however is low (10%). Changing the incubation times and concentration of ATP and biotin added did not affect the product yield, with 10 % product being the maximum obtained. Although a promising labelling reaction in respect to the specificity achieved, a 9:1 mixture of product, with the 10 % being the unlabelled product was not a high enough yield to take this attachment method any further. Therefore, a more universally used attachment method for peptide displaying scaffolds was adopted – attachment via a single cysteine residue.

4.3 Introduction of a single C-terminal cysteine residue

Peptide displaying scaffolds are often designed to not include any cysteine residues, this enables a single cysteine amino acid to be added to the protein sequence at a later stage for specific targeted attachment – preventing heterogeneous labelling of the protein. Heterogeneous labelling and attachment often leads to decreased binding between the protein and target ligand, as seen in section 4.2. The cysteine residue can be added to any point along the polypeptide chain, however it is most commonly fused to the end of the chain, therefore making it more likely to be accessible for binding and not disrupt the protein secondary or tertiary structure. The side chain of cysteine contains a thiol (-SH) group and so can be attached to drugs, dyes or antibodies through a disulphide bridge or maleimide linkage, both of these strategies were investigated.

4.3.1 QuikChange™ site-directed mutagenesis

A single cysteine residue was added to the C-terminus of the MIA proteins to enable homogeneous attachment of a variety of molecules. The extra amino acid was attached using the QuikChange™ site-directed mutagenesis method which enables site-specific mutations using double-stranded plasmid DNA as a template for the reaction. Forward and reverse primers that were complimentary to the opposite strands of the plasmid were designed; these primers also contained the sequence for the cysteine insertion mutation (the sequence of primers used is provided in the appendix (4.2). PCR was used to amplify the mutated MIA-containing pPR-IBA1 vector, the reaction product yielded the new mutated plasmid, however this plasmid contained nicks. The DNA template (that did not contain the cysteine mutation) was digested using a Dpn1 enzymatic digest, which cut all the remaining methylated parental DNA. The desired, mutated DNA was then transformed into chemically competent *E. coli* cells (XL10 Gold). The bacteria contained ligase to 'fix' the nicks in the

plasmid and therefore the new DNA, containing the cysteine residue was able to infect the cells and colonies containing the desired mutation grew on LB agar plates (containing the required antibiotic).

Individual colonies that had grown on the plates overnight were picked and grown in and LB medium containing antibiotic. The cells were then pelleted using centrifugation and prepared for sequencing using a MiniPrep kit. Sequencing for mutated MIAs A3 (A3C), E8 (E8C) and the control protein (non-binding Adhiron; controlC) came back positive – indicating the presence of a single C-terminal cysteine residue for each of the proteins. With the mutation reaction appearing to be a success, the protein was then produced. Protein expression and purification was conducted in the same way as the non-mutated MIA protein production (chapter 3). The cysteine residue did not appear to affect the protein yields using these expression and purification methods, when compared to the yields achieved for the non-mutated MIAs.

Once the mutated proteins had been synthesised and dialysed into water, they were characterised using MS. The resulting spectrum and table showing expected m/z peaks is shown in figure 52. Analysis showed the expected M^+ peak for A3C (12106), with no peak observed at 12003 (M^+ for A3) – indicating the successful mutagenesis reaction for cysteine addition. There was also no peak present in the spectrum for E8C, at 11909 which would show E8 with no cysteine attached. However, no peak was observed at 12012 either, which would correspond to E8C. Instead the M^+ peak was observed as an intense peak at m/z = 24022, which was double the expected MW of the protein.

MIA	Expected M+ No Cysteine	Expected M+ with Cysteine	Observed M+
A3	12002.68	12105.82	12106.29
E8	11908.62	12011.76	24022.07

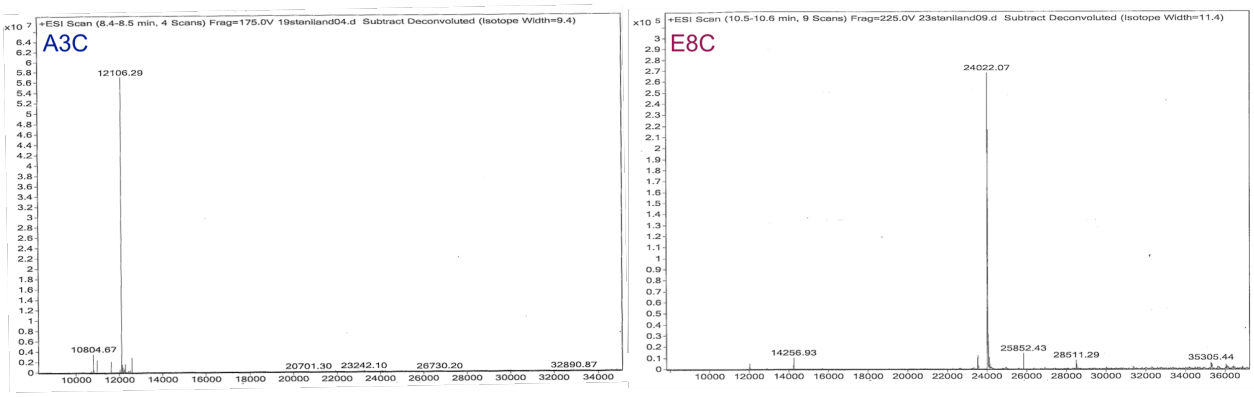

Figure 52 Mass spectra for A3C (left) and E8C (right). Both proteins were diluted to 1 mg/mL in ultrapure water prior to analysis.The table (top) shows the expected and observed position of the molecular ion peak for the proteins. The observed and expected were similar for MIA A3, however the observed was approximately double the expected for MIA E8. Indicating a possible dimer.

The peak at double the expected m/z for E8C suggests the presence of a dimer. As a peak corresponding to a dimer is not visible when analysing E8 using MS, it is likely that E8C is dimerising through an interaction between the inserted cysteine residues through the formation of a disulphide bridge. It was likely that A3C was also capable for forming disulphide bridges under the correct redox conditions.

The sulfhydryl groups of the cysteine side chains of nearby proteins, peptides or molecules are able to interact and form intermolecular disulphide bonds (known as a disulphide bridge) through a hydrolysis reaction. During the reaction, the sulfhydryl groups are oxidised, losing a total of two electrons during the covalent bond formation therefore disulfide bind formation is redox sensitive. It is this reaction that likely produced the E8C dimer witnessed using MS.

4.3.2 Attachment via a disulphide bridge

A sample of A3C was then analysed again using MS and the resulting spectrum is shown in figure 53. This time a peak was observed at m/z = 24210, the position expected for the A3C dimer. The A3C and E8C dimers were also analysed using SDS-PAGE.

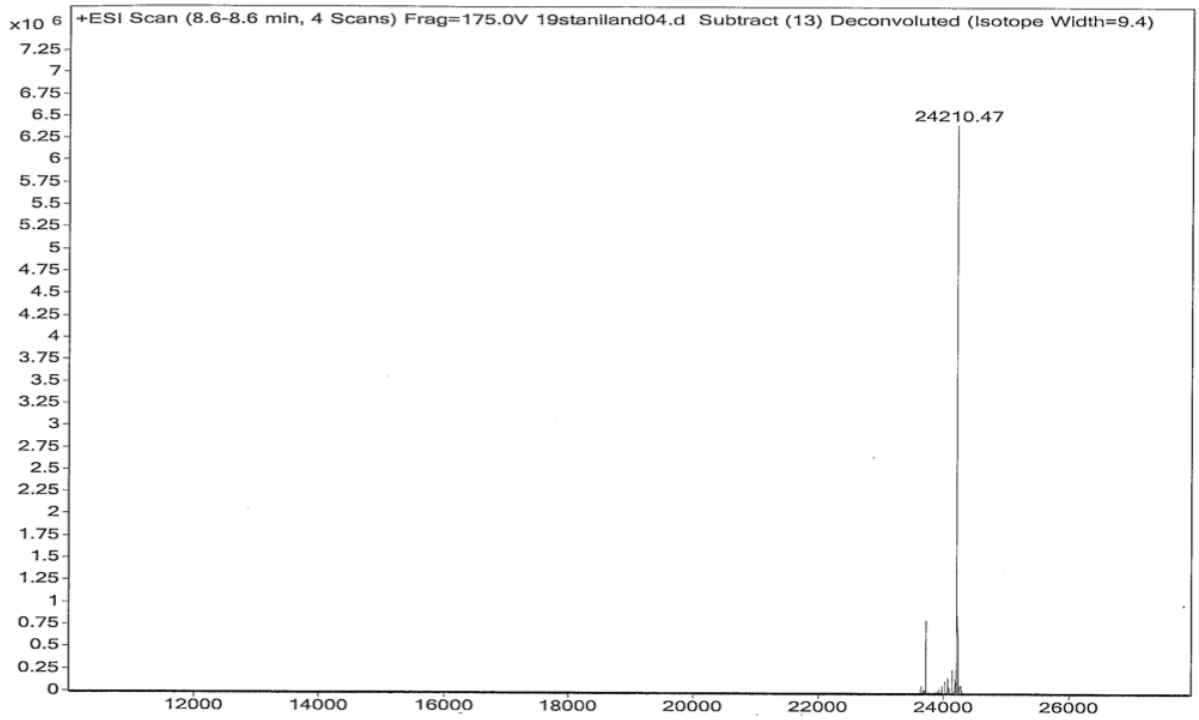

Figure 53 A3C was characterised using mass spectrometry. The protein was diluted to 1 mg/mL in ultrapure water prior to analysis. The observed molecular ion peak at 24210 is predicted to be the dimer (assuming a single charge on the protein fragment).

The reversibility of the disulphide bridge formation was investigated, to ensure the cysteine residues could be prepared so that they were accessible for further labelling and attachment studies. The reduction of the bond was tracked using SDS-PAGE. The gels shown in figure 55 suggest that the intermolecular disulphide bridge that forms between the cysteine tagged MIA proteins can be easily reduced using reducing agents such as DTT or TCEP, ensuring that the cysteine tag is available for protein labelling and attachment. The bands observed around 12 kDa show the reduced cysteine tagged proteins, adopting a monomeric structure, whereas the bands present around 25 kDa are the dimerised MIA samples. The proteins were also analysed using western blotting to ensure that the proteins witnessed on the SDS-PAGE were the desired proteins, which containing a Strep-II tag. This tag was recognised and bound using a HRP-conjugated antibody. The detection of bands using a chemiluminescent response indicated that the proteins were Strep-II and were the proteins of interest. The initial formation of dimers for A3C and E8C is promising as it suggests that the cysteine tag is present and accessible. Even more promising is that this disulphide bond can be reduced for binding of A3C or E8C to other thiol containing species.

4.3.2.1 Dyes and sensors for disease

A secondment at the spin-out company BioForDrug, based at Bari University in Italy, investigated the

design and synthesis of a copper chelating dye to aid diagnosis of Alzheimer's disease (AD). The aim of this work was to use robust, well expressing MIA proteins to attach a desired diagnostic molecule to MNPs via a disulphide bridge. During the time in Bari the work focused on drug synthesis relating to previous work based on the link between prions AD. AD is a neurodegenerative disease which causes progressive memory loss and is associated with aggregates of amyloid-beta (Aβ) peptides. Cellular prion proteins make up prions; PrP^c is a form of one form of cellular prion protein that has been identified as a cell surface receptor for Aβ oligomers. Prions are capable of infecting healthy tissue, causing proteins to misfold. PrP^c octo-repeat units chelate divalent copper ions and so can be used to detect copper levels in the blood. As Cu^{2+} is important for enzymatic activity in the body, an imbalance of the metallic ion induces neurotoxicity which can lead to neurodegenerative disorders including AD. Therefore, detection of copper levels in the blood can result in an early diagnosis of patients with AD. The complex designed was used to carry out this function (figure 54).

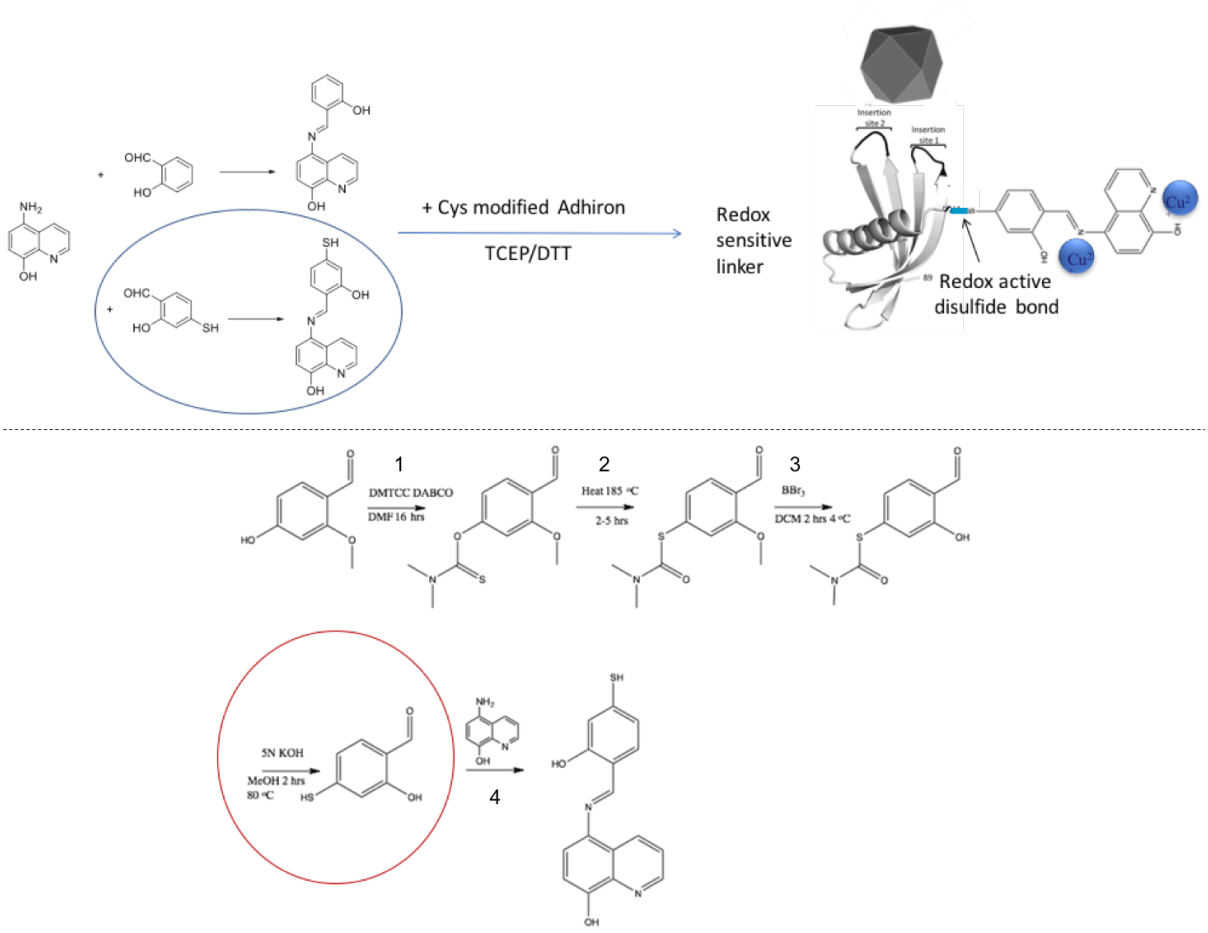

Figure 54 Reaction scheme for the drug synthesis at BioForDrug, Bari. The top diagram shows the overall reaction scheme and desired product. The bottom diagram shows the organic synthesis employed to produce the dye. The red circle indicates the product synthesised.

In the presence of copper, the electronic properties of the complex (figure 54) is altered, resulting in

a redox-sensitive shift in absorbance. Fluorescent imaging could be utilised due to the shift in the excitation wavelength of the ligand when bound to copper ions. The intensity of the signal would indicate the concentration of copper detected. The problem with this method of detection and diagnosis however, is that the copper detected is present in samples of blood and serum, making it difficult to get an accurate measurement of the fluorescent signal, due to the intense colour and viscosity of the sample. This is where the functionality of the MIA and MNPs is essential. The MIAs are used to bind and coat the MNPs and the fluorescently active copper-binding molecule is attached to the cysteine-tagged MIA through a disulphide bond. After incubation of the complex in a sample of blood or serum MNPs can be magnetically extracted from the sample, with the copper ions bound, concentrating the sample and thus the signal, allowing for easier and more accurate detection of copper ion levels.

The synthetic route for the production of the fluorescently-active dye is shown in figure 54. After each stage of the reaction the product was isolated and analysed using gas chromatography (GC). The molecular weight of the product was calculated using the retention time and this was compared to the predicted time and therefore MW of the desired product. Conclusive results were obtained for steps 1-4, however the final step proved problematic. Steps 4 and 5 were reversed but the final product could still not be produced in the time-scale allowed. The synthesis was thought to be simple, however it ended up being non-trivial. This would have been a useful project to test the attachment of the MIAs to clinically-relevant molecules, however the initial synthesis of the dye should be performed by a synthetic organic chemist.

4.4 Attachment via a maleimide linker

Although formation of intermolecular disulphide interactions has been shown through dimerisation of the cysteine tagged MIAs, the formation of this redox active link proved difficult for other molecules. Another common form of attachment via the thiol group of the cysteine sidechain uses a maleimide interaction. The maleimide functional group interacts specifically with sulfhydryl groups, such as the sidechain of cysteine, this reaction occurs at around neutral pH (pH= 6.5-7.5) therefore making it an ideal reaction to use as the MIAs are stable when stored in water or PBS. The reaction can be quenched at a higher pH, promoting the hydrolysis of the maleimide group. Another favourable feature of the reaction is that a TCEP reducing agent (shown to be successful in reducing the link between the MIA dimers) does not have to be excluded as the maleimide is not sensitive to it. A further advantage of using the maleimide linkage is that unlike disulphide bridges, the reaction is irreducible.

A fluorescent dye was attached via the C-terminal cysteine. The dye chosen for this function was the DyLight 650 Maleimide (Thermo Fisher Scientific), which had a useful Ex/Em of 652/672 nm. The dye gives impressive far-red fluorescence and has high water solubility enabling a good dye-protein ratio in protein samples stored in water. The labelling reaction occurs through the interaction between the reduced sulfhydryl group of the cysteine and the maleimide-activated dye, producing a stable thioether bond between the species (figure 56).

The extent of fluorescent labelling was measured using a number of different methods: UV/Vis spectroscopy; SDS-PAGE; MS; fluorescent spectroscopy/fluorescent microscopy. Firstly, UV/Vis spectroscopy was used to give an indication of the success of the labelling; giving the percentage of protein labelled using the maximum absorbance of the sample at 655 nm. The calculation used is shown below:

$$nDye\ nProtein^{-1} = \frac{A_{max}655\ nm\ \times\ dilution\ factor}{\varepsilon_{fluor}\ (M^{-1}\ cm^{-1}) \times\ protein\ conc\ (M)}$$

The dilution factor used for each labelling reaction was 2 (diluted in PBS); the protein concentration used was 50 μM; the molar extinction coefficient for the DyLight 650 maleimide dye was 2.5 x 10^5 M^{-1} cm^{-1}. An average measurement of A_{max} at 655 nm for $A3_{fluoro}$ and $E8_{fluoro}$ respectively was 2.7 and 5.5 resulting in the number of moles of dye per mole of protein calculated as: $A3_{fluoro}$ = 0.43 and $E8_{fluoro}$ = 0.88. There is only one available cysteine residue (reactive sulfhydryl group) per protein and therefore values of 0.43 and 0.88 correspond to 43 % and 88 % labelled sample. SDS-PAGE and MS analysis were used to confirm this calculation. Two labelling reactions were run in parallel to determine the method for optimum labelling. The first reaction was performed in the presence of TCEP and the second without (all reducing agent was removed prior to the reaction by dialysis). SDS-PAGE was used to compare the products obtained for each of the reactions (figure 55). Lane 1 contained the phage ruler, lanes 2-4 contained $A3_{fluoro}$ that had been fluorescently tagged and incubated with TCEP. Lane 5 contained $A3_{fluoro}$ where no additional TCEP was added to the labelling reaction mixture. Lanes 6-8 show $E8_{fluoro}$ incubated with DyLight 650 in the presence of TCEP and finally lane 9 shows $E8_{fluoro}$ with no additional TCEP added. Two intense bands for each of the wells containing fluorescently tagged MIA with the addition of the TCEP reducing agent were observed on the gel, the lower band around 12 kDa, the expected MW for A3C and E8C; the upper band around 13 kDa, the expected molecular weight for the $A3_{fluoro}$ and $E8_{fluoro}$ complexes. This suggest the labelling reaction produced the desired fluorescently tagged MIA complex to some extent, however

the intensities of the bands observed on the gel suggest a lower percentage of labelled sampled compared to the UV/Vis measurements and calculation. Also, the upper band around 13 kDa for $A3_{fluoro}$ and $E8_{fluoro}$ is much less intense when TCEP was not used as a reducing reagent as the labelling reaction was run and there was a much more intense band around 25 kDa due to the likely formation of MIA dimers. This suggests that in the absence of a reducing agent, the formation of disulphide bonds between the cysteine residues of the MIAs is more favourable than the formation of a thioester bond between the cysteine and maleimide activated dye. It may be possible to move the equilibrium towards thioester formation if a higher excess of dye was added to the reaction, however, the dye is relatively expensive and increasing the concentration required for labelling the MIA is not desirable.

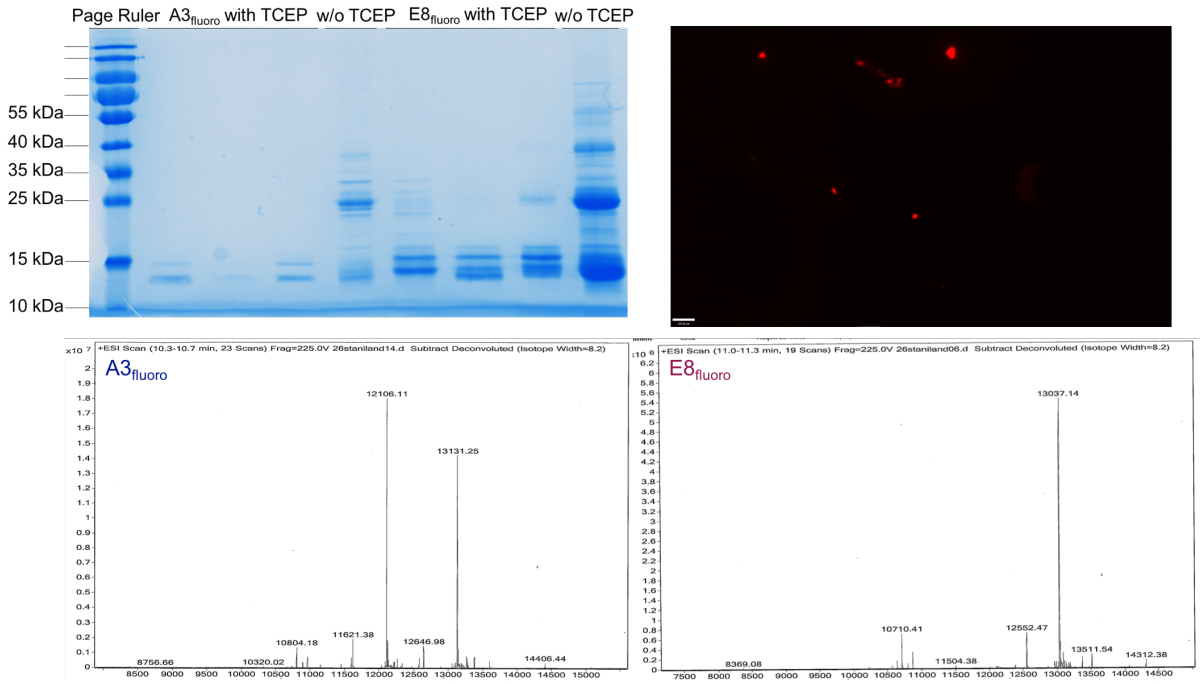

Sample	M^+	Predicted M^+ with DyLight tag	Observed M^+	UV-Vis Tagged sample (%)	Mass Spec Tagged sample (%)
A3C	12105	13197	12106; 13131	43	45
E8C	12011	13102	13037	88	95

Figure 55 Analysis of DyLight 650-tagged MIA A3C and E8C. Data collected using SDS-PAGE (top left), fluorescent microscopy (top right) and mass spectrometry (middle). Fluorescently-tagged MNPs in 1 x PBS buffer were analysed by fluorescent microscopy using a 633/647 nm laser line and Cy5 common filter set. ES-MS was used to confirm the extent of successful labelling of the MIA samples. The proteins were analysed in PBS buffer. $A3_{fluoro}$ labelled sample was calculated to be 45 %; for $E8_{fluoro}$ the value was calculated as 95 %

ES-MS was used to confirm the extent of successful labelling of the MIA samples. The resultant spectra are shown in figure 55. Using the intensities of the peaks, the calculated percent of sample labelled closely matched the calculated percentage using the UV/Vis calculation above. For $A3_{fluoro}$, using the data collected using mass spectrometry, the proportion on labelled sample was calculated to be 45 %; for $E8_{fluoro}$ the value was calculated as 95 %. It is possible these results varied when using SDS-PAGE as the dye may have been degraded by the harsh conditions used in the gel, however this has not been confirmed. Also, interestingly, the observed peaks for the fluorescently labelled MIAs vary slightly compared to the predicted m/z of the complexes. It is clear that the sample has been labelled as the values are around that expected for the addition of the dye and the errors calculated for both A3C and E8C samples were the same, each peak was 65 Da smaller than predicted from the labelling (see table, figure 55). This may be due to the dye having a slightly MS. However, no additional peaks at m/z = 65 appeared on the spectrum.

Finally, to test that a fluorescent signal was measureable for the DyLight 650-tagged MIAs, NPs coated in $E8_{fluoro}$ were analysed using fluorescent microscopy. A fluorescent signal on a black background should be observed, indicating the attachment of a fluorophore to the MNP (linked via the MIA). Due to extensive wash steps, no unbound fluorophore was present in the sample (this was confirmed in a control reaction). An image from this analysis is shown in figure 55 above. The fluorescently-tagged MNPs were analysed by fluorescent microscopy using a 633/647 nm laser line and Cy5 common filter set. The DyLight 650 dye can be used as an alternative to the Cy5 fluorescent dye, which is also a far-red-fluorescent dye and exhibits comparable performance. Figure 55 shows the detection of the fluorophore on the NPs. There were problems with fixing the particles directly to the sample slide and aggregation of the particles during the drying/fixing steps, resulting in only a select number of NP aggregates being observed by the microscope. This characterisation technique was used as an initial proof of principle and successfully showed that the fluorescently tagged MIAs had bound to the MNPs and the fluorescence was not quenched by the magnetite NPs.

4.4.1 Antibody attachment (RAGE and AP)

At Swansea University, α-RAGE, a novel biological target for ovarian cancer had been identified and was known to be over expressed in diseased tissue. Furthermore, ligands that bind this receptor are subjected to rapid internalization and membrane recycling. Antibodies that bind this cell surface receptor have been extensively studied and have been attached to MNPs for the development of targeted delivery and hyperthermia-based treatments of ovarian cancer. High expression of this receptor had been noted in a variety of human tumors including brain, breast, colon, colorectal, lung, prostate, oral squamous cell, and ovarian cancer, as well as lymphoma and melanoma. Within

ovarian cancer specifically, high expression has been detected by immunohistochemistry. The strong association between the RAGE receptor and tumor has also been identified as therapeutically relevant, and mice deficient in the target receptor were resistant to chemically-induced skin carcinogenesis.

Following verification of the association between increased target expression and ovarian cancer, and the differential expression between malignant and non-malignant tissues, Professor Steve Conlan and his group at Swansea university had undertaken extensive analysis of antibodies that target this specific receptor. Rapid internalisation and membrane recycling of bound ligands has been reported. Internalisation of binding antibodies within ovarian cancer cell lines was explored. Internalisation in as little as fifteen minutes had been observed (which is significantly faster than reported for the anti-human epidermal growth factor receptor 2 (HER2) antibody, Trastuzumab).

With the addition of a maleimide linked fluorescent dye showing that attachment via the MIA cysteine is possible through the formation of a thioether bond, the attachment using maleimide linkage to the MIA was investigated. AP and RAGE antibodies were used to test the attachment mechanism and optimise protocol. The design of the complex was independent of the antibody used and could be applied to the attachment of any antibody or protein to the cysteine labelled MIAs. Two complexes were designed (shown in figure 56): the first containing a single sulfo-SMCC linker; the second containing a cleavable dipeptide flanked by two sulfo SMCC groups. In the initial complex the sulfo-SMCC linker was attached to the MIA through the maleimide group (orange in figure 56), forming a thioether bond with the sulfhydryl group of the cysteine. The antibody would then be attached to the linker through the NHS ester group by formation of an amide bond with available lysine groups on the surface of the antibody (shown in purple in figure 56). Attachment in this orientation prevented blocking of the MIA binding site which was previously witnessed for NHS ester binding to the lysine groups. Also, it would minimise the interference with the intramolecular disulphide bonds within the antibody, preventing a change in structure which could inhibit specific binding to the complimentary receptors and antigens. A schematic of this design can be found in figure 56.

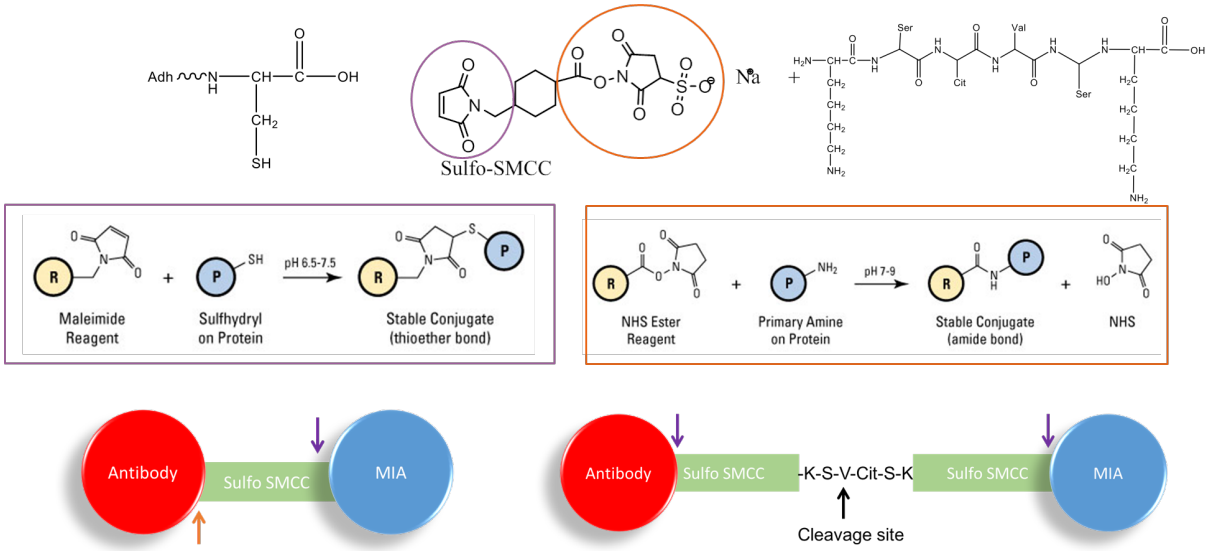

Figure 56 A schematic showing the design for the attachment of an antibody to a MIA protein using a sulfo SMCC linker group which forms a maleimide thioether bond with the sulfhydryl group of the terminal cysteine (orange) and amide bond with the primary amine groups of proteins or peptides (purple). The reaction mechanism diagrams were taken from the reagent manuals available on the ThermoScientific webpages.

The dipeptide complex was considered as it would enable selective cleavage of the MIA and therefore MNP from the antibody if required, giving a degree of flexibility to the applications the complex could be used for. The Val-Cit dipeptide site sits at the centre of the complex and is cleavable using Cathepsin B enzymatic cleavage. The peptide was designed and ordered from ThermoScientific. The serine groups of the peptide act as a small spacer between the lysine and Vit-Cit, minimising steric bulk at the dipeptide region, aiding accessibility of the protease. The lysine residues flanking the peptide were used to attach the sulfo-SMCC linkers through the NHS ester group, forming an amide bond between the primary amine of the lysine sidechain and the NHS ester of the linker. The maleimide group was then used to form a thioether bond between the linker and the cysteine sidechain of the MIA and available sidechains on the antibody. See figure 56 for a schematic of the designed complex.

For the attachment of the sulfo-SMCC maleimide groups to the sulfhydyl groups on the antibody, 2-Mercaptoethylamine.HCl (2-MEA) was used to reduce any disulphide bonds. 2-MEA is a mild reducing agent, selectively reducing disulphide bridges present in hinge regions of IgG heavy chains. This method of IgG antibody reduction leaves intact essential intramolecular disulphide bonds and generates two functional half-antibodies with surface sulfhydryl groups accessible for labelling.

Binding of the dipeptide complex (MIA-x-pep-x-AB) was analysed using MS. The desired complex consisted of the peptide (KSVCitSK) flanked by two sulfo-SMCC groups which were then linked to the

MIA and antibody. As it is difficult to observe the antibody using MS due to extensive fragmentation and large size, only data for the formation of the initial linker is shown (figure 57). The spectrum showed that the most intense peak was for the unbound sulfo-SMCC with m/z = 431, this was predicted as the cross-linker was added in excess to the peptide. There were also two other major peaks observed with m/z equal to 1142 and 1556; these peaks correspond to the predicted peak position of the dipeptide fused to a single sulfo-SMCC group and the dipeptide flanked by two sulfo-SMCC groups respectively. This indicated that a longer reaction time was required, however any unreacted product could be removed using size-exclusion chromatography before use.

Compound	Predicted m/z peak	Observed m/z peak
Dipeptide (KSVCitSK)	706	-
Dipeptide + Sulfo-SMCC	1137	1142
Dipeptide + 2 x Sulfo-SMCC	1550	1556

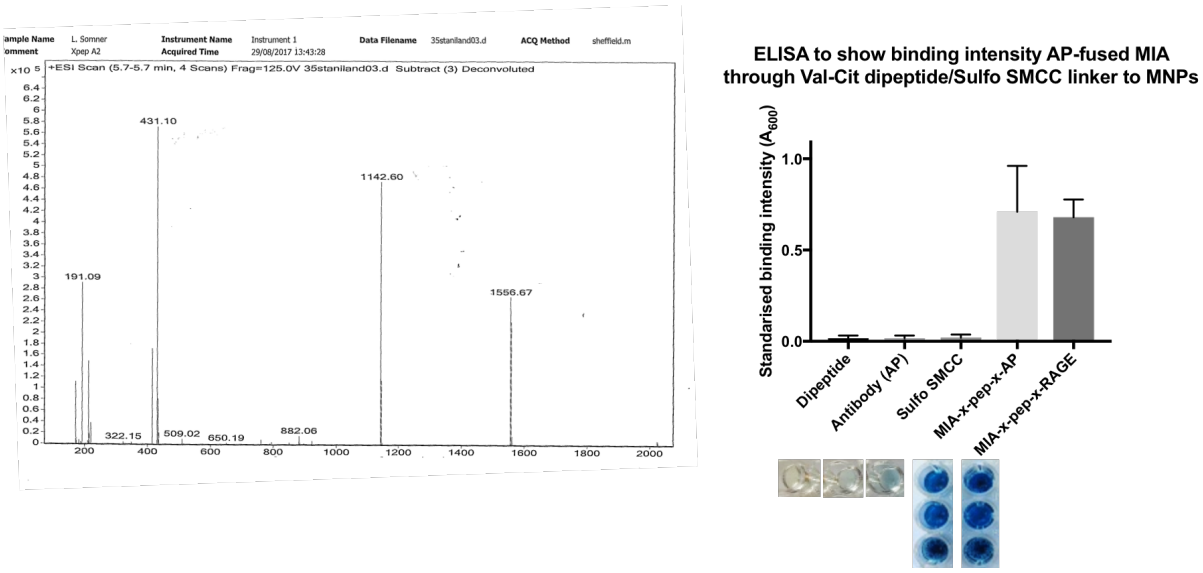

Figure 57 Analysis of the formation of the dipeptide linker for antibody attachment to the MIA protein. Results show the mass spectrum of the dipeptide binding Sulfo SMCC (left) and an ELISA showing the binding of the complex to MNPs (right). Multiple peaks on the ES-MS plot shows that it is difficult to control the reaction. In the ELISA the blue colour of the reaction wells indicate a strong binding reaction. A colourless or yellow solution in the well suggests no or little binding of the ligand. ELISA measurements were normalised. Maximum binding was made equal to 1 and no binding equal to 0.

With MS confirming the successful formation of the linker group, this linker could then be incubated with MIA and antibody. As both groups were attached to the linker through the formation of a thioether bond resulting in the reaction between reduced cysteine residues and a maleimide group, it was difficult to control the reaction. An excess of linker and cysteine-tagged MIA were used as it was likely the antibody contained multiple available sulfhydryl groups that would react. The formation of the final complex (MIA-x-pep-x-AB) was analysed using an ELISA (three technical repeats). The complex was allowed to bind through the MIA to MNPs; the presence of the AP antibody was then detected using a BluePhos detection reagent, resulting in a colorimetric response when the antibody was present. Negative controls applied included the dipeptide, the AP antibody and the sulfo-SMCC cross-linker, each incubated with MNPs before the washing and detection steps. There was no colour change observed for these controls (figure 57), suggesting that if a colour change to blue/purple was detected, the complete complex would be present. There was a colour change from colourless to blue observed for the MIA-x-pep-AP complex. There was also a colour change observed for the MIA-x-pep-RAGE complex; this ELISA used a secondary antibody to

specifically target the RAGE antibody. The intensity of the colour change was similar for both antibody complexes, suggesting that this could be a universal approach for attaching antibodies to MNPs.

Another complex designed and synthesised connected the cysteine-tagged MIA to the antibody directing through a sulfo-SMCC linker. This complex was non-cleavable, suiting some applications and was advantageous over the production of the complex containing the peptide linker as the synthesis could be controlled. The MIA and antibody attach to the linker through different bonds and mechanisms, therefore one bond could be formed before the other. Using the manufacturer's instructions, the amide bond between the linker and antibody was generated first, followed by the thioether between the MIA and linker. Also, as suggested previously, it did not require the reduction of intramolecular disulphide bonds in the antibody, which could affect the antibody specificity and function.

A number of different synthesis conditions were tested, including the use of varying ratios of sulfo-SMCC to MIA. A 5-fold excess of the of cross-linker to MIA was found to produce optimum results. This was analysed using an ELISA to test the binding intensity of the MIA-x-AP complex to MNPs (three technical repeats). The greatest binding intensity was observed using a 5-fold excess of sulfo-SMCC during synthesis. The plot of the measured binding intensities is shown in figure 58 below. The complex was also analysed using western blot with a Strep-II tag specific antibody. A3C, sulfo-SMCC and MIA-x-RAGE were run on a SDS-containing gel. The bands of the gel were then transferred to a nitrocellulose membrane, which was treated with Strep-II specific, HRP-conjugated antibody. A band for unbound A3C can be seen in lane 1, figure 58; there are no bands present in the lanes containing only cross-linker; bands in lanes 5 and 6 show a dramatic increase in estimated molecular weight. These lanes contained the MIA-x-RAGE complex and therefore the blot suggests that the RAGE antibody has been successfully attached to the cysteine tagged MIA, through the sulfo-SMCC cross-linker.

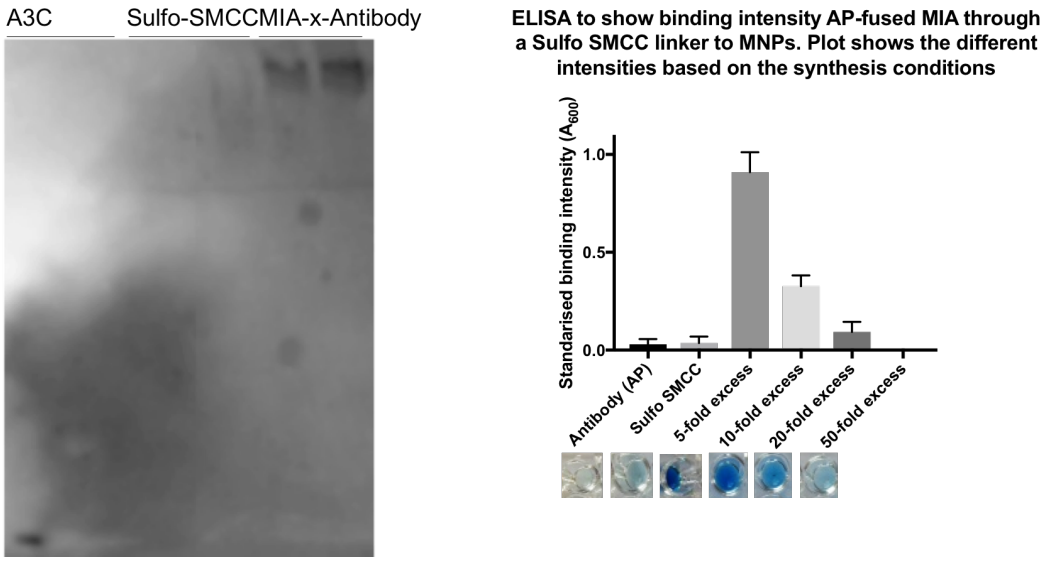

Figure 58 Western blot looking at Strep-II tag detection: lane 1 and 2 is the MIA; lane 3 and 4 is sulfo-SMCC; lane 5 and 6 is the Sulfo-SMCC linked MIA and antibody. A band for unbound A3C can be seen in lane 1, no bands present in the lanes containing only cross-linker and lanes 5 and 6 show a dramatic increase in estimated molecular weight. The ELISA data shows the binding of the complex to MNPs. A strong blue colour in the well suggests an intense binding interaction, therefore a more intese peak for binding intensity. The 5-fold excess shows the most promising binding interaction.

This complex, consisting of A3C, fused to an α-RAGE antibody via a Sulfo-SMCC cross-linker was taken further to assess the capability of the complex to be used *in vivo* for biomedically useful applications.

4.5 RAGE antibody attachment for biomedical applications

Attaching magnets to the RAGE antibody, known to target specific cancers, is beneficial for a couple of reasons. Firstly, the MNPs can further enhance targeting, using an external magnetic field to produce a magnetic gradient within the body. Secondly, MNPs can act as a drug. The MNPs can act as localised sources of heat following exposure to an AMF. This heating can result in specific cell death. With the MNPs attached to the antibody, uptake and cytotoxicity experiments were conducted. The antibody has been shown to target the receptor of interest but examples in the literature suggest it may be possible to enhance this targeting through the action of external magnetic fields. Finally, the effects of induced magnetic hyperthermia on the cells was investigated. Once the NPs and antibody were internalised within the cancer cell line, the aim was to subject the cells to an AMF, flipping MNPs or electron spins and causing the particles to heat, this was done with the aim of heating and killing cancer cells. As the tagged NPs should preferentially be taken up by diseased cells (due to antibody and magnetic targeting) healthy cells should be mostly unaffected.

4.5.1 Analysis of the ability of the antibody complex to bind the MNPs

For this specific study, the magnetite NPs were assumed to act as the 'drug' region of the complex as the aim was to use the NPs to heat surrounding tissue by employing hyperthermia-based treatments. The complex synthesised could therefore be likened to an antibody-drug conjugate (ADC). Vast amounts of research have been conducted into the use of ADCs as an alternative treatment for cancer. They offer targeted therapies based on novel drug systems to prevent the life-limiting side effects of commonly used cancer therapies such as radiotherapy and chemotherapy. Before this novel ADC could be tested using mammalian cell cultures, the binding of the antibody linked MIA to the magnetite NPs needed to be confirmed. The antibody is much larger than the MIA, so analysis was required to ensure that binding ability of the MIAs to the NPs was not compromised. MNPs with an average diameter of 5 nm were used to study the biomedical implications of the ADC as smaller NPs should be taken up more easily by the cell. Visualisation of the NPs using TEM and analysis of their diameter is shown in figure 59. The image does show a small amount of impurity present in the sample; however, this small amount was not expected to cause any problems as it is unlikely to be magnetic and will therefore be removed by magnetic extraction.

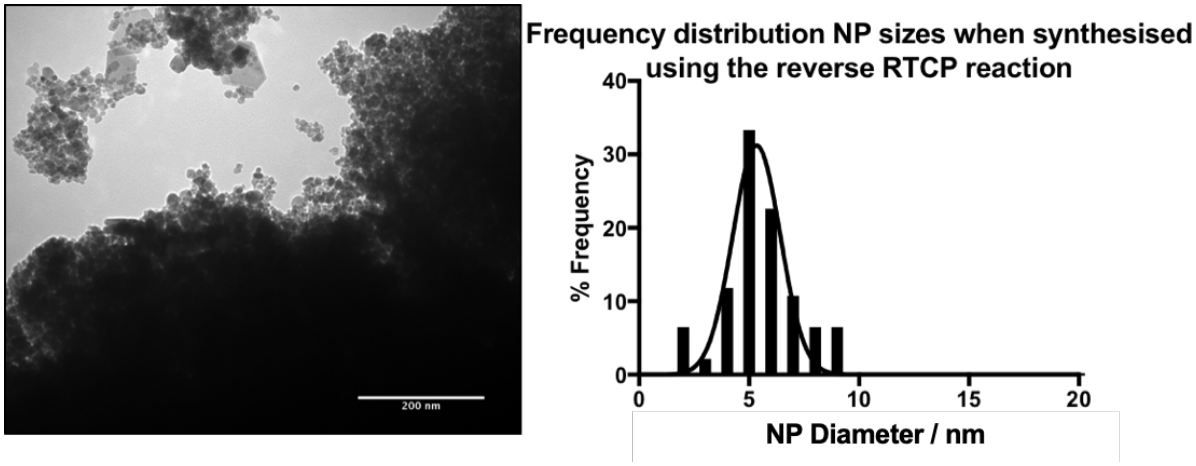

Figure 59 TEM image and grainsize analysis of the magnetite NPs used to attach the antibody. Average NP diameter was 5.58 nm ± 3.13 nm calculated using a frequency distribution plot created in GraphPad Prism. The NPs were synthesised using the reverse RTCP reaction with no protein additives. TEM images were captured using the Technai microscope and drying the NPs on to carbon coated copper TEM grids. 100+ particles were measured for each independent repeat – each repeat yielded statistically similar frequency distributions.

A binding ELISA was used to test the binding strength of the MIAs to the MNPs for the generation of the new ADC. Two independent ELISAs were performed. The first was an ELISA on the MNPs and the second was an ELISA on streptavidin coated plates. The HRP-conjugated antibody targeted the RAGE antibody that had been bound to the MIA, oxidation of the detection reagent by the HRP then produced a colorimetric response when the RAGE antibody was present. The ELISA on the

streptavidin coated plates was essential to show that the RAGE antibody was bound exclusively via the MIA. The biotin-labelled MIA was confirmed to bind directly to the plate, whereas the RAGE antibody alone did not bind to the plate. Therefore, for a positive binding result, the MIA must be present to bind to the plate and the RAGE antibody must be of been present in order to bind the HRP-conjugated antibody for detection. The results from this ELISA can be seen in figure 60. The plot suggests that a minimal binding response was observed for the NPs, MIA or RAGE antibody alone, however when the ADC was analysed substantial binding was detected (figure 60, ADC labelled 'RAGE-MIA'). The binding intensity was normalised in order to compare the results from the MNPs and Strep plates. Figure 60 shows images of the three technical repeats from a single independent repeat.

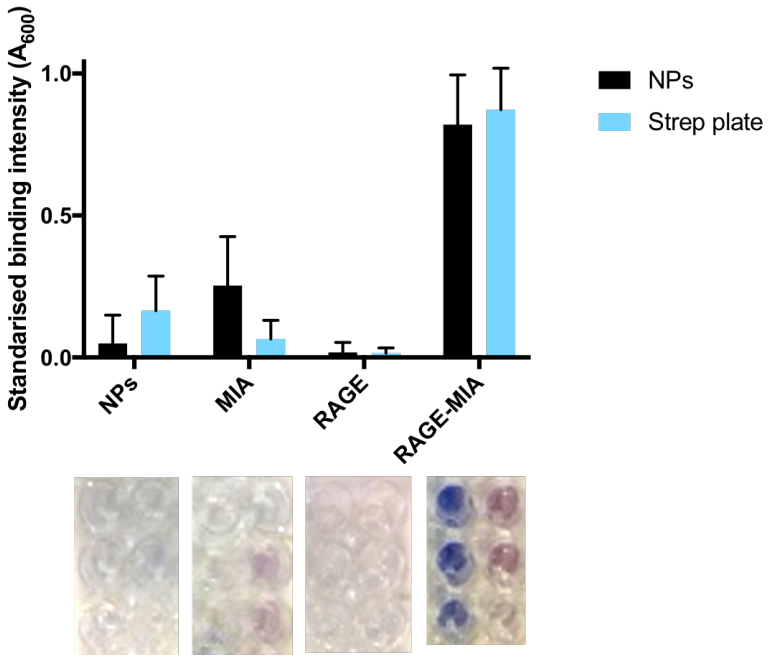

Figure 60 ELISA showing the binding of the MIA-RAGE complex to Strep-plate (cyan) and to magnetite NPs (black). Binding intensities resulting from detection using HRP-conjugated anti-mouse IgG and absorbance at 600 nm. An intense blue colour in the reaction wells indicated a strong binding reaction. This lead to an increased binding intensity peak, plot in GraphPad Prism. As expected the most intense binding interaction occurred for the RAGE-MIA complex in 1 x PBS buffer (independent of other whether MNPs or the Strep-plate were used as the stationary binding phase).

Once it had been confirmed that the RAGE had bound directly to the MIA the ELISA was performed on the MNPs. The same HRP-conjugated antibody was used for detection of binding. No binding colour change was observed for the NPs or RAGE antibody alone however binding was apparent for the RAGE-MIA ADC. Analysis of the ELISA assays confirmed that the RAGE-antibody was bound to the MIA via the sulfo-SMCC linker (as suggested by the western blot analysis discussed and shown in figure 58). It also showed that the RAGE antibody bound MIA was still able to form strong

interactions with the magnetite NPs and that a steric clash arising from the bulky antibody did not inhibit binding.

4.5.2 Assessing the uptake of the NPs

A SKOV-3 cell line was used to analyse the uptake of the ADC. This cell line is a human ovarian cancer cell line that is known to overexpress RAGE antigens on the cell surface. The display of the antigens on the cell enables analysis of the possible targeted uptake of the RAGE ADC compared to MNPs that are not conjugated to the antibody.

Visualisation and quantification of MNP uptake by cells is required to gain a better understanding of NP behaviour in biological systems and more than this, analyse the safety of the uptake for clinical therapies or diagnostics. Electron microscopy-based techniques can be acquired for this process, specifically scanning electron microscopy (SEM). SEM enables imaging of the cell and NPs at high resolution, it was chosen oven TEM for this application as although both techniques have similar resolution, SEM has the advantage that ultrathin sectioning is not required (unlike in TEM).

SKOV-3 cells were trypsinised at 70% confluency and reseeded on sterile silicon wafers, then placed in a 6-well plate. The cells were left to grow before incubation with the ADC for 2 days. The treated cells were fixed on silicon wafers using glutaraldehyde attachment. Before analysing the samples on the SEM, the cells were dehydrated using a series of ethanol washes. Images were acquired using the Hitachi S4800 scanning electron microscope with energy dispersive x-ray spectroscopy (EDX) capabilities for composition mapping.

The SEM images of the cells treated with the ADC are shown in figure 61. The images show the successful uptake of the magnetite NPs into the cells, with the majority of the particles aggregating around the cell nucleus. As the image is in 2D it is difficult to determine whether the NPs images were on top of the nucleus are sitting on top, of whether they had entered the nucleus. The location of the NPs show promise for the use of the ADC for hyperthermia-based therapies as if the particles are close to the nucleus heating will cause rapid and extensive cell death.

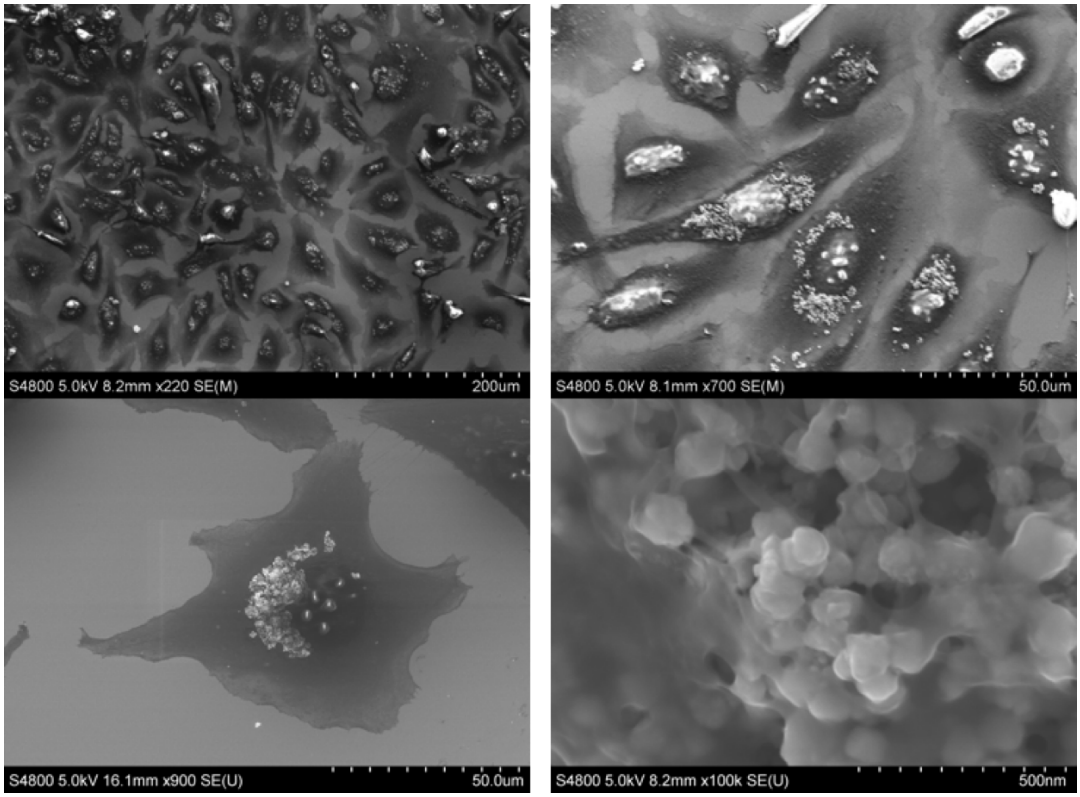

Figure 61 SEM images showing the uptake of magnetite nanoparticles into SKOV-3 cells. Images A to D increase in magnification (A = 220X, B = 700X, C = 900X and D = 100k X). Cells treated with 100 μg/mL of RAGE-coated NPs were fixed to silicon wafers using glutaraldehyde in PBS.

Figure 61 shows the cells and NPs with no coating. A 5 nm chromium coating was also applied to the sample. Upon the application of the coating, the NPs were masked from the electron beam, confirming that the NPs were located inside the cell and were not just bound to the cell surface.

The EDX capabilities of the microscope were utilised to confirm the species within the cells were the iron oxide NPs that the cells had been incubated with. The resultant spectra and an SEM image showing the location tested within the cell is shown in figure 62 below. The top image shows the EDX spectra of the cell cytoplasm where no NPs are visible. As predicted there is no iron present with the most intense peak corresponding to Silicon (SiKα 1.74 keV) originating from the silicon wafer. However, the bottom spectrum was obtained from a region that looked dense in MNPs; substantial amounts of iron and oxygen (FeLα 0.71 and OKα 0.53 keV) were measured at this point and the silicon peak has disappeared. This is due to the NPs blocking the beam, therefore it can no longer reach the wafer to detect the silicon.

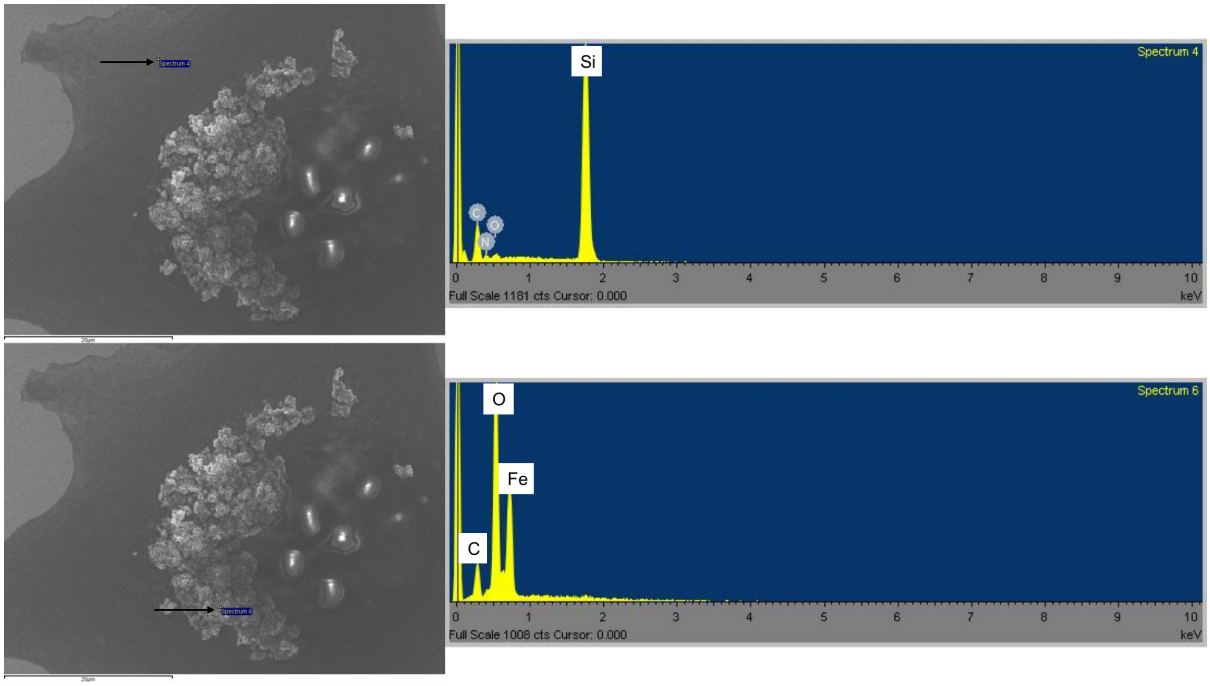

Figure 62 SEM images and subsequent EDX spectra to show the NPs inside the cell consist of iron oxide. The top image gives an EDX spectrum of the components believed to be the cell cytoplasm (no substantial iron concentration is measured). The bottom image shows the EDX spectra of the nanoparticles with a substantial iron concentration measured and no or minimal silicon is detected (beam hits iron containing NPs, blocking Si wafer). SKOV-3 cells treated with 100 μg/mL of RAGE-coated NPs and fixed to Si wafers using glutaraldehyde in PBS.

Although the uptake of the MNPs can be confirmed using SEM, it is not a useful technique to study the route used by the cell to encapsulate the NPs. There are two common routes that MNPs are taken up by cells. The first is passive diffusion. With NPs 5 nm or smaller it has been shown that passive diffusion through the cell membrane can result in the uptake of the NPs from outside the cell to inside the cytosol.[146] Passive transport is dependent on the temperature of the sample (at temperatures below 37 °C the cell membrane can become rigid, preventing diffusion of molecules/particles). As no invagination of the cell membrane is apparent, this route of entry in to the cell could be a possibility. A more likely route is entry via endocytosis. Endocytosis is the route adopted most often by cells to transport species into the cell. During this process, the NPs are engulfed in membrane invaginations which eventually come away from the cell membrane forming internal vesicles. These vesicles are then sorted and trafficked to the appropriate cell compartment. Although membrane invaginations cannot be seen on the SEM, this may be due to the timescale allowed for the ADCs to be taken up by the cells. When the cells were prepared for electron microscopy the process of cellular uptake may have been completed and the NPs already sorted in the cell – positioning them near the nucleus. This may be a likely explanation of the cell uptake process of the ADC by the SKOV-3 cells as reports from the literature suggest a RAGE-mediated endocytosis process has already been discovered. RAGE has been shown to aid the extracellular Aβ translocation into intracellular space in AD and age-related macular degeneration.[147]

It is also difficult to confirm using SEM and EDX analysis whether the NPs taken up by the cell remain part of the ADC or if the washing and dehydration steps required for sample preparation disrupt the interactions between the MIA, antibody and NP. With carbon and oxygen observed in the EDX spectrum, some organic species may be attached to the NPs, however these peaks could also arise from detection of the dehydrated cell. To establish whether the proteins were still bound further uptake analysis was needed. An InCell assay and confocal microscopy were adopted to confirm the ADC was still intact. The fluorescent signal measured, alongside visualisation of the MNPs using EM were able to confirm the presence of the full construct. The ADCs were subjected to similar washing conditions and UV sterilisation prior the analysis. Two fluorescent signals were expected. Firstly, a signal corresponding to the DAPI (4', 6-diamidino-2-phenylindole) stain and showing the presence of the cell nucleus. Secondly, a FITC (fluorescein) stain of the labelled MIA ADC.

SKOV-3 cells were fixed (using IPA) in a 12-well plate, with each well containing roughly 50 x 10^3 cells. The cells had been treated with varying concentrations of FITC-tagged ADC. The cells were then stained with DAPI; a nuclear counterstain commonly used in fluorescence microscopy. The excitation maxima/emission maxima (Ex/Em) was 350/470 nm, these spectral properties make it an ideal stain to use with green fluorophores such as FITC. The FITC fluorophore fused to the MIA of the ADC was chosen due to its good water solubility and high absorptivity. The Ex/Em of the stain was 490/525 nm.

For the InCell assay 42 randomised fields for each well were measured using bright field detection of the DAPI and FITC stains. Two independent repeats were performed – the images obtained from one set of data are shown in figure 63 and 64. The first set of measurements shown in the top left image of figure 63 correspond to the negative control. In this control, no ADC was added to the cells therefore no FITC (green) stain should be visible – only DAPI (blue). The results were as predicted, and a useful number of cells were visualised in the negative control. ADC to final concentrations of 25, 50 and 100 μg mL^{-1} were incubated with the cells in the remaining wells. Promising levels of uptake were apparent from the fluorescent images for each of the concentrations. However, as the ADC concentration increased towards 100 μg mL^{-1} (bottom right image in figure 63) large areas of green stain become apparent on the images, suggesting increased aggregation of the NPs at high concentrations. Therefore, for future work ADC concentrations of 25 to 50 μg mL^{-1} would be optimum. The images obtained from the InCell assay are also in good agreement with the SEM images, indicating that the complex is able to enter the cell and are located in close proximity to the

cell nucleus. The majority of the green FITC dots appear to be next to or on top of the blue DAPI spheres. Successful visualisation of the FITC stain that is attached via the MIA of the ADC suggests that the complex is still complete.

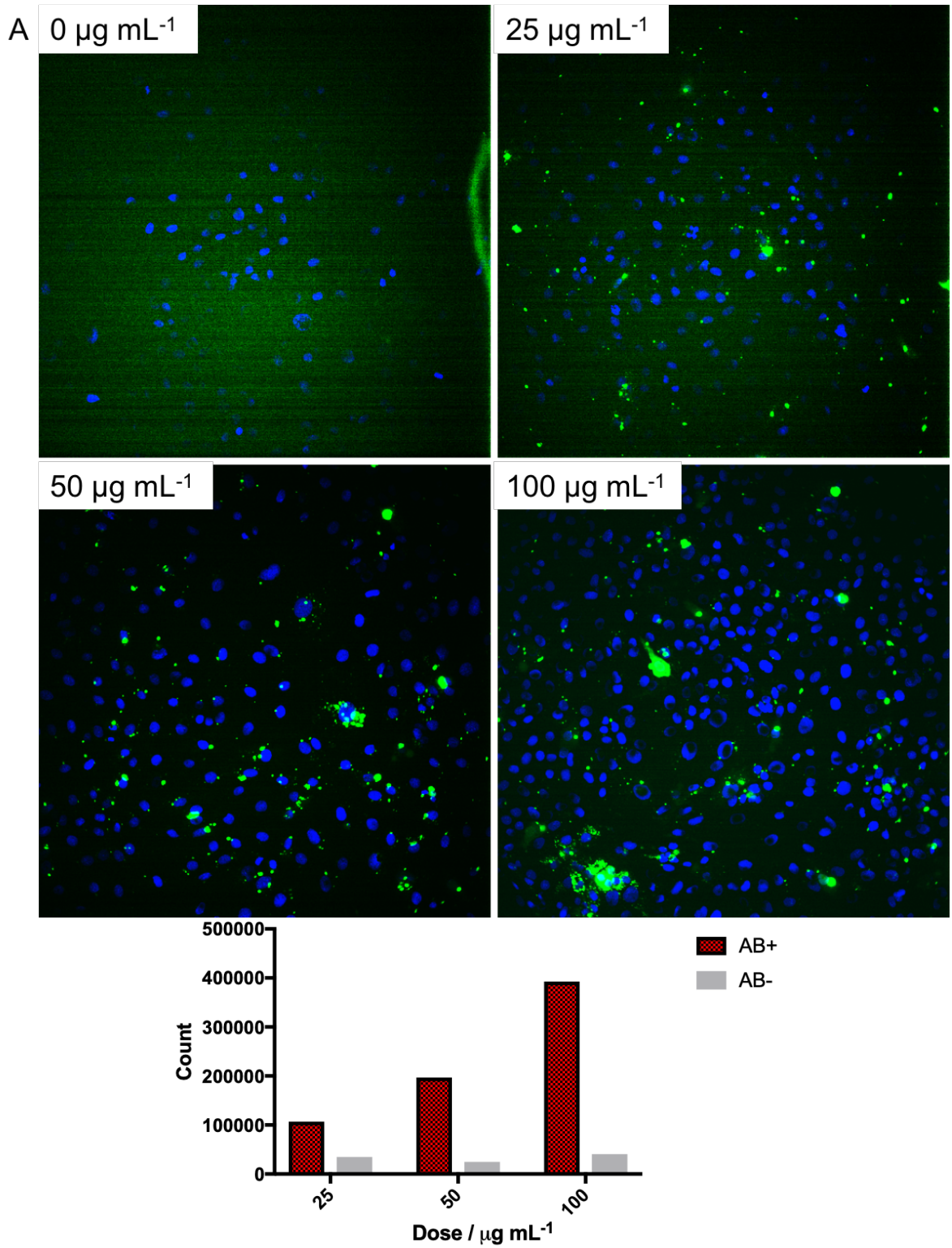

Figure 63 IN CELL images of the FITC tagged NP-RAGE complex, showing the uptake of magnetite NPs with (red on graph)and without (grey on graph) RAGE antibody conjugate after 24 hours. A is the negative control, cells containing no nanoparticles. Image B shows the uptake of the nanoparticle-RAGE complex, tagged with FITC, at 25 µg mL^{-1}. Image C shows the uptake of the nanoparticle-RAGE complex, tagged with FITC, at 50 µg mL^{-1}. Image C shows the uptake of NP-RAGE complex tagged with FITC, at 100 µg mL^{-1}. 2D images captured using the In-Cell Analyser 2000, scanning 42 random fields at 20X magnification. Cells were incubated in growth media before being fixed to the plate using PFA. The samples were imaged in PBS buffer. Below shows analysis of the InCell assay providing the number of NPs taken up by the cells 24

hours after treatment (count) at doses of 25, 50 and 100 μg mL^{-1}. Red bars represent sample with the RAGE antibody present and the grey bars represent with the antibody is not present (NPs conjugated to FITC fluorophore)

The images shown in figure 63 are for the complete ADC complex containing the MNP, MIA, sulfo-SMCC linker and RAGE antibody. The assay was performed to analyse the uptake of the MNPs into the cell when the antibody was not present. The same number of SKOV-3 cells were fixed in a 12-well plate, however, this time they were incubated with FITC-fused-MIA-coated magnetite NPs (no linker or antibody). The images obtained appeared to mimic the negative control, with very few FITC signals being detected. Quantification of the FITC signals detected in the InCell assay is shown in the plot in figure 63. Interestingly, the low count for the complex missing the antibody and the relatively high count for when the antibody is present suggests that the RAGE antibody plays an essential role in the uptake of the MNPs by the cell. Indicating targeted uptake of the MNPs by the SKOV-3 cells, likely via receptor-mediated endocytosis; specifically, RAGE-mediated endocytosis.

One problem with the SEM and InCell data collection and analysis is that it is difficult to tell for certain whether the NPs and ADC are located inside the cell, or just bound to the cell surface. Although coating the cells during SEM analysis gave a good indication internalisation of the ADC, confocal laser scanning microscopy (CLSM) was used to clearly differentiate between the two possible locations; providing increased optical resolution and contrast compared to the InCell microscope. SKOV-3 cells that had been incubated with the ADC for 24 hours were fixed to glass side in preparation for visualisation using confocal microscopy. As for the InCell assay, the microscope was used to detect and image the DAPI nuclear stain and the FITC fluorophore fused to the ADC. However, unlike the InCell assay, CLSM provided Z-stacked images by scanning the sample and providing a 3D map of the cell. Therefore, clarifying whether the NPs were located inside the cell. An example of a Z-stacked image is provided in figure 64. These images were collected using an ADC concentration of 25 μg mL^{-1}. The data suggests that NPs are located inside the cell. As the scan of the cells is completed, green dots resulting from detection of the FITC fluorophore are only present alongside the blue DAPI nuclear stain. When the DAPI stain is no longer detected, neither is the FITC, therefore the ADC is only located in the same plane as the nucleus and therefore must have been taken up by the cell.

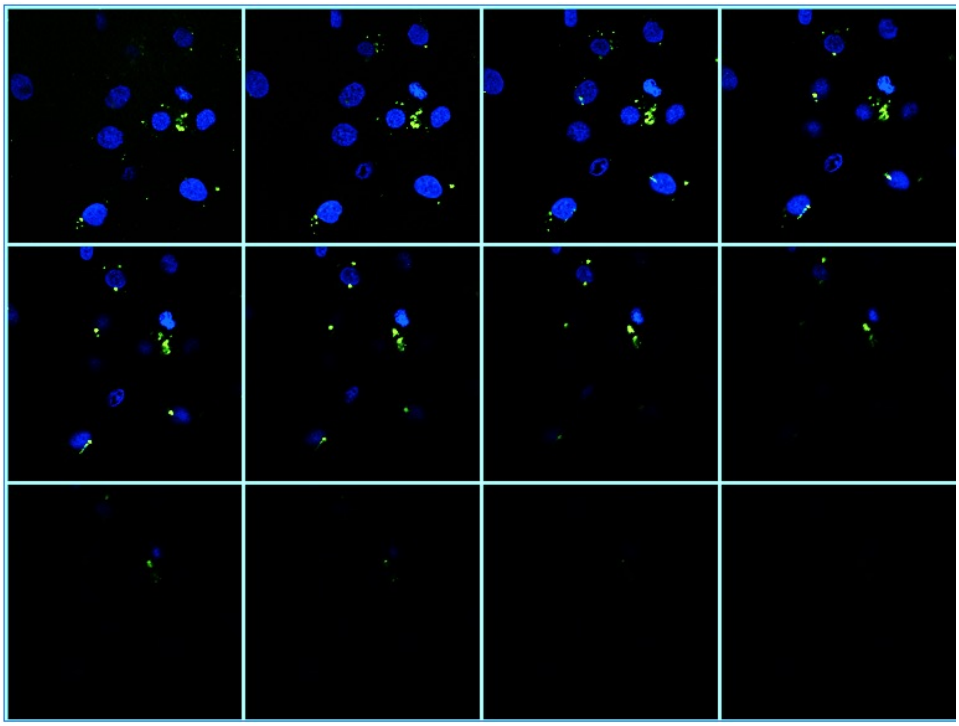

Figure 64 A montage of Z Stack confocal images for AB+ and AB- magnetite NPs. Images were taken using Zeiss LSM 710 confocal microscope with Zeiss AX10 observer ZI, HAL, HXP 120C illuminator. Z-stacking used sequential 1 µM steps. DAPI stains the nucleus and can be seen in blue, FITC is conjugated to the protein coated NPs and appears green. Cells were fixed to standard glass coverslips using PFA and mounted on to poly-L-lysine coated glass slides using cell mounting media.

4.5.3 Determination of the cytotoxicity of the complex

Following confirmation that the MNPs were being taken up successfully by the SKOV-3 cells, the effect of the cell viability needed to be assessed. If the ADC was cytotoxic to the cells, a response similar to the SAHA positive control would be expected and the cell viability would decrease dramatically over time, even at low concentrations. If the complex was not damaging to the cell, only a minimal response of cell viability to time and dose would be observed. The Promega RealTime-Glo MT Cell Viability Assay was used to monitor cell viability of a single sample, continually, for 96 hours. SKOV-3 cells were harvested and plated for a final cell density of 500 cells per well. The cells were incubated and treated with the ADC. Immediately after treatment with the nanoparticles the MT cell viability substrate and the NanoLuc© enzyme from the RealTime-Glo kit were added to the cell suspension for a final dilution of 1 in 500. The luminescent response from the wells was measured. The cell viability data was analysed using GraphPad prism to determine the dose-dependent response and the time-dependent response of the cells to the ADC. The plots are shown in figure 65 below.

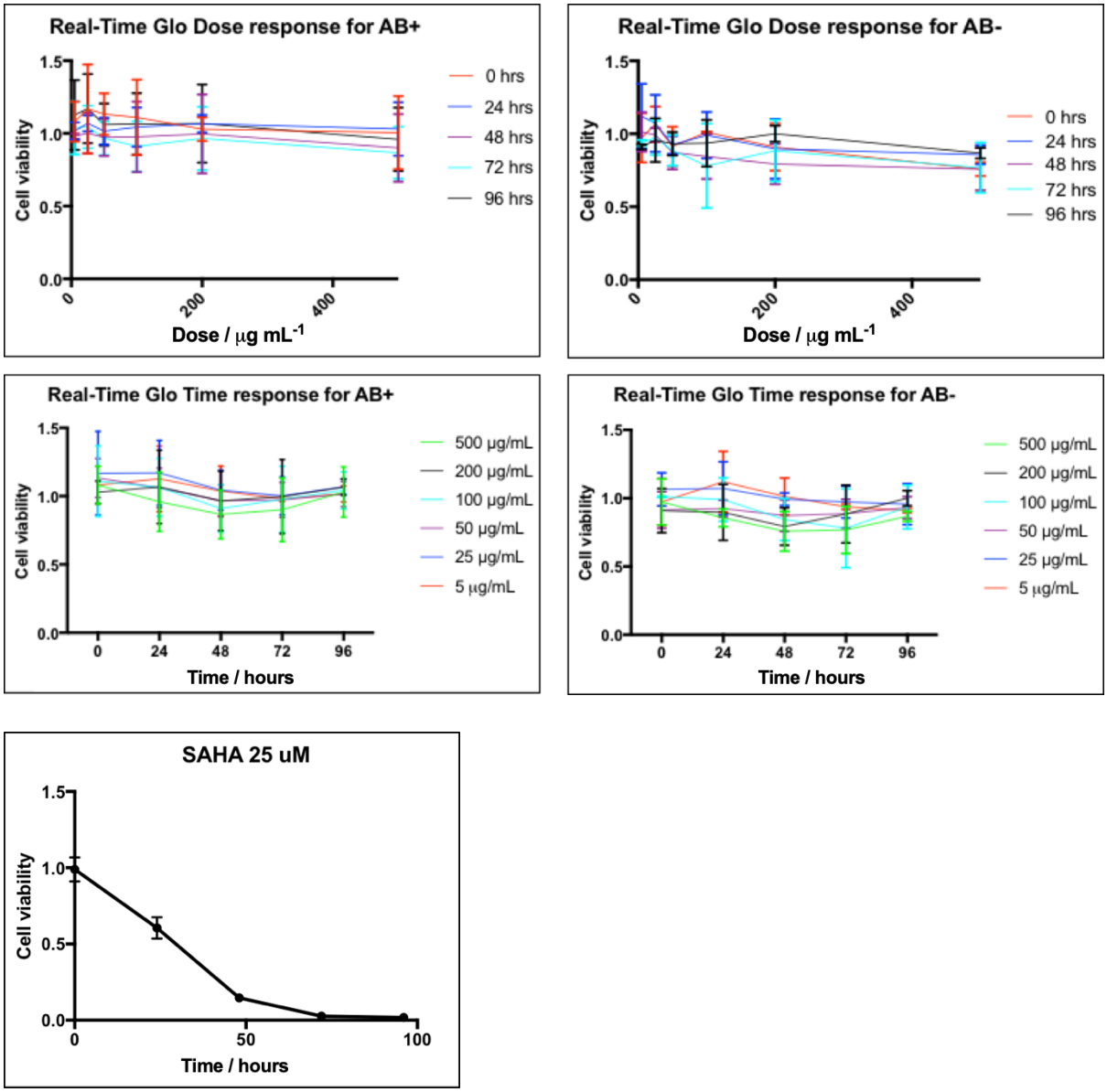

Figure 65 Real Time Glo analyses showing the effect of a high dose of magnetite nanoparticles over time on SKOV-3 cells in cell growth media, the effect of long incubation times with various doses of magnetite nanoparticles on SKOV-3 cells and a positive control showing cell death over-time after treatment with SAHA. Cells remain viable throughout the experiment with incubation times of 0 to 96 hours when treated with MNPs, unlike treatment with SAHA. Images A and B the dose response of MNPs in the presence and absence of RAGE respectively, at various time points. The presence of the antibody appears to have little effect on the cell viability under these conditions. Images C and D so the time response using realtime Glo. Image E shows the time response in the presence of SAHA.

Analysis shows the cells remain viable after exposure to high doses of ADC (doses up to 500 µg mL^{-1}). It also shows the cells remain viable throughout the experiment with incubation times of 0 to 96 hours. Between 72 and 96 hours of incubation with the ADC the cells begin to recover from the small cytotoxic effect with the cell viability data reaching the values obtained at the initial time point (within error). The ADC complex therefore does not appear to be cytotoxic to the SKOV-3 cells. This is a promising result as it means that non-targeted delivery of the ADC to non-diseased cells should

not result in cell death. Uptake by healthy cells should be reduced by the targeted drug delivery resulting from the receptor-specific RAGE antibody and magnetic translocation of the MNPs.

A positive control and negative control were also included in the cell viability assay. The negative control contained SKOV-3 cells that had not been exposed to the ADC and the positive control used SKOV-3 cells exposed to SAHA (suberoylanilide hydroxamic acid; N-hydroxy-N'-phenyl-octanediamine also known commercially as Vorinostat). The SAHA compound had previously been show by Swansea University to kill all cells when present at a 0.1 % concentration. It is a small bioactive molecule that promotes cell cycle arrest and cellular apoptosis. The non-treated cells gave similar results to the ADC treated cells throughout the RealTime-Glo assay. The cellular response on exposure to SAHA is shown in figure 65. The cell viability decreases by approximately 50 % after 24 hours of exposure to SAHA and resulted in almost 100 % cell death after 72 hours. When compared to exposure to the ADC and no cell treatment, the cell viability did not fall below 50 %, even after 72 hours of exposure.

Following from the promising cytotoxicity data reviewed to this point, the effect was further analysed in SKOV-3 spheroids. Until this point the analysis had been of 2D monolayers of cells that had been attached to T75 flasks and the wells in sample plates. Spheroid analysis was particularly relevant for the ovarian cancer cell line SKOV-3 as ovarian cancers often grow as spheroids in patients, making the 3D culture physiologically relevant.[148] The promega CellTiter-Glo® 3D Cell Viability Assay was used to determine cell viability in 3D microtissue spheroids. Pre-grown SKOV-3 spheroids were visualised under an optical microscope and then transferred into a black 96-well tissue-culture plate. The 3D spheroids were immediately treated with the ADC. The luminescent response was recorded using the BMG labtech FLUOstar Omega with an integration time of 1 second per well. Data was analysed using MARS and Reader Control Software by BMG labtech. The response was then translated into cell viability and the results were plot using GraphPad prism. The data for three technical repeats is shown in figure 66 below. To further validate the findings, additional independent repeats would be required.

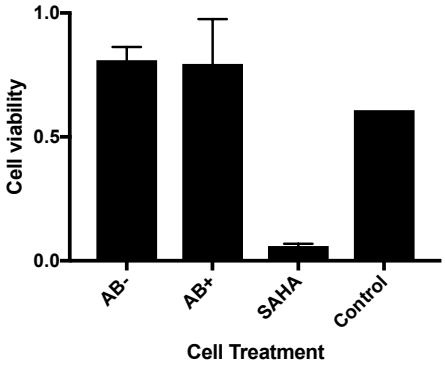

Figure 66 Cell viability analysis after treatment of SKOV-3 spheroids with AB+ and AB- NPs (500 μg mL^{-1}, after 96 hours). The cell viability of cells treated with SAHA is also shown as a positive control. Cell viability was measured using the CellTitre Glo kit. The negative control is labelled control and is the cell viability of untreated SKOV-3 cells in cell growth media.

The results obtained from the cell viability assay of the 3D SKOV-3 spheroids were similar to those calculated for the 2D cell arrays. The cell viability of the untreated (control) spheroids and the spheroids treated with the ADC and the MNP-MIA complex were similar. Suggesting no substantial cell death occurred due to incubation with the complex. As in the 2D cell arrays, the positive SAHA control produced a significant cytotoxic response by the cells.

Significant cell death was not observed for 2D monolayer cultures of SKOV-3 or for 3D microtissue spheroids of SKOV-3 suggesting uptake of the ADC did not promote a cytotoxic effect on this ovarian cancer cell line and therefore did not affect the viability of the cell for doses up to 500 μg mL^{-1} and exposure times of up to 96 hours. This is a promising result for the continued investigation into the possible use of the ADC for hyperthermia-based treatments. Hyperthermia may be beneficial in producing a heating effect of the MNPs, resulting in targeted and selective cell death.

4.5.4 Initial hyperthermia results for the MIA bound NPs

Magnetic hyperthermia tests were conducted to calculate the heating ability of the MNPs when placed in an alternating current. The AMF causes the magnetic moment of the particles to flip and the motion of this flipping results in the heating of the particle and therefore the environment around the particle. The measurements were obtained using a Nanotherics Magnetherm system, with the field strength dependent on the power and frequency supplied to the system. The sample was placed inside the coil whilst water was continually run through the coil to prevent overheating.

A range of different particle types were subjected to hyperthermia tests. The same mass of NPs, suspended in water, was used in each of the samples. MNPs were synthesised using the RTCP and samples included NPs synthesised with no protein additives (normal RTCP) and NPs synthesised with MIA E8 and MIA A3. The samples synthesised in the presence of MIA were also coated in the MIA to determine whether the coating would result in a decrease in the measured heating ability of the

MNPs. The ADC system was also analysed, with the MNPs synthesised in the presence of A3. This complex was tested, again to ensure that the presence of the organic coating did not limit the heating experienced by the MNPs when subjected to an alternating magnetic field. The results from the hyperthermia tests, using 15.1 V are shown in figure 67. The SAR and ILP values were calculated from this data and are shown in the table in figure 67.

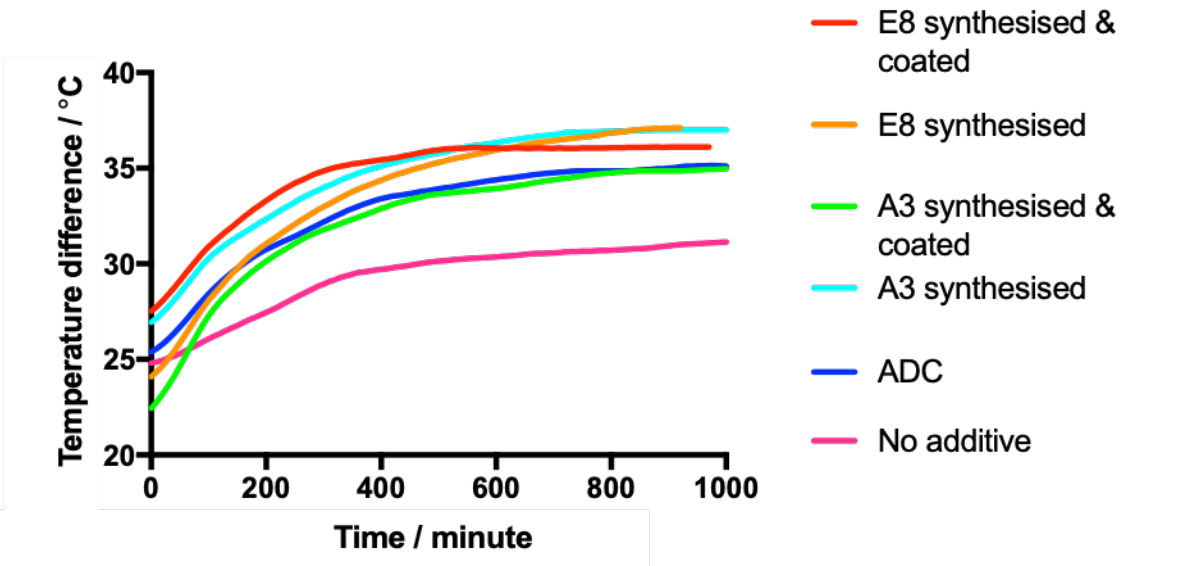

Particle type	Average SAR (W g^{-1})	Average ILP (nHm^2 kg^{-1})
E8 synthesised	28.97 ± 1.307	2.81 ± 0.127
E8 synthesised & coated	23.58 ± 0.952	2.29 ± 0.092
A3 synthesised	22.77 ± 0.715	2.21 ± 0.069
A3 synthesised & coated	22.03 ± 0.090	2.14 ± 0.009
A3 synthesised ADC	21.54 ± 0.189	2.09 ± 0.018
No additive	15.04 ± 0.598	1.46 ± 0.058

Figure 67 The resultant heating curve following hyperthermia treatment of MNPs in ultrapure water. Red indicated MNPs synthesised in the presence with MIA E8 and then recoated with MIA E8. Orange are MNPs synthesised in the presence of MIA E8, Green are MNPs synthesised and the coated with MIA A3. Light blue are MNPs coated with MIA A3. Dark blue MNPs are coated with ADC containing RAGE. Pink have not been synthesised or coated in protein (no additive). The table below shows the calculated SAR and ILP values of the MNPs.

The heating curves appear to be similar for each of the MNP samples synthesised with the addition of MIA protein. The calculated SAR and ILP values confirm this with each of the values lying between 28.97 and 21.54 W g^{-1}. There does appear to be a small decrease in heating ability when a coating is applied to the MNP. Lower values were calculated for particles synthesised and coated with E8 than for particles lacking the coating and the same is seen for A3 coated particles, however the effect is less intense. However, the decrease in values is small, and a good degree of particle heating is still observed. There is a further decrease in heating for the ADC, therefore it appears that the thicker the coating the MNP the more substantial the decrease in heating is. However, again this decrease is small, and a useful heating effect was still observed for the ADC, further suggesting that it possesses

promising properties for use in the treatment of RAGE-expressing cancers such as ovarian cancer. The lowest SAR and ILP values were calculated for the control MNPs, synthesised in the absence of the MIA additive. This was expected due to the poor quality of the particles produced in this way. The magnetic properties and therefore response to an alternating magnetic field rely on well controlled, monodisperse NPs in terms of size, shape and composition. The MNPs synthesised with MIA additives have been shown to be superior in quality compared to MNPs synthesised in the absence of the proteins.

There is some speculation over the accuracy of the data collected from hyperthermia tests. The collection of reliable data is difficult as there are numerous parameters that affect MNP heating. The main error is thought to be the transfer of heat between the sample and the surrounding environment. To obtain accurate and universal measurements the test would need to be performed under adiabatic conditions - which are difficult, if not impossible, to acquire. However, for this analysis the accuracy of the SAR and ILP values is not a significant problem as the conclusions drawn here suggest a comparison between coated and uncoated MNPs, with each of the samples measured using identical apparatus and methods.

4.6 ScFv antibody attachment for biomedical applications

ScFv (single-chain variable fragments) are active, low MW regions of antibodies which are used in preference to the full-size monoclonal antibody. These fragments are generated by creating a protein fusion between variable regions of the heavy (V_H) and light (V_L) chains. The chain regions are often connected by a short peptide region and the complete complex is then able to act as a functional antigen-binding fragment. There are numerous advantages of using scFv antibodies in place of monoclonal antibodies, including the possible production of these protein fusions using bacterial systems. Another advantage of the small size is the rapid clearance from the blood stream and shorter wait times between administration and surgery when used *in vivo* for clinical diagnoses and therapies. The scFv used in this project was shMFE-23 which was designed and acquired from Prof Kerry Chester and her group at UCL. ShMFE is a known tumour associated antigen.[149] A carcinoembryonic antigen (CEA) specific scFv. The scFv was isolated from phage display libraries for the use in radioimmunodetection and radioimmunotherapy and since its discover has been shown to successfully target colon cancer and has been used in surgery to treat colorectal cancers.[150, 151] The scFv is interesting due to its tested diagnostic and therapeutic ability. It offers promising applications for the field of biomedicine - reducing the unfavourable entropic effect associated with

the binding of the free peptide to MNPs and increasing thermal stability above 37 °C, therefore reducing thermal degradation *in vivo* compared to full molecular weight antibodies.

The aim was to attach the scFv to the MNPs by via protein fusion. The production of a protein fusion linking the scFv to a MIA peptide would be a promising start with the possibility of introducing magnetically targeted delivery of the scFv plus hyperthermia-based treatments.

4.6.1 Protein fusion design

A Gene String was designed and ordered from ThermoScientific that would be used to clone the scFv generated at UCL. Initially, the DNA sequence of green fluorescent protein (GFP) was encoded into the gene string in place of the scFv to aid the visualisation of the uptake of the complex by *E. coli*, causing positive colonies to appear green. Nhe1 and Not1 restriction sites flanked the GFP gene to enable exchange between GFP and the scFv DNA sequence using restriction digest and ligation (figure 68).

A PelB leader sequence was added to the N-terminus to enable expression in the periplasm as inclusion body formation could be a problem when cloning the scFv. The PelB sequence self-cleaves and therefore would not be present in the purified protein. A His_6 purification tag was incorporated into the DNA sequence of the gene string and was used for detection in blots and ELISAs as well as purification. It was followed by a TEV cleavage site which would allow cleavage of the His_6 tag which is required for purification but also binds to some other transition metal ions, therefore the binding strength of the His_6 tag to magnetite was investigated. This interaction could compete for MNP binding.

The DNA sequence for an AviTag was added to the designed gene string following the purification tag at the N-terminus (figure 68) to offer the possibility of using specific biotinylation (see section 4.2). If it became a problem that the AviTag was not at a terminus the TEV cleavage site would allow it to become an N-terminal tag. Therefore, fluorescent markers etc. may be incorporated via biontinyaltion. A short linker was included, acting as a spacer group to ensure that when the scFV insert replaced GFP the presence of bulky scFv near the MIA peptide would not alter the structure or sterically hinder the peptide binding. Also, it would allow the protein to protrude through any dextran coating on the NPs (currently used by UCL). Finally, as suggested, an MIA peptide (A3 binding analysed in chapter 3) is present at the C-terminus which will bind strongly and specifically to magnetite [100] facets allowing the protein to act as a coating for the MNPs and therefore

increasing the biocompatibility of the MNPs. The A3 sequence is used as this has one of the highest peptide binding strengths to magnetite and appears to be able to displace any bound DNA.

PelB leader sequence: KYLLPTAAAGLLLLAAQPAMA

His-Tag: GSSHHHHHH

TEV cleavage site: ENLYFQG

Avi-Tag: GLNDIFEAQKIEWHE

Nhe1 Site

GFP
MSKGEELFTGVVPILVELDGDVNGHKFSVSGEGTLKFICTTGKLPVPWPTLVTTFSYGVQCFSRYPDHMKQHDFFKSA
MPEGYVQERTIFFKDDGNYKTRAEVKFEGDTLVNRIELKGIDFKEDGNILGHKLEYNYNSHNVYIMADKQKNGIKVNFKI
RHNIEDGSVQLADHYQQNTPIGDGPVLLPDNHYLSTQSALSKDPNEKRDHMVLLEFVTAAGITHGMDELYK

Not1 site

Linker (Gly4-Ser): GGGGS

ADHA3 (peptide): HNHKSKKHK

DNA:

AAATACCTGCTGCCGACCGCTGCTGCTGGTCTGCTGCTCCTCGCTGCCCAGCCGGCGATGGCCGGTAGCAGCCATC
ACCATCATCATCATGAAAACCTGTACTTCCAGGGTGGTCTGAACGATATTTTTGAGGCCCAGAAAATTGAATGGCA
TGAAGCTAGCATGAGCAAAGGTGAAGAACTGTTTACCGGTGTTGTTCCGATTCTGGTTGAACTGGATGGTGACGT
TAATGGTCACAAATTTTCAGTTAGCGGTGAAGGCGAAGGTGATGCAACCTATGGTAAACTGACCCTGAAATTTATC
TGTACCACCGGCAAACTGCCGGTTCCGTGGCCGACACTGGTTACCACCTTTAGCTATGGTGTTCAGTGTTTTAGCC
GTTATCCGGATCATATGAAACAGCACGATTTTTTCAAAAGCGCAATGCCGGAAGGTTATGTTCAAGAACGTACCAT
CTTCTTCAAAGATGACGGCAACTATAAAACCCGTGCCGAAGTTAAATTTGAAGGTGATACCCTGGTGAATCGCATT
GAACTGAAAGGCATCGATTTTAAAGAGGATGGTAATATCCTGGGCCACAAACTGGAATATAATTATAATAGCCAC
AACGTGTACATCATGGCCGACAAACAGAAAAATGGCATCAAAGTGAACTTCAAGATCCGCCATAATATTGAAGAT
GGTTCAGTTCAGCTGGCCGATCATTATCAGCAGAATACCCCGATTGGTGATGGTCCGGTTCTGCTGCCGGATAATC
ATTATCTGAGCACCCAGAGCGCACTGAGCAAAGATCCGAATGAAAAACGTGATCACATGGTGCTGCTGGAATTTG
TTACCGCAGCAGGTATTACCCATGGTATGGATGAACTGTATAAAGCGGCCGCCGGTGGTGGTGGTAGCCATAATC
ATAAAAGCAAAAAGCATAAA

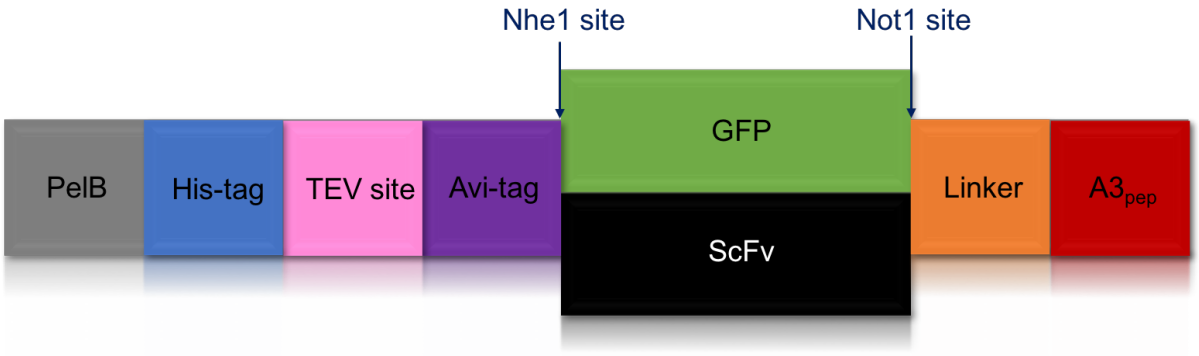

Figure 68 Gene string design ready to insert the scFv DNA sequence. The DNA sequence is colour coded to aid identification of the function of each region. The GFP region is shown alongside the ScFv region as the two segments are interchangeable.

4.6.2 Cloning steps for generating the scFv-A3$_{pep}$ fusion

After the initial design of the Gene String containing GFP, the DNA sequence was codon optimised for the greatest expression yields in *E. coli*. No additional Not1 or Nhe1 restriction sites were located when the sequence was analysed using the NEB cutter 2.0 software. Primers were designed for amplification of the Gene String, containing Bsa1 restriction sites for cloning into the pPR-IBA1 vector (appendix 2.1). A gradient PCR reaction was used to determine the optimum annealing temperature for the primers. The annealing temperatures tested were (°C): 72.0, 68.6, 61.4, 58.3 and 55.0 and the PCR products generated in the reaction were analysed using agarose gel electrophoresis. An image of the resulting gel can be seen in figure 69. As the same amount of each sample was analysed on the gel, a more intense peak would indicate a higher yield of product and therefore optimum annealing temperature. The image shows that the most intense band at the expected size (around 600 bp) corresponded to the lowest temperature tested, 55 °C. For each of the samples analysed there was also a less intense band that appeared below 100 bp. This band could be due to amplification of the primers and the low MW band was removed during a successive PCR purification step.

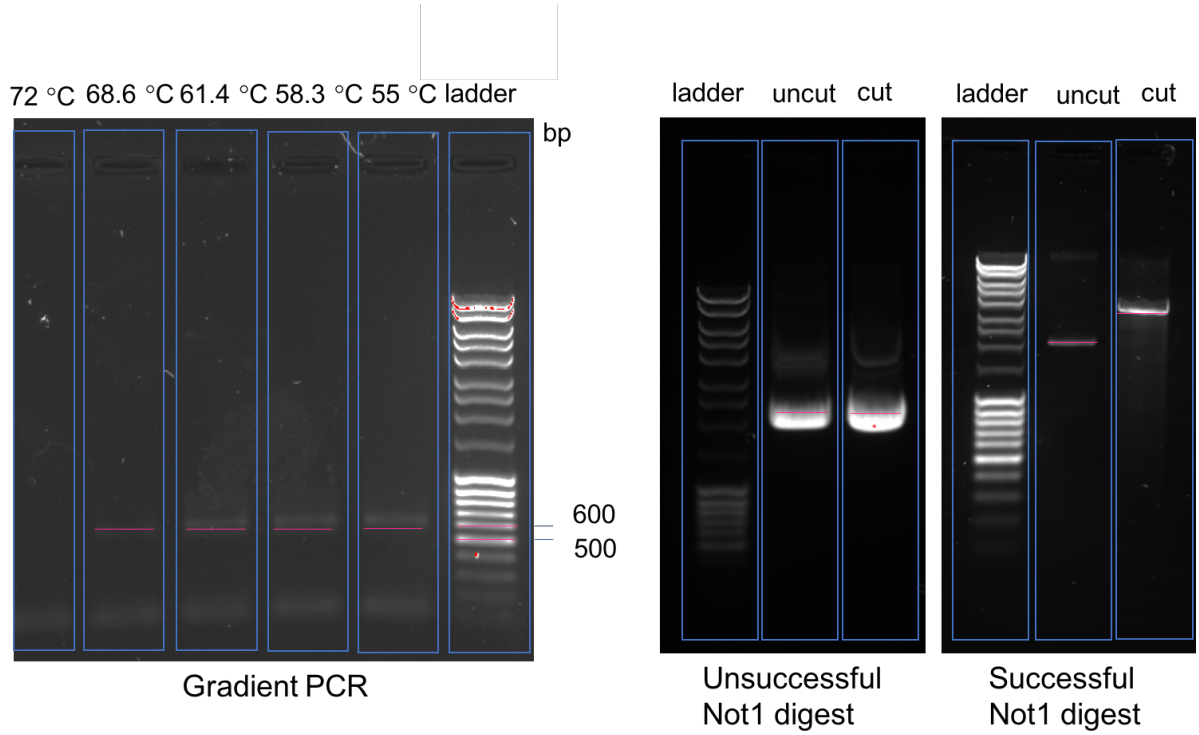

Figure 69 1 % agarose gels showing the PCR optimisation, using a heat gradient (left) and Not1 test digest (right) for the UCL Gene String. Examples of both the unsuccessful digest and and successful Not1 digest are shown.

With the successful amplification of the Gene String using the primers designed to add Bsa1 sites for ligation into a pPR-IBA1 plasmid, the next stage was to digest the plasmid and Gene String and ligate the insert into the vector. The success of the ligation was concluded following sequencing of the

recombinant DNA. The sequencing results and test digest (see figure 69), highlighted a mistake in the DNA sequence of the Gene String. There was a single base deletion in the Not1 site, which generated a frame shift after the deletion and resulted in the Not1 enzyme not able to recognise the cutting sequence and digest the DNA. The process to generate pPR-IBA1 containing the Gene String was repeated and this time the sequencing and digestion test confirmed the correct DNA sequence (see figure 69 showing the Not1 digest). A pPR-IBA1 vector containing the tags and sequences required had been generated and the complete plasmid was now ready for scFv insertion between the Not1 and Nhe1 sites.

The scFv was sent from UCL to the University of Sheffield in a pFUSE plasmid. This plasmid is often used for high expression yields in yeast (see appendix 2.3 for vector map). It contains a gene for Zeocin™ antibody resistance. Zeocin^{TM} was added to low salt LB agar plates (NaCl at 5 g L^{-1}, usual LB contains 10 g L^{-1}) and the pFUSE plasmid containing the scFv DNA sequence was transformed into chemically competent *E. coli* cells. Colonies took longer to grow than previous growth times required for XL10 gold competent *E. coli* on LB agar plates. This was likely to do the lower salt content and therefore less rich growth medium. A useable number of colonies were present on the plate after 24 hours. Individual colonies were picked and grown overnight in low salt LB media containing Zeocin^{TM} before the cells were pelleted. The scFv insert was amplified using PCR and primers designed to incorporate Nhe1 and Not1 restriction sites to the scFv insert. The PCR product was then analysed using agarose gel electrophoresis and an image of the gel is shown in figure 70. Bands were visualised at the expected molecular weight (around 750 bp), suggesting successful amplification of the scFv sequence. The next step was to digest the scFv insert with the Nhe1 and Not1 restriction endonucleases, however, during this process it became apparent that there was an internal Nhe1 recognition sequence within the scFv DNA sequence. The restriction site was located using the NEB cutter 2.0 tool. The site needed to be removed before cloning could be continued.

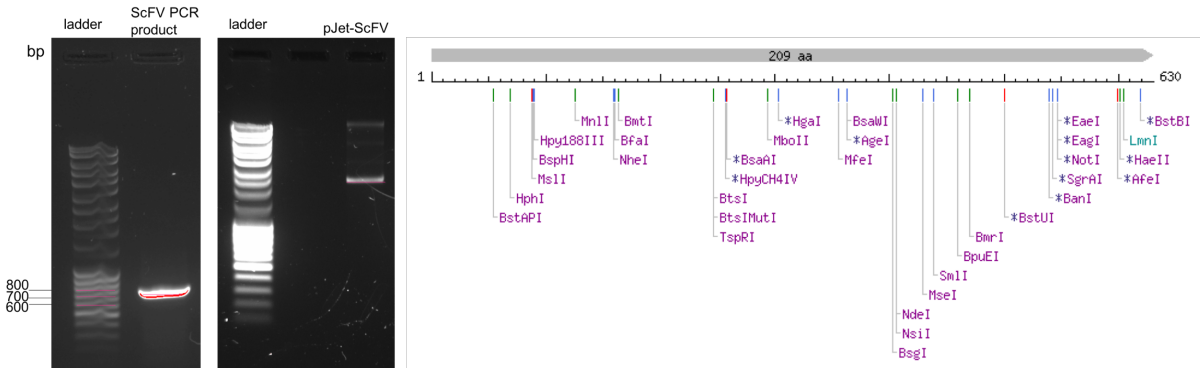

Figure 70 Gel electrophoresis images for amplification of the scFv insert and cloning of the insert into a pJet vector using blunt end cloning. NEB cutter 2.0 tool analysis shows only the desired Not1/Nhe1 restriction sites

QuikChange™ site directed mutagenesis was employed to remove the internal Nhe1 recognition site. The scFv fragment was cloned into a pJet vector using blunt end cloning. The pJet plasmid was used for ease of sequencing as it contained a T7 sequence and enhanced expression in *E. coli* as Zeocin™ was no longer required. A vector map can be found in appendix 2.2. The blunt end cloning was analysed using agarose gel electrophoresis (shown in figure 70) which suggested the correct product had been generated. To confirm this the complex was sent for sequencing, which came back positive. The mutagenesis reaction was performed using primers that had been designed to generate a single base mutation in the internal restriction site, without changing amino acid encoded. The sequence was analysed using the NEB cutter 2.0 tool which showed that there was no longer an internal Nhe1 site within the scFv sequence (see figure 70). Sequencing results confirmed the success of the mutation and the scFv insert could now be generated by digesting the pJet vector with Nhe1 and Not1 restriction enzymes. A complete pPR-IBA1 vector containing the required tags and sites, and a complete pJet vector containing the scFv (with internal Nhe1 site removed) was produced and were prepared for Nhe1 and Not1 digestion, gel extraction and ligation to produce a single pPR-IBA1 vector containing the scFv sequence.

The pPR-IBA1 plasmid and pJet containing scFv plasmid were both digested using Nhe1 and Not1 enzymes. The activity of the enzymes was assessed by performing the digestions using the two enzymes separately. Agarose gel electrophoresis was used to analyse the success of the digests, the resulting gel images are shown in figure 71 below. The figure for the pPR-IBA1 digest indicates successful cutting with the vector band around 3000 bp. The image of the pJet vector shows the successful digest with a band between 700 and 800 bp, matching the molecular weight predicted for the vector and 750 bp matching the predicted size of the insert. Gel extraction was used to remove the unwanted insert cut from the pPR-IBA1 plasmid and the unwanted pJet vector of which the required scFv DNA sequence was cut. An agarose gel analysing the fragments for gel filtration can be seen in figure 71.

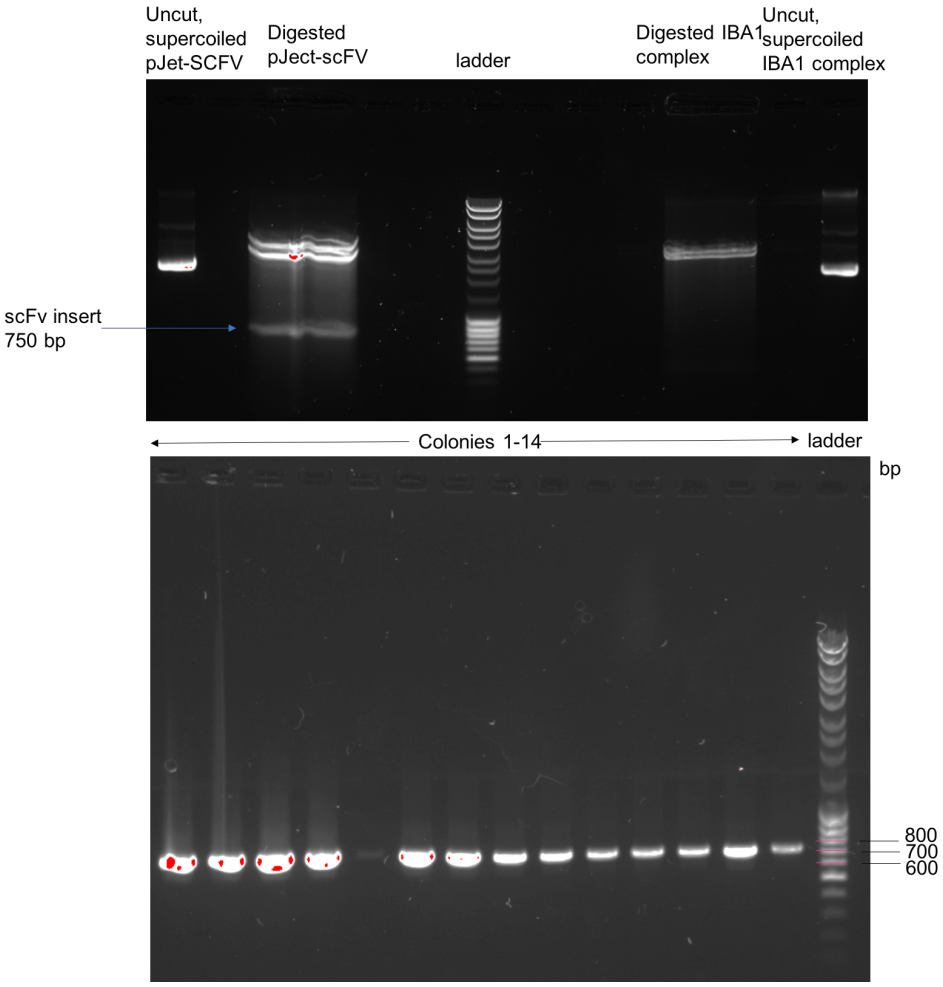

Figure 71 Gel extraction of the scFV insert and IBA1-complex plasmid, shown on a 1% agarose gel. Colony PCR showing the successful uptake of the ligated plasmid by E. coli cells. Colonies that appear to contain the DNA of interest are visible in lanes 1-13, however lane 5 is inconclusive.

With the vector containing the designed sequence of tags and sites and the insert consisting of the scFv flanked by digested Nhe1 and Not1 sites extracted the samples were mixed together with instant sticky-end ligase to aid the ligation reaction between the products and produce the designed and desired recombinant DNA complex. The ligated species were then transformed into competent *E. coli* cells, which were plate on LB agar and incubated overnight. There were a good number of colonies present on the LB agar plate the following day. These colonies were analysed using colony PCR to determine whether the insert had been ligated into the vector. The use of two different sticky ends should of prevent the recirculation of the vector during ligation. The colony PCR appeared to show the successful generation of the desired complex with a band present at 750 bp for most of the colonies tested. Primers were used to identify and amplify the scFv insert. An image of the agarose gel used to visualise the samples is shown in figure 71. With the colony PCR results appearing to be a success, the samples could then be sent for further sequencing to confirm the correct DNA sequence of the complex.

Unfortunately, the sequencing did not produce a positive result, with a mixture of different complexes confirmed in the various samples sent. At this point the project had to be stopped due to time restrictions. A number of problems that required extensive troubleshooting had arisen which meant that the work overran the critical slot to work on this at UCL. If the project was continued a Nco1 digest would be a reasonable next step as this would cut the unwanted pJet vector, however the final plasmid does not contain a Nco1 site and therefore would remain intact. Protein expression trials had also been planned for when the correct complex had been obtained. Optimising the yield of the scFv-$A3_{pep}$ fusion for protein production. Protein purification would be possible through the His_6 purification tag and the C-terminal Strep-II tag provided from the pPR-IBA1 vector. With the His_6 tag at the N-terminal and Strep-II tag at the C-terminal the two tags could be used to ensure the full protein was produced and eliminate the possibility of fragmentation. Further future work with the complex would look at binding analysis of the scFv-$A3_{pep}$ to the MNPs before analysis of the uptake, cytotoxicity and response to hyperthermia in CEA expressing cells.

4.7 Chapter summary

Four different attachment methods were studied, each accompanied by its own purpose and pros and cons. The first method tested was chemical biotinylation. Biotin labelling of the MIA and therefore MNP appeared useful due to the possibility of binding other interesting molecules to the system through extremely strong avidin-biotin interactions. Chemical methods of labelling were appealing due to the apparent ease of the reaction. A kit to label the primary amine groups of the lysine residues was used. The problem with this method was that lysine residues appear to be important for the binding of the MIA to the MNP, with a number of these basic residues in close proximity to the active region of the protein. Biotinytlation of the MIA proteins appeared successful, however, this lead to a dramatic decrease in the binding capabilities of the MIA to the magnetite NPs. The binding intensity was decreased by 50 % upon labelling, which was due to the blocking of the active binding region on the MIA.

Specific, enzymatic biotinylation was then considered. A tag was incorporated to the terminus of the MIA protein – away from the binding loop. This method of labelling was much more complex than chemical biotin labelling. The AviTag-MIA fusion and BirA proteins were produced, purified and characterised. As the site of biotinylation was away from the binding region, the process showed promise in not reducing the binding capacity of the MIA to the MNP. Unfortunately, the reaction

was complex and lead to a low yield of labelled complex, making it an undesirable form of attachment.

Next, attachment via a single C-terminal cysteine residue was investigated. The MIA sequence does not naturally contain any cysteine residues therefore a single cysteine was added at a later date, at a specific point in the sequence (away from the binding loop). This residue was available for interaction and attachment. The terminal residue could interact via the formation of a disulphide bridge (in the formation of dimers) or through a maleimide linkage, which would prove useful for the attachment of the RAGE antibody and fluorescent dye. The formation of disulphide links is reversible and highly redox sensitive and so were not useful in the attachment of other molecules to the MIA. The maleimide interaction was irreversible and not sensitive to the presence of TCEP reducing agent – ensuring that dimerisation of the MIAs was overcome, without compromising the formation of maleimide links.

Finally, the attachment via a protein fusion was analysed, using the ShMFE scFv. The purpose of the protein was to incorporate an additional length of DNA sequence, without the possibility of cleavage or fragmentation. The protein fusion showed promise, however the sequence designed in this project was complex, with lots of time intensive steps that needed to be overcome.

In summary, this chapter has shown that fluorescent dyes such as maleimide activated DyLight 650 can be attached to a mutated C-terminal cysteine residue on the MIA proteins. Attachment of therapeutically relevant antibodies, such as the α-RAGE antibody can also be attached to MNPs using maleimide chemistry and a Sulfo-SMCC/MIA linker. This complex exhibited promising uptake and negligible cytotoxicity when tested using SKOV-3 mammalian cell cultures (both in 2D and 3D models) and showed useful heating capabilities when subjected to an AMF during hyperthermia treatment.

Chapter 5: The coiled coil scaffold

5.1 Magnetosome membrane specific (Mms) proteins

Work in this chapter looks to mimic magnetosome membrane specific (Mms) biomineralisation proteins, for use *in vitro,* to mediate controlled synthesis of magnetite NP. A number of transmembrane proteins have been identified within the magnetosome of MTB that are known to control magnetite formation within the cell. The specific proteins investigated here were discovered in the α-proteobacteria *Magnetospirillum magneticum* strain AMB-1. There is one main barrier to studying these proteins *in vitro* – they are transmembrane proteins and so are inherently difficult to work with. The hydrophobic coiled region spans the phospholipid bilayer membrane when present in the bacteria. Outside the bacteria this large hydrophobic region leads to poor solubility, difficult extraction and purification and ultimately low yields of protein. It is for this reason that a mimic of the proteins was designed and synthesised.

The coiled coil peptide displaying scaffold was designed as an alternative to the Adhiron scaffold. The Adhiron scaffold has shown promise in controlling magnetite NP synthesis, producing NP shapes and sizes that are not commonly witnessed in nature. The coiled coil scaffold mimics more closely the transmembrane helices observed in the naturally occurring Mms proteins and should form a small monomer protein, making it an interesting and novel additive for producing magnetite NPs to the same specificity as witnessed in MTB.

The aims of this chapter are;

- To synthesise mimics of a number of different Mms proteins, using the coiled coil scaffold protein
- Determine whether the coiled coil scaffold is a promising alternative to monoclonal antibodies and other artificial peptide displaying proteins
- Characterisation of protein size; monomeric structure; and binding of the complexes to magnetite NPs
- To investigate the importance of different residues in the Mms binding loops using a comparison to inactive homologs and carefully designed mutants
- Assess the ability of the coiled coil to act as a universal scaffold protein by incorporating non-Mms binding loops and functionalising the scaffold

5.1.1 Mms13

Mms13 is a low molecular weight protein with a molecular weight of around 15 kDa, consisting of 145 amino acid residues. It is a biomineralisation protein, located in the magnetosome membrane of AMB-1, identified as a homolog of MamC – a similar biomineralisation protein found in MTB species *M. gryphiswaldense*. The discovery and identification of Mms13 was detailed in the journal of biological chemistry in 'A novel protein tightly bound to bacterial magnetite particles in *Magnetospirillum magneticum* strain AMB-1'.[72] The paper analyses the magnetosome of AMB-1 with the aim to identify new proteins which interact strongly with the magnetite crystal. Over 60 % of the proteins located in the magnetosome were removed from the sample through addition of urea, thiourea and CHAPS. The remaining proteins were classed as tightly associated to the crystal and required more extensive washes for removal. These proteins were removed by immersing the crystal in boiled SDS. The proteins that were removed during this stage were analysed using gel electrophoresis and N-terminal amino acid sequencing. Novel proteins were identified from the fraction with sequencing identifying one of the proteins as a homolog of the already known MamC protein, found in *M. gryphiswalense* (80 % identity). Mms13, like Mms6, MamC and other tightly associated proteins, has a characteristic hydrophobic N-terminal region and hydrophilic C-terminal region.

The transmembrane (TM) regions of the Mms13 sequence were predicted using the ExPASy TMpred software.[152] The resulting plot is given in figure 72. The data suggests that a Mms13 model consisting of two transmembrane helices is strongly preferred. TM1 is located between residues S_{33} and A_{51} and TM2 between A_{83} and A_{110} (shown in the orange columns in figure 72). Interestingly, between these TM regions, is a flexible peptide loop that protrudes into the interior space of the magnetosome, placing it within close proximity of the forming magnetite crystal. The location and projection of this sequence indicates involvement in binding the magnetite crystals and therefore aiding control of nucleation or growth processes within the magnetosome. The model also indicates that the hydrophilic C-terminal region is located outside the magnetosome and so is unlikely to be responsible for the strong binding observed between the protein and the crystal. The strong binding does suggest that the protein has an important role *in vivo*, carrying out one of two functions: initiation of crystal nucleation; or, regulation of crystal growth.

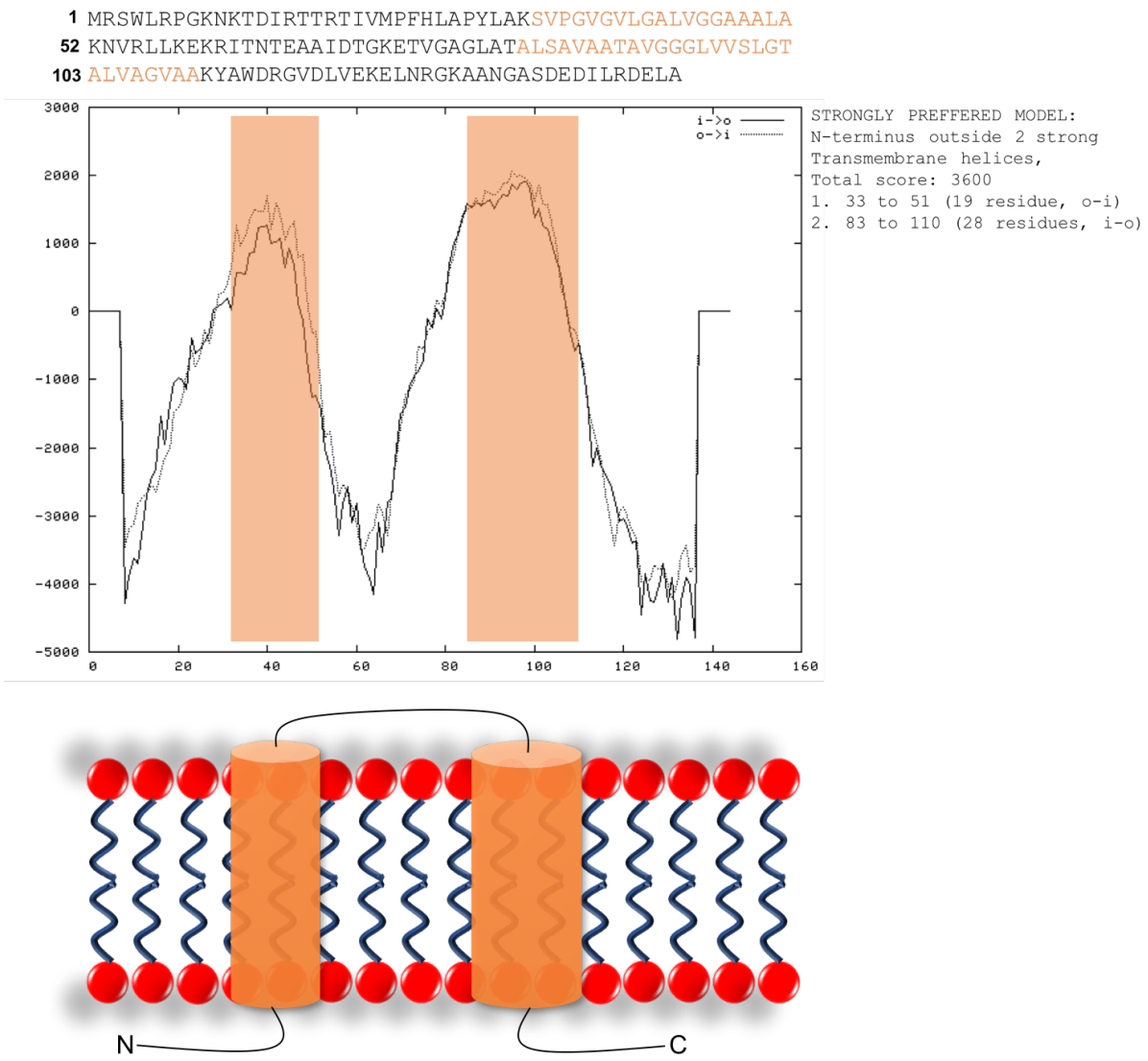

Figure 72 Model of the transmembrane regions of Mms13 using ExPASy TMpred. The analysis indicated that the protein is highly likely to contain two transmembrane regions with a flexible loop linking the helices. The peptide linker between TM1 and TM2 lies inside the magnetosome

5.1.2 MmsF

MmsF is a relatively small, 107 residue, 20 kDa, protein that is located within the magnetosome membrane of MTB. It has a highly conserved sequence and is seen as a master protein regulator of particle morphology, both *in vivo* and *in vitro (see section 1.4)*. The (TM) regions of the sequence were predicted using the ExPASy TMpred software.[152] The result plot is given in figure 73. The data suggests that a MmsF model consisting of three transmembrane helices is strongly preferred. TM1 is located between residues T_{14} and V_{33}; TM2 between G_{47} and L_{66}; and TM between W_{69} and F_{91} (shown in the blue columns in figure 73). Between these TM regions, are flexible peptide loops that protrude into the interior space of the magnetosome, or away from the magnetosome, into the bacterial cytoplasm. Interestingly, the peptide loop linking helices of TM1 and TM2 has been shown to be located inside the magnetosome, placing it within close proximity of the forming magnetite

crystal. When considering the predicted TM model, it is suggested that the loop between TM1 and TM2 is located inside the magnetosome as the terminal residues of the TM helices are labelled with either 'i' for inside, or 'o' for outside of the organelle. The location and projection of this sequence indicates that it is likely to be important for controlling magnetite nucleation or growth within the magnetosome. In addition to this, the loop between TM1 and TM2 contains a high proportion of acidic amino acid residues, this is similar to the biomineralisation protein Mms6 which binds strongly to the enveloped magnetite crystal within the magnetosome and has been shown to regulate crystal formation *in vivo*.[64, 72] These acidic sidechains likely interact with iron ions and the growing magnetite crystal through electrostatic interactions and formation of salt bridges.

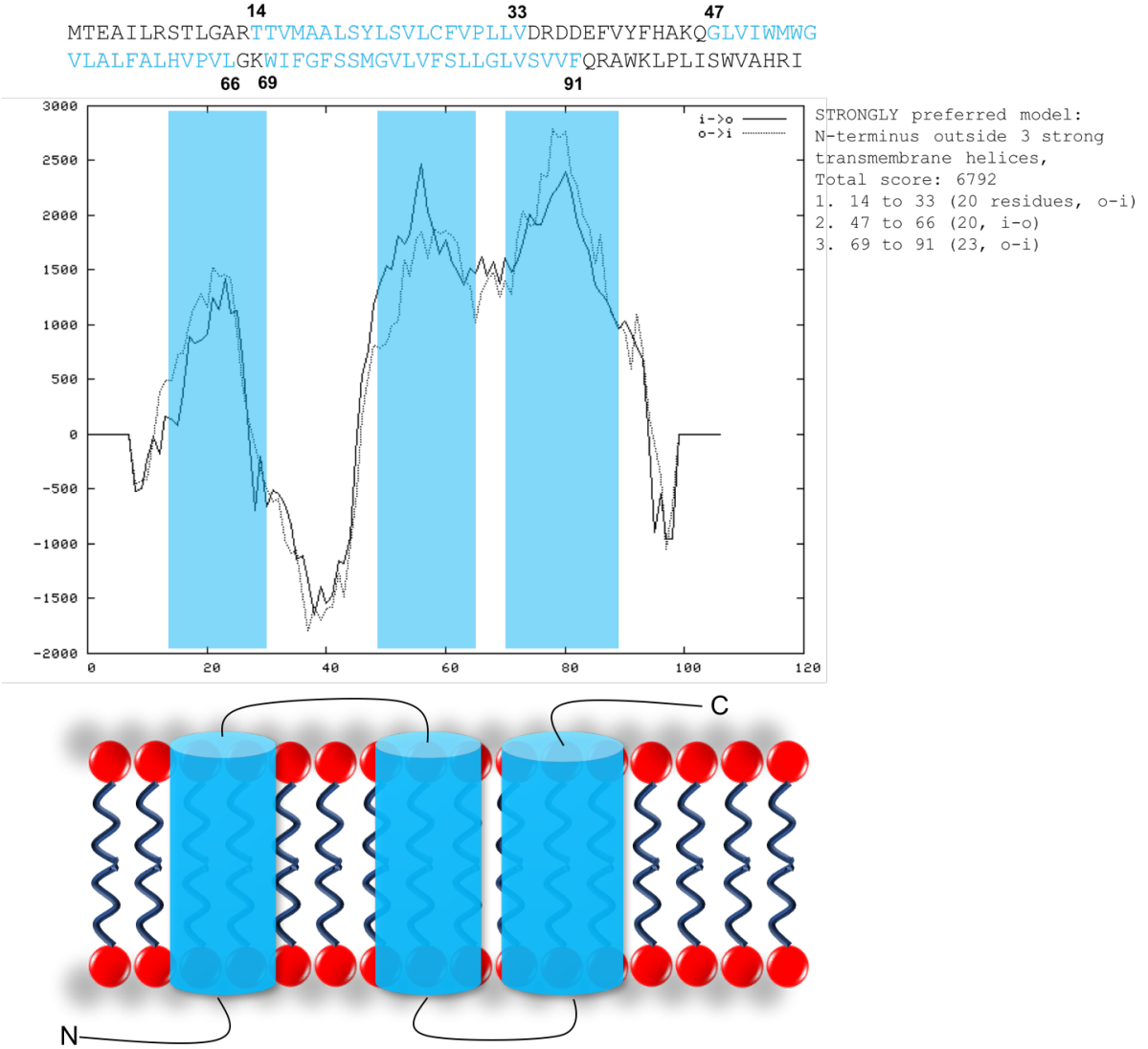

Figure 73 Model of the transmembrane regions of MmsF using ExPASy TMpred. The analysis indicated that the protein is highly likely to contain three transmembrane regions with flexible loops linking the helices. The peptide linker between TM1 and TM2 lies inside the magnetosome.

Fluorescence measurements detailed in 'The magnetosome membrane protein, MmsF, is a major regulator of magnetite biomineralisation in *Magnetospirillum magneticum* AMB-1' gave further analysis of the localisation of MmsF in the bacteria.[75] GFP was conjugated to the N-terminus of MmsF with the aim of tracking the protein. It was found that in cells containing a gene knockout (ΔMAI) where magnetosome organelles are unable to form, MmsF was found to homogenously sit around the cell membrane. This was a predicted response as it was expected that MmsF is commonly localised at the magnetosome membrane. A biochemical fractionation experiment was also conducted to investigate MmsF localisation, this experiment used wild-type MTB cells and magnetosomes. This assay, analysed using western blot, discovered that almost all of the GFP-tagged MmsF was found in the magnetosome fraction of the blot, providing further evidence that MmsF is located in the magnetosome membrane with access to the forming magnetite crystal. It is likely that MmsF is similar to other Mms proteins, MamA/J/I/C that localise in a straight line along the longer axis of the cell, without spanning the entire cell length.[64, 75]

With the location of MmsF traced to the magnetosome membrane, the function of the protein *in vivo* was investigated further. In a knockout experiment, the eight genes, grouped in a chromosomal region of AMB-1, named R3, were deleted.[75] These genes included *mms6*, *amb0950*, *amb0955* and *mmsF* – resulting in a deletion of proteins MamF, MamD, MamC, Mms6 and MmsF. On deletion of this gene cluster (ΔR3) a severe change in crystal phenotype was observed. The crystals formed by ΔR3 AMB-1 were much smaller and elongated, with the crystal length reduced by 60 % and width reduced by 72 % compared to wild-type crystals. These changes in width and length resulted in a shift of crystal shape for cubooctahedral in wild-type samples, to more rod-like, poorly formed elongated structures following the deletion. As a number of genes were deleted to cause this effect, various individual reintroductions were conducted to assess which genes in the R3 cluster were responsible for the change in phenotype.

After reintroducing the genes one-by-one it became clear that the introduction of *mms6*, *amb0955* or *amb0950* alone could not produce crystals with the size and geometry of that observed for the wild-type crystals.[75] However, when *mmsF* was introduced to ΔR3, even in the absence of the other deleted genes, the crystals produced were very similar to the crystals produced by wild-type AMB-1 in terms of size, geometry and C_{mag} values. The main difference between the two sets of crystals synthesised was a slightly smaller size of the particles formed by ΔR3 + *mmsF*, compared to wild-type. This could be predicted as the gene cluster remained deficient in *mms6* which had previously been shown to regulate magnetite synthesis *in vivo*, in respect to size.[71]

The crystals generated by wild-type AMB-1 and crystals from a Δ*mmsF* mutant were compared using HR-XRD and HR-TEM with the aim of determining the effect of the MmsF protein on crystal chemical composition, size and shape.[75] HR-XRD data confirmed that the lattice parameters were unchanged in the mutant (8.394 < a < 8.397 Å, characteristic of magnetite)[153], suggesting MmsF does not affect chemical composition. On the other hand, a difference was observed in the size and geometry of the crystals produced that were lacking MmsF. HR-TEM showed that the wild-type crystals had an aspect ratio of around 1, adopting a cubooctahedral geometry with [100] either similar to- or more extended than [111]; whereas Δ*mmsF* crystals had a lower aspect ratio of around 0.7, with the [111] plane elongated, causing a variation in the cubooctahedral geometry. These findings suggest that MmsF plays a major role in controlling the size and/or shape by controlling crystal nucleation or growth in AMB-1.

As the size and/or shape of the crystal appeared to be affected my MmsF *in vivo*, the stage at which the effect becomes apparent was analysed.[75] The timing of the initiation of nucleation and growth in AMB-1 was studied by calculating cell growth, C_{mag} values and magnetite formation over the course of 24 hours. The results gathered for the wild-type and Δ*mmsF* mutant were comparable for the duration of the first four hours. After four hours however, the crystal size distribution remained unchanged for the mutant and became broader for the wild-type sample, with a higher number of crystals becoming larger. After around five hours crystals produced by the mutant were heterogeneous in terms of shape while the majority of wild-type crystals adopted a cubooctahedral geometry.[75] These results suggest that MmsF is important for the maturation of the crystal and control of the crystal shape.

Biomineralisation by MTB produce highly uniform crystals within the magnetosome. The control over magnetite synthesis could be extended to *in vitro* biomineralisation reactions. The activity of the MmsF protein was initially studied *in vitro* by Dr Andrea Rawlings in the Staniland research group at the University of Sheffield.[76] It was found that MmsF proteins self-assemble into nanoscale proteinosomes. Expression levels would be lower in the MTB; therefore, they are more likely to form assembly rafts within the magnetosome membrane. Upon addition of the MmsF proteinosomes to *in vitro* magnetite synthesis reactions, the particles generated exhibited a much greater degree of homogeneity of shape and size compared to control reactions with a preference for the formation of octahedral particles.[76] The particles formed were also found to be significantly larger than particles produced using control reactions . These findings suggest that MmsF is active both within the

magnetosome and as an individual entity. The ability of two other similar proteins were analysed alongside MmsF to determine their effect *in vitro*. These proteins were MamF and MmxF.

5.1.3 MamF and MmxF

MmxF and MamF are two transmembrane proteins that were identified in *Magnetospirillum magneticum* MS-1, however they have also since been observed in AMB-1. They are highly similar homologues of MmsF. The *mamF* gene is located in the gene cluster neighbouring that of *mmsF* and these proteins contain 65 % identity. The *mmxF* gene is located around seventy genes downstream to *mmsF* and has 66 % identity. A comparison of the primary sequence of the three proteins is shown in figure 74. The ***** indicates conserved residues; **:** indicated residues that have the same chemical properties (for example hydrophilic, hydrophobic or aromatic) and **.** indicates residues with relatively similar chemical properties. The gaps indicate residues that are different and have differing properties. The regions highlighted in blue show the predicted TM regions and the red box shows the peptide sequence located inside the magnetosome.

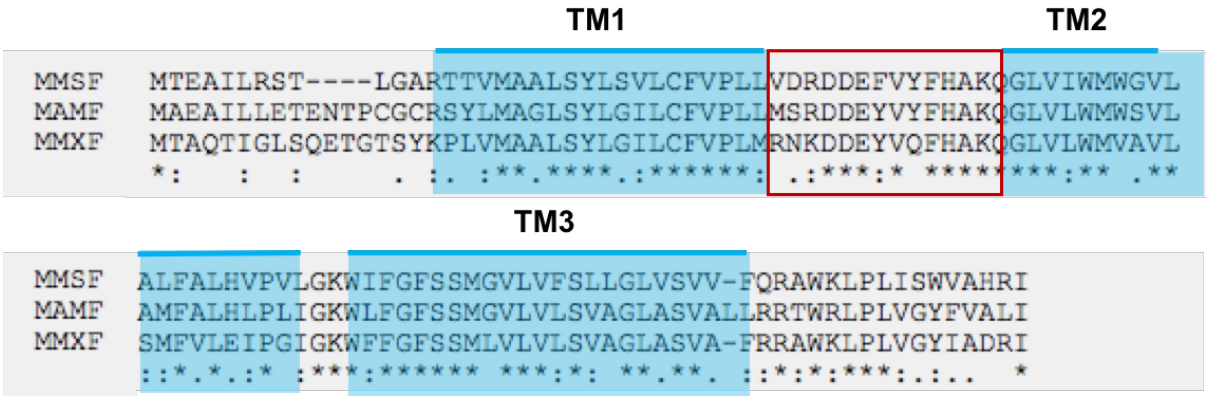

*Figure 74 A ClustalW2 sequence alignment between MmsF and homologues MamF and MmxF. Regions highlighted in blue show the TM regions and the red box highlights the sequences located within the magnetosome. * shows identical residues; : indicates highly conserved properties; . are similar residues and a space indicates a large discrepancy between the properties of the residues at a given position.*

The sequences are highly conserved between different species of MTB. The sequences between the three proteins are extremely similar, with the greatest variability in sequence present at the protein termini. It is for this reason the TM prediction is similar and it would also be predicted that the proteins would have a similar effect on the forming magnetite crystal. This is not the case. Gene knockout studies have shown that MamF and MmxF proteins are not capable of rescuing the magnetite crystal upon ΔmmsF mutation.[75] They do not mimic the control exhibited by MmsF on magnetite NP formation *in vitro* either.[76] When MamF and MmxF were used as additives in benchtop magnetite precipitation reactions, the particles produced were not uniform or

homogeneous like those synthesised in the presence of MmsF. The particles synthesised were poor quality, with various iron oxides forming and no control observed over the size or shape of the products.

The difference in activity between the three proteins is surprising. As shown in the sequence alignment, the loop between TM1 and TM2 is highly conserved (see red box, figure 74). With the sequence so similar, similar control would be expected. Interestingly, the main difference between the sequences is the first residue of the loop. In MmsF this is an acidic aspartic acid group; neither of the homologues have an acidic amino acid at this position. As emphasised above, acidic residues appear to be crucial for biomineralisation, again using Mms6 as an example.[64] A similar sequence of amino acids is observed for MmsF and Mms6: acidic-acidic-acidic-X-acidic. This sequence is not present in MamF and MmxF and could therefore be essential for binding iron ions or forming magnetite crystals. There are a couple of other differences between the loop sequence of the proteins: a change from phenylalanine to tyrosine and a change from tyrosine to glutamine. Each of the changes will be individually analysed following the design and synthesis of easy to work with Mms mimics.

5.2 Design of the coiled coil peptide displaying scaffold

Coiled coils contain two or more α-helices wrapped around each other, creating a protein complex. An α-helix is one type of secondary structure a protein can adopt. It has 3.6 amino acid residues per turn allowing hydrogen bonding between the carbonyl (C=O) and amine (-NH) groups of the amino acids. A heptad repeat unit of amino acids is characteristic of coiled coil proteins. The residues of the heptad are labelled from a to g (and a' to g' on the opposite strand) based on their position in the coil (see figure 74). The hydrophobicity, charge and position of the residues within the helices dictates how they coil. Residues occupying the a and d positions are on the same surface and are usually hydrophobic residues such as alanine, valine, leucine or isoleucine, whereas charged residues such as glutamic acid, aspartic acid and lysine tend to occupy positions e and g. The electronic properties of opposing strands dictate the form that the complex takes. A coiled coil, containing two strands, can run parallel to each other, or alternatively can run in an antiparallel orientation. This orientation depends on the interactions between a/a' and d/d' (which often produce a hydrophobic core for the stabilisation of the complex), however the orientation is often easier to control using charge.

In 2003 Gurnon *et al*. designed and characterized an antiparallel homodimeric coiled coil, with the coulombic and hydrophobic properties optimised to promote the formation of an antiparallel alignment of strands.[154] Within the structure, residues in position a interact with d'; d interacts with a'; e interacts with e'; and g interacts with g' (see figure 75). Each of these interactions were designed to form favourable salt bridges between the e and g positions and favourable hydrophobic interactions between a and d positions, when in an antiparallel orientation. In contrast to this, if the helices were to adopt a parallel alignment, this would result in the existence of electronically repulsive interactions between the e and g positions and sterically unfavourable clashes between the hydrophobic positions. These characteristics strongly promote the formation of an antiparallel coiled coil for the homodimer.

The homodimeric antiparallel coiled coil had useful thermal and the chemical stability - comparable to the stability exhibited by the leucine zipper.[154] Also, the structure showed promising bacterial expression yields, allowing expression in competent *E. coli* cells, which is often challenging for *de novo* designed coiled coils.[155] These properties made it an interesting option for the design of a novel protein scaffold protein.

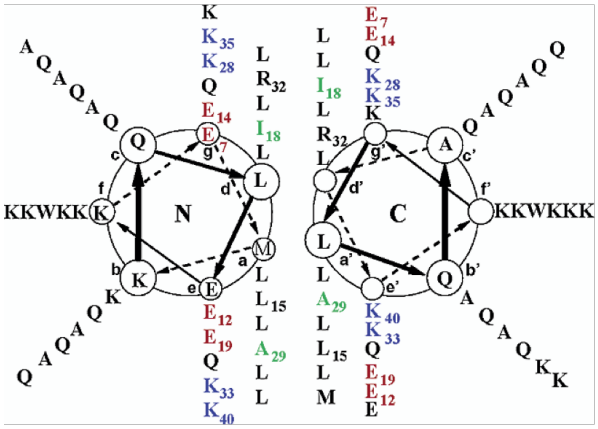

Antiparallel Alignment (favourable):
e-e': E_{12}-$K_{40'}$; E_{19}-$K_{33'}$; K_{33}-$E_{19'}$; K_{40}-$E_{12'}$
g-g': E_7-$K_{35'}$; E_{14} – $K_{28'}$; K_{28}-$E_{14'}$; K_{35}-$E_{7'}$
a-d': A_{29}-$I_{18'}$; L_{15}-$R_{32'}$
d-a': I_{18}-$A_{29'}$; R_{32}-$L_{15'}$

Parallel Alignment (unfavourable):
e-g': E_{12}-$E_{7'}$; E_{19}-$E_{14'}$; K_{33}-$K_{28'}$; K_{40}-$K_{35'}$
g-e': E_7-$E_{12'}$; E_{14} – $E_{19'}$; K_{28}-$K_{3'}$; K_{35}-$K_{40'}$
a-a': A_{29}-$A_{29'}$; L_{15}-$L_{15'}$
d-d': I_{18}-$I_{18'}$; R_{32}-$R_{32'}$

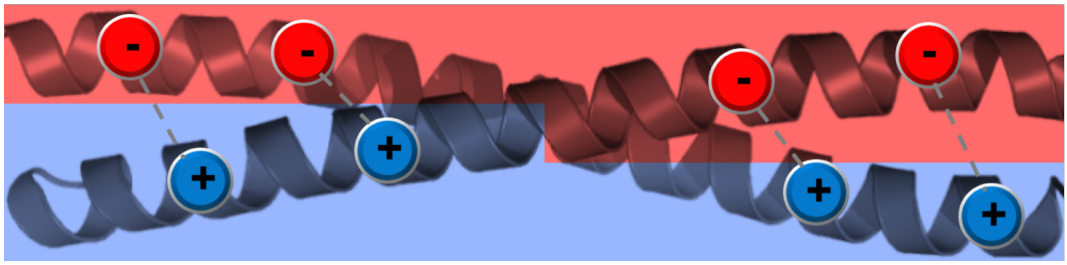

Figure 75 Top left shows a heptad wheel depicting the formation of a homodimeric antiparallel coiled coil structure. The basic residues are coloured blue; acidic red; and hydrophobic green. The image below shows the overall coulombic interactions between the two strands – represented in the same colour scheme.

The aim was to synthesise an alternative protein scaffold, that would closely mimic the characteristics of transmembrane biomineralisation proteins but increase the solubility and expression yields compared to the wild-type proteins. Thus the coiled coil structure designed by Gurnon *et al*. was modified in order to display variable peptides as a hairpin loop, linking the two helices.[154] The formation of a bridge was predicted to increase the stability of the structure by reducing an unfavourable entropic effect upon interaction between two 'free' helical peptides. The protein scaffold displaying the active peptide regions of Mms13, MmsF, MamF and MmxF (and a control protein, AcrB), were designed by Dr Andrea Rawlings and ordered as Gene Strings from Thermo Fischer Scientific. Ultimately, the MmsCC mimics would then be used in bio-inspired RTCP reactions for controlled magnetite synthesis. The peptide sequences displayed as the active loop (AL) region of the scaffold are shown in figure 76 below. The figure also gives the peptide sequence of the homodimeric coiled coil domain.

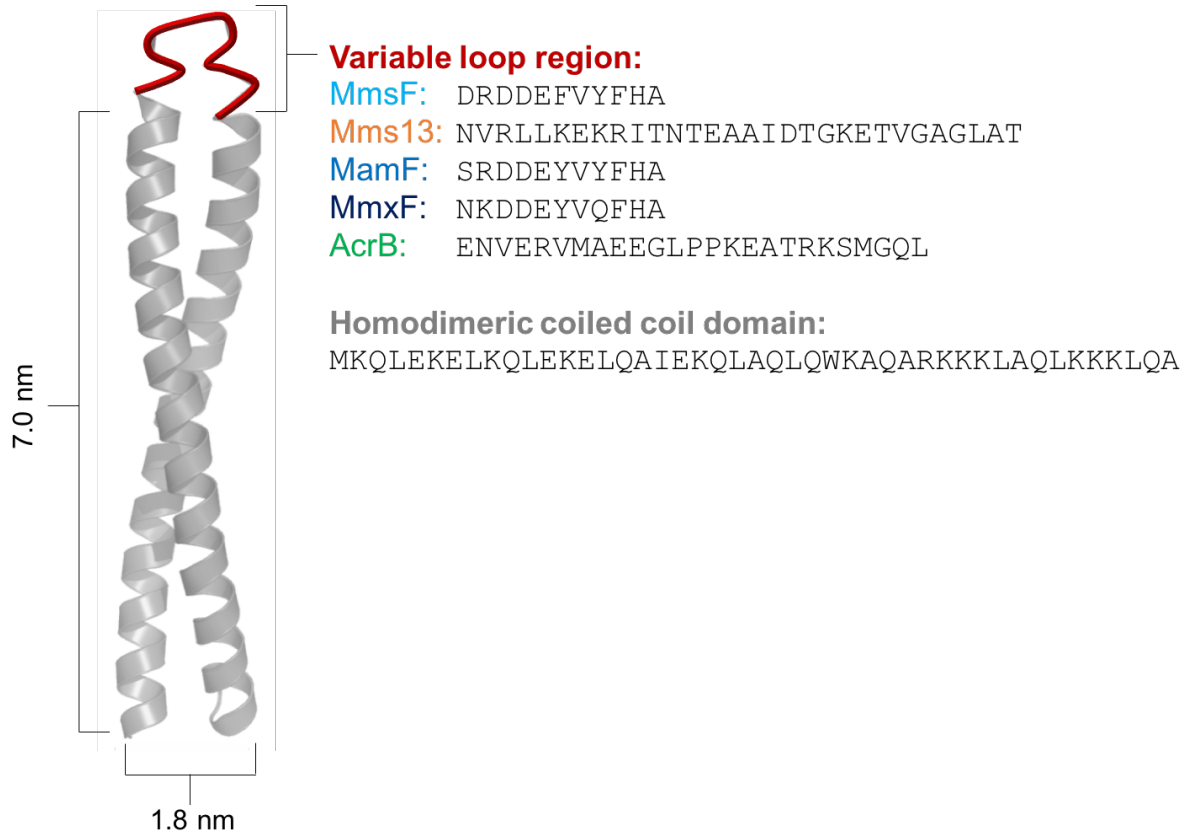

Figure 76 A Robetta schematic model of the coiled coil scaffold and the different peptide sequences displayed at the variable loop region (shown in red).[157]

Following the design of the new protein scaffold and possession of the Gene String, molecular cloning and protein production strategies were then optimised by myself to give the highest achievable yield of the complex.

5.3 Optimisation of cloning and protein production

The mmsCC and acrBCC DNA sequences were inserted into the pPR-IBA1 vector (appendix 2.1), between the Bsa1 restriction sites. An example of the gradient PCR used to optimise amplification of the Gene String is shown in figure 77. The example shows the amplification of the mmsFCC sequence and suggests that a low annealing temperature of 55 °C produces the optimum yield for the desired PCR product. This was also consistent with the results analysed for the mamFCC, mmxFCC, mms13CC and acrBCC sequences. Temperatures lower than this were not tested as below 55 °C primer annealing becomes less specific, leading to a range of products.

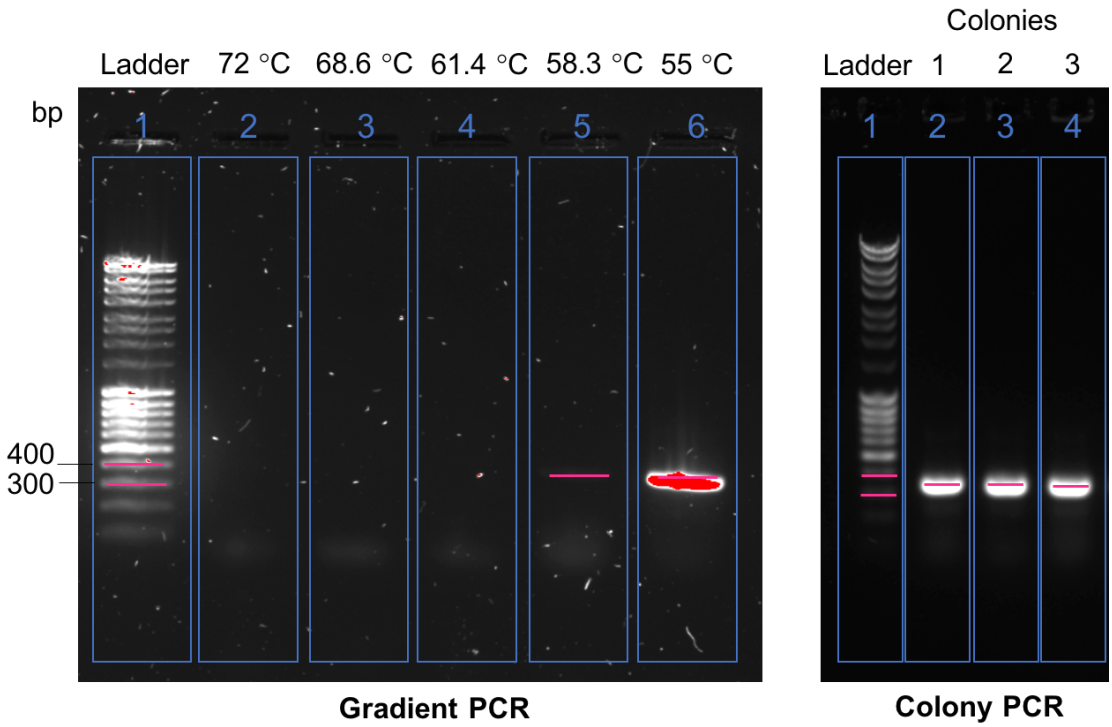

Figure 77 An example of the gradient PCR (left) and colony PCR (right) products for the molecular cloning of MmsFCC analysed using 1% agarose gel electrophoresis.. Gradient PCR indicated that the optimum annealing temperature is 55 ℃; while the colony PCR suggests the successful uptake of the plasmid by the bacterial colonies.

Also shown in figure 77 is an example of a colony PCR reaction analysed for mmsFCC. The figure shows three colonies that had been analysed using agarose gel electrophoresis, following a PCR reaction using mmsFCC specific primers. The mmsFCC DNA insert is around 400 bp and this is consistent with what is present on the gel (when compared to the DNA ladder in lane 1). Bands should only be observed using gel electrophoresis if the correct sequence is present as it shows that the complimentary primers were able to bind successfully and amplify the DNA sequence. Therefore, it was likely that all three colonies tested contained the desired DNA insert. To confirm that the sequence was correct samples of mmsFCC, mms13CC and acrBCC were sent for sequencing,

which confirmed the presence of the designed DNA sequence for each CC sample, the recombinant DNA could then be used for protein production.

Optimisation of the CC protein expression and purification steps was essential to ensure an optimum yield of the correct protein product, using the simplest and least time-consuming methods. Firstly, the process of protein expression was analysed and optimised, followed by the purification process. Initially, two routes of protein expression were compared: expression using autoinduction; and expression using IPTG. Autoinduction appeared to produce higher yields of protein, when compared to expression using IPTG, therefore this route was analysed more extensively to further increase protein yields. To optimise the purification protocol for the CC proteins, four mediums were tested with varying nutrient content. Each media was a mixture of salt, yeast extract and tryptone, in varying proportions. The four autoinduction media were: LB, 2 x YT, TB an SB (appendix 1.9). Two temperatures were also compared: 25 °C and 37 °C with all conditions measured between 0 and 60 hours. Cultures of *E. coli* containing known sequences of the CC DNA were grown and added to the autoinduction mediums containing the desired antibiotics before incubation. At each time point a sample of the autoinduction reaction was taken and spun to pellet the cells. The lysed cell pellets were resuspended in dot blot buffer and a sample was added to a nitrocellulose membrane – this provided quantification of the total amount of protein produced. Following this, the remaining sample was subjected to centrifugation to remove the insoluble debris and leave the soluble protein fraction in the supernatant. The results from one of the two independent dot blot repeats can be seen in figures 78 and 79.

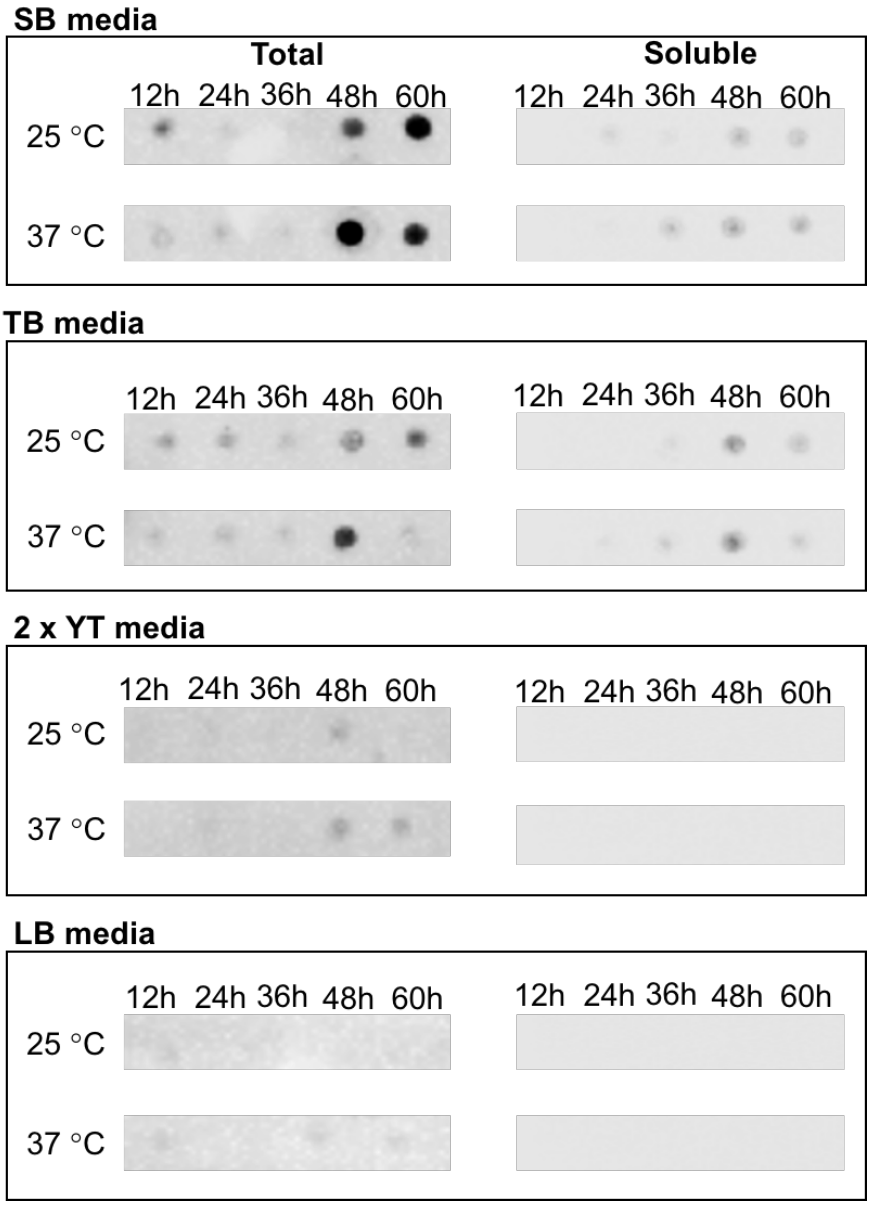

Figure 78 Auto induction expression trial for MmsFCC, analysed using westernblot on nitrocellulose membrane. Four mediums were tested (SB, TB, 2 x YT and LB), with varying nutrient content and two temperatures were tested (20 and 37 ℃. The blot for total protein (left) is compared to soluble protein (right)

When comparing the total amount of protein produced in each of the conditions from figure 78 above, it became clear that there was a significant difference in the expression levels achieved for each of the different growth conditions. The dots corresponding to the protein fractions achieved from the LB and 2 x YT media were extremely faint and suggested that very little protein was being produced. Similar results were observed for both temperatures tested with these media. On the other hand, a much higher expression level was observed for the SB and TB media, particularly the SB auto induction medium. When comparing the two temperatures used in conjunction to these mediums, there was no significant difference observed, the main difference was that in SB auto induction media, a higher degree of protein production was achieved in a slightly shorter timescale

at 37 °C compared to 25 °C. The trend of these results was also consistent with the analysis of the soluble protein fractions. However, after consideration of the amounts of protein produced in the total and soluble fractions, it was decided that the total protein fractions for expression of the CC proteins would be optimised further to obtain the greatest protein yield.

Further analysis of the intensities observed for the total protein fractions is shown in the plot in figure 79. The blot intensity was normalised so that values fit between 1 and 0 to compare the experimental repeats. This plot indicated a significant difference between the use of an SB autoinduction medium compared to the other medias, with TB media appearing to give the next best yield. This was expected as these mediums have a higher nutrient content compared to LB and 2 x YT mediums. The plot indicates that optimum protein production in SB media occurs at 37 °C around 48 hours. After 48 hours, the expression levels begin to drop as the *E. coli* levels increase to levels that are no longer sustainable; oxygen is being used up resulting in levels lower than necessary to keep the cells replicating, causing cell death. Higher temperatures often result in faster bacterial replication times therefore it makes sense that the expression levels would be higher at 37 °C compared to 25 °C at any given time point. It would be expected that the protein production in SB media at 25 °C would begin to drop off after 60 hours, for the reasons mentioned previously.

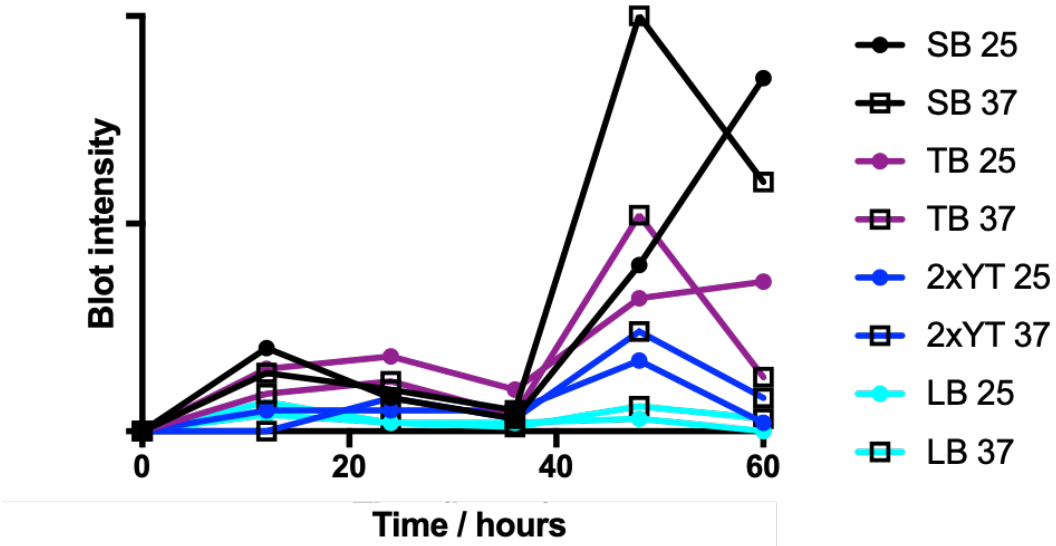

Figure 79 Plot of total protein production of MmsFCC in an autoinduction expression trial. Four mediums are labelled in separate colours and the two temperatures different shapes (solid circle for 25 °C and empty square for 37 °C). Measurements during the trials were taken between 0 and 60 hours.

The results from the expression trial suggest that protein expression should be conducted in SB auto induction media, incubated at 37 °C for approximately 48 hours to achieve optimum protein yields.

Therefore, all the work past this point involving CC protein expression uses these conditions with the protein harvested after 40-48 hours of incubation.

With protein expression optimised, the protein purification protocol was considered. The CC proteins were designed to incorporate a His_6 purification tag to the N-terminus which was available for purification and detection purposes. A TAA stop codon was added to the end of the DNA sequence to prevent expression of the Strep-II tag encoded in the pPR-IBA1 plasmid. The His_6 sequence is a small tag that was unlikely to result in any change of protein folding or conformation and so was the chosen purification tag for the CC proteins. The presence of the tag and the thermal stability of the complex ensured an uncomplicated start to planning the purification, however the relatively low solubility of the protein needed to be addressed. Therefore, a denaturation and refolding step was incorporated into the purification process.

Following protein expression using auto induction, the cells containing the CC protein were pelleted and resuspened in buffer before the first round of lysis. The dot blot showed that the majority of the protein was in the total protein fraction with much lower amounts in the soluble fraction therefore the cells were then pelleted again using centrifugation, before resuspension in a denaturing buffer containing GuHCl. Refolding of the proteins was then achieved on a Ni-NTA column using washes with decreasing concentration of denaturation buffer. An additional wash step using a solution with a low imidazole concentration was used to remove any contaminants that were not tightly associated to the column; before the His_6-tagged, CC proteins were eluted using a higher concentration of imidazole. The Ni-NTA affinity chromatography purification was achieved using reusable Ni-NTA resin in a disposable column on the bench-top or alternatively using a HisTrap™ HP column supplied by GE Healthcare on the AKTA. The purity of each of the CC proteins was assessed. Following purification, the eluted protein fractions were analysed using SDS-PAGE and the results are shown in figure 80. Lane 1 on each of the gels contains the page ruler and the remaining lanes contain the eluted purified proteins.

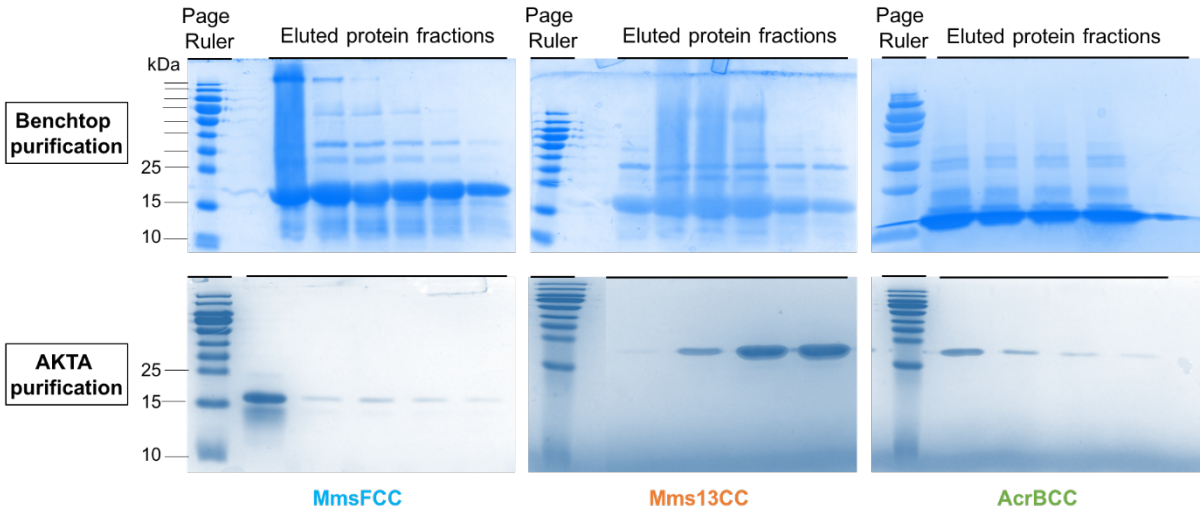

Figure 80 12% SDS-PAGE following the Ni-NTA affinity chromatography purification for MmsFCC, Mms13CC and AcrBCC. The figure compares the purity of the samples purified on the benchtop vs AKTA. Clear sharp bands are visible for the AKTA purification. The bands are not as sharp for benchtop purification.

Each of the SDS-PAGE gels analysed appear to contain protein of the desired molecular weight (15 kDa for MmsFCC; 16 kDa for AcrBCC and 17 kDa for Mms13CC), with an intense band observed for each of the samples. Suggesting the production of the CC proteins had been a success. However, the top three gels in figure 80, also, show a range of other bands, indicating that the protein samples contain contaminants, or have not refolded correctly, possibly leading to the formation of dimers or higher order oligomers. These samples were purified on the bench-top. The bottom three gels in figure 80 were obtained from CC samples purified on the AKTA at 4 °C. The eluted purified proteins in each of these cases appear to be much purer, with no extra bands present at unpredicted molecular weights. Each of the samples appear to be clean, and correctly folded. Therefore, AKTA purification appeared to be superior to bench-top purification. This is likely due to the accuracy of the addition of the refolding buffers, with the correct volumes or the correct concentration added at the required time. Preventing combination and dilution of the buffers that may have occurred during manual use of the HisTrap™ column. It may also have been due to the activity of the resin in the different columns.

The SDS-PAGE analysis of the purified CC proteins shows the samples are clean and correctly folded, but the proteins were also analysed using western blot to ensure the observed protein bands were the His_6-tagged proteins predicted. The protein was linearised and run on an SDS-PAGE gel to separate species present in the mixture by molecular weight. The contents of the gel were then transferred onto the nitrocellulose membrane, before the His_6-tag was detected using a HRP-conjugated antibody system for the recognition of the tag. A photometric assay was used to amplify the HRP signal, catalysing the conversion of the chemiluminescent substrate for protein detection.

The luminescent substrate was oxidised by the HRP, resulting in the emission of light. It was this photo-emission that was visualised. A signal would only be visible if the tag was present for the primary antibody to bind to and the only tagged proteins present were the CCs. Therefore, if a band was at the correct molecular weight, it could be accurately assumed that the protein was the protein of interest.

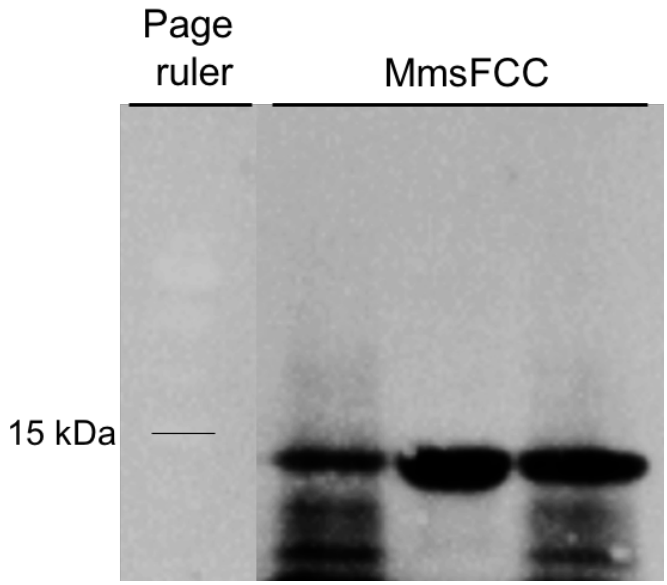

Figure 81 Western blot of MmsFcc after purification. Identification of His-tagged protein at the predicted molecular weight for MmsFCC. A page ruler was added to lane one of the SDS PAGE gel and sample of MmsFCC protein to lanes 2-4.

Figure 81 above shows bands present on the nitrocellulose membrane, around 15 kDa in size – the size expected for MmsFCC. The MmsFCC protein analysed was purified on the bench-top and therefore more than one band is present on the gel and membrane. The bands that occurred on the SDS-PAGE further up the gels are not observed, suggesting they were not the CC proteins, they were contaminants. However, the bands lower down the gel, consistent with a lower molecular were observed, suggesting these are fragments of the His_6-tagged CC proteins. This shows that it is important to purify the proteins on the AKTA, to prevent any fragmentation of misfolding of the proteins during the purification process. The most intense band was observed at the predicted molecular weight for MmsFCC suggesting that the desired proteins had been produced in useable concentrations. It also shows that the tag remains conjugated to the CC proteins throughout the expression and purification stages.

5.4 Characterisation of the MmsCC proteins

After the initial protein characterisation data showed that the proteins produced were likely to be the desired CCs, the exact mass of the proteins was analysed using ESI-MS. The MS for MmsFCC is shown in figure 82. The attached table shows the expected M^+, the calculated M^+; no other major peaks were observed in the spectrum. The positions of the expected peaks assumed a single charge on the protein fragment. If ionisation of the protein resulted is a dication – the m/z ratio would result in the peak at half the expected m/z. Although ESI-MS is a soft ionisation technique, ionisation and fragmention of the protein can still occur and should be considered when interpreting the spectra. The M^+ peak was predicted to be present at m/z = 14986 when lacking the N-terminal methionine. The peak observed matches the predicted peak and so confirms the production of MmsFCC with the correct amino acid sequence and indicates a monomeric protein (if z=1). Analysis of MamFCC, MmxFCC, Mms13CC and AcrBCC using MS can be found in the appendix 5.1-3 showing the protein molecular weights.

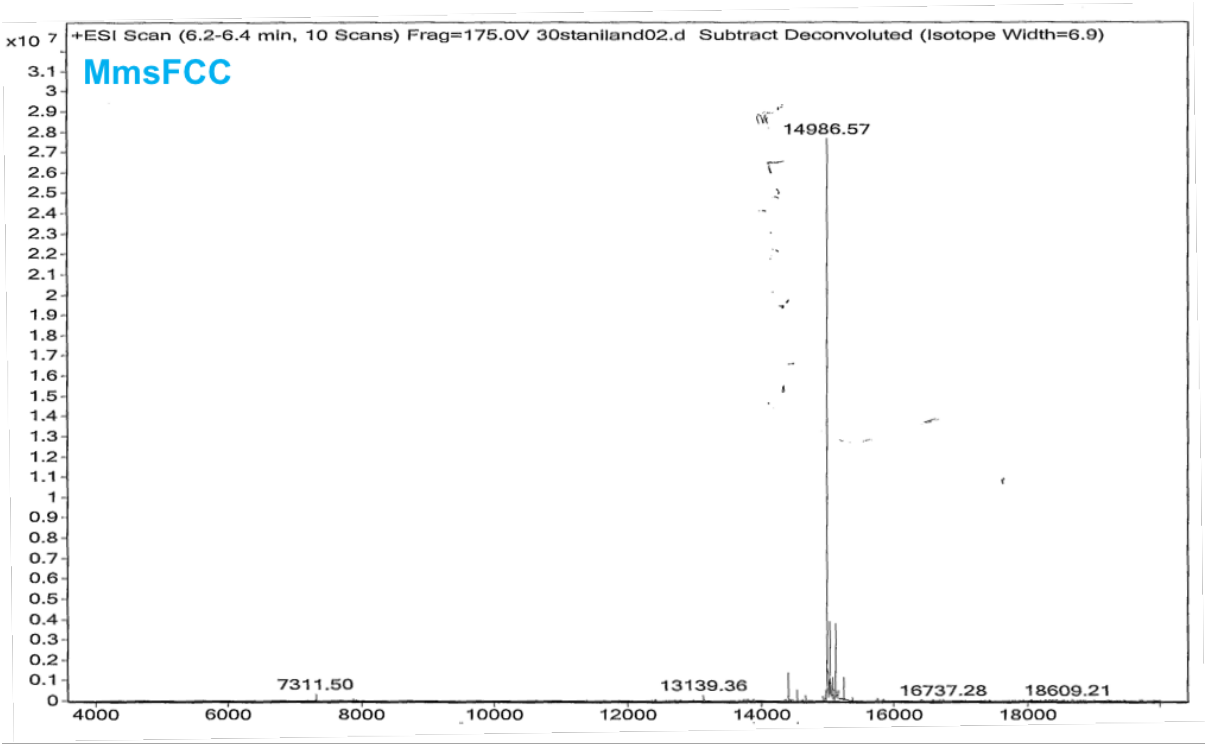

Protein sample	Predicted M^+ (m/z)	Observed M^+ (m/z)
MmsFCC	14986	14987
MamFCC	14975	14975
MmxFCC	14954	14955
Mms13CC	17384	17384
AcrBCC	16686	16686

Figure 82 ESI-Mass spectroscopy data for MmsFCC. The table shows the predicted and observed position (m/z) of the molecular ion peak assuming the protein fragments have a single charge.

The expected M^+ for each of the proteins was calculated using the ExPASy Compute pI/Mw online tool.[142] The matching values indicated with even more certainty that the proteins produced were the desired CCs. MS could also be used to indicate the purity of the of the proteins. A clean spectrum with a single major peak would indicate a single protein product, however, a spectrum containing a variety of other major peaks would suggest the presence of contaminating proteins or molecules within the protein solution, or fragmentation and degradation of the product. It can be seen in figure 82 that there is only one major peak at the predicted molecular weight for MmsFCC, therefore the sample was pure and intact. It also showed that the protein was monomeric as when the mass spectrometer scanned to the m/z expected for dimers or trimers, there were no peaks present (matching data shown in the SDS-PAGE and western blot analysis).

Following confirmation of the protein sequence, the secondary structure of the CC proteins was investigated using CD. The most intense response occurs for alpha-helical structures present in the sample. As the coiled coil proteins were predicted to have over 50 % helical content, CD was an obvious choice of analysis to decipher the folding of the proteins. Intense negative peaks at 222 nm and 208 nm were predicted to be observed for each of the proteins, characteristic if α-helical secondary structure. The baseline corrected CD spectra for MmsFCC, Mms13CC and AcrBCC in water is shown in figure 83. The data for each of the proteins was analysed using Dichroweb where an algorithm was applied to fit a predicted model to the CD data that had been input into the system.[120] The plots showing the fit of the applied models in shown in figure 83. The green line represents the experimental data, the blue line is the reconstructed data using the model and the pink dashed line shows the calculated difference between the experimental and reconstructed data. Higher, longer and more intense pink lines indicate a larger discrepancy between the two data sets. If the pink dashes are small dots, this suggests a good fit of the model. There is an excellent fit between the experimental and reconstructed date for each of the CC proteins. A table has also been included to show the helical content predicted from the experimental data and the helical content predicted using Dicrobweb and the CDSSTR algorithm. The content calculated from the experimental data assumes that all the residues of the coiled coil peptide (producing the coiled coil scaffold) are positioned in an α-helix and that the variable peptide loop and purification are not. Therefore, a higher helical content was calculated for MmsFCC compared to AcrBCC and Mms13CC as all three proteins contain the same coiled coil protein scaffold, however, MmsFCC has the shortest peptide displayed and would therefore possess the highest degree of α-helix. Similarly, Mms13CC displays the longest peptide loop and therefore the lowest helical content of the three. These predictions

matched well to the helical content of each of the proteins using the reconstructed data, with the percent of helical content following the same trend.

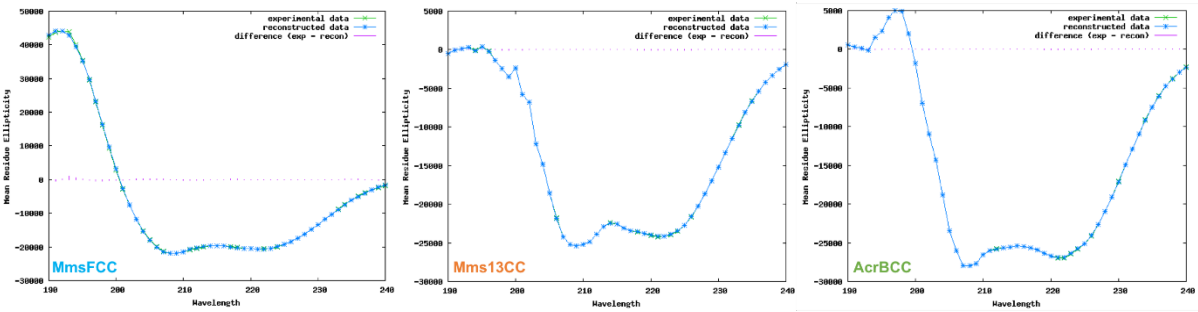

Protein sample	Helical content from sequence (%)	Helical content predicted (Dichroweb, %)	Model fit
MmsFCC	69	66	CDSSTR
Mms13CC	59	59	CDSSTR
AcrBCC	63	64	CDSSTR

Table 11 Predicted helical content of MmsFCC (blue), Mms13CC (orange) and AcrBCC (green) using Dichroweb and CDSSTR model. secondary structure predicted and observed are similar. Alll three of the proteins appeared to fold in a similar manner

The secondary structure of the CC proteins appeared to be as predicted. Interestingly, all three of the proteins also appeared to fold in a similar manner, suggesting that the protein scaffold for each protein remained consistent. This was an important characteristic required of the CC peptide displaying scaffold to ensure it could be used universally to display a host of different peptide sequences. To assess the behaviour and to ensure it has the thermal and chemical stability required for a peptide displaying scaffold, the proteins were analysed further. More extensive CD experiments were conducted. One of the experiments was a heat-ramp of each of the proteins to estimate a melting temperature (T_M), where 50 % the protein became denatured. The other tested the stability of the protein in varying pH solutions from a pH of 7-9, this pH range was chosen as it is the change in pH over the *in vitro* biomineralisation magnetite precipitation reactions. The results from these tests are shown in table 12. The table presents the molar elipticity of the samples calculated at 222 nm. The number in brackets indicates how the intensity of the peak compares to the peak at room temperature. From this analysis, it appears that all of the CC proteins behave in a similar way with similar thermal stabilities observed. With sample temperature reaching 100 °C and being held at that temperature for a couple of minutes, it can be concluded that the CC protein scaffold if extremely thermally stable. The lowest degree of secondary structure remaining, compared to when the proteins were held at room temperature, is 75 % (at 100 °C, Mms13CC).

Similar results were obtained for MmsFCC (76 %) and AcrBCC (79 %). This impressive stability makes the CC peptide displaying scaffold a promising alternative to other artificial scaffold proteins.

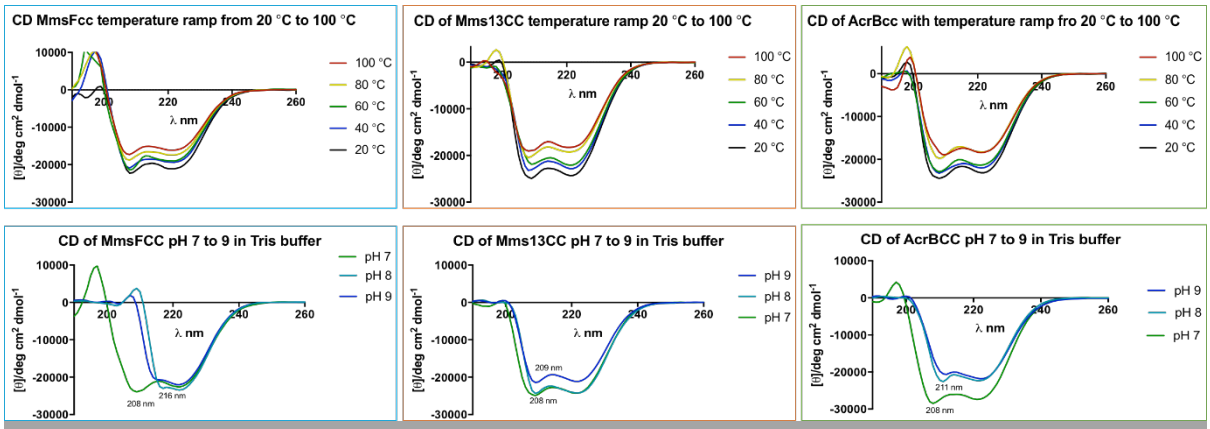

Conditions	MmsFCC ([θ] x 10^5 at λ_{222})	Mms13CC ([θ]x 10^5 at λ_{222})	AcrBCC ([θ] x 10^5 at λ_{222})
20 °C (pH 7)	2.11 (100%)	2.43 (100 %)	2.33 (100 %)
40 °C (pH 7)	1.93 (92 %)	2.29 (94 %)	2.20 (94 %)
60 °C (pH 7)	1.91 (91 %)	2.21 (91 %)	2.13 (91 %)
80 °C (pH 7)	1.74 (82 %)	1.92 (79 %)	1.83 (79 %)
100 °C (pH 7)	1.61 (76 %)	1.82 (75 %)	1.85 (79 %)
pH 7 (25 °C)	2.30 (100 %)	2.40 (100 %)	2.70 (100 %)
pH 8 (25 °C)	2.30 (100 %)	2.40 (100 %)	2.20 (81 %)
pH 9 (25 °C)	2.20 (96 %)	2.10 (88 %)	2.20 (81 %)

Table 12 CD heat ramp from room temperature to 100 °C (boiling point of the ultra pure water buffer), held for 2 minutes and pH effects (pH 7-9), using Tris buffer of the MmsFCC proteins with A values at 222 nm

Table 12 also shows the stability of the proteins from pH 7 to pH 9 using CD. A Tris buffer system was the buffer of choice as it does not absorb over 195 nm and so should not affect the peak intensities observed for the protein samples. A Tris only sample was run on the CD using the same experimental conditions and the resulting spectrum was subtracted from the sample data obtained. Again, each of the CC proteins appear to have similar stabilities over a range of temperatures and pH regardless of its active loop sequence, showing a universal scaffold protein displaying various peptide sequences. There was a slight difference in CD spectrum for MmsF at pH 7 compared to pH 8 and 9, however the [θ] at 222 nm remained consistent, suggesting retention of the α-helical secondary structure. Minimal unfolding is observed, showing the good chemical stability of the proteins and providing evidence that it would be a useful protein complex to be used in RTCP as it would not suffer from denaturation or precipitation towards more alkaline pH. Each of the pH measurements were recorded at room temperature, mimicking the conditions of the RTCP magnetite precipitation reaction.

CD was useful in confirming the high degree of α-helix secondary structure for each of the CC proteins analysed and indicating the high thermal and chemical stability. The majority of the protein sample remained folded in solution at temperatures reaching the boiling point of the buffer and the pH stability suggests that it would be a good protein to add to an *in vitro* magnetite chemical precipitation reaction.

The thermal stability was also analysed using DSC and DSF up to 70 °C. For the DSF analysis of the CC proteins, a fluorescent dye, Sypro Orange, was used to measure the protein unfolding as a function of time and temperature. The dye binds specifically to the hydrophobic residues within the protein and the increase in fluorescence upon binding was measured using a qPCR machine. As the hydrophobic residues are located within the core of the protein, they are inaccessible for binding by the fluorophore when coiled but become exposed and accessible as the protein unfolds as the temperature (or concentration of denaturant) increases. Therefore, the measure of the increase in fluorescence is proportional to the extent of protein unfolding and can be used to calculate the T_M of the protein.

Three MmsCC proteins, MmsFCC, Mms13CC and AcrBCC were analysed using DSF with Syrpo Orange. Two control reaction were also monitored. A positive control containing MmsFCC in a denaturing buffer; and a negative control containing only PBS with no protein present. The PBS sample showed no fluorescent response to the change in time or temperature (figure 83), whereas the positive control showed a significant increase in fluorescence that peaked around 30 °C. The T_M for the positive control was calculated as 22 °C (half the height of the major peak). The CC proteins, in PBS, each behaved in a similar way to the PBS negative control. No major transition peaks were observed for any of the MmsCC proteins. The samples appear to show a slight increase in fluorescence above 70 °C but appear to be thermally stable until this point as no fluorescent binding was observed, suggesting that the protein remained folded. These results match those collected from the CD analysis showing the proteins remain thermally stable at temperatures above 70 °C, making them a promising alternative for existing protein scaffolds.

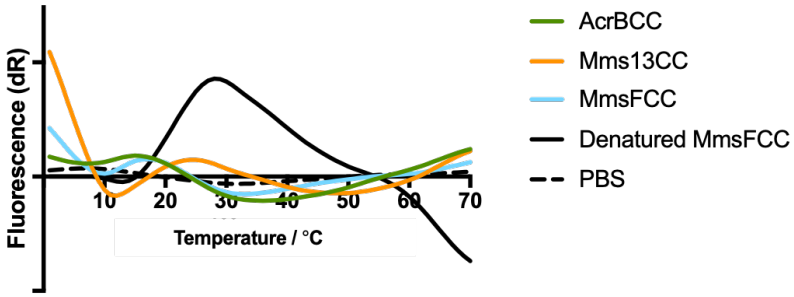

Figure 83 DSF unfolding data for the coiled coil proteins MmsFCC, Mms13CC and ArcBCC. Tracking the fluorescent signal upon unfolding for binding of Sypro Orange to hydrophobic residues. Peaks suggest a large degree of unfolding and therefore exposure of the hydrophobic core – therefore binding of the hydrophobic fluorescent dye was possible. The only major peak witnessed below 70 ℃ was for denatured MmsFCC. Proteins (1 mg mL^{-1}) were stabilised in a 1 x PBS buffer for analysis.

With the stability of the CC scaffold confirmed for use as a peptide displaying scaffold for MNP synthesis, the physical structure was analysed in more detail. A key characteristic for an artificial scaffold protein is for it to possess a small, monomeric structure. All of the analysis so far (SDS-PAGE, western blot, mass spectroscopy and CD) indicated that the CC proteins were forming monomeric complexes, but to confirm this, size exclusion chromatography was used. Firstly, samples of CC proteins were sent to the molecular interactions lab at the University of York, to be tested by Dr Andrew Leech, using SEC-MALLS. SEC-MALLS is a form of size exclusion chromatography that uses multi-angle laser light scattering to calculate the size of the eluted samples in terms of hydrodynamic radius and molecular weight. Each of the samples were prepared in PBS buffer at room temperature, as it had been confirmed that the CC proteins were stable in PBS and that the low salt buffer should not interfere with the binding of the sample to the stationary phase of the size exclusion column.

The SEC-MALLS plot is shown in figure 82 and gives data collected for the hydrodynamic radius of the proteins (using QELS). The analysis showed that the main peaks in the Mms13CC and AcrBCC samples had a R_h of roughly 2.7 nm (compared to BSA at 66 kDa with R_h around 3.4 nm). The MmsFCC signal is weaker, yet consistent with the other two CC proteins, implying that the material is smaller than would be inferred from the molecular weight estimates. R_h however is dependent on shape and so may not be a very reliable method for distinguishing monomer from dimer. It can be seen that the molecular weight estimates at the start of the peak are about 50 - 70 kDa but then rise steeply at the trailing side of the peak. This arises because the LS signal is declining slowly but the RI signal drops much faster. The RI signal is effectively a weight concentration measure, but the LS signal is proportional to molecular weight as well as to concentration. In size exclusion chromatography, large species are expected to elute earlier. One interpretation of the behaviour observed here for the C proteins is that there is an interaction with the column matrix delaying

elution which would explain the absence of material at the void volume. Unfortunately, it is very difficult to correct for this because the molecular weight estimates are being calculated on a mixture of different size species not separating in a normal manner. The estimated molecular weights will be higher than the true values but will not necessarily represent particular molecular species (oligomers). Therefore, SEC-MALLS using this set-up appeared to be unreliable for confirmation of the formation of monomers or higher order oligomers by the CC proteins.

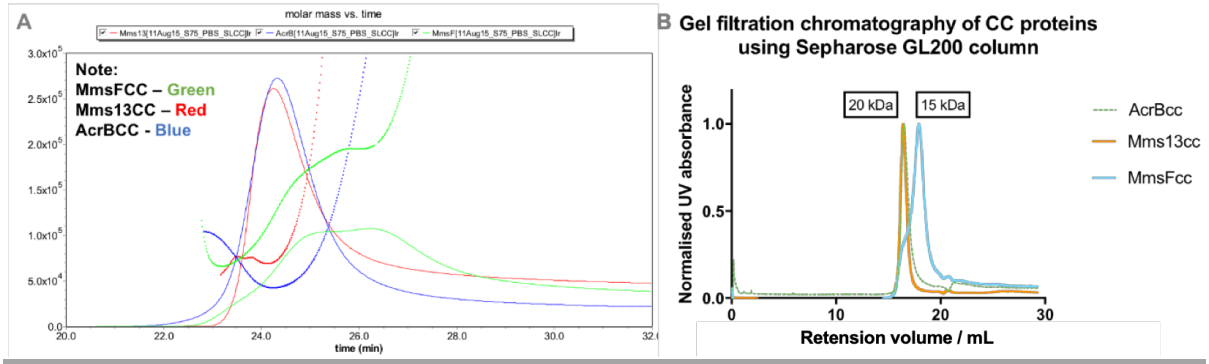

Sample	Expected MW/kDa	Vol/mL	(V_e/V_0)/mL	LogMW	Calculated MW/kDa
MmsFCC	15.0	17.5	1.11	1.17	14.9
Mms13CC	17.4	16.9	1.04	1,29	19.5
AcrBCC	16.3	17.0	1.05	1.27	18.6

Figure 84 The light scattering (LS) trace is solid, the refractive index (RI) trace dashed and the UV trace dotted. The molecular weight estimate is the thicker overlaid trace. A shows the SEC-MALLS data for the coiled coil proteins; note the change of colour for the samples. This data is likely to give an over estimate of the molecular weight of the proteins as described in the text. B is the gel filtration gathered using a Superdex GL200 size exclusion column to analyse the CC proteins based on size, the table shows the expected and calculated molecular weights. The plot was normalised for the three proteins, therefore maximum absorbance was measured as 1 and no absorbance was 0. Normalised data allowed comparison of the proteins that were measured at different concentrations (between 0.5 and 1 mg mL^{-1})

Therefore, a size exclusion column was tested to see if the CC proteins bound to the stationary phase. A Superdex 200 10/30 GL column was used for further size exclusion chromatography of the CC proteins. The column was run in the cold room using the AKTA system. Each of the proteins were analysed in PBS buffer as before. The retention volumes and therefore molecular weight of eluted samples had been calibrated for the column (see figure 33 for the calibration curve). The plot in figure 84B shows the retention volumes recorded for protein MmsFCC, Mms13CC and AcrBCC. Each of the samples gave a single sharp peak, indicating that a single protein species was present in the sample and also that the sample was clear of contamination. Also, as expected the Mms13CC and AcrBCC samples were eluted slightly before the MmsFCC, as they are larger proteins with a higher molecular weight and there are retained for less time in the stationary phase of the column. After comparing the results with the calibration plot the molecular weight of the proteins were calculated as: MmsFCC = 14.9 kDa; Mms13CC = 19.5 kDa; and AcrBCC = 18.6 kDa. MamFCC and MmxFCC samples also gave a single sharp peak, indicating that a single protein species was present in the

sample and also that the sample was clear of contamination. As expected each of the proteins eluted at a very similar time, suggesting they were the expected molecular weight and that each was monomeric. After comparing the results with the calibration plot the molecular weight of the proteins were calculated as: MamFCC = 15.1 kDa; and MmxFCC = 15.1 kDa. The MmsFCC and homologues match the predicted molecular weight, almost exactly. The other two samples appear slightly larger than would be predicted, however each of the peaks observed appear to indicate the formation of a protein monomer. The retention volumes are much too low (even for Mms13CC and AcrBCC) to suggest the existence of a dimeric or trimeric species. Therefore, it appeared that gel filtration successfully predicted the formation of a monomer for each of the CC proteins and importantly, each of the complexes appeared to be similar in this respect.

Finally, SAXS was used as a final confirmation of the morphology adopted by the CC proteins. This final technique aimed to conclusively confirm the presence of a rod-shaped hairpin structure for the monomer. SAXS was performed by Thomas Neal and Dr Oleksandr Mykhaylyk in the SMALL lab at the University of Sheffield. A SAXS experiment with purified MmsFCC was performed to determine the shape and overall dimensions of the coiled coil scaffold. A smooth curve was fit to the experimental data using GNOM software (see figure 85A), which yielded the pair-distance distribution function ($P(r)$) and a radius of gyration (R_g) of the scattering objects.[123] The obtained $P(r)$ pattern revealed that the MmsFcc protein did indeed adopt a rod-like shape with a maximum length of between 7 and 12 nm. Excitingly, these measurements were consistent with a MmsFCC structural model generated in Robetta with the His_6-tag present.[157] This model is shown in grey in figure 85B. Regular oscillations observed in the $P(r)$ are commonly observed for CC constructs and are due to the periodic nature coil. The (R_g) for MmsFCC in PBS was calculated as 3.7 ± 0.2 nm.

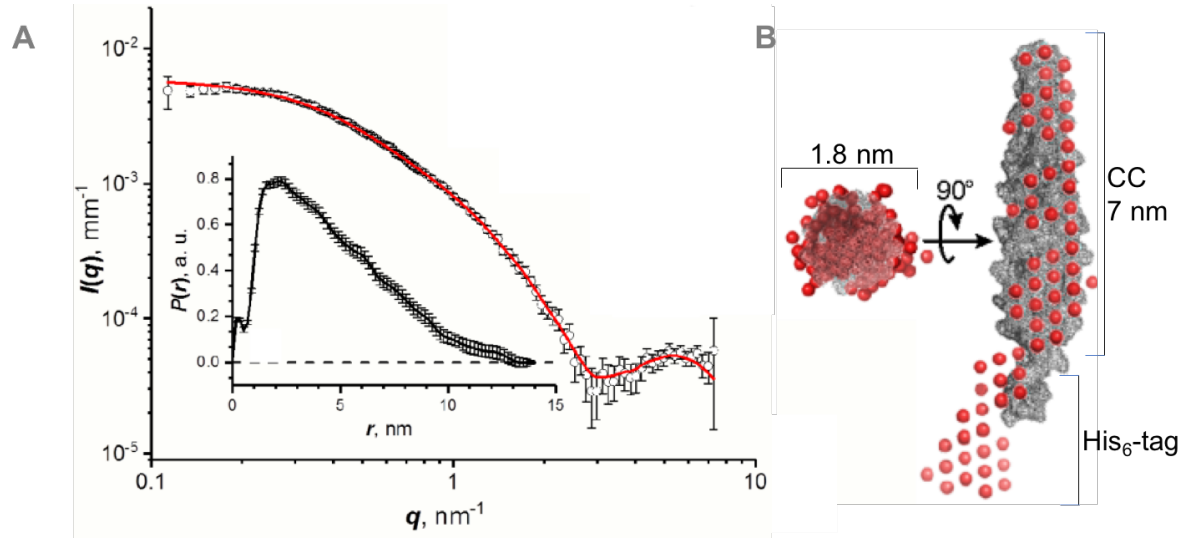

Figure 85 A shows the SAXS data collected for MmsFCC in PBS (700 µL, 2-3 mg mL^{-1}). The experimental data (open circles with fitted red line is shown in the large images, with the pair-distance distribution function inset. B is a schematic of the predicted protein structure using ab initio shape determinations (red spheres) overlapped on to a space filling model for MmsFCC using Robetta.[157]

The rod-like structure predicted using the experimental data obtained by SAXS further demonstrates a monomeric coiled coil construct. The dimensions predicted using this analysis also fit well with the predicted dimensions for monomeric, rod-shaped MmsFCC. Therefore, with SDS-PAGE, western blot, CD, gel filtration and SAXS in agreement, it is reasonable to suggest that the CC proteins adopt a monomeric, rod-like structure, with height in the region of 7 nm (12 nm inclusive of the His_6-tag) and a width of around 1.8 nm.

5.5 MmsCC additives in biomineralisation reactions

5.5.1 Optimisation of room temperature co precipitation (RTCP) reactions

Magnetite NPs were synthesised using the RTCP and the particles were analysed using TEM (figure 85). Grainsize and shape analysis was then performed on the images. The TEM image of the control particles in figure 85 gives an indication of the quality of the NPs with no protein additives. The particles include a variety of different shapes, sizes and morphologies which was expected when using the RTCP. Rod or needle-shaped particles are unlikely to be pure magnetite, with the reaction producing a mixture of iron oxides. These linear products are likely to be an iron oxide that is capable of forming elongated, acicular particles such as maghemite or goethite (γ-Fe_2O_3, α-FeO(OH) respectively).

CC proteins were introduced to normal RTCP and their effect on the MNP products was analysed. MmsF and Mms13 were predicted to bind to the magnetite or iron-containing precursors as the crystal was forming, promoting the formation of cubooctahedral magnetite nanoparticles as

observed in AMB-1 MTB. Figure 85 shows the NP characterisation resulting from the RTCP reaction with the addition of MmsFCC. Following the optimisation protocol established for the MIA proteins (section 3.5), MmsFCC concentrations of 5, 50 and 500 μg per reaction was analysed to confirm the optimum amount of protein required for the largest effect on particle size and shape. Magnetite NPs were synthesised using the RTCP method with the addition of 5, 50 and 500 μg of MmsFCC. The NP products were initially visualised using TEM and the images can be seen in figure 86, labelled 5 μg, 50 μg and 500 μg. The products from each of these reactions were visualised using TEM and powder X-ray diffraction. Grain size analysis was performed on around one-hundred particles from each reaction and the results were: upon the addition of 5 μg of MmsFCC the particle size was found to be 56 nm ± 22 nm; when 50 μg of MmsFCC was added, the size was 49 nm ± 28 nm; and for the addition of 500 μg the size was 77 nm ± 50 nm. There is no significant difference in size between the 5 and 50 μg reactions, however there is a significant increase in NP diameter and distribution of sizes when 500 μg of protein was added. The may be due to the excess protein acting as a contaminant in the reaction and leading to the formation of undesirable iron oxide products. Additional, unwanted iron oxide products are able to form platelets, rods and a number of different morphologies, giving a greater size and wider size distribution curve when compared to monodisperse magnetite products.

The largest difference observed between the reactions at the three MmsFCC protein concentrations was the shape analysis of the NP products. An initial indication of the shape of particle was obtained following visualisation of TEM images (figure 86). Analysis of the shape was not a trivial task, as it was difficult to group the NP shapes and morphologies allowing them to be presented in a way that would accurately represent the particles. ImageJ was used to measure the aspect ratios of roughly one-hundred particles from each of the reactions, the shape by eye was also accounted for. The particles were grouped into four classes: Misshapen; angular/cubooctahedral; spherical; linear. NPs were classified as misshapen if the aspect ratio was calculated to be between 0.25 and 0.75 and did not appear to exhibit any vertices equal to 90°. Angular or cubic NPs were found to have an aspect ratio of close to 1 (>0.75) and also appear to have corners equivalent or close to 90°. The sides of the particles also appeared straight when examined by the naked eye. Spherical NPs also had an aspect ratio of close to 1, however these particles did not have any obvious vertices and the sides were curved. Finally, NPs were classified as linear if the aspect ratio was close to 0 (<0.25), giving them a needle- or rod-like appearance.

The particles generated in the control RTCP reaction were mainly misshapen, therefore there was poor control over the shape of the NPs during synthesis, as discussed previously. The addition of 50

μg of MmsFCC to the 10 mL reaction volume resulted in the highest percentage of angular (likely cubooctahedral) particles and lowest number of misshapen particles. There were also the lowest number of linear particles observed out of each of the reaction conditions tested – suggesting that the sample contained the highest proportion of magnetite and lowest proportion of unwanted iron oxide side-products. Below the addition of 50 μg, it is unlikely that there is enough protein present to bind to the forming crystals and additionally, the protein mixture would be diluted, meaning that interactions between the crystal and MmsFCC would occur less often. This results in poorer size control compared to the use of higher protein concentrations. Above this concentration the CC may start to act as a contaminant, resulting in poorer quality products. The images of the particles synthesised with 500 μg of protein show a range of different shaped products, particularly the presence of thin plates of products suggesting that the reaction pathway is sensitive to changes in conditions and the increased organic content may push the dynamic equilibrium of the reaction towards the production of other types of iron oxides (plates are characteristic of green rust). However, there is still a significant percentage of cubooctahedral particles present in the RTCP reaction product, indicating that the MmsFCC does maintain some ability to control the shape of the forming crystals.

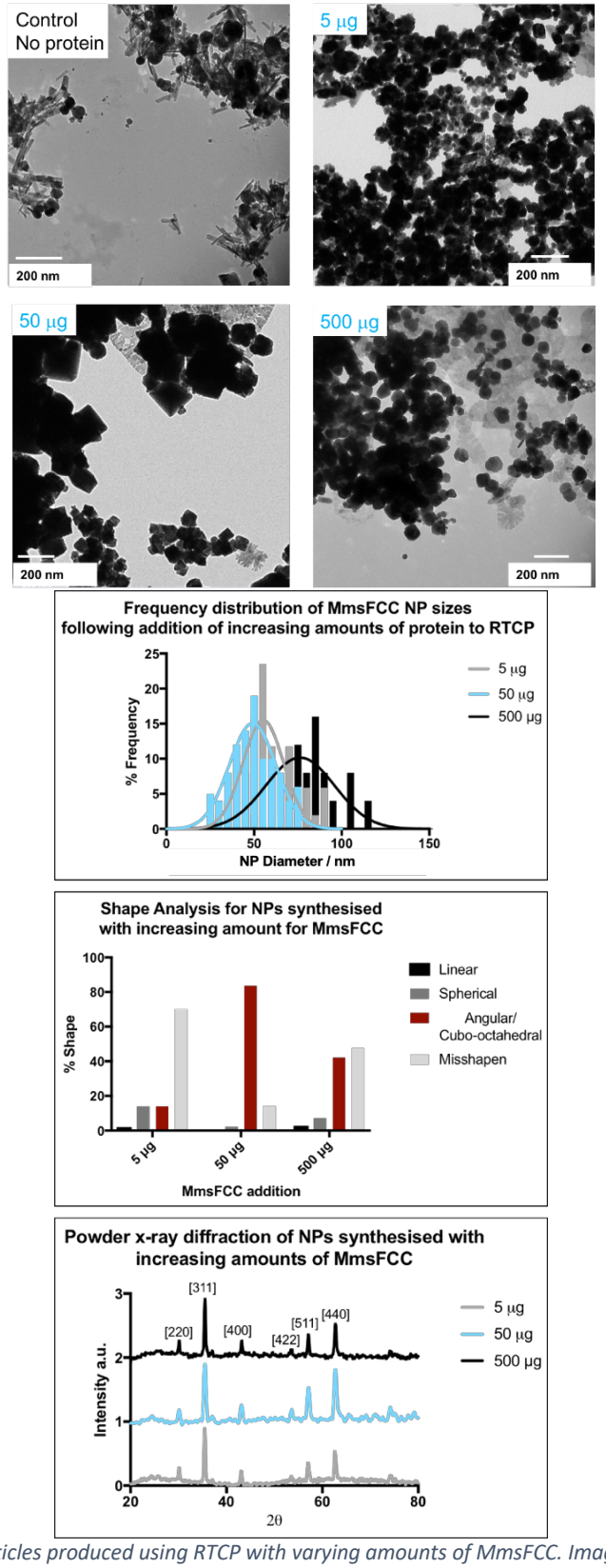

Figure 86 TEM images of particles produced using RTCP with varying amounts of MmsFCC. Images were obtained using Technai TEM. The negative control contains no protein and the other reactions had 5, 50 and 500 µg of MmsFCC added. Size and shape analysis were then performed using the TEM images and ImageJ software and were plot in GraphPad Prism for 100+ particle measurements. The NPs from each of the reactions were also analysed using powder XRD (5 µg grey, 50 µg blue, 500 µg black from 20 - 80 °). Each of the magnetite peaks are labelled, following comparison to literature values.

The composition of the magnetite crystals formed in the RTCP with increasing amounts of MmsFCC protein, were analysed using powder XRD between 20 and 80°. The position of the peaks from the base-line corrected data was converted into d-spacing, giving the inter-atomic distances within the crystals. It was expected that these peaks would match those reported in the literature and this was found to be the case for each of the samples. The labelled XRD peaks are shown in figure 86. From the XRD plot and the comparison to the literature values for d-spacing in magnetite it can be confirmed that the NPs produced in all three reactions consist mainly of magnetite. The crystallographic spectrum of the three samples (5, 50 and 500 μg) are similar and so the amount of protein added does not appear to have a significant effect on the crystal composition. As with XRD data obtained for previous magnetite samples, it is difficult to tell the difference between magnetite and other iron oxides such as maghemite and amorphous phases such as ferrihydrite, which would not show up. When looking at the TEM images after the addition of 500 μg of MmsFCC to the RTCP reaction, there does appear to be a visible amount of alterative product present, making these conditions unsuitable for controlling the reaction to the degree required. As mentioned above this is due to the protein beginning to behave as a contaminant, the additional organic content may be responsible to altering the pH of the reaction, shifting the established phases of the RTCP.

From this point forward RTCP were run with the addition of 50 μg of CC protein in the 10 mL reaction volume. This concentration gave the shape control desired for MmsFCC, whereas higher and lower concentrations of MIA were not able to match this effect. Additionally, at higher protein concentrations, other iron oxide products began to form, leading to weaker magnetic properties and large distributions in NP size and shape.

5.5.2 Particle characterisation

Following the optimisation of the RTCP with CC additives, particles were synthesised with the aim to characterise and understand their properties, including the magnetic properties; in order to generate a comparison with particles biomineralised by MTB and asses their use as potential biomedical agents. MmsFCC, Mms13CC and AcrBCC were initially used as additives for the RTCP as well as a control reaction with no protein. The particles were visualised using TEM shown in figure 87. The size and shape of the NPs were analysed as before with histograms, also shown in figure 87. The average size of the particles synthesised in the presence of: MmsFCC was 49 nm $\pm$ 28 nm; Mms13CC was 31 nm $\pm$ 20 nm; AcrBCC was 28 nm $\pm$ 32. The MNPs synthesised in the presence of AcrBCC had the smallest average size and largest distribution of sizes, similar to particles produced with no protein additives, as predicted. MmsFCC produced the largest particles, this result was in

agreement with the particles produced using MmsF wild type in RTCP reactions, where an increase in particle size, compared to the negative control, was observed. This is likely to be due to the availability of the AL as a binding surface, promoting crystal growth. Mms13CC particles were slightly larger than the control particles, again suggesting binding to the active peptide loop displayed on the CC scaffold, however the effect witnessed was not as severe as for MmsFCC. Mms13CC appeared to have the narrowest distributions of sizes, suggesting that the protein was able to control and limit crystal growth upon binding the particles. This may be due to strong binding interaction that occurs between the Mms13CC and the magnetite crystal.[72] Thus the binding of the CC proteins to iron ions and magnetite NP required further investigation.

The shapes of the particles generated in the presence of MmsFCC, Mms13CC and AcrBCC were compared. The bar graph depicting the shapes is shown in figure 87. The most interesting and promising shape observed was angular, likely cubooctahedral, represented by the red bar. AMB-1 MTB produce highly specific cubooctahedral magnetite crystals *in vivo*, therefore observation of this morphology *in vitro*, using a peptide displaying scaffold, shows great promise for mimicking the biomineralisation proteins in simple magnetite synthesis reactions. The number of angular NPs observed for the control RTCP reaction and after addition of AcrBCC was similar, with less than 5 % of the particles adopting this shape. The majority of the particles resulting from each of the reactions were misshapen (>80 %). Mms13CC also displayed a relatively low number of angular NPs, although slightly more were observed compared to reactions using AcrBCC and no protein additives. Around 15 % of the particles analysed appeared to adopt this shape, roughly triple the percentage for the control reactions. This suggests that Mms13CC and therefore Mms13 wild type are unlikely to play a role in controlling the shape of the forming magnetite crystal. The strong binding observed between the protein and the particle appears to have more of an effect when controlling the size of the particle produced, rather than the shape.

In contrast to this, MmsFCC appeared to have a significant amount of control over the morphology of the MNP synthesised using RTCP. The vast majority of the NPs produced were angular (likely cubooctahedral) and only a small number were misshapen. Over 80 % of the particles analysed adopted the desired shape, a substantial improvement compared to the other three reactions. This result aligns with the finding that MmsF plays an important role *in vivo* regarding control over the magnetite crystal formation and the adopted morphology. It thus strongly suggests that the MmsFCC construct is able to mimic this behaviour of MmsF *in vitro*, using ambient reaction conditions and a stable protein that can be easily produced using bacterial expression. As the size

and shape of the particles produced in the presence of MmsFCC differ significantly from the particles produced using AcrBCC, it is clear that the CC scaffold is not responsible to the results witnessed and the AL taken from the MTB is required for the activity.

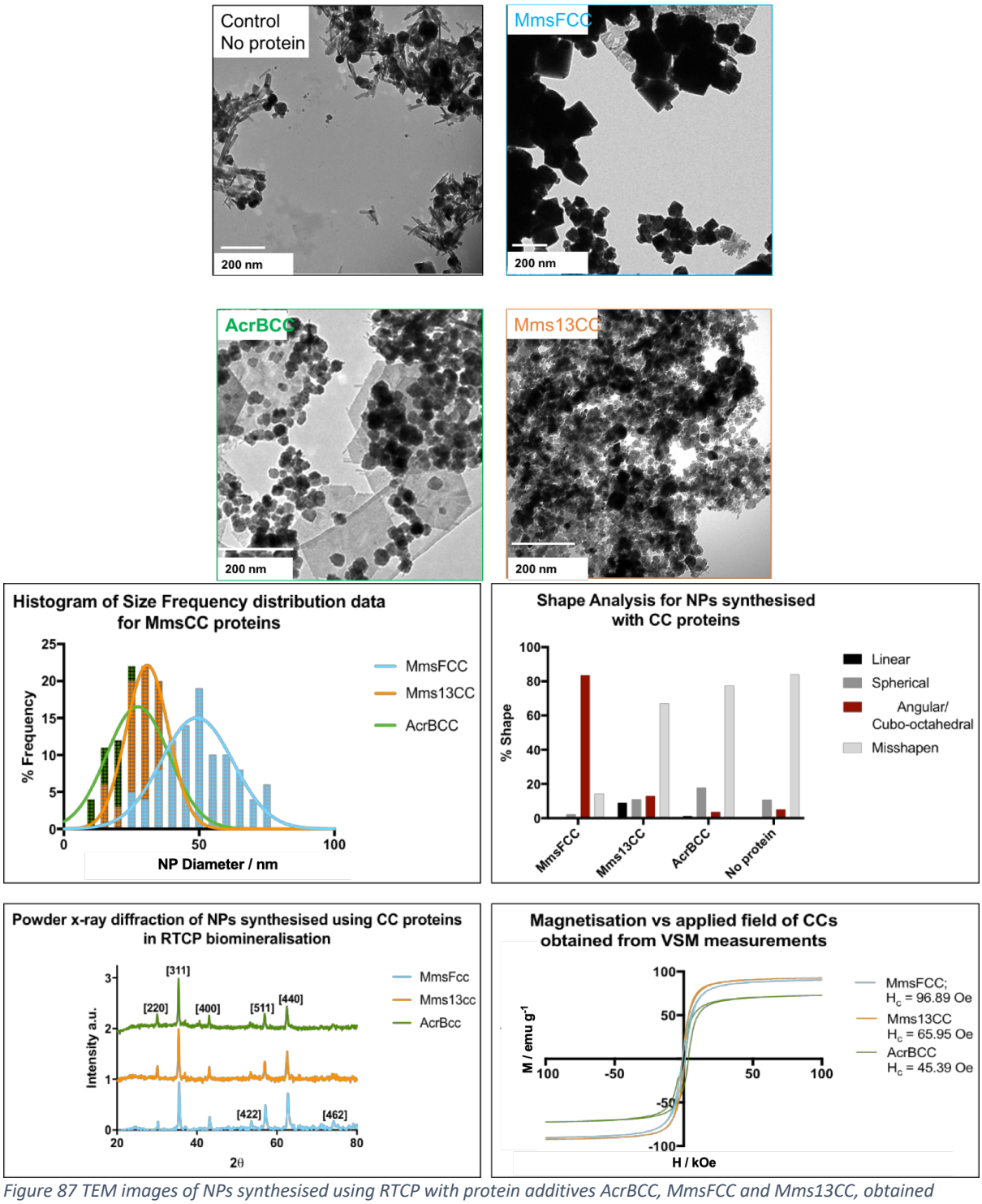

Figure 87 TEM images of NPs synthesised using RTCP with protein additives AcrBCC, MmsFCC and Mms13CC, obtained using Techain TEM. Analysis shows the grain size analysis, shape analysis, powder XRD data and VSM data (MmsFCC = blue, Mms13CC = orange and AcrBCC = green, all plot on Graphpad Prism). When particles required a buffer 1 x PBS was used.

For further confirmation of the crystal structure adopted by MNPs synthesised with MmsFCC additives, HR-TEM was used. Allowing the study of crystal lattices and specific facets which then describe the mineral morphology. Although regular TEM was able to give a good indication of the shape and size of the MNPs, the resolution was not high enough to observe and calculate the crystal

planes within a single particle. HR-TEM was used for this purpose. The sample was visualised at the electron microscopy and spectroscopy centre at Leeds University, with the help of Dr Zabeada Aslam. An image captured, with the electron diffraction figure inset, is shown below in figure 88. The crystal lattice planes were observed, and ImageJ was used to measure the distance between the planes. The average spacing between ten observed planes was calculated and compared to the value expected for magnetite. Analysis of the lattice fringes from MmsFcc prepared particles using HR-TEM confirmed the presence of [111] and [311] planes of magnetite, consistent with an octahedral morphology. This was not observed in the samples produced with any of the alternative coiled coil constructs.

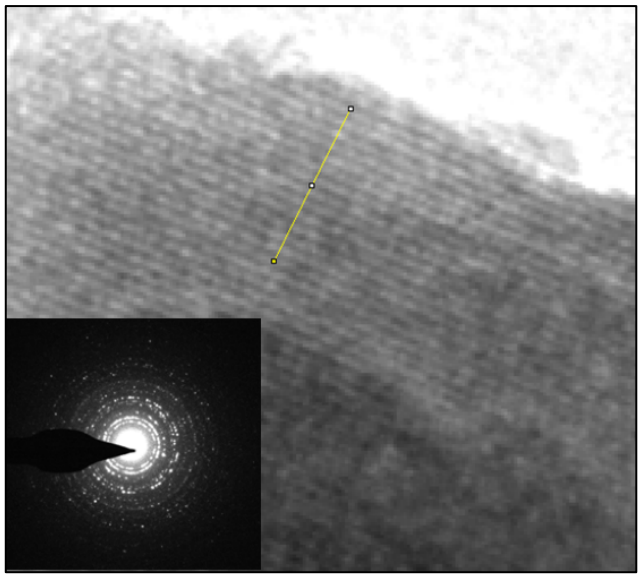

Figure 88 HR-TEM image and electron diffraction of a NP synthesised in the presence of MmsFCC. The image shows the lattice fringes visible on the particle and was used to confirm an octahedral morphology formed by the magnetite NP.

Powder XRD with an incident X-ray source of λ = 1.5418 Å was used to confirm the major product of the RTCP reaction was magnetite. This was shown for each of the CC constructs. The data did indicate the formation of magnetite with peaks at 2θ equal to that expected for magnetite (shown in table 13).

Table 13 Powder XRD peaks and d-spacing comparing the synthesised MNPs to known facets of magnetite

CC XRD peak (°)	Calculated d-spacing (Å)	d-spacing in magnetite (Å)	Magnetite facet
30.32	2.95	2.966	[220]
35.70	2.52	2.530	[311]
43.41	2.09	2.096	[220]
53.58	1.71	1.712	[422]
57.30	1.61	1.614	[511]
62.84	1.48	1.483	[440]
74.39	1.28	1.279	[462]

The data fits well to the d-spacing expected for magnetite and so strongly suggests that the majority of the crystals formed in a RTCP with the addition of MmsFCC, Mms13CC and AcrBCC are magnetite. It also suggests that the crystals are somewhat resistant to oxidation or hydrolysis which would result in the conversion of magnetite to other forms of iron oxide. It is important to note however, that some other forms of iron oxide are difficult to observe using powder XRD. When comparing the XRD data to the TEM images it is clear to see that the control and AcrBCC reactions contain other mineral deposits such as platelets and needles. These are not magnetite but are not picked up on the XRD spectra. The MmsFCC and Mms13CC appear much purer based on the TEM images, suggesting that they promote the formation of magnetite, as they do in MTB.

VSM can be used to compliment XRD as magnetite is the most magnetic form of iron oxide and it would be expected that if the sample was magnetite it would show a greater response to an applied magnetic field. Although VSM is unable to distinguish between a less magnetic mineral and two mixed very magnetic and non-magnetic minerals, it can show pure magnetite verses an impure sample. VSM at room temperature was used to analyse the magnetic response of the MNPs synthesised in the presence of the CC proteins. For particles synthesised with MmsFCC or Mms13CC a uniform magnetic response would be expected as the particles were relatively uniform in size, shape and morphology. This is vital for the MNPs use in applications for example in clinical therapies or diagnostics. The majority of the NPs synthesised in this way have a diameter which lies above 30 nm. This size means that the NPs are single domain MNPs, not superparamagnetic as observed for particles synthesised with MIA additives (chapter 3). Magnetite particles below 80-90 nm are often classed as single domain and those below 20 nm are superparamagnetic. The VSM plot in figure 89

shows the effect on the particle magnetisation on the addition of an applied magnetic field. Analysis of the data allowed the magnetic saturation and the coercivity (H_c) of the NPs to be calculated.

The saturation magnetisation was calculated as a function of the mass of product analysed. The magnetic saturation values were similar for particles synthesised with MmsFCC and those synthesised with Mms13CC (88.35 emu g^{-1} and 89.69 emu g^{-1} respectively). These values also fit with the expected magnetic saturation of pure magnetite – 91 emu g^{-1}. The magnetic saturation of AcrBCC synthesised MNPs and MNPs synthesised in the absence of protein additives was significantly lower (around 71 emu g^{-1}), suggesting that the sample was not pure magnetite, with other mineral forms present. The hysteresis loop for each sample is relatively narrow, with H_c values of 96.89 Oe, 65.95 Oe and 45.39 Oe for MmsFCC, Mms13CC and AcrBCC particles respectively. The width of the hysteresis loop suggests that the magnetite NPs are soft magnets, the presence of the loop confirms they do not fit within the SPM boundaries. MmsFCC particles were found to have the largest hysteresis loop out of each of the constructs examined. This can be a favourable trait for a number of applications as the particles are easy to magnetise and demagnetise, making ideal temporary magnets. AcrBCC particles had the narrowest hysteresis loop, again indicating the presence of amorphous iron oxide within the sample.

The presented magnetic data suggests that the addition of the MmsFCC and Mms13CC increases the magnetic saturation and coercitivty of the magnetite NPs by forming a pure magnetite sample compared to the control reactions. The uniform magnetic properties observed make them promising particles for a range of applications. These magnetic properties are the result of more highly controlled synthesis reactions, leading to increasing purity and monodispersity.

5.5.3 Investigating MmsF peptide in RTCP reactions

RTCP reactions were also performed in the presence of wild type MmsF ($MmsF_{wt}$) and the MmsF peptide (the peptide region linking TM helices 1 and 2, figure 89) to access the need of the CC scaffold. As before, the resulting particles were visualised using TEM and the same and size calculated from the images (figure 89). MmsFCC and $MmsF_{wt}$ particles were similar in size and shape to each other and to the magnetite crystal formed *in vivo* (MmsFCC = 49 nm $\pm$ 28 nm; $MmsF_{wt}$ = 53 nm $\pm$ 23 nm; and 56 nm *in vivo*). Also, for each of these reactions around 80 % of the resulting MNPs adopted a cubooctahedral morphology, similar to the magnetite crystal synthesised by MTB. This confirms the activity of the protein is largely due to the active peptide region, accessible to the forming magnetite crystal. The TM regions of the protein and the CC scaffold of the MmsF construct

do not appear to possess any activity for controlling magnetite synthesis. These regions of the protein are responsible to holding the flexible peptide region in position, preventing conformational freedom and promoting binding. As the peptide region was confirmed to be the essential region of the protein, the activity of the flexible peptide alone was analysed.

MNPs were synthesised in the presence of the MmsF peptide ($MmsF_{pep}$) and visualised using TEM. The size and shape of the particles varied significantly compared to the MmsFCC and $MmsF_{wt}$ synthesised particles. There was a much wider distribution of particle sizes calculated for the peptide-synthesised MNPs (see figure 89). The average size was also larger compared to the protein samples: Mms_{pep} = 126 nm $\pm$ 98 nm, suggesting that it does alter the reaction product compared to the control reactions (addition of AcrBCC or no protein) however the control of the particle synthesis is extremely poor.

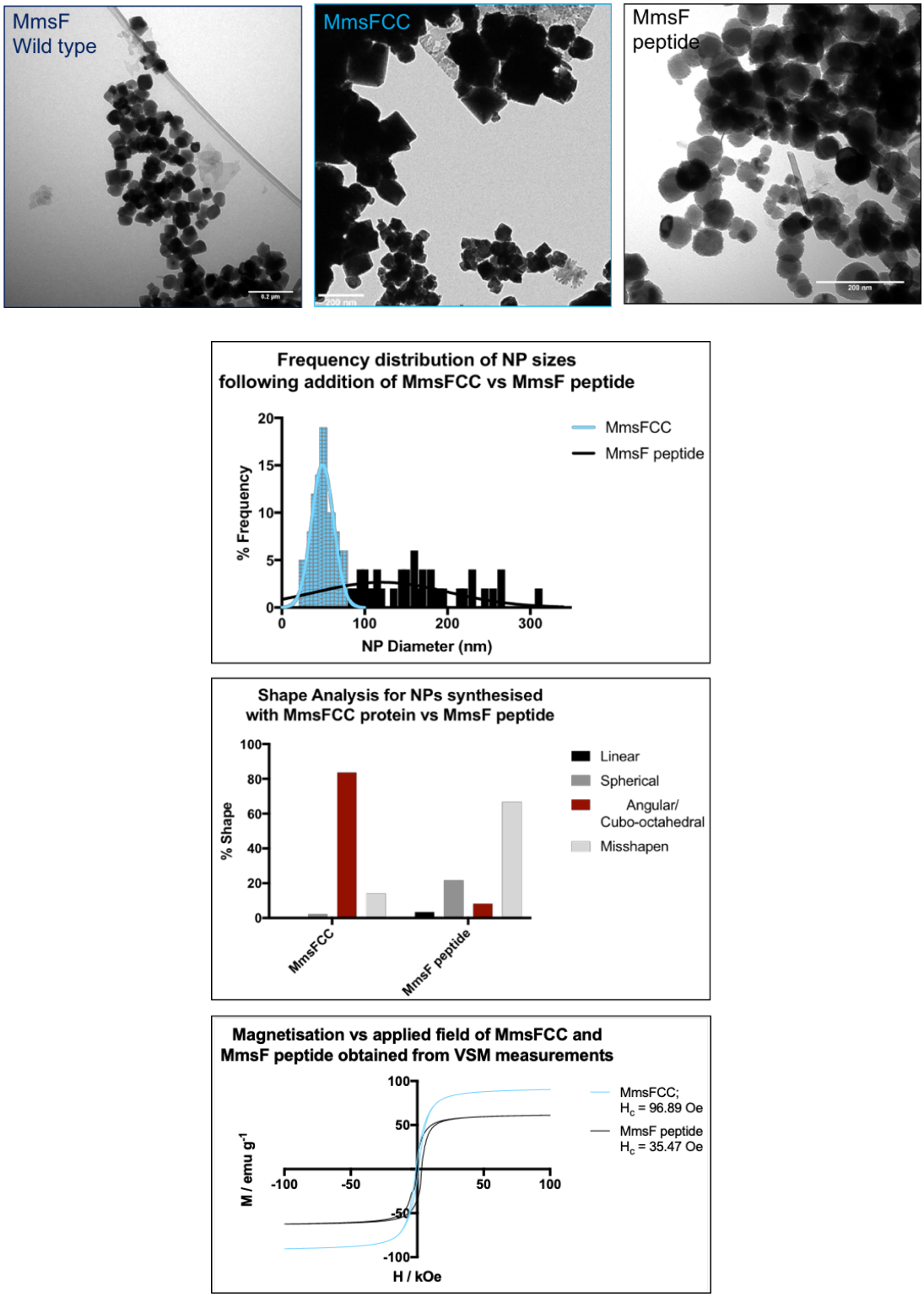

Figure 89 TEM images of MNPs synthesised using RTCP with $MmsF_{wt}$, MmsFCC and $MmsF_{pep}$ obtained from Technai TEM. Analysis of the size, shape and magnetic properties of the MNPs were prepared using GraphPad prism and are presented to compare the properties of the MNPs synthesised with MmsFCC (blue) and $MmsF_{pep}$ (black). Size, shape and magnetic properties varied significantly between the protein scaffold and the peptide.

This is likely due to the formation of undesirable iron oxide products in the $MmsF_{pep}$ synthesis reaction. The poor control of $MmsF_{pep}$ was also observed when analysing the shape of the particles

produced. The percent of angular particles generated reverted to that of the control reactions (around 5 %) and the majority of the observed MNPs appeared misshapen. Therefore, $MmsF_{pep}$ did not appear to have any control over the shape of the magnetite particles synthesised, confirming the need for a rigid scaffold capable of holding the peptide in the required position for binding.

The magnetic properties of the crystals synthesised with $MmsF_{pep}$ were also analysed. The magnetic analysis was carried out using VSM as a comparison between MmsFCC and $MmsF_{pep}$ synthesised MNPs (figure 89). Both the saturation magnetisation and coercivity of the MNPs were much lower for the $MmsF_{pep}$ products compared to MmsFCC products (M_s/H_c for MmsFpep = 52 emu g^{-1}/35.47 Oe; for MmsFCC = 88.35 emu g^{-1}/96.89 Oe). The quality of NPs synthesised with $MmsF_{pep}$ is decreased, even compared to the control reaction. The reason for this is likely to be similar to the MIA peptide control. Although the peptide may be able to bind to the magnetite or magnetite precursors in the reaction, it cannot template the crystal formation as the reacting species are able to access the sequence from any direction and angle. This also explains why the particles are larger than particles synthesised with no additives, or additives that are unable to bind magnetite/magnetite precursors. The peptide could act as a nucleating site, promoting early crystal formation, which also provides a site to promote crystal growth – resulting in large, misshapen crystal products. However, if this was the case it would be expected that the magnetic data for $MmsF_{pep}$ would be similar to MmsFCC and $MmsF_{wt}$. This is not the case; therefore, it is unlikely that it promotes the formation of magnetite and so is unlikely to act as a nucleating surface. It is interesting that the NP quality is drastically worse than the control MNPs.

Therefore, a form of protein scaffold is required to mimic MTB in the synthesis of magnetite NPs. A flexible peptide is unable to control the size and shape of the resulting particles. It could be that the peptide is able to bind any oxide, with no preference of specificity. This poor control lead to poor magnetic properties and therefore the particles would not be useful for applications requiring a high degree of control. The CC scaffold displays the active loop region from the Mms proteins in a similar configuration to that proposed to be displayed in the native protein. It offers a simple, soluble, scaffold to display and topologically constrain functional peptide loops from difficult to work with proteins. This has promising implications, including: a platform for the study of the active region of membrane proteins, enabling in-depth characterisation; the use of previously inaccessible proteins for synthesis in biotechnology and; the possibility of scaling up to commercial levels of synthesis.

5.6 Binding of the MmsCC to MNPs

5.6.1 Binding to magnetite NPs vs iron ions

Binding strength and interaction between the NPs and the CC proteins was analysed using an ELISA and secondary recognition antibody, tagged with AP, on pre-synthesised magnetite MNPs. Magnetite NPs with a size of roughly 30 nm were synthesised using RTCP, however there were a range of sizes present as no biomineralisation protein or other additive had been used to control the products. As no protein was present in the RTCP, it could not give a false positive in the binding assay. Firstly, the binding of MmsFCC, Mms13CC and AcrBCC to these magnetite MNPs was measured. The binding intensities are shown in figure 90. Minimal binding was observed for AcrBCC, as predicted (roughly 66 % weaker than Mms13CC to magnetite NPs and 88 % weaker than for MmsFCC to magnetite NPs). The subtle colour change suggested a potential low-level interaction. The results from the negative control (AcrBCC binding) indicate that the CC scaffold, or the presence of the His_6-tag alone, were not sufficient in providing a strong, positive interaction with magnetite. Therefore, if a strong binding event was observed for the other CC proteins, it would be confirmed that the AL was the site of binding.

MmsFCC and Mms13CC both produced a high intensity colour change during the ELISA, suggesting a positive binding event. MmsFCC appeared to bind more strongly to the magnetite NPs compared to Mms13CC. Although both proteins were expected to bind after reviewing previous literature, it was suggested that Mms13CC would bind most strongly as this was a protein identified to remain bound to the magnetite crystal formed in MTB after harsh and extensive washing stages.[72] Interestingly, MmsFCC was not identified in this study, however it showed stronger binding capabilities under the conditions used in the ELISA. These reaction conditions differ to the harsh conditions used in the previous study, therefore the charges present on amino acid side chains of the active loops will be different, resulting in slightly different binding strengths observed. It is important to compare this result to data obtained for Mms6. Mms6 was identified at the same time as Mms13 and does not bind to magnetite surfaces. Mms6 and Mms13 are nucleating proteins and so are only stuck to the crystal if the mineral has been formed on them. MmsF is the opposite to this – it is able to bind after formation and involved in the growth of the crystal.

Binding of the CC proteins to iron (II) ions was also analysed. This was done using a pull-down assay where protein samples were applied to a nitrocellulose membrane, before the membrane was exposed to a solution of the iron salt. Increased iron binding produced a darker spot on the membrane. Ferritin samples were also added to the nitrocellulose membrane, alongside the CC proteins, to act as a positive control. It is well documented in the literature that ferritin binds

strongly to iron (II) ions and therefore a strong signal was predicted for the ferritin dots.[156] This was observed and shown in figure 90. The ferritin binding was much more intense than any of the CC proteins. However, the opposite preference for binding, compared to the magnetite NP binding, was observed, with significant binding measured for Mms13CC binding iron. No significant binding was observed for AcrBCC or MmsFCC suggesting that MmsF does not play a role in recruiting the iron ions during the initiation of the crystallisation (nucleation), binding occurs at a later stage of the reaction, closer to the final formation of magnetite and is therefore likely to be essential for the growth and shape definition of the magnetite crystal, not the nucleation. Alternatively, Mms13CC appears to have a different role and is able to bind throughout the crystal formation process which may influence both the nucleation and growth stages; explaining the control observed over the size but not the shape of the MNPs synthesised.

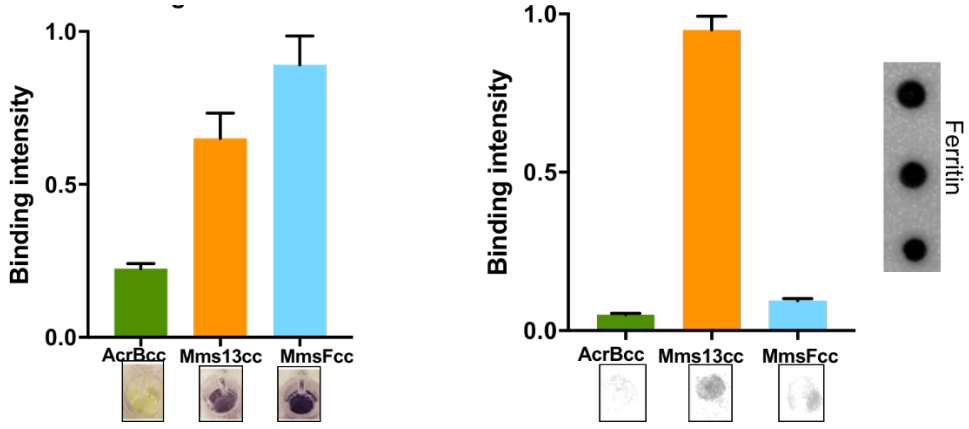

Figure 90 Binding analysis of CC proteins to pre-made magnetite NPs using an ELISA (left) and binding of CC proteins to ferrous ions was measured and displayed using a dot blot/pull-down protocol (right). AcrBCC is indicated in green, Mms13CC in orange and MmsFCC in blue. Normalised binding intensity was calculated to draw clear conclusions between the two experimental protocols. In the results for the ELISA binding assay, a yellow colour suggested no or minimal binding of the protein ligand and for the western blot, the darker the 'dot' the stronger the binding. Binding of ferritin to Fe(II) was used as a positive control and showed intense 'dots' on the western blot – suggesting strong and specific binding.

The capability to bind ferrous ions (which are present at the initiation of the RTCP reaction) rather than the growing magnetite MNP, is characteristic of a nucleating function, rather than morphological control. The data here shows that Mms13CC is able to bind ferrous ions, whereas MmsFCC does not, indicating a different type of control over crystallisation between these two proteins. If extrapolated further, it could be suggested that Mms13 is a nucleation protein and therefore may require self-assembly functionality. The native Mms13 protein has the ability to aggregate, however, this aggregation is not observed for the Mms13CC construct, which could be a reason for no significant control over the NP formation being observed. MmsFCC on the other hand, does not bind ferrous ions and does exhibit morphological control over the MNP formation. This indicates that MmsFCC is

employed later on in crystal formation and does not need to aggregate to be effective. This comparison can be used as evidence for the different roles Mms proteins, specifically MmsFCC and Mms13CC, have in the crystallisation process and the different characteristics required to perform each of these roles.

The stage at which MmsFCC showed optimum binding was examined further. The RTCP reaction was performed (in the absence of protein additive) and tracked using pH measurements. The pH curve was used to indicate where to quench the reaction following the formation of different iron oxide products. The initial product formed was ferrous hydroxide (orange product show in figure 91). Next was green rust and finally, magnetite was formed. An ELISA was then used to measure the binding intensity of MmsFCC to each of the reaction products. These measurements are shown in figure 91. In agreement with the previous iron binding assay, the weakest binding was observed for the ferrous hydroxide product, towards the start of the reaction. Optimum binding appeared to be achieved around the time of the formation of green rust ($[Fe_4^{2+}Fe_2^{3+}(OH^-)_{12}]^{2+}$. $[SO_4^{2-} . 2H_2O]$) in the middle of the reaction. During the formation of GR ferrous ions become oxidised, resulting in a mixture of ferrous and ferric ions. The iron ions fill octahedral sites of the hexagonal crystal structure, generating positively charged sheets with sulfate anions intercalated between the sheets. The increased proportion of ferric ions present in the reaction mixture, and the accessibility of positively charged layers is likely to be preferential for binding of the acidic groups of the MmsFCC AL. This gives a stronger binding interaction between MmsFCC and GR, compared to ferrous hydroxide. The binding of MmsFCC during the GR stage of the reaction suggests that the protein is required to be bound to the magnetite precursors, prior to the formation of magnetite, to ensure early and complete control over the shape of the MNP synthesised. The binding then decreased slightly for the final magnetite product.

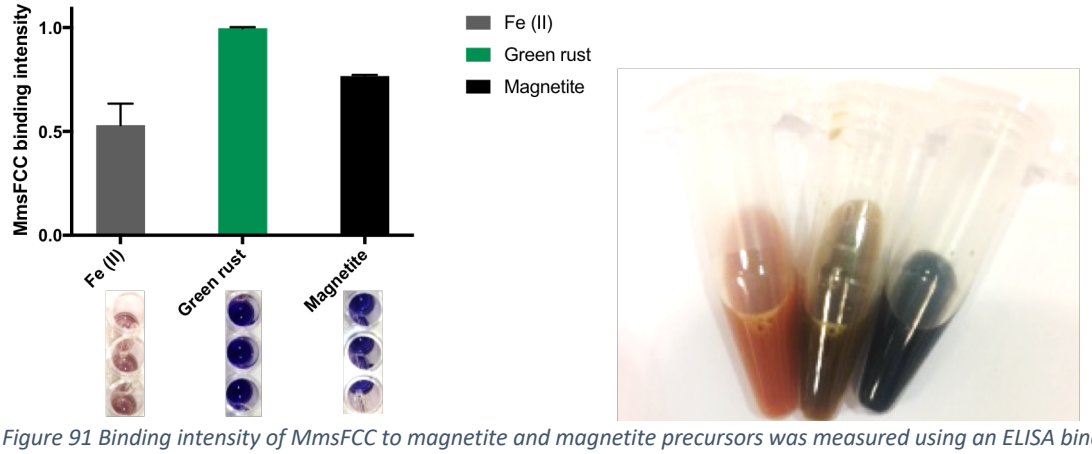

Figure 91 Binding intensity of MmsFCC to magnetite and magnetite precursors was measured using an ELISA binding assay, measuring final A_{600} values. The results were recorded and shown of the plot created in GraphPad prism. The first bar

represents binding of MmsFCC to Fe(II), the middle, green bar shows binding intensity of MmsFCC to green rust (a precursor to magnetite when using iron sulfate salts) and the black bar shows binding intensity to magnetite NPs. For the ELISA a more intense blue/purple colour suggests stronger and more specific binding. The aqueous RTCP reaction products are shown (left)

5.6.2 Binding of MamFCC and MmxFCC to MNPs

Binding strength and interaction between the NPs and MamFCC and MmxFCC proteins was analysed using an ELISA on pre-synthesised magnetite MNPs and compared to the binding intensities observed for MmsFCC and AcrBCC when binding magnetite. A system utilising AP was used. Magnetite NPs with a size of roughly 30 nm were synthesised using RTCP, however there were a range of sizes present as no biomineralisation protein had been added to control the products. As no protein was present in the RTCP, it could not give a false positive in the binding assay. The binding intensities are shown in figure 92.

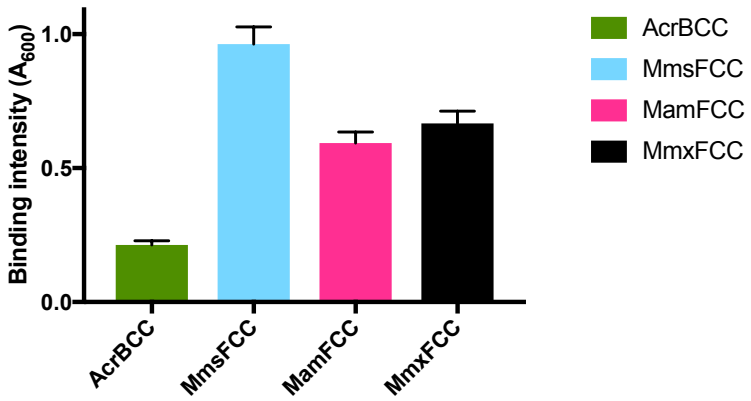

Figure 92 A plot of the binding intensities of AcrBCC (negative control, green), MmsFCC (blue), MamFCC (pink) and MmxFCC (black) to magnetite NPs is shown. Data collected using an ELISA protocol in 1 x PBS buffer at room temperature.

As before, minimal binding was observed for AcrBCC (roughly 88 % weaker than for MmsFCC, 60 % weaker than MmxFCC and 55 % weaker than MamFCC to magnetite NPs).

MmsFCC produced a high intensity colour change during the ELISA, suggesting a positive binding event. MmsFCC appeared to bind more strongly to the magnetite NPs than either MamFCC or MmxFCC, however, both of the other proteins did appear to bind to the MNPs to some degree. MmxFCC appeared to bind slightly more strongly than MamFCC. The decrease in binding of MamFCC and MmxFCC to magnetite NPs could provide clarification as to why they do not show the same ability to control the size, shape or composition of magnetite crystals when synthesised *in vivo* or *in vitro*.

5.7 MmsF mutants

To examine the source of activity of the MmsF active loop region and understand why MamF and MmxF proteins do not display the same control over magnetite crystal synthesis, *in vivo* or *in vitro*, a number of mutant proteins were designed and synthesised. The sequences ranged from MamF, making point mutations to reach MmsF and the mutating further to give MmxF. Each of these peptide sequences were displayed on the CC protein scaffold and added to RTCP reactions.

5.7.1 Design of the MmsFCC mutants

The mutant constructs were generated using site directed mutagenesis of MmsFCC. The mutant oligonucleotide primers for each of these mutations were purchased from Thermo FisherScientific and the sequences can be found in the appendix (4.4). The AL for each of the homologues and mutants are displayed in figure 93. The CC scaffold was unchanged from the scaffold used to display the active loops of MmsF, MamF, MmxF, Mms13 and AcrB and therefore it can be confidently assumed that any activity arising from the new constructs can be ascribable to the AL sequence.

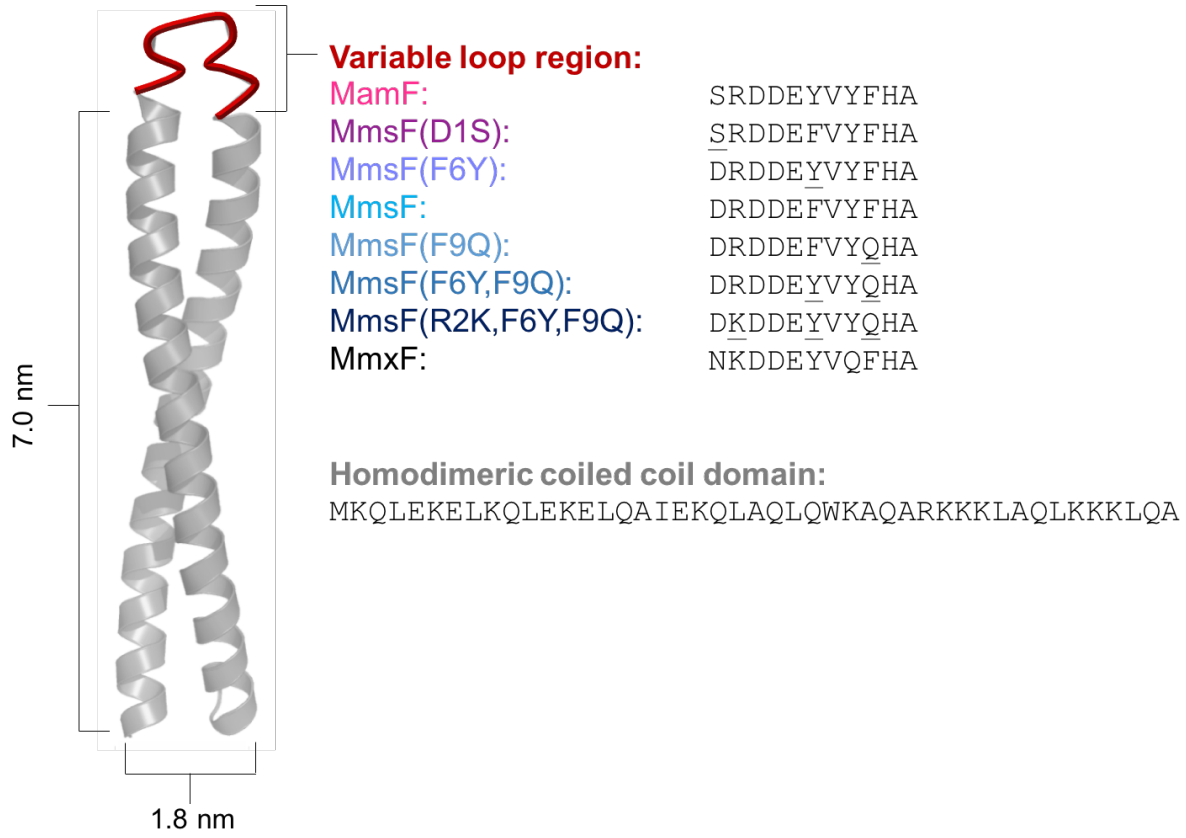

Figure 93 A Robetta schematic of the CC peptide displaying scaffold, with the sequence of each of the MmsFCC muatnts designed, synthesised and analysed.[157] The red hairpin loop at the top of the scaffold shows were the variable sequences are displayed.

The loop sequence of MmsF is split into three regions with different properties: the initial five residue region is highly-charged and consists mostly of acidic residues; next is an aromatic-rich region consisting of four residues; finally followed by four charged or polar residues. The variability between the MmsF, MamF and MmxF proteins is located to the first two regions. The charged/polar region is conserved between the homologues and was therefore left unchanged. The design and synthesis of the new mutant constructs comprised of the alteration of a single amino acid in both of the variable regions; generating MamFCC (D1S, F6Y) and two amino acids mutations in both of the regions to generate MmxFCC (D1N, R2K, F6Y, F9Q). As MmsF was sequentially mutated to yield MamFCC and MmxFCC, the sequences resulting from each of these point mutations were analysed. When mutating from MmsFCC to MmxFCC, (compared to MamFCC) there was an extra mutation in the aromatic region.

5.7.2 Mutant production

Each of the mutants were synthesised using site directed mutagenesis starting from MmsFCC, MamFCC or MmxFCC – whichever sequence required the smallest number of mutations. The PCR products were analysed using gel electrophoresis before being sent for sequencing to confirm the success of the mutagenesis reaction. Sequencing for each of the MmsFCC mutants yielded a positive result with the sequence appearing identical to that designed. Protein production and characterisation was then performed using the same methods as used for the other CC proteins.

5.7.3 Additives in biomineralisation reaction

Following the synthesis of MmsFCC mutants, particles were synthesised in the presence of the CC additives. The MNP properties were characterised with the aim of understand how the proteins affected their formation, by identifying important residues and characteristic regions required for the control of magnetite synthesis. MmsFCC, MamFCC, MmxFCC and each of the sequential mutants were initially used as additives for the RTCP. The particles were visualised using TEM with images shown in figure 94. The shapes and sizes of the NPs synthesised were analysed using ImageJ, the data plot and a Gaussian curve fitted to obtain a size distribution. It should be noted that the large, hexagonal, green rust platelets, observed for some of the MNP samples, were not included in the size analysis. Three histograms of the frequency distributions observed are also shown in figure 94. The first graph shows how the size MNPs synthesised in the presence of MmsFCC varies compared to when synthesised with MamFCC or MmxFCC additives. The average size of the particles synthesised in the presence of: MmsFCC was 49 nm $\pm$ 18 nm; MamFCC was 81 nm $\pm$ 45 nm; MmxFCC was 71 nm $\pm$ 41. MmsFCC produced particles with the smallest average diameter and the size most

closely resembling MNPs formed in AMB-1 magnetosomes. MamFCC and MmxFCC particles were slightly larger than both the control particles and particles synthesised with MmsFCC additives. There was also a much larger distribution of sizes observed for these reaction products, suggesting poor shape control, as predicted when considering the full-length protein.

The second histogram shown in figure 94 (from left to right) presents the size distribution of the MNPs synthesised with MmsFCC, MamFCC and the constructs containing point mutations for the transition of MmsFCC to MamFCC. As explained above, MmsFCC gave particles of a similar size to wild-type particles and MamFCC gave much larger particles with a wide distribution of diameters. Interestingly, the MNPs synthesised with the MmsFCC(F6Y) mutant gave particles with an average size extremely similar to that of MmsFCC (51 nm $\pm$ 13 nm). On the other hand, MNPs synthesised in the presence of the MmsFCC(D1S) mutant yielded much smaller particles compared to the MmsFCC (22 nm $\pm$ 18 nm). This particle size is similar to NP diameters observed for control RTCP reactions, with no protein additives. However, the size distribution of the particles synthesised with MmsFCC(D1S) is narrower than observed for control MNPS.

The final histogram of the frequency distribution of NP size is shown in the right of figure 94. The plot presents the measurements and distribution of sizes for MNPs synthesised with MmsFCC and MmxFCC additives, alongside the mutants containing point mutations for the transition between the two homologues (darker blue lines on the graph indicate a sequence more similar to MmxF, whereas lighter blue lines indicate a sequence more similar to MmsFCC). With the MmsFCC NPs appearing similar in size to wild-type particles and MmxFCC NPs much larger and with a wider size distribution, some of the mutants fit between these two curves. The average size of the MNPs synthesised in the presence of MmsFCC(F9Q) and MmsFCC(F6Y, F9Q) was slightly larger than for MmsFCC, but smaller than MmxFCC. This effect was more prominent for the double mutation, with MmsFCC(F6Y, F9Q) MNPs larger than MmsFCC(F9Q) and with a larger distribution of sizes (57 nm $\pm$ 38 nm and 61 nm $\pm$ 19 nm; mutations F9Q and F6Y,F9Q respectively). However, the MNPs synthesised with MmsFCC(R2K, F6Y, F9Q) additive, were much smaller, with a narrow distribution of sizes and more closely resembled particles synthesised in the control RTCP reactions, containing no protein additives (28 nm $\pm$ 22 nm). This suggests that mutations in the acidic region of the peptide loop results in MNPs that appear similar in nature to magnetite NPs synthesised in the absence of biomineralisation protein additives.

Two interesting conclusions can be drawn from the sizing and distribution analysis. Firstly, changes in the initial, highly charged region of the AL result in a significant reduction in particle size, with the MNP sizes then comparable to MNPs synthesised with the negative control protein, AcrBCC, or with no protein additives. This suggests a loss of function of constructs containing a mutation in this region. It is likely that this initial region interacts most strongly to the forming MNP, due to the high charge density and therefore formation of salt bridges and polar interactions. These interactions may be responsible for stabilising the conversion of precursor material and the formation of magnetite crystals. Secondly, substitutions at the beginning of the central aromatic region appeared to have little effect on the resulting particle sizes. Suggesting that it is the charged region involved in particle growth and stabilisation.

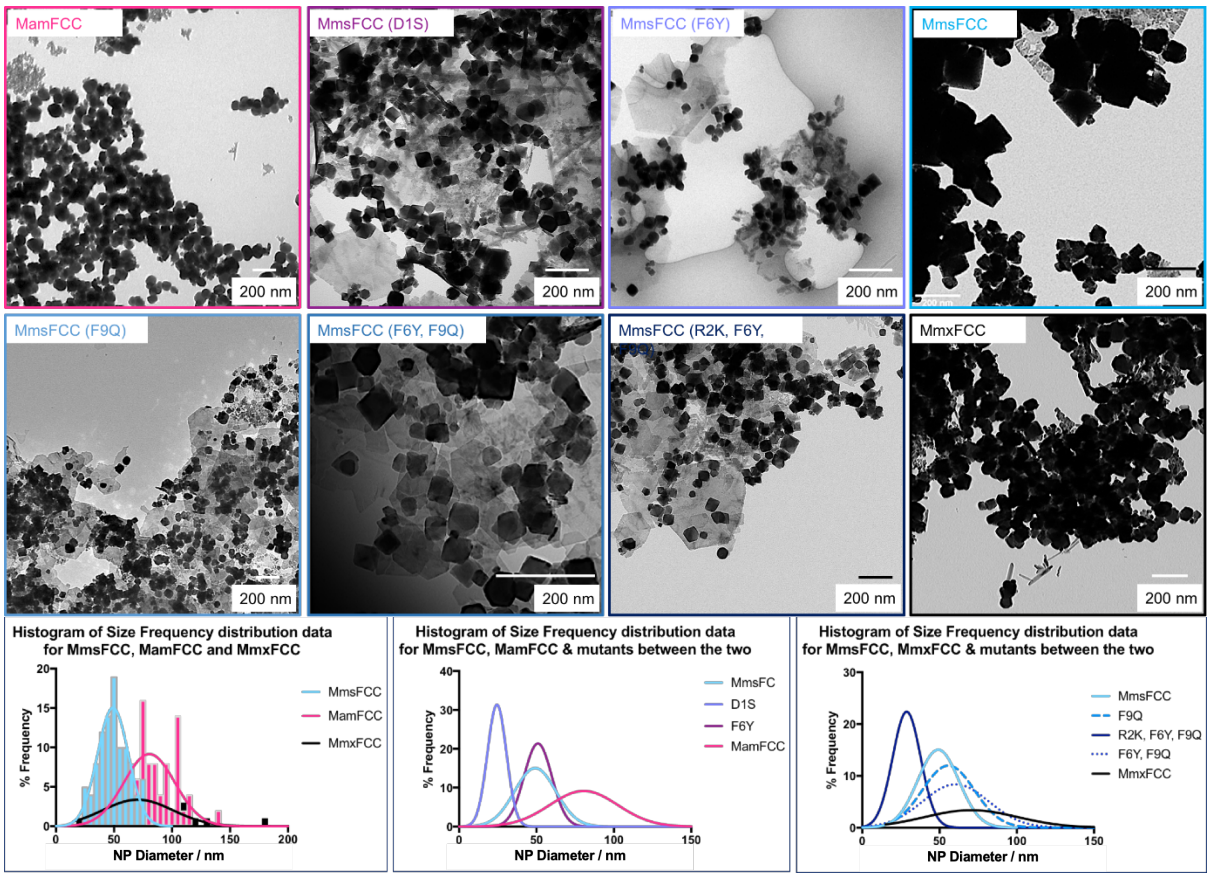

Figure 94 TEM analysis for each of the MmsFCC mutants. Images were collected on Technail TEM. A 200 nm scale bar can be seen on each image and each image is labelled with the protein name. Underneath is the frequency distribution of MNP sizes synthesised with the mutants. Analsyis of MmsFCC, MamFCC and MmxFCC is shown in the first histogram (left to righ); mutants formed in the transitionof MmsFCC to MamFCC is the second; and mutants formed in the transition of MmsFCC to MmxFCC in the third. A key of the coloured lines used is shown for each image.

The shape of the particles was also analysed. A grouped bar chart depicting the shape of the MNPs synthesised with each of the mutated constructs is shown in figure 95. If the shape was calculated to be 'angular' it was assumed that these particles were cubooctahdral, following the HR-TEM and

visualisation of the lattice fringes for MmsFCC synthesised MNPs. As previously observed and therefore predicted for this study, the majority of the MNPs (>70 %) synthesised with MamFCC or MmxFCC had no defined morphology and were categorised as 'misshapen'. Mutants that possessed similar sequence properties to MmsFCC, with fewer mutations, had a tendency to form well-defined, octahedral products. This was true for each of the mutants, apart from MmsFCC(F9Q). The shape observed for the particles synthesised with this mutant was similar to the MmxFCC synthesised particles. Each of the other mutations of MmsFCC did not appear to have a significant effect on the shape of the particle produced.

The most dramatic decrease in octahedral morphology was observed for the single mutation within the aromatic region during the transition of MmsFCC to MmxFCC (MmsFCC(F9Q) and MmsFCC(F6Y) and (F6Y/F9Q)). The aromatic residues mutated during this transition, flank the central region of the AL and for this study were mutated into two more polar residues. As the major decrease in shape control was observed when only one of these residues was mutated, it is likely an interaction between the two flanking aromatic residues F6 and F9 is essential for morphological control over the MNPs. This interaction may be required to template the shape of the MNP and produce a specific structural confirmation. When both residues are mutated into polar residues, this interaction is likely re-established due to the similar properties of the residues and the formation of dipole-dipole interactions.

In summary, the MamFCC and MmxFCC RTCP products appeared to contain no- or few octahedral particles, similar to control RTCP reactions, and also an increase in the production of alternative iron oxide phases such as linear, needle-like particles, characteristic of goethite and hexagonal plates, characteristic of GR. Therefore, these proteins do not appear to have any significant morphological or iron oxide species control over the MNPs and promote the formation of other iron oxides. The mutations in the initial charged region of the AL gave a small decrease in the number of octahedral particles. A double mutation within the aromatic region did not appear to reduce the number of octahedral particles produced, emphasising the importance of the pair of residues occupying these positions working in unison to template the shape of the magnetite crystal.

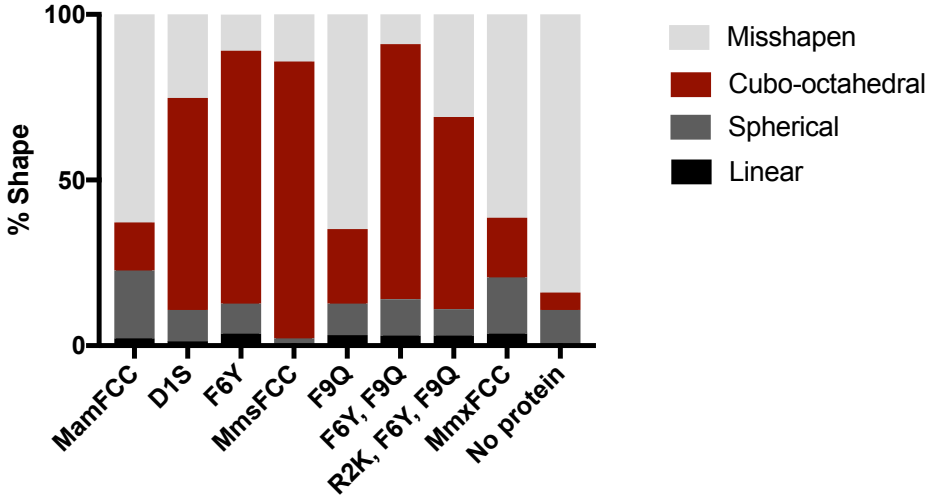

Figure 95 Shape analysis for the MNPs synthesised with MmsFCC mutants. The ImageJ TEM images were used to estimate the shape distribution of the MNPs produced when various MmsFCC mutants were added to the RTCP in place of MmsFCC. 100+ particles were classed as: Misshapen (light grey), Angular/cubo-octahedral (red), spherical (dark grey) or linear (black). Depending on their aspect ratio (measured using imageJ) and angular appearance to the naked eye.

Table 14 Particle properties of MNPs synthesised with MmsFCC mutants

Protein	Loop	Size (nm)	Shape	Composition
MamFCC	SRDDEYVYFHA	80.52 ± 44.70	Misshapen	Magnetite + other iron oxide
D1S	SRDDEFVYFHA	22.42 ± 18.76	Octahedral (64 %)	Magnetite + other iron oxide
F6Y	DRDDEYVYFHA	46.91 ± 18.36	Octahedral (76 %)	Magnetite + other iron oxide
MmsFCC	DRDDEFVYFHA	49.22 ± 18.01	Octahedral (86 %)	Magnetite
F9Q	DRDDEFVYQHA	50.72 ± 13.53	Misshapen	Magnetite + other iron oxide
F6Y, F9Q	DRDDEYVYQHA	60.45 ± 19.07	Octahedral (77 %)	Magnetite
R2K, F6Y, F9Q	DKDDEYVYQHA	28.73 ± 21.40	Octahedral (58 %)	Magnetite + other iron oxide
MmxFCC	NKDDEYVQFHA	70.55 ± 40.69	Misshapen	Magnetite + other iron oxide

5.8 Display of MIA E8 peptide

As proof of concept that the CC scaffold could be used as a universal scaffold the AL was substituted to a peptide sequence that had not been inspired by MTB. Instead, the VR of MIA E8 was displayed on the scaffold. The scaffold was obtained by designing and ordering a Gene String of the desired DNA sequence. As previous, the sequence was amplified using PCR with compatible oligonucleotide primers (containing a Bsa1 restriction site for cloning into a pPR-IBA1 vector). The scaffold sequence remained identical that used for the MTB inspired CC proteins (as shown in figure 96).

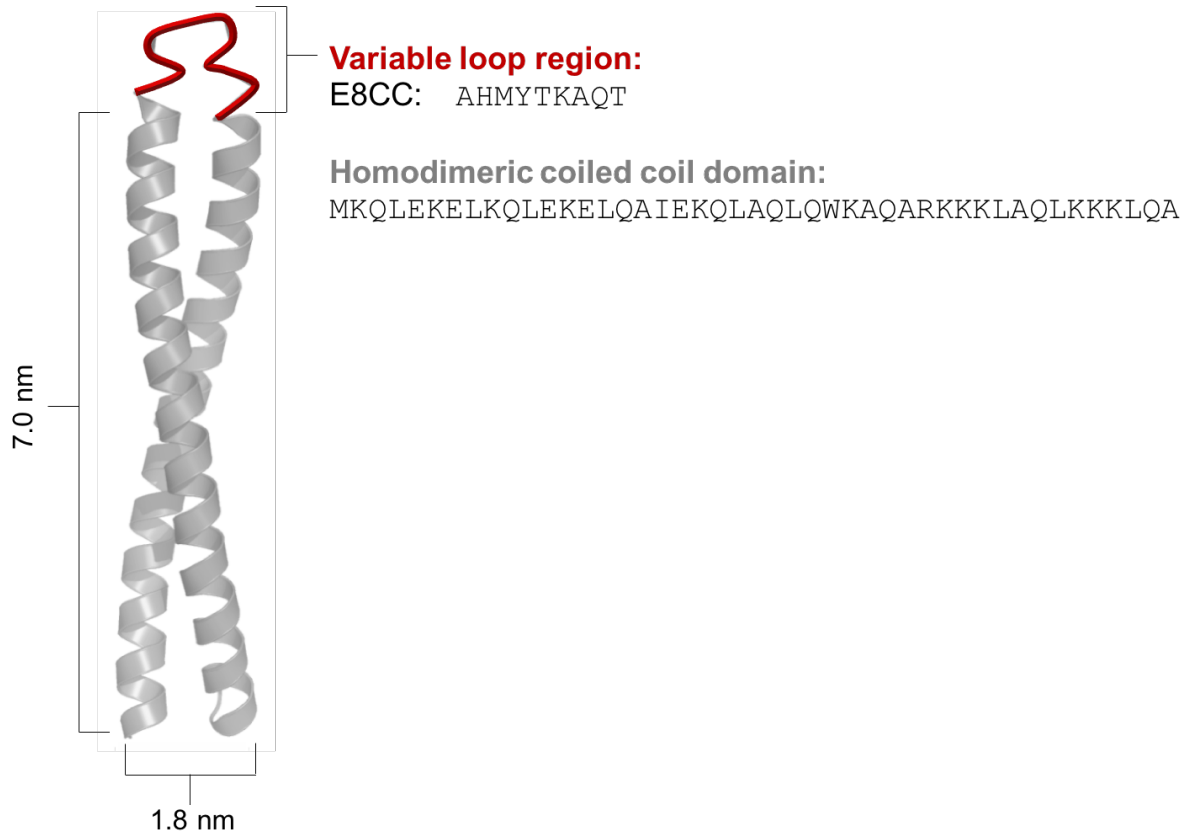

Figure 96 The E8CC construct with the CC scaffold shown in grey and the AL in red. Model produced using Robetta software for protein modelling.[157]

5.8.1 Production of E8CC protein

The E8CC construct was synthesised in the same way as the other CC proteins. The idea was that the scaffold was capable of displaying any short, active peptide region, without affecting the structure of functionality, therefore it was assumed that any molecular cloning or protein production could be conducted in the same way. This proved correct. Figure 97 shows the successful cloning of the construct with a single band present on the agarose gel at around 400 bp (expected size of E8CC). The SDS-PAGE analysis also gave a promising result with a single band present at around 15 kDa (expected size of E8CC). This gel was run after the completion of protein purification using the His_6-tag for affinity chromatography.

Purified E8CC was dialysed into water to remove any residual imidazole buffer. The sample was then analysed using ES-MS. A single peak at m/z = 14367 was observed, confirming that the sequence was likely correct, and the protein had not fragmented during synthesis, purification or analysis. At this point the scaffold displaying the E8 AL was behaving in an identical way to the MTB-inspired CC proteins.

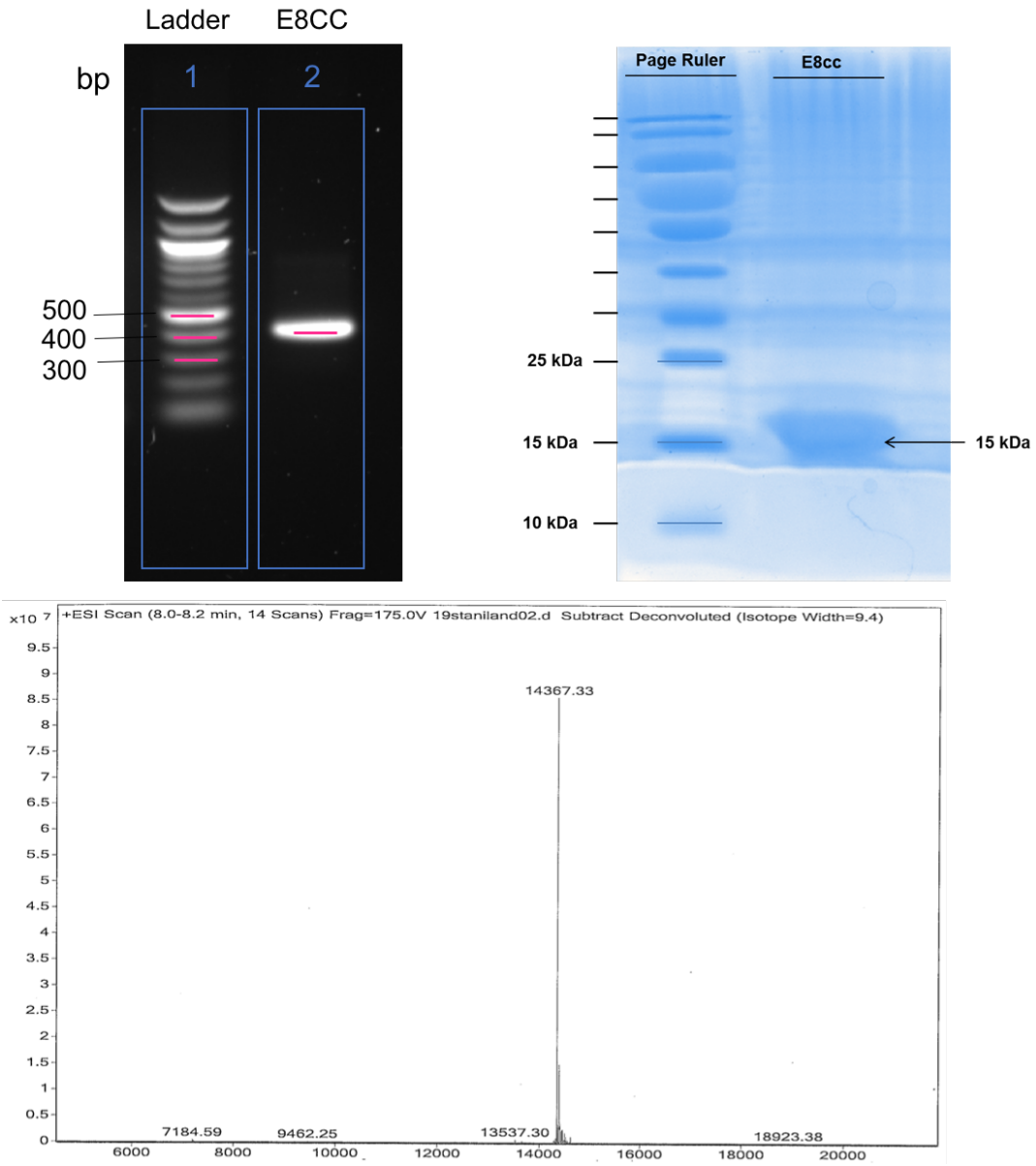

Figure 97 Top left shows the 1 % agarose gel electrophoresis of E8CC with a single band around 400 bp present in lane 2. Top right shows a SDS-PAGE gel with a single band around 15 kDa for purfied E8CC, indicating the correct, pure, protein. Below is the ES-MS spectrum for E8CC with a single major peak at 14.4 kDa, again suggesting the correct and pure protein sample.

5.8.2 Protein characterisation – universal application of the CC scaffold

It was important to confirm that the scaffold could not only be produced using the same methods as previously tested, but also that it behaved in the same way. For the scaffold to be classed as a universal scaffold in the future the structure and functionality should remain unchanged upon altering the AL displayed. CD was the most obvious characterisation technique use initially. The helical content of the protein was measured and if there was any discrepancy, this would indicate the AL does affect the structure in a major way. The CD analysis is shown in figure 98. It can be seen from the spectra and the table presented that displaying the E8 sequence does not disrupt the folding of the scaffold. The helical content predicted for the sequence is a good fit to the helical

content predicted using Dichroweb. As the sequence is slightly shorter (9 amino acids) than the AL of the MTB-inspired CC proteins, a slightly higher helical content was expected and observed.

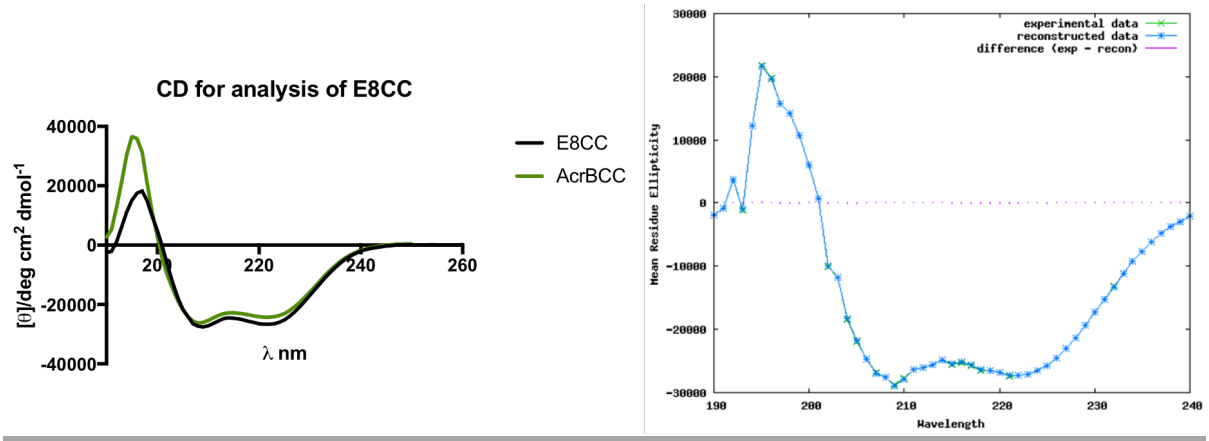

Protein sample	Helical content from sequence (%)	Helical content predicted (Dichroweb, %)	Model fit
MmsFCC	69	66	CDSSTR
Mms13CC	59	59	CDSSTR
AcrBCC	63	64	CDSSTR
E8CC	71.5	71	CDSSTR

Figure 98 CD analysis of E8CC compared to other CC proteins. A shows the molar elipticity of E8CC (black) vs AcrBCC control (green) in ultrapure water. B is the plot for E8CC obtained from the Dichroweb analysis. The height of the pink lines indicate the degree of discrepency between the predicted and actual protein structure. The small pink lines observed indicate a good fit. The table displays the helical conetnt calculated from the sequcne alone and form the Dichroweb using the CDSSRT model. E8CC appears to be a good fit to the other CC proteins.

The CD analysis therefore confirms no structural change in the CC scaffold when displaying alternative biomineralisation sequences. The activity and functionality of the AL was then tested.

5.8.3 Interaction of E8CC with DNA

It was shown in chapter 3 that a problem with MIA E8 was that it bound DNA molecules, making purification process and protein concentration measurements problematic. The interaction of E8CC with DNA was also assessed using the 260/280 nm reading from the NanoDrop 2000. The 260/280 readings and spectra for MIA E8 compared to E8CC are shown in figure 99.

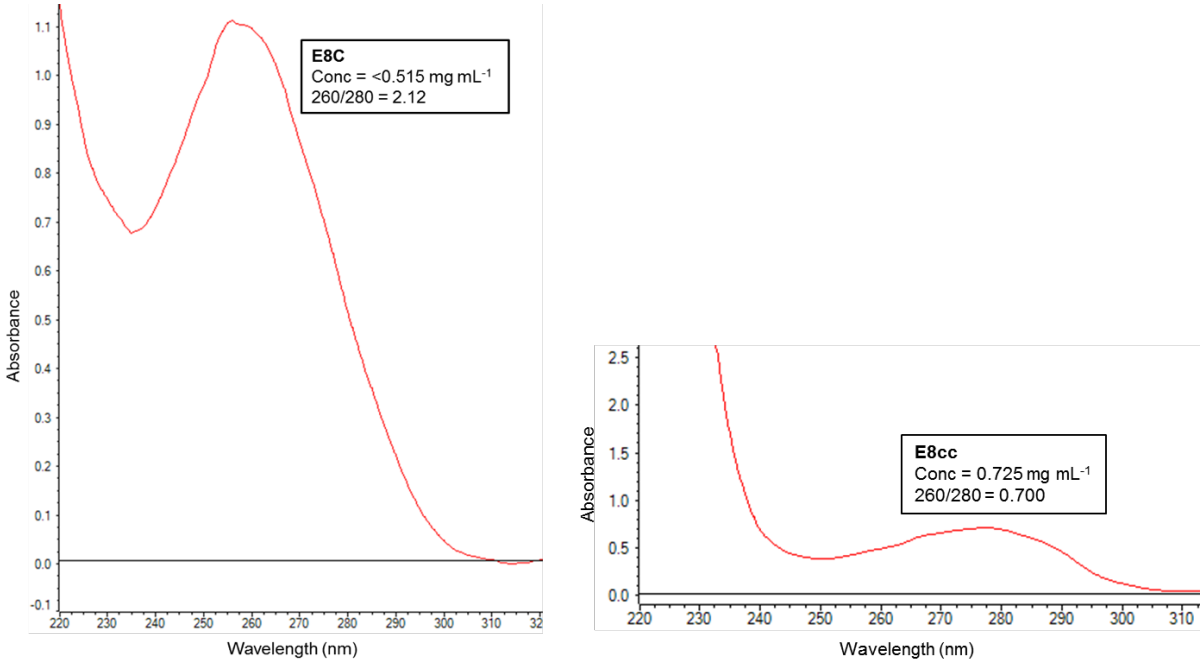

Figure 99 UV-Vis spectra showing DNA binding to MIA E8 and E8CC dialysed into ultrapure water. Peaks were measured using the Nanodrop 2000.

The 260/280 data obtained suggested E8CC does not bind significant amounts of DNA that would hinder purification on concentration measurements. As can be seen in figure 99, this was not true for MIA E8. This result was somewhat surprising as it was expected that the AL displayed was the binding site of DNA. This conclusion was reached as previous studies of the Adhiron protein displaying non-magnetite binding VRs did not appear to bind DNA. Also, the MIA sequences were often rich in basic residues such as lysine. It was likely that the sequence would therefore act in a similar way to polylysine which has been documented to bind DNA. An explanation for the reason that E8CC does not bind DNA could be due to the harsher protein purification techniques used. During the production of the CC constructs, denaturation and refolding is required and during purification increasing concentrations of imidazole is used. This denaturant or imidazole could disrupt the interactions formed between the DNA and the E8CC complex.

During the denaturing stages GuHCl is used – a chaotropic, denaturing agent which is capable of destroying the hydrate shell around nucleic acids, producing a hydrophobic environment. It also aids the disruption of hydrogen bonds. The formation of this hydrophobic environment prevents the binding of the DNA to the protein and instead makes it more likely to bind to the stationary phase of the column. Therefore, decreasing the concentration of DNA molecules bound to the protein produced using this method, compared to a protein that does not require denaturation and refolding (MIA E8). This is just one possible explanation for the decrease in DNA. Whatever the reason for the decrease, it is beneficial for protein characterisation and binding.

After observing that E8CC does not bind DNA to the same extent as MIA E8, the protein was analysed using gel filtration. Although the complex was still relatively 'sticky' causing retention on the column, as seen with MIA E8, an increase in the salt concertation of the elution buffer did appear to have more of an effect on the complex and make analysis of the protein possible using this technique. Figure 100 shows that as the NaCl concertation is increased above 1 M, interactions between the column and a E8CC are overcome and a clean spectrum can be obtained. This is another advantage of using this scaffold compared to E8 displayed on the Adhiron.

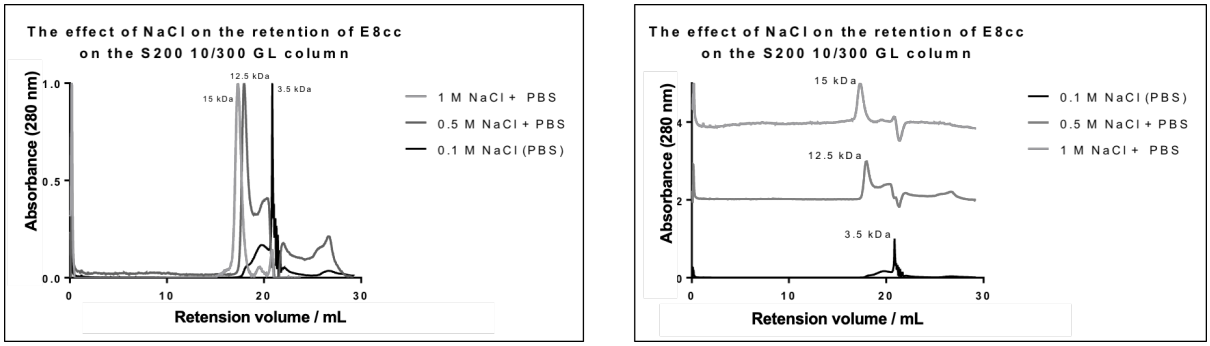

Figure 100 Gel filtration analysis of E8CC using elution buffer with increasing concentration of salt to prevent interactions between the protein and the column.

5.8.4 E8cc vs MIA E8 as additives in biomineralisation reactions

It was essential to ensure that E8CC was able to control magnetite synthesis in the same way as MIA was. This would confirm that the control was due to the peptide sequence displayed on the scaffold and not the scaffold itself. It would also show that the CC scaffold was acting as a scaffold and was capable to holding the peptide in the active conformation. The proteins were added to RTCP reactions and the resulting particles were analysed. This data is shown in figure 101. Looking initially at the TEM images of the resulting particles, both sets of MNPs appear to have a cubic morphology and be similar in size. The size and shape analysis confirmed this. Analysis was carried out using the same protocol as used throughout this project.

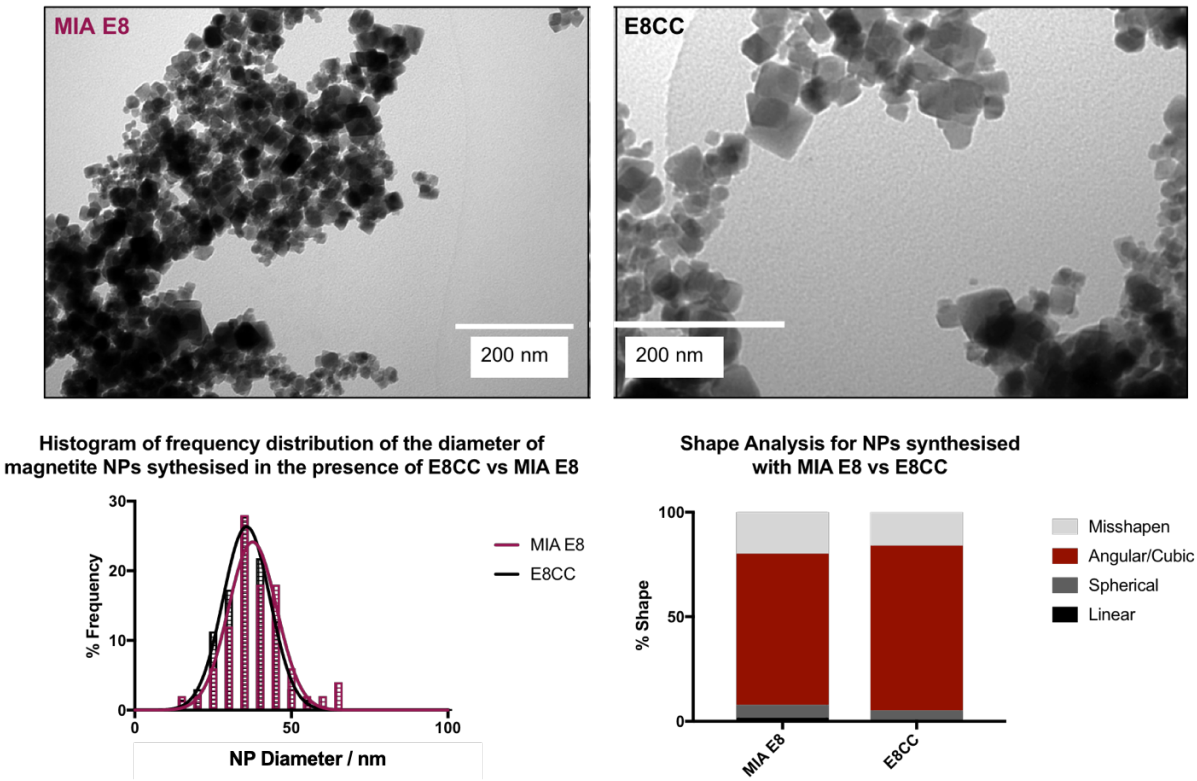

Figure 101 Analysis of magnetite NPs produced using MIA E8 vs E8CC in a RTCP reaction. Top left is the TEM of particles produced in the presence of MIA E8 and top right is the TEM image of NPs produced in the presence of E8CC. Bottom left is the grainsize analysis and frequency distribution of the MNPs (MIA E8 in red and E8CC in black), analysed using GraphPad Prism and meaurement off 100+ particles. Bottom right is the shape analysis of the NPs with the percentage of angular NPs shown in red.

The grainsize analysis and frequency distribution for particles produced in the presence of MIA E8 vs E8CC were almost identical with the average particle diameter just below 40 nm. This result was mimicked in the shape analysis with around 80 % of the particles produced forming an angular – most likely cubic, morphology. These results go a long was in showing the adaptability of the CC protein scaffold and confirm the E8 peptide loop is the active region within the two protein constructs.

5.9 Functionalisation of the scaffold

The possibility for functionalisation of a protein scaffold is a desired characteristic for future applications, including applications in the biomedical field. As introduced in section 4.2, biotinylation is the process of covalently attaching biotin molecules to a protein. Due to the small size of biotin (226 g mol^{-1}) minimal interference regarding the activity or folding of the protein is observed.

A chemical biotinylation method was adopted to biotin-label MmsFCC, with the assumption that the other CC proteins could be modified in a similar manner. The *in vitro* reaction used the

ThermoScientific EZ-link™ Sulfo-NHS-Biotin kit to label each of the primary amine groups of the lysine side chains and N-terminus of the construct with biotin. The reagent was water soluble and produced a non-cleavable, covalent interaction between the biotin and amine by formation of an amide bond. The success of the chemical biotinylation was analysed using MS. If biotinylation did not occur, a peak corresponding to M^+ at m/z = 14986 would be present – this was not observed in the spectrum shown in figure 102. Instead m/z peaks matching predicted peaks for varying degrees of biotin labelling were observed. A table is shown in figure 102, presenting the expected m/z peak position for various numbers of biotin molecules attached. The table also indicates the position of the observed peaks. A good match between the predicted and m/z positions was apparent, suggesting successful biotinylation of the MmsFCC protein. Between 6 and 10 sites were most commonly biotinylated. A total of 24 lysine residues are present in MmsFCC therefore there are some residues that do not appear to be accessible for biotinyaltion and are likely involved in the interaction between the two α-helical strands or are hidden towards the hydrophobic core of the coiled coil.

The peptide loop displayed on the MmsFCC does not contain any lysine residues (unlike the MIA peptide sequences) and therefore it is unlikely that multiple, unspecific addition of biotin would result in a decrease in binding to magnetite NPs. Biotinylation therefore appeared to be a promising technique for functionalising the CC protein in a quick and simple process.

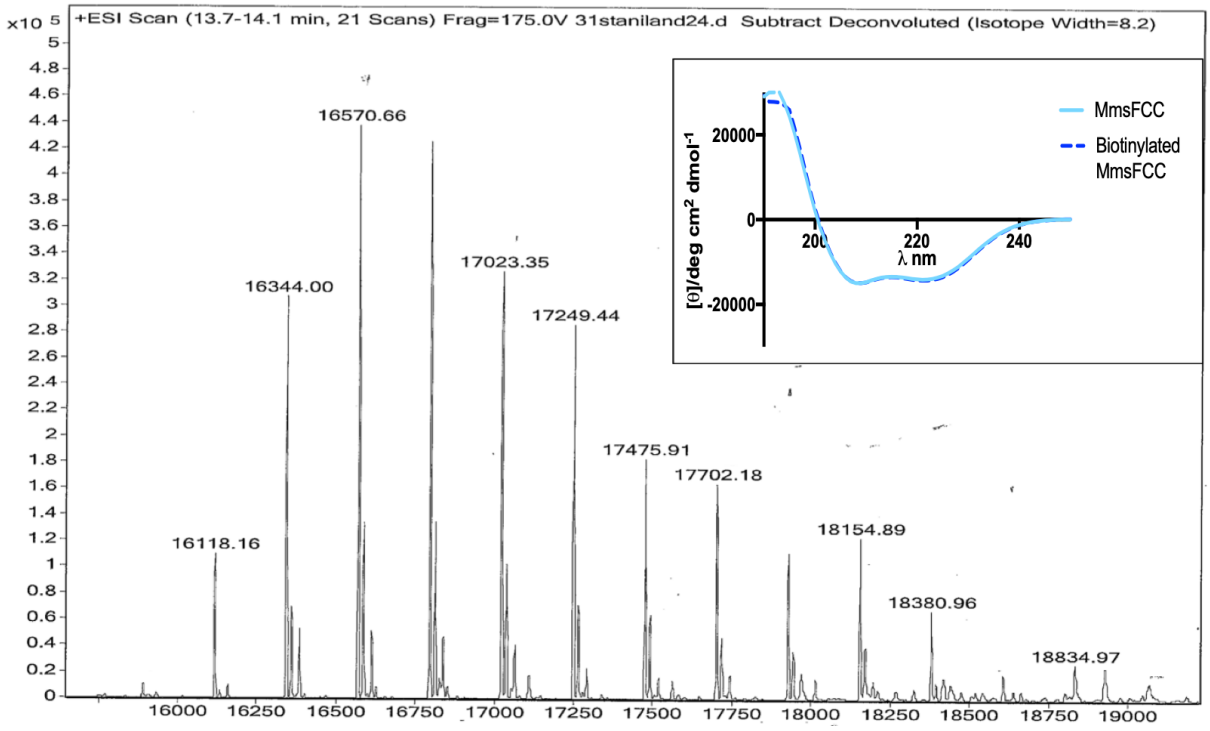

Number of biotin	Expected m/z	Observed m/z	% of sample
0	14986	-	0
1	15212	-	0
2	15438	-	0
3	15664	-	0
4	15891	15891	0.4
5	16118	16118	4.3
6	16344	16344	12.0
7	16570	16570	16.7
8	16797	16797	12.9
9	17022	17023	11.4
10	17249	17249	10.6
11	17475	17475	7.6
12	17701	17702	6.5
13	17928	17928	4.8
14	18154	18154	5.3
15	18380	18380	3.0
16	18606	18606	1.1
17	18833	18834	1.5
18	19060	19060	0.8

Figure 102 ES-Mass spectrometry data for biotinylated MmsFCC in ultrapure water shows between 4 and 18 conjugated biotin molecules per protein (assuming a single-charge on the protein fragments). Inset into the spectrum is CD analysis comparing the structure of MmsFCC and biotin-labelled MmsFCC in ultrapure water.

A problem that could arise for the biotinylation of MmsFCC is that it may disrupt the secondary structure of the CC scaffold, decreasing the stability and therefore affecting MNP binding due to the change in conformation of the active site. CD was used to analyse the secondary structure of the biotinylated MmsFCC construct compared to the original, non-labelled protein. The resulting spectrum is shown as an insert in figure 102. The curve for the biotinylated protein overlays the curve for the unlabelled protein almost perfectly. The intensity of the peaks at 208 nm and 222 nm are almost identical and therefore it is unlikely there is any change in secondary structure of the labelled protein.

The CC scaffold became more and more interesting as an alternative for other artificial display scaffolds. Although the purification stage required an additional refolding step, all other aspects of its design and production were simple and convenient. The protein was small, monomeric, could be functionalised, contained no cysteine residues and expressed well in *E. coli* – all desirable traits of a peptide displaying scaffold.

5.10 Chapter summary

This chapter has introduced the coiled coil scaffold protein as an alternative structure to display active peptide sequences. The CC protein is antiparallel and homodimeric, promoting the formation of a hairpin loop which is changeable for a range of ALs. The current work focuses on the active sequences of biomineralisation proteins identified in MTB. These sequences are located inside the magnetosome and are in close proximity to the forming magnetite crystal within the bacteria. The full-length, wild-type biomineralisation proteins are transmembrane proteins and are therefore difficult to work with, due to problems with solubility and therefore yield. This was the inspiration for the use of the CC scaffold. The scaffold mimics the α-helical nature of the proteins, however greatly simplifying the structure, making them easier to work with whilst retaining the functionality.

A number of CC proteins inspired by MTB biomineralisation proteins were designed and examined. These proteins were Mms13CC, MmsFCC, MmxFCC and MamFCC. A control protein was also used – AcrBCC, displaying a loop region identified in *E. coli* and therefore exhibiting no biomineralisation functionality. The proteins were produced, purified and characterised. The CC structure was found to be consistent in each of the constructs, an important characteristic of a peptide displaying scaffold. The activity of each of the CC constructs *in vitro* was analysed. The proteins were added to RTCP reactions and the resulting magnetite NPs were visualised using TEM and analysed. Similar to $MmsF_{wt}$, MmsFCC appeared to exert the greatest control over the crystal nucleation and growth of the magnetite NPs. The NPs appeared to favour an angular – most likely cubooctahedral geometry. This effect was not witnessed for MmsF homologues MamFCC and MmxFCC or for the control protein AcrBCC. The effect witnessed for Mms13CC was much subtler.

To determine why the control over the NP shape was possible using MmsFCC and not MamFCC or MmxFCC a number of mutations were made to the AL sequence. The aim of these mutations was to identify important residues for biomineralisation of magnetite, assessing the effect of the residue property and position within the sequence. The initial acidic residue was found to play an important role as did the pair of aromatic residues further within the sequence. This pair of residues are likely to template the forming crystal, therefore helping to control the shape.

Finally, it has been shown in the chapter that the CC scaffold has the potential to act as a universal peptide displaying scaffold protein. Analysing E8CC, compared to MIA E8 and the MTB-inspired CC proteins showed that the AL remained active, producing cubic-shaped magnetite NPs in both cases, with almost identical average size and shape. This also proved that the scaffold was not the source

of the control. Functionality arose from the AL/VR, E8 sequence. Characterisation of the E8CC protein showed that there was no change in folding or structure compared to the other CC proteins. A promising start for the CC capabilities of becoming a universal scaffold protein.[143]

Chapter 6: Conclusions and future work

6.1. Conclusion and future direction of chapter 3: MIA scaffold

Chapter 3 introduced the Adhiron as an artificial peptide displaying scaffold. An explanation of the development of the protein was provided; detailing the evolution of the scaffold into a useful tool which was proven to aid the synthesis of highly controlled, uniform MNPs. The dual functionality of the MIA scaffold was realised - controlling crystal nucleation and growth during MNP synthesis and behaving as an attachment device to adhere drugs, dyes and antibodies to the surface of the magnetite particles (investigated further in chapter 4). An investigation into the essential properties of the MIA for binding magnetite NPs concluded that single loop MIAs were able to form stronger interactions with MNPs than DNA molecules. It also showed that basic residues, particularly lysine, were important for binding the magnetite [100] facet. The binding strength of free MIA peptides to MNPs were also compared to the binding strength of the rigid MIA displaying scaffold. With the binding region conformationally restrained within a scaffold protein, binding was improved. This was not a surprise as the VR was held in the optimum binding position. However, some peptide binding to magnetite NPs was also observed (namely MIA_{pep} A3), this could therefore be used in the design of future fusion proteins (see scFv in chapter 4).

The work surrounding the MIA scaffold has reached a good stopping point for this project, with a thorough investigation reaching completion. The work has moved forward in chapter 4, looking at the applications of the protein complexes. One way this research could be added to in the future would be to analyse the binding strengths between the MIA proteins and the MNPs and the MIA proteins and DNA molecules in more depth. Specificity of binding to different DNA sequences could be investigated and bioinformatics would be beneficial to model the possible interactions. The strength could also be quantified using techniques such as ITC. It could be important for future biomedical applications to have a sound understanding of how the MIA complex interacts with DNA and what effect this could have on the body if used as an *in vivo* diagnostic or therapeutic.

Also, future work for this section of the project may include further characterisation of the MIA. The BST group at Leeds university were able to provide an X-ray crystal structure of the Adhiron scaffold protein and therefore further structural characterisation was not required to complete this project in the timeline given. It could be reasonably assumed that the structure would not be changed with the display of magnetite interacting VRs as BSTG had previously tested the display of a range of

different target sequences which did not appear to change the structure. This could be tested further using techniques such as SAXS.

Finally, the Adhiron scaffold could be developed to display other mineral-interacting VRs. With research in practical bionanoscience is moving towards materials such as FePt and CoPt due to the different magnetic properties the materials offer. The scaffold could be designed for this mineral synthesis. With this project focusing on bioinspired and environmentally sensitive syntheses the main focus was magnetite NP biomineralisation using the RTCP reaction, however the Adhiron scaffold could be used to produce an extensive toolbox for the controlled synthesis of wide range of materials of differing shapes, sizes and morphologies.

6.2 Conclusion and future direction of chapter 4: Functionalisation of MNPs for biomedical applications

Chapter 4 has shown that fluorescent maleimide activated dyes can be attached to a mutated C-terminal cysteine residue on the MIA proteins. The possible attachment of a variety of dyes enables *in vivo* and *in vitro* tracking of the MNP-scaffold complex which may prove essential for future theragnostics applications. The chapter also presented the successful attachment of therapeutically relevant antibodies, including the α-RAGE antibody, provided by Prof Steve Conlan and his research group at Swansea university. The RAGE antibody was attached to MNPs using maleimide chemistry, utilising a sulfo-SMCC/MIA linker. This complex exhibited promising levels of uptake and negligible cytotoxicity when tested using SKOV-3 mammalian cell cultures (in both 2D and 3D models). The heating capabilities of the complex was also analysed where the MNPs were subjected to an AMF during hyperthermia treatment. The SAR and ILP values measured were in the same region as others found for magnetite NP heating *in vitro*, in the literature. This suggested that the antibody-MNP ADC complex could realistically be developed into a novel therapeutic agent for the treatment of cancers expressing surface α-RAGE receptors (such as some ovarian tumours).

There are a number of next steps that could be carried out to continue and improve upon the work conducted for chapter 4 of this thesis. Firstly, work on the scFv could be optimised. The molecular cloning stages for this project are almost complete and so optimisation of protein production would be the next logical step. A PelB leader sequence has been incorporated into the DNA sequence for the scFv-MIA_{pep} complex and so expression both within the cell periplasm and cytoplasm could be compared. There is also an Avi-Tag fused which can be used to analyse the protein concentration within the periplasm. With optimised protein production and protein characterisation to confirm the

complex has the desired properties the ultimate purpose of the scFv-MIA_{pep} complex is binding to MNPs for hyperthermia-based treatment of cell lines specific to the scFv supplied by Prof Kerry Chester at UCL.

For both the collaborative projects – RAGE antibody attachment at Swansea university and the scFv attachment at UCL, hyperthermia would need to be tested in-cell. Currently the only hyperthermia data collected was *in vitro*. Firstly, heating of the MNP complexes should be measured in 2D cell models. Following optimisation and promising readings, 3D-spherical cell models should then be used. Eventually, this could be moved further towards testing on live models.

6.3 Conclusion and future direction of chapter 5: Coiled coil scaffold

Chapter 5 detailed the design, production and characterisation of the novel CC peptide displaying scaffold. Important regions of biomineralisation proteins from MTB were incorporated into the AL of the proteins and used as additives for the synthesis of MNPs. It was concluded that the peptide region displayed had little effect on the folding or stability of the construct. MmsFCC showed promising activity when used in RTCP reactions, appearing to control the synthesis of magnetite NPs, leading to a uniform cubooctahedral geometry. Sequences homologous to MmsF (MmxF and MamF) did not appear to exhibit the same activity *in vitro*. This lack of activity has also been noted *in vivo* and was therefore expected. Mutagenesis experiments reported in this chapter began to give an understanding of the importance of certain residues in given positions in the variable hairpin loop. For example, the initial acidic residue in MmsF, which is missing in MmxF and MamF, was found to be essential for the effect witnessed on magnetite NP synthesis, as did the aromatic region of the sequence.

This chapter also introduced the idea of a universal scaffold, able to display a wide range of active peptides. This was demonstrated by displaying the E8 sequence, previously displayed on the MIA scaffold protein. The activity of the construct was similar to that of MIA E8 and protein characterisation showed that the CC scaffold folding, and stability was similar to the scaffold displaying Mms/Mam regions. This is exciting. It shows the flexibility and adaptability of the scaffold protein – especially as an alternative to studying insoluble transmembrane protein activity *in vitro*.

Future work within this area of the project is extensive. Firstly, adding to the library of peptides displayed on the coiled coil would be beneficial, giving a tool box of constructs for various applications. Initially these applications could focus on biomineralisation alternatives, however it

could move away from magnetite NP synthesis, towards synthesis of minerals such as CoPt and FePt or other magnetically hard, inorganic compounds. Additionally, the focus could move away from mineralisation processes all together, towards other technologically interesting loop sequences. These sequences could include target drug molecules or receptors.

Further functionalisation of the coiled coil scaffold protein may also be studied. Functionalisation using a range of methods would be useful for future applications. These methods could include those studied in previous chapters (i.e. chapter 4) such as biotin-labelling (chemically or enzymatically); NHS-ester formation or maleimide linkage. Another widely used method that should be studied in the future is click-chemistry, incorporating alkynes or azides that do not form naturally in proteins.

Finally, after studying other useful active peptides and functionalisation of the scaffold protein a more extensive study into the use as diagnostic and therapeutic agents may be conducted. Using magnetite-interacting sequences, techniques such as magnetic hyperthermia and MRI of the complex may be studied, both *in vitro* and *in vivo*, in a variety of different cell lines and linked with a variety of different targeting molecules, such as antibodies and scFv constructs. Linking to heat-sensitive drug molecules would also be interesting when studied in conjunction with magnetic hyperthermia of the MNPs.

6.4 Project Summary

Recently, bioengineered scaffold molecules have become an area of intense interest. The use of small, robust, monomeric proteins has become a viable alternative to complex and expensive antibodies. CC and MIA scaffolds have been designed and synthesised, displaying active peptide sequences that have been characterised and shown to be capable of controlling the nucleation and growth of magnetic NP crystallization. The constructs promote the synthesis of NPs with favourable crystal morphologies, such as cubic and cubooctahdral geometries. The structural limit to conformational changes keep the displayed region in the most active conformation. The protein scaffolds have also been used as attachment devices for dyes and antibodies - making these proteins possible alternatives to ADC systems, providing the basis for new diagnostic and therapeutic strategies such as hyperthermia-based treatments and cancer-cell targeting.

A host of specialised proteins involved in the production and regulation of the magnetosomes – including MmsF, MmxF, MamF and Mms13 have been studied. The active regions of these

biomineralisation proteins were successfully displayed on the CC protein scaffold. Each of the protein constructs were characterised and showed uniform folding and stability. MmsF and MmsFCC were found to be responsible for synthesising high quality, uniform, MNPs under ambient conditions in synthetic magnetite precipitation reactions, improving both the homogeneity and morphology of the crystals. Wild-type MmsF, MmxF, MamF are membrane spanning proteins resulting in difficult protein production and characterisation. This research met the aims initially laid out in the abstract and introduction and was able to identify regions and residues of importance for biomineralisation activity by studying the hydrophilic loops that link the transmembrane helices using both free peptides and constrained stem loop coiled coil scaffolds. This approach has generated novel biomimetic reagents for precision NP synthesis, as well as improving the inherent solubility issues of the full membrane protein.

Bibliography

1. Coey, J. M. D., *Magnetism and magnetic materials [electronic resource]*. Cambridge : Cambridge University Press, 2010: Cambridge, 2010.
2. Pankhurst, Q. A.; Connolly, J.; Jones, S. K.; Dobson, J., Applications of magnetic nanoparticles in biomedicine. *Journal of Physics D: Applied Physics* **2003,** *36* (13), 167-181.
3. Brown, W. F., Thermal fluctuations of a single-domain particle. *Physical Review* **1963,** *130* (5), 1677.
4. Papaefthymiou, G. C., Nanoparticle magnetism. *Nano Today* **2009,** *4* (5), 438-447.
5. Stoner, E. C.; Wohlfarth, E. P., A mechanism of magnetic hysteresis in heterogeneous alloys. *Magnetics, IEEE Transactions on* **1991,** *27* (4), 3475-3518.
6. Kirschvink, J. L.; Kobayashi-Kirschvink, A.; Woodford, B. J., Magnetite biomineralization in the human brain. *Proceedings of the National Academy of Sciences of the United States of America* **1992,** *89* (16), 7683.
7. Zhang, Z.; Satpathy, S., Electron-states, magnetism, and the Verwey transition in magnetite. *Physical Review B* **1991,** *44* (24), 13319-13331.
8. Cornell, R. M., *The iron oxides : structure, properties, reactions, occurrence and uses*. Weinheim ; Cambridge : VCH, c1996: Weinheim ; Cambridge, 1996.
9. Sun, C.; Lee, J. S. H.; Zhang, M. Q., Magnetic nanoparticles in MR imaging and drug delivery. *Advanced Drug Delivery Reviews* **2008,** *60* (11), 1252-1265.
10. Laurent, S.; Forge, D.; Port, M.; Roch, A.; Robic, C.; Elst, L. V.; Muller, R. N., Magnetic iron oxide nanoparticles: Synthesis, stabilization, vectorization, physicochemical characterizations, and biological applications. *Chemical Review.*, **2008**; 108, 2064-2110.
11. Gupta, M.; Gupta, A. K.; Gupta, M., Synthesis and surface engineering of iron oxide nanoparticles for biomedical applications. *Biomaterials.* **2005,** *26* (18), 3995-4021.
12. Peng, Y. K.; Lui, C. N. P.; Chen, Y. W.; Chou, S. W.; Chou, P. T.; Yung, K. K. L.; Tsang, S. C. E., Engineered core-shell magnetic nanoparticle for MR dual-modal tracking and safe magnetic manipulation of ependymal cells in live rodents. *Nanotechnology* **2018,** *29* (1), 8.
13. Rashid, Z.; Soleimani, M.; Ghahremanzadeh, R.; Vossoughi, M.; Esmaeili, E., Effective surface modification of $MnFe_2O_4SiO_2$PMIDA magnetic nanoparticles for rapid and high-density antibody immobilization. *Applied Surface Science* **2017,** *426*, 1023-1029.
14. Tibbe, A. G. J.; de Grooth, B. G.; Greve, J.; Liberti, P. A.; Dolan, G. J.; Terstappen, L., Optical tracking and detection of immunomagnetically selected and aligned cells. *Nature Biotechnology* **1999,** *17* (12), 1210-1213.
15. Morisada, S.; Miyata, N.; Iwahori, K., Immunomagnetic separation of scum-forming bacteria using polyclonal antibody that recognizes mycolic acids. *Journal of Microbiological Methods* **2002,** *51* (2), 141-148.
16. Muthana, M.; Kennerley, A.; Hughes, R.; Fagnano, E.; Richardson, J.; Paul, M.; Murdoch, C.; Wright, F.; Payne, C.; Lythgoe, M.; Farrow, N.; Dobson, J.; Conner, J.; Wild, J.; Lewis, C., Directing cell therapy to anatomic target sites in vivo with magnetic resonance targeting. *Nature Communications* **2015,** *6* (8009), 8009.
17. Widder, K. J.; Senyei, A. E.; Scarpelli, D. G., Magnetic microspheres - model system for site specific drug delivery *in vivo*. *Proceedings of the Society for Experimental Biology and Medicine* **1978,** *158* (2), 141-146.

18. Lubbe, A. S.; Bergemann, C.; Riess, H.; Schriever, F.; Reichardt, P.; Possinger, K.; Matthias, M.; Dorken, B.; Herrmann, F.; Gurtler, R.; Hohenberger, P.; Haas, N.; Sohr, R.; Sander, B.; Lemke, A. J.; Ohlendorf, D.; Huhnt, W.; Huhn, D., Clinical experiences with magnetic drag targeting: A phase I study with 4'-epidoxorubicin in 14 patients with advanced solid tumors. *Cancer Research* **1996,** *56* (20), 4686-4693.
19. Widder, K. J.; Morris, R. M.; Poore, G. A.; Howard, D. P.; Senyei, A. E., Selective trageting of magnetic albumin microspheres containing low-dose doxorubicin - total remission in Yoshida sarcoma-bearing rats. *European Journal of Cancer & Clinical Oncology* **1983,** *19* (1), 135-139.
20. Zhang, X.; Wan, J.; Chen, K.; Wang, S., Controlled synthesis of spherical and cubic magnetite nanocrystal clusters. *Journal of Crystal Growth* **2013,** *372* (0), 170-174.
21. Majeed, M. I.; Lu, Q.; Yan, W.; Li, Z.; Hussain, I.; Tahir, M. N.; Tremel, W.; Tan, B., Highly water-soluble magnetic iron oxide (Fe_3O_4) nanoparticles for drug delivery: enhanced in vitro therapeutic efficacy of doxorubicin and MION conjugates. *Journal of Materials Chemistry B* **2013,** *1* (22), 2874-2884.
22. Wu, W.; Jiang, C. Z.; Roy, V. A. L., Recent progress in magnetic iron oxide-semiconductor composite nanomaterials as promising photocatalysts. *Nanoscale* **2015,** *7* (1), 38-58.
23. Gilchrist, R. K.; Medal, R.; Shorey, W. D.; Hanselman, R. C.; Parrott, J. C.; Taylor, C. B., Selective inductive heating of lymph nodes. *Annals of Surgery* **1957,** *146* (4), 596-606.
24. Perigo, E. A.; Hemery, G.; Sandre, O.; Ortega, D.; Garaio, E.; Plazaola, F.; Teran, F. J., Fundamentals and advances in magnetic hyperthermia. *Applied Physics Reviews* **2015,** *2* (4), 35.
25. Wildeboer, R. R.; Southern, P.; Pankhurst, Q. A., On the reliable measurement of specific absorption rates and intrinsic loss parameters in magnetic hyperthermia materials. *On the reliable measurement of specific absorption rates and intrinsic loss parameters in magnetic hyperthermia materials* **2014,** *47* (49), 5003.
26. Martinez-Boubeta, C.; Simeonidis, K.; Makridis, A.; Angelakeris, M.; Iglesias, O.; Guardia, P.; Cabot, A.; Yedra, L.; Estrade, S.; Peiro, F.; Saghi, Z.; Midgley, P. A.; Conde-Leboran, I.; Serantes, D.; Baldomir, D., Learning from Nature to Improve the Heat Generation of Iron-Oxide Nanoparticles for Magnetic Hyperthermia Applications. *Scientific Reports* **2013,** *3*.
27. Lampman, G. M., *Spectroscopy*. 4th ed., International ed. ed.; Belmont, Calif. : Brooks/Cole Cengage Learning, c2010: Belmont, Calif., 2010.
28. Lartigue, L.; Alloyeau, D.; Kolosnjaj-Tabi, J.; Javed, Y.; Guardia, P.; Riedinger, A.; Péchoux, C.; Pellegrino, T.; Wilhelm, C.; Gazeau, F., Biodegradation of iron oxide nanocubes: High- resolution in situ monitoring. *ACS Nano* **2013,** *7* (5), 3939-3952.
29. Atkinson, W. J.; Brezovich, I. A.; Chakraborty, D. P., Useable frequencies in hyperthermia with thermal seeds. *IEEE Transactions on Biomedical Engineering* **1984,** *31* (1), 70-75.
30. Connord, V.; Clerc, P.; Hallali, N.; El Hajj Diab, D.; Fourmy, D.; Gigoux, V.; Carrey, J., Real- Time Analysis of Magnetic Hyperthermia Experiments on Living Cells under a Confocal Microscope. *Small* **2015,** *11* (20), 2437-2445.
31. Tietze, R.; Lyer, S.; Durr, S.; Struffert, T.; Engelhorn, T.; Schwarz, M.; Eckert, E.; Goen, T.; Vasylyev, S.; Peukert, W.; Wiekhorst, F.; Trahms, L.; Dorfler, A.; Alexiou, C., Efficient drug-delivery using magnetic nanoparticles - biodistribution and therapeutic effects in tumour bearing rabbits. *Nanomedicine-Nanotechnology Biology and Medicine* **2013,** *9* (7), 961-971.

32. Gneveckow, U.; Jordan, A.; Scholz, R.; Bruss, V.; Waldofner, N.; Ricke, J.; Feussner, A.; Hildebrandt, B.; Rau, B.; Wust, P., Description and characterization of the novel hyperthermia- and thermoablation-system MFH (R) 300F for clinical magnetic fluid hyperthermia. *Medical Physics* **2004,** *31* (6), 1444-1451.
33. Revia, R. A.; Zhang, M. Q., Magnetite nanoparticles for cancer diagnosis, treatment, and treatment monitoring: recent advances. *Materials Today* **2016,** *19* (3), 157-168.
34. Gallo, J.; Kamaly, N.; Lavdas, I.; Stevens, E.; Nguyen, Q. D.; Wylezinska-Arridge, M.; Aboagye, E. O.; Long, N. J., CXCR4- Targeted and MMP- Responsive Iron Oxide Nanoparticles for Enhanced Magnetic Resonance Imaging. *Angewandte Chemie International Edition* **2014,** *53* (36), 9550-9554.
35. Smith, B. R.; Gambhir, S. S., Nanomaterials for In Vivo Imaging. *Chemical Reviews* **2017,** *117* (3), 901-986.
36. Daldrup-Link, H. E.; Golovko, D.; Ruffell, B.; Denardo, D. G.; Castaneda, R.; Ansari, C.; Rao, J.; Tikhomirov, G. A.; Wendland, M. F.; Corot, C.; Coussens, L. M., MRI of tumor-associated macrophages with clinically applicable iron oxide nanoparticles. *Clinical cancer research : an official journal of the American Association for Cancer Research* **2011,** *17* (17), 5695.
37. Mao, B.; Kang, Z.; Wang, E.; Lian, S.; Gao, L.; Tian, C.; Wang, C., Synthesis of magnetite octahedrons from iron powders through a mild hydrothermal method. *Materials Research Bulletin* **2006,** *41* (12), 2226-2231.
38. Gedanken, A., Using sonochemistry for the fabrication of nanomaterials. *Ultrasonics Sonochemistry* **2004,** *11* (2), 47-55.
39. Kumar, R. V.; Koltypin, Y.; Xu, X. N.; Yeshurun, Y.; Gedanken, A.; Felner, I., Fabrication of magnetite nanorods by ultrasound irradiation. *Journal of Applied Physics* **2001,** *89* (11), 6324-6328.
40. Park, J.; Joo, J.; Kwon, S. G.; Jang, Y.; Hyeon, T., Synthesis of monodisperse spherical nanocrystals. *Angewandte Chemie-International Edition* **2007,** *46* (25), 4630-4660.
41. Cho, M. J.; Cervadoro, A.; Ramirez, M. R.; Stigliano, C.; Brazdeikis, A.; Colvin, V. L.; Civera, P.; Key, J.; Decuzzi, P., Assembly of Iron Oxide Nanocubes for Enhanced Cancer Hyperthermia and Magnetic Resonance Imaging. *Nanomaterials* **2017,** *7* (4). 72
42. Ooi, F.; DuChene, J. S.; Qiu, J. J.; Graham, J. O.; Engelhard, M. H.; Cao, G. X.; Gai, Z.; Wei, W. D., A Facile Solvothermal Synthesis of Octahedral Fe_3O_4 Nanoparticles. *Small* **2015,** *11* (22), 2649-2653.
43. Li, Z.; Godsell, J. F.; Byrne, J. P.; Petkov, N.; Morris, M. A.; Roy, S.; Holmes, J. D., Supercritical fluid synthesis of magnetic hexagonal nanoplatelets of magnetite. *Journal of the American Chemical Society* **2010,** *132* (36), 12540.
44. Huang, H.-H., The Eh-pH Diagram and Its Advances. *Metals.* **2016,** *6* (1), 23.
45. Schueler, D.; Faivre, D.; Schüler, D., Magnetotactic Bacteria and Magnetosomes. *Chemical reviews.* **2008,** *108* (11), 4875-4898.
46. Ruby, C.; Aissa, R.; Gehin, A.; Cortot, J.; Abdelmoula, M.; Genin, J., Green rusts synthesis by coprecipitation of Fe-II-Fe-III ions and mass-balance diagram. *C. R. Geoscience.* **2006,** *338* (6-7), 420-432.
47. Rawlings, A. E.; Bramble, J. P.; Hounslow, A. M.; Williamson, M. P.; Monnington, A. E.; Cooke, D. J.; Staniland, S. S., Ferrous Iron Binding Key to Mms6 Magnetite Biomineralisation: A Mechanistic Study to Understand Magnetite Formation Using pH Titration and NMR Spectroscopy. *Chemistry – A European Journal* **2016,** *22* (23), 7885-7894.

48. Lenders, J. J. M.; Altan, C. L.; Bomans, P. H. H.; Arakaki, A.; Bucak, S.; de With, G.; Sommerdijk, N., A Bioinspired Coprecipitation Method for the Controlled Synthesis of Magnetite Nanoparticles. *Crystal Growth & Design* **2014,** *14* (11), 5561-5568.
49. Wiltschko, R.; Wiltschko, W., The magnetite- based receptors in the beak of birds and their role in avian navigation. *Neuroethology, Sensory, Neural, and Behavioral Physiology* **2013,** *199* (2), 89-98.
50. Delong, E. F.; Frankel, R. B.; Bazylinski, D. A., Multiple evolutionary origins of magnetotaxis in bacteria. *Science* **1993,** *259* (5096), 803-806.
51. Jimenez-Lopez, C.; Romanek, C. S.; Bazylinski, D. A., Magnetite as a prokaryotic biomarker: A review. *Journal of Geophysical Research: Biogeosciences* **2010,** *115* (G2), 19.
52. Nudelman, F.; Sommerdijk, N. A. J. M., Biomineralization as an Inspiration for Materials Chemistry. *Weinheim*, **2012**; 51, 6582-6596.
53. Durak, G. M.; Brownlee, C.; Wheeler, G. L., The role of the cytoskeleton in biomineralisation in haptophyte algae. *Scientific Reports* **2017,** *7*.
54. Langer, G.; de Nooijer, L. J.; Oetjen, K., On the role of the cytoskeleton in Coccolith morphogenesis: The effect of cytoskeleton inhibitors. *Journal of Phycology* **2010,** *46* (6), 1252-1256.
55. Blakemore, R., Magnetotactic bacteria. *Science* **1975,** *190* (4212), 377-379.
56. Bellini, S., Further studies on "magnetosensitive bacteria". *Chinese Journal of Oceanology and Limnology* **2009,** *27* (1), 6-12.
57. Lefevre, C. T.; Bazylinski, D., Ecology, Diversity, and Evolution of Magnetotactic Bacteria. In *Microbiology. Molecular Biology Review.*, **2013**; 77, 497-526.
58. Komeili, A., Molecular mechanisms of compartmentalization and biomineralization in magnetotactic bacteria. FEMS microbiological review **2012**; 36, 232-255.
59. Kopp, R. E.; Kirschvink, J. L., The identification and biogeochemical interpretation of fossil magnetotactic bacteria. *Earth-Science Reviews* **2008,** *86* (1-4), 42-61.
60. Staniland, S. S.; Rawlings, A. E., Crystallizing the function of the magnetosome membrane mineralization protein Mms6. *Biochemical Society Transactions* **2016,** *44*, 883-890.
61. Lefèvre, C. T.; Abreu, F.; Schmidt, M. L.; Lins, U.; Frankel, R. B.; Hedlund, B. P.; Bazylinski, D. A., Moderately thermophilic magnetotactic bacteria from hot springs in Nevada. *Applied and environmental microbiology* **2010,** *76* (11), 3740.
62. Lefèvre, C. T.; Frankel, R. B.; Pósfai, M.; Prozorov, T.; Bazylinski, D. A., Isolation of obligately alkaliphilic magnetotactic bacteria from extremely alkaline environments. *Environmental Microbiology* **2011,** *13* (8), 2342-2350.
63. Fukuda, Y.; Okamura, Y.; Takeyama, H.; Matsunaga, T., Dynamic analysis of a genomic island in Magnetospirillum sp. strain AMB- 1 reveals how magnetosome synthesis developed. *FEBS Letters* **2006,** *580* (3), 801-812.
64. Murat, D.; Quinlan, A.; Vali, H.; Komeili, A., Comprehensive genetic dissection of the magnetosome gene island reveals the step-wise assembly of a prokaryotic organelle. *Proceedings of the national academy of sciences of the United States of America.* **2010,** *107* (12), 5593-5598.
65. Komeili, A.; Li, Z.; Newman, D. K.; Jensen, G. J., Magnetosomes are cell membrane invaginations organized by the actin- like protein MamK. *Science* **2006,** *311* (5758), 242.
66. André, S.; Manuela, G.; Damien, F.; Alexandros, L.; Jürgen, M. P.; Dirk, S., An acidic protein aligns magnetosomes along a filamentous structure in magnetotactic bacteria. *Nature* **2005,** *440* (7080), 110.

67. Judith, B.; Manuela, R., Siderophores: More than Stealing Iron. *mBio* **2016,** *7* (6), 1906.
68. Calugay, R. J.; Miyashita, H.; Okamura, Y.; Matsunaga, T., Siderophore production by the magnetic bacterium Magnetospirillum magneticum AMB-1. *FEMS Microbiology Letters* **2003,** *218* (2), 371-375.
69. Frankel, R. B.; Papaefthymiou, G. C.; Blakemore, R. P.; amp; Amp; Apos; Brien, W., Fe 3O 4 precipitation in magnetotactic bacteria. *BBA - Molecular Cell Research* **1983,** *763* (2), 147-159.
70. Scheffel, A.; Gärdes, A.; Grünberg, K.; Wanner, G.; Schüler, D., The Major Magnetosome Proteins MamGFDC Are Not Essential for Magnetite Biomineralization in Magnetospirilum gryphis waldense b Ut Regulate the Size of Magnetosome Crystals. *Journal of Bacteriology* **2008,** *190* (1), 377.
71. Tanaka, M.; Mazuyama, E.; Arakaki, A.; Matsunaga, T., MMS6 protein regulates crystal morphology during nano- sized magnetite biomineralization in vivo. *The Journal of biological chemistry* **2011,** *286* (8), 6386.
72. Arakaki, A.; Webb, J.; Matsunaga, T., A novel protein tightly bound to bacterial magnetic particles in Magnetospirillum magneticum strain AMB-1. *Journal of Biological Chemistry* **2003,** *278* (10), 8745-8750.
73. Zhou, C. Z.; Confalonieri, F.; Jacquet, M.; Perasso, R.; Li, Z. G.; Janin, J., Silk fibroin: Structural implications of a remarkable amino acid sequence. *Proteins: Structure, Function, and Bioinformatics* **2001,** *44* (2), 119-122.
74. Galloway, J. M.; Arakaki, A.; Masuda, F.; Tanaka, T.; Matsunaga, T.; Staniland, S. S., Magnetic bacterial protein Mms6 controls morphology, crystallinity and magnetism of cobalt-doped magnetite nanoparticles in vitro. *Journal of Materials Chemistry* **2011,** *21* (39), 15244-15254.
75. Murat, D.; Falahati, V.; Bertinetti, L.; Csencsits, R.; Kornig, A.; Downing, K.; Faivre, D.; Komeili, A., The magnetosome membrane protein, MmsF, is a major regulator of magnetite biomineralization in Magnetospirillum magneticum AMB-1. *Molecular Microbiology* **2012,** *85* (4), 684-699.
76. Rawlings, A. E.; Bramble, J. P.; Walker, R.; Bain, J.; Staniland, S. S.; Galloway, J. M., Self-assembled MmsF proteinosomes control magnetite nanoparticle formation in vitro. *Proceedings of the National Academy of Sciences of the United States of America* **2014,** *111* (45), 19094-19099.
77. Marks, J.; Hoogenboom, H.; Griffiths, A. D.; Winter, G., Molecular evolution of proteins on filamentous phage. Mimicking the strategy of the immune system. *Journal of biological chemistry*. **1992**; 267, 16007-16010.
78. Aitken, R., *Antibody Phage Display [electronic resource] : Methods and Protocols*. Totowa, NJ : Humana Press, **2009**
79. Rothenstein, D.; Claasen, B.; Omiecienski, B.; Lammel, P.; Bill, J., Isolation of ZnO-binding 12- mer peptides and determination of their binding epitopes by NMR spectroscopy. *Journal of the American Chemical Society* **2012,** *134* (30), 12547.
80. Baumgartner, J.; Carillo, M. A.; Eckes, K.; Werner, P.; Faivre, D., Biomimetic Magnetite Formation: From Biocombinatorial Approaches to Mineralization Effects. *Langmuir* **2014,** *30* (8), 2129-2136.
81. Nord, K.; Gunneriusson, E.; Ringdahl, J.; Stahl, S.; Uhlen, M.; Nygren, P. A., Binding proteins selected from combinatorial libraries of an alpha-helical bacterial receptor domain. *Nature Biotechnology* **1997,** *15* (8), 772-777.

82. Elisabet, W.; Christofer, L.; Magnus, H.; Peter, A.; Vildan, D.-R.; Anders, H.; Helena, B.; Per-Åke, N.; Torleif, H., An affibody in complex with a target protein: Structure and coupled folding. *Proceedings of the National Academy of Sciences of the United States of America* **2003,** *100* (6), 3185.
83. Seeger, M. A.; Zbinden, R.; Flütsch, A.; Gutte, P. G. M.; Engeler, S.; Roschitzki-Voser, H.; Grütter, M. G., Design, construction, and characterization of a second- generation DARPin library with reduced hydrophobicity. *Protein Science* **2013,** *22* (9), 1239-1257.
84. Tiede, C.; Tang, A. A. S.; Deacon, S.; Mandal, U.; Nettleship, J.; Owen, R.; George, S.; Harrison, D.; Owens, R.; Tomlinson, D. C.; McPherson, M., Adhiron: a stable and versatile peptide display scaffold for molecular recognition applications. *Protein engineering, design and selection* **2014,** *27* (5), 145-155.
85. Lundberg, E.; Höidén-Guthenberg, I.; Larsson, B.; Uhlén, M.; Gräslund, T., Site-specifically conjugated anti- HER2 Affibody® molecules as one- step reagents for target expression analyses on cells and xenograft samples. *Journal of Immunological Methods* **2007,** *319* (1), 53-63.
86. Nord, K.; Gunneriusson, E.; Uhlén, M.; Nygren, P. A., Ligands selected from combinatorial libraries of protein A for use in affinity capture of apolipoprotein A- 1M and taq DNA polymerase. *Journal of biotechnology* **2000,** *80* (1), 45.
87. Löfblom, J.; Feldwisch, J.; Tolmachev, V.; Carlsson, J.; Ståhl, S.; Frejd, F. Y., Affibody molecules: Engineered proteins for therapeutic, diagnostic and biotechnological applications. *FEBS Letters* **2010,** *584* (12), 2670-2680.
88. Kramer-Marek, G.; Kiesewetter, D. O.; Martiniova, L.; Jagoda, E.; Lee, S. B.; Capala, J., 18 FFBEM-Z HER2: 342 - Affibody molecule—a new molecular tracer for in vivo monitoring of HER2 expression by positron emission tomography. *European Journal of Nuclear Medicine and Molecular Imaging* **2008,** *35* (5), 1008-1018.
89. Bennett, V.; Stenbuck, P. J., Identification and partial purification of ankyrin, the high affinity membrane attachment site for human erythrocyte spectrin. *Journal of Biological Chemistry* **1979,** *254* (7), 2533-2541.
90. Schott, J. J.; Charpentier, F.; Peltier, S.; Foley, P.; Drouin, E.; Bouhour, J. B.; Donnelly, P.; Vergnaud, G.; Bachner, L.; Moisan, J. P.; Le Marec, H.; Pascal, O., Mapping of a gene for long QT syndrome to chromosome 4q25- 27. *American Journal of Human Genetics* **1995,** *57* (5), 1114-1122.
91. Manuel, A. R. F.; Michael, C. O. D.; Yan, A. M.; Ian, R. J.; Douglas, M. R.; Lisa, J.; Jinbo, F.; George, K.; Roy, H. P.; Elaine, K. G.; Jordan, W. S.; Detelina, G.; Jennifer, S.; Ivan, N.; Kimberly, C.; Marian, L. H.; Vishwajit, L. N.; Valentina, M.; Michael, E. T.; Sian, C.; Gary, S. S.; Jennifer, F.; Katherine, G.-S.; Kristin, G. A.; Stacey, B. G.; Christine, F.; Brendan, B.; Matthew, D.; Gerome, B.; Michael, G.; Derek, W. M.; Amanda, E.; Walter, J. M.; Kevin, A. M.; Richard, W.; Donald, J. M.; Alan, W. M.; David St, C.; Michelle, R.; Margaret Van, B.; Ana, C. P. P.; Radhika, K.; Andrew, M.; David, A. C.; Nicholas, J. B.; Allan, H. Y.; Jacob, L.; Ferrier, I. N.; Adebayo, A.; Anne, F.; David, C.; Edward, M. S.; Peter, M.; Mark, J. D.; Aiden, P. C.; Peter, A. H.; Douglas, H. B.; Hugh, M. G.; Michael, J. O.; Shaun, M. P.; Pamela, S.; Nick, C., Collaborative genome- wide association analysis supports a role for ANK3 and CACNA1C in bipolar disorder. *Nature Genetics* **2008,** *40* (9), 1056.
92. Plckthun, A., Designed Ankyrin Repeat Proteins (DARPins): Binding Proteins for Research, Diagnostics, and Therapy. *Annual review of pharmacological Toxicology* **2015,** *55*, 489-511.

93. Lutz, K.; Petra, P.; Peter, R.; Bastian, M.; Anke, P.; Peer, R. E. M.; Melanie, K.; Bastian, Z.; Friedrich, W. H.; Andreas, P., Structural and functional analysis of phosphorylation-specific binders of the kinase ERK from designed ankyrin repeat protein libraries. *Proceedings of the National Academy of Sciences* **2012,** *109* (34), E2248.
94. Souied, E. H.; Devin, F.; Mauget-Faÿsse, M.; Kolář, P.; Wolf-Schnurrbusch, U.; Framme, C.; Gaucher, D.; Querques, G.; Stumpp, M. T.; Wolf, S., Treatment of Exudative Age- Related Macular Degeneration with a Designed Ankyrin Repeat Protein that Binds Vascular Endothelial Growth Factor: a Phase I/ II Study. *American Journal of Ophthalmology* **2014,** *158* (4), 724-732.
95. AG, M. P. A Phase I Multi-centre, Open-label, Repeated-dose, Dose-escalation Study to Assess Safety, Tolerability and Pharmacokinetics of MP0250 in Patients With Advanced Solid Tumours. (accessed 09/03/2018).
96. Jost, C.; Schilling, J.; Tamaskovic, R.; Schwill, M.; Honegger, A.; Plückthun, A., Structural Basis for Eliciting a Cytotoxic Effect in HER2- Overexpressing Cancer Cells via Binding to the Extracellular Domain of HER2. *Structure* **2013,** *21* (11), 1979-1991.
97. Forrer, P.; Binz, H. K.; Stumpp, M. T.; Pluckthun, A., Consensus design of repeat proteins. *Chembiochem* **2004,** *5* (2), 183-189.
98. Arai, S.; Matsumoto, I.; Abe, K., Phytocystatins and their target enzymes: From molecular biology to practical application: A review. *Journal of Food Biochemistry* **1998,** *22* (4), 287-299.
99. Hughes, D. J.; Tiede, C.; Penswick, N.; Tang, A. A. S.; Trinh, C. H.; Mandal, U.; Zajac, K. Z.; Gaule, T.; Howell, G.; Edwards, T. A.; Duan, J. X.; Feyfant, E.; McPherson, M. J.; Tomlinson, D. C.; Whitehouse, A., Generation of specific inhibitors of SUMO-1-and SUMO-2/3-mediated protein-protein interactions using Affimer (Adhiron) technology. *Science Signaling* **2017,** *10* (505), 13.
100. Lee, S. C.; Park, K.; Han, J.; Lee, J. J.; Kim, H. J.; Hong, S.; Heu, W.; Kim, Y. J.; Ha, J. S.; Lee, S. G.; Cheong, H. K.; Jeon, Y. H.; Kim, D.; Kim, H. S., Design of a binding scaffold based on variable lymphocyte receptors of jawless vertebrates by module engineering. *Proceedings of the National Academy of Sciences of the United States of America* **2012,** *109* (9), 3299-3304.
101. Schlehuber, S.; Beste, G.; Skerra, A., A novel type of receptor protein, based on the lipocalin scaffold, with specificity for digoxigenin. *Journal of Molecular Biology* **2000,** *297* (5), 1105-1120.
102. Koide, A.; Bailey, C. W.; Huang, X. L.; Koide, S., The fibronectin type III domain as a scaffold for novel binding proteins. *Journal Of Molecular Biology* **1998,** *284* (4), 1141-1151.
103. Nixon, A. E.; Wood, C. R., Engineered protein inhibitors of proteases. *Current Opinion in Drug Discovery & Development* **2006,** *9* (2), 261-268.
104. Rossmann, M.; Greive, S. J.; Moschetti, T.; Dinan, M.; Hyvonen, M., Development of a multipurpose scaffold for the display of peptide loops. *Protein Engineering Design & Selection* **2017,** *30* (6), 419-430.
105. Varadamsetty, G.; Tremmel, D.; Hansen, S.; Parmeggiani, F.; Plückthun, A., Designed Armadillo Repeat Proteins: Library Generation, Characterization and Selection of Peptide Binders with High Specificity. *Journal of Molecular Biology* **2012,** *424* (1-2), 68-87.
106. Silacci, M.; Baenziger-Tobler, N.; Lembke, W.; Zha, W.; Batey, S.; Bertschinger, J.; Grabulovski, D., Linker length matters, fynomer- Fc fusion with an optimized linker displaying picomolar IL- 17A inhibition potency. *The Journal of biological chemistry* **2014,** *289* (20), 14392.

107. Diem, M. D.; Hyun, L.; Yi, F.; Hippensteel, R.; Kuhar, E.; Lowenstein, C.; Swift, E. J.; Neil, K. T.; Jacobs, S. A., Selection of high- affinity Centyrin FN3 domains from a simple library diversified at a combination of strand and loop positions. *Protein Engineering, Design & Selection* **2014,** *27* (10), 419-429.
108. Kibbe, W. A., OligoCalc: an online oligonucleotide properties calculator. *Nucleic Acids Research* **2007,** *35* (Web Server issue), W43-W46.
109. Wilson, K.; Walker, J. M.; Walker, J. M., *Principles and techniques of biochemistry and molecular biology*. 7th ed. ed.; Cambridge : Cambridge University Press, 2010: Cambridge, 2010.
110. Lee, P. Y.; Costumbrado, J.; Hsu, C. Y.; Kim, Y. H., Agarose Gel Electrophoresis for the Separation of DNA Fragments. *Jove-Journal of Visualized Experiments* **2012,** (62), 5.
111. Green, M. R., *Molecular cloning : a laboratory manual. Vol. 1, Essentials*. 4th ed. ed.; Cold Spring Harbor, N.Y. : Cold Spring Harbor Laboratory Press, c2012: Cold Spring Harbor, N.Y., **2012**.
112. Sanger, F.; Nicklen, S.; Coulson, A. R., DNA sequencing with chain-terminating inhibitors. *Proceedings of the National Academy of Sciences of the United States of America* **1977,** *74* (12), 5463-5467.
113. Ho, S. N.; Hunt, H. D.; Horton, R. M.; Pullen, J. K.; Pease, L. R., Site-directed mutagenesis by overlap extension using the polymerase chain-reaction. *Gene* **1989,** *77* (1), 51-59.
114. Studier, F. W., Protein production by auto-induction in high-density shaking cultures. *Protein Expression and Purification* **2005,** *41* (1), 207-234.
115. Sivashanmugam, A.; Murray, V.; Cui, C. X.; Zhang, Y. H.; Wang, J. J.; Li, Q. Q., Practical protocols for production of very high yields of recombinant proteins using Escherichia coli. *Protein Science* **2009,** *18* (5), 936-948.
116. Schmidt, T. G. M.; Skerra, A., The Strep-tag system for one-step purification and high-affinity detection or capturing of proteins. *Nature Protocols* **2007,** *2* (6), 1528-1535.
117. Bornhorst, J. A.; Falke, J. J., Purification of proteins using polyhistidine affinity tags. *Applications of Chimeric Genes and Hybrid Proteins, Pt A* **2000,** *326*, 245-254.
118. Hengen, P. N., Purification of His-Tag fusion proteins from Escherichia coli. *Trends in Biochemical Sciences* **1995,** *20* (7), 285-286.
119. Gasteiger, E.; Gattiker, A.; Hoogland, C.; Ivanyi, I.; Appel, R.; Bairoch, A., ExPASy: the proteomics server for in-depth protein knowledge and analysis. *Nucleic Acids Research* **2003,** *31* (13), 3784-8.
120. Whitmore, L.; Wallace, B. A., DICHROWEB, an online server for protein secondary structure analyses from circular dichroism spectroscopic data. *Nucleic Acids Research* **2004,** *32*, W668-W673.
121. Niesen, F. H.; Berglund, H.; Vedadi, M., The use of differential scanning fluorimetry to detect ligand interactions that promote protein stability. *Nature Protocols* **2007,** *2* (9), 2212-2221.
122. Chaires, J. B., Calorimetry and thermodynamics in drug design. In *Annual Review of Biophysics*, Annual Reviews, **2008**; 37, 135-151.
123. Svergun, D. I., Determination of the regularization parameter in indirect-transform methods using perceptual criteria. *Journal of Applied Crystallography* **1992,** *25*, 495-503.
124. Aono, H.; Hirazawa, H.; Naohara, T.; Maehara, T.; Kikkawa, H.; Watanabe, Y., Synthesis of fine magnetite powder using reverse coprecipitation method and its heating

properties by applying AC magnetic field. *Materials Research Bulletin* **2005,** *40* (7), 1126-1135.
125. Regazzoni, A. E.; Urrutia, G. A.; Blesa, M. A.; Maroto, A. J. G., Some observations on the composition and morphology of synthetic magnetites obtained by different routes. *Journal of Inorganic & Nuclear Chemistry* **1981,** *43* (7), 1489-1493.
126. Date, A. R.; Gray, A. L., Plasma source-mass spectrometry using an inductively coupled plasma anda high-resolution quadrupole mass filter. *Analyst* **1981,** *106* (1269), 1255-1267.
127. Bragg, W. L.; Thomson, J. J., The diffraction of short electromagnetic waves by a crystal. *Proceedings of the Cambridge Philosophical Society* **1914,** *17*, 43-57.
128. Lim, J.; Yeap, S. P.; Che, H. X.; Low, S. C., Characterization of magnetic nanoparticle by dynamic light scattering. *Nanoscale Research Letters* **2013,** *8*, 14.
129. Flegler, S. L., *Scanning and transmission electron microscopy : an introduction*. New York : Oxford University Press, 1993: New York, **1995**.
130. Schneider, C.; Rasband, W.; Eliceiri, K., NIH Image to ImageJ: 25 years of image analysis. *Nature Methods* **2012,** *9* (7), 671-675.
131. Leavitt, S.; Freire, E., Direct measurement of protein binding energetics by isothermal titration calorimetry. *Current Opinion in Structural Biology* **2001,** *11* (5), 560-566.
132. Li, Y. F.; Sousa, R., Expression and purification of E. coli BirA biotin ligase for in vitro biotinylation. *Protein Expression and Purification* **2012,** *82* (1), 162-167.
133. Reichert, J. M., Antibodies to watch in 2010. *mAbs* **2010,** *2* (1), 84-100.
134. Schäffer Alejandro, A.; Agarwala, R.; Yu, Y.-K.; Gertz, E. M.; Altschul Stephen, F., Composition-based statistics and translated nucleotide searches: Improving the TBLASTN module of BLAST. *BMC Biology* **2006,** *4* (1), 41.
135. Corpet, F., Multiple sequence alignment with hierarchical clustering. *Nucleic Acids Research* **1988,** *16* (22), 10881-10890.
136. Horton, R. M.; Cai, Z.; Ho, S. M.; Pease, L. R., Gene splicing by overlap extension: tailor- made genes using the polymerase chain reaction. *BioTechniques* **2013,** *54* (3), 129.
137. Walter, T. S.; Mayo, C. J.; Brown, J.; Carter, L.; Diprose, J. M.; Siebold, C.; Pickford, M. G.; Sutton, G. C.; Berrow, N. S.; Berry, I. M.; Stewart-Jones, G. B. E.; Grimes, J. M.; Stammers, D. K.; Jones, E. Y.; Esnouf, R. M.; Owens, R. J.; Stuart, D. I.; Harlos, K., A procedure for setting up high- throughput nanolitre crystallization experiments. Crystallization workflow for initial screening, automated storage, imaging and optimization. *Acta Crystallographica Section D* **2005,** *61* (6), 651-657.
138. Nagata, K.; Kudo, N.; Tanokura, K.; Abe, S.; Arai, M.; Tanokura, M., Three-dimensional solution structure of oryzacystatin- I, a cysteine proteinase inhibitor of the rice, Oryza sativa L. japonica. *Biochemistry* **2000,** *39* (48), 14753-14760.
139. Rawlings, A.; Bramble, J.; Tang, A.; Somner, L.; Monnington, A.; Cooke, D.; McPherson, M.; Tomlinson, D.; Staniland, S., Phage display selected magnetite interacting Adhirons for shape controlled nanoparticle synthesis. **2015**, 6, 5586-5594
140. Elder, R. M.; Jayaraman, A.; Emrick, T., Understanding the effect of polylysine architecture on DNA binding using molecular dynamics simulations. *Biomacromolecules* **2011,** *12* (11), 3870-3879.
141. Mx, T.; Fc, S., The influence of polymer structure on the interactions of cationic polymers with DNA and morphology of the resulting complexes. *Gene Therapy* **1997,** *4* (8), 823.

142. Walker, J. M., *The Proteomics Protocols Handbook [electronic resource]*. Totowa, NJ : Humana Press, 2005: Totowa, NJ, **2005**.
143. Aires, A.; Ocampo, S. M.; Cabrera, D.; Cueva, L. D. L.; Salas, G.; Teran, F. J.; Cortajarena, A. L., BSA- coated magnetic nanoparticles for improved therapeutic properties. *Journal of material chemistry B* **2015,** *3* (30), 6239-6247.
144. Shubayev, V. I.; Jin, S.; Pisanic Ii, T. R., Magnetic nanoparticles for theragnostics. *Advanced Drug Delivery Reviews* **2009,** *61* (6), 467-477.
145. Guex, N.; Peitsch, M. C.; Schwede, T., Automated comparative protein structure modeling with SWISS- MODEL and Swiss- PdbViewer: A historical perspective. *Electrophoresis* **2009,** *30* (S1), S162-S173.
146. Wang, T.; Bai, J.; Jiang, X.; Nienhaus, G., Cellular Uptake of Nanoparticles by Membrane Penetration: A Study Combining Confocal Microscopy with FTIR Spectroelectrochemistry. *ACS Nano* **2012,** *6* (2), 1251-1259-1251-1259.
147. Park, S.; Kim, J.; Park, S. M.; Moon, M.; Lee, K.; Park, K.; Park, W., RAGE mediated intracellular A beta uptake contributes to the breakdown of tight junction in retinal pigment epithelium. *Oncotarget* **2015,** *6* (34), 35263-35273.
148. Raghavan, S.; Ward, M. R.; Rowley, K. R.; Wold, R. M.; Takayama, S.; Buckanovich, R. J.; Mehta, G., Formation of stable small cell number three- dimensional ovarian cancer spheroids using hanging drop arrays for preclinical drug sensitivity assays. *Gynecologic Oncology* **2015,** *138* (1), 181-189.
149. Graff, C. P.; Chester, K.; Begent, R.; Wittrup, K. D., Directed evolution of an anti-carcinoembryonic antigen scFv with a 4- day monovalent dissociation half- time at 37C. *Protein Engineering, Design and Selection* **2004,** *17* (4), 293-304.
150. Chester, K. A.; Begent, R. H. J.; Robson, L.; Keep, P. A.; Pedley, R. B.; Boden Libiol, J. A.; Boxer, G.; Green, A.; Winter, G.; Cochet, O.; Hawkins, R. E., Phage libraries for generation of clinically useful antibodies. *The Lancet* **1994,** *343* (8895), 455-456.
151. Mayer, A.; Tsiompanou, E.; O'Malley, D.; Boxer, G. M.; Bhatia, J.; Flynn, A. A.; Chester, K. A.; Begent, R. H. J.; Davidson, B. R.; Lewis, A. A. M.; Winslet, M. C.; Dhillon, A. P.; Hilson, A. J. W., Radioimmunoguided surgery in colorectal cancer using a genetically engineered anti- CEA single- chain Fv antibody. *Clinical Cancer Research* **2000,** *6* (5), 1711-1719.
152. TMbase – a database of membrane spanning proteins segments. *Biological chemistry Hoppe-Seyler.* **1993,** *374*, 166-173.
153. Faivre, D.; Fischer, A.; Garcia-Rubio, I.; Mastrogiacomo, G.; Gehring, A. U., Development of Cellular Magnetic Dipoles in Magnetotactic Bacteria. *Biophysical Journal* **2010,** *99* (4), 1268-1273.
154. Gurnon, D. G.; Whitaker, J.; Oakley, M. G., Design and characterization of a homodimeric antiparallel coiled coil. *Journal of American chemical society.* **2003,** *125* (25), 7518-7519.
155. Muller, K. M.; Arndt, K. M.; Alber, T., Protein fusions to coiled- coil domains. *Methods in Enzymology* **2000,** *328*, 261-282.
156. Jutz, G.; van Rijn, P.; Miranda, B. S.; Boker, A., Ferritin: A Versatile Building Block for Bionanotechnology. *Chemical Reviews* **2015,** *115* (4), 1653-1701.
157. Kim, D. E.; Chivan, D.; Baker, D., Protein structure prediction analysis using the Robetta server. *Nucleic acids research.* **2004**, 32, 526-531

Appendices

1.1 1 L 10X TAE buffer

Component	Final Concentration (M)	Mass (g)
TRIS Base	0.40	48.46
Sodium Acetate	0.40	32.80
EDTA	0.01	2.92

pH 8.2-8.4 (made up to 1 L with deionised water)

1.2 6X loading dye

Component	Final concentration
Tris-HCl	10 mM
Bromophenol blue	0.03%
Xylene cyanol FF	0.03%
Glycerol	60%
EDTA	60 mM

pH 7.6 at 25 °C

1.3 CutSmart buffer

Component	Final Concentration
Potassium Acetate	50 mM
Tris-acetate	20 mM
Magnesium Acetate	10 mM
Bolvine Serum Albumin (BSA)	100 µg mL^{-1}

pH 7.9 at 25 °C

1.4 T4 DNA ligase buffer

Component	Final Concentration (mM)
Tris-HCl	50
$MgCl_2$	10
Adenosine triphosphate (ATP)	1
Dithiothreitol (DTT)	10

pH 7.5 at 25 °C

1.5 LB medium

Component	Mass used (g)
Tryptone	10
Yeast extract	5
NaCl	10

pH 7.5 using NaOH, make up to 1 L with ultrapure water, autoclave to sterilise

1.6 TfbI

Component	Final concentration	Amount used
RbCl	125 mM	7.25 g
$MnCl_2.4H_2O$	50 mM	5 g

CH_3CO_2K	300 mM	14.7 g
$CaCl_2.2H_2O$	8 mM	0.75 g
Glycerol	15%	75 mL

Made up to 500 mL with ultrapure water

1.7 TfbII

Component	Final concentration	Amount used
0.2 M MOPS	5%	20 mL
RbCl	10 mM	0.48 g
$CaCl_2$	60 mM	4.4 g
Glycerol	15%	60 mL

Made up to 400 mL with ultrapure water

1.8 LB agar

Component	Mass used (g)
Tryptone	10
Yeast extract	5
NaCl	10
Agar	15

pH 7.5 using NaOH, make up to 1 L with ultrapure water, autOclave to sterilise

1.9 auto induction media

Component	Mass (g L^{-1})	Mass (g 400 mL^{-1})
Tryptone	12	4.8
Yeast extract	24	9.6
$(NH_4)_2SO_4$	3.3	1.3
KH_2PO_4	6.8	2.7
Na_2HPO_4	7.1	2.8
Glucose	0.5	0.2
α-lactose	2	0.8
$MgSO_4$	0.15	0.06
Trace elements	0.03	0.01

1.10 1 x PBS

Component	Final concentration (mM)	Mass (g L^{-1})
NaCl	134	8
KCl	2.5	0.2
Na_2HPO_4	10	1.44
KH_2PO_4	2	0.24

pH 7.4 at 25 °C, made up to 1 L with ultrapure water

1.11 Denaturation buffer

Component	Final concentration (M)	Amount used
Guanidine hydrochloride	8	152 g
Tris (1 M)	0.05	10 mL

Made up to 200 mL with ultrapure water, pH 7.4

1.12 Dilution buffer

Component	Final concentration (mM)	Mass used (g)
Tris	50	0.3
NaCl	300	8.75

Made up to 500 mL with ultrapure water, pH 7.4 at 25 °C

1.13 Refolding buffers

Refolding buffer	Denaturation buffer (mL)	Dilution buffer (mL)
A	30	30
B	15	45
C	7.5	52.5
D	3.75	56.25

1.14 Elution buffer

Component	Volume (mL)
Dilution buffer	40
Imidazole (2 M)	10

1.15 Resolving gel

Component	Volume (mL)
UltraPure water	3.40
30 % Acrylamide Acrylamide: Bisacrylamide (37.5:1)	4.00
Resolving gel buffer	2.50
10% APS in water	0.060
TEMED	0.012

1.16 Stacking gel

Component	Volume (mL)
UltraPure water	3.00
30 % Acrylamide Acrylamide: Bisacrylamide (37.5:1)	0.70
Resolving gel buffer	1.25
10% APS in water	0.025
TEMED	0.020

1.17 Resolving gel buffer

Component	Final concentration	Mass (g L^{-1})
Tris-HCl	1.5 M	180
SDS	0.4 %	4

pH 8.8 at 25 °C, made up to 1 L with ultrapure water

1.18 Stacking gel buffer

Component	Final concentration	Mass (g L^{-1})
Tris-HCl	0.5 M	60
SDS	0.4 %	4

pH 6.8 at 25 °C, made up to 1 L with ultrapure water

1.19 Towbin transfer buffer

Component	Final Concentration	Amount used
Tris-HCl	25 mM	1.5 g
Glycine	200 mM	7.2 g
Methanol	20%	100 mL

Made up to 500 mL using ultrapure water

1.20 Dot blot buffer

Component	Final concentration (M)	Mass (g L^{-1})
Guanidine-HCl	8.00	76.4
Sodium chloride	0.30	7.5
Tris (pH 8)	0.05	5.0

Made up to 1 L with ultrapure water

1.21 Reducing buffer

Component	Final concentration	Volume (µL)
1 M Sodium phosphate (pH 6)	10%	100
0.5 M EDTA	5%	5

Made up to 1 L with ultrapure water

1.22 Conjugation buffer

Component	Volume (mL)
0.5 M EDTA	0.02
PBS	10

2.1 pPR-IBA1 vector map

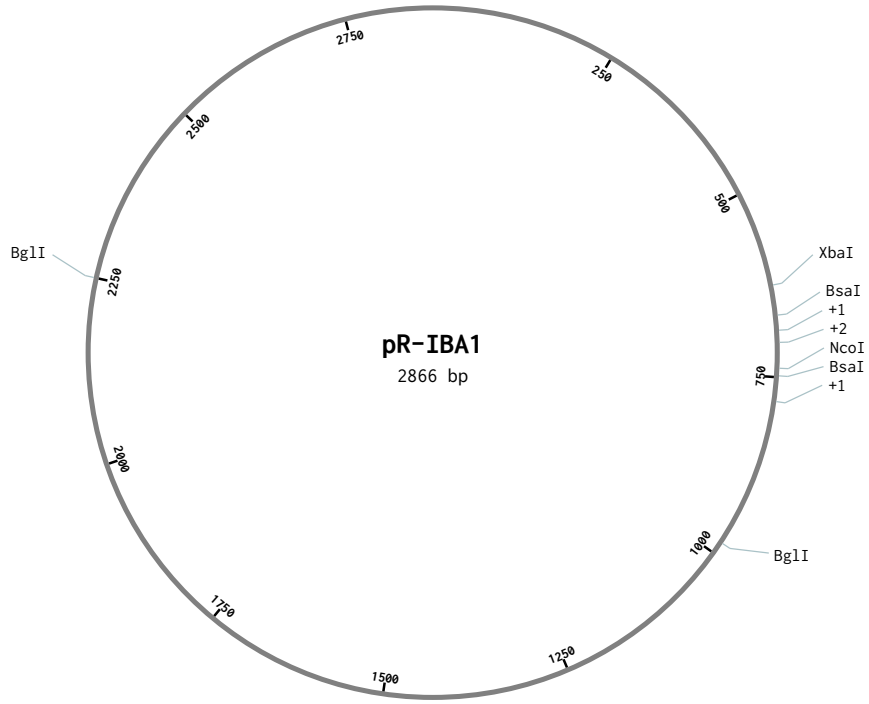

2.2 pJet vector map

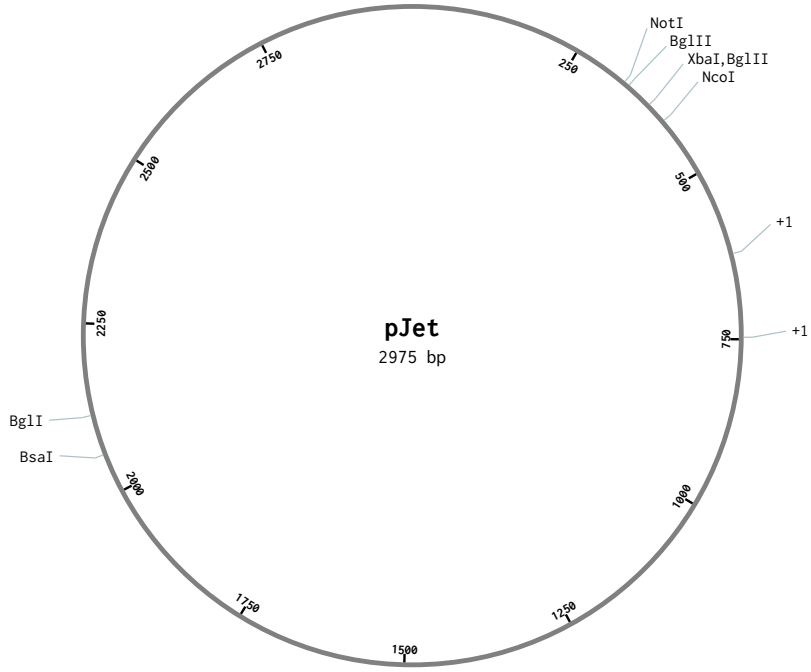

2.3 pFUSE vector map

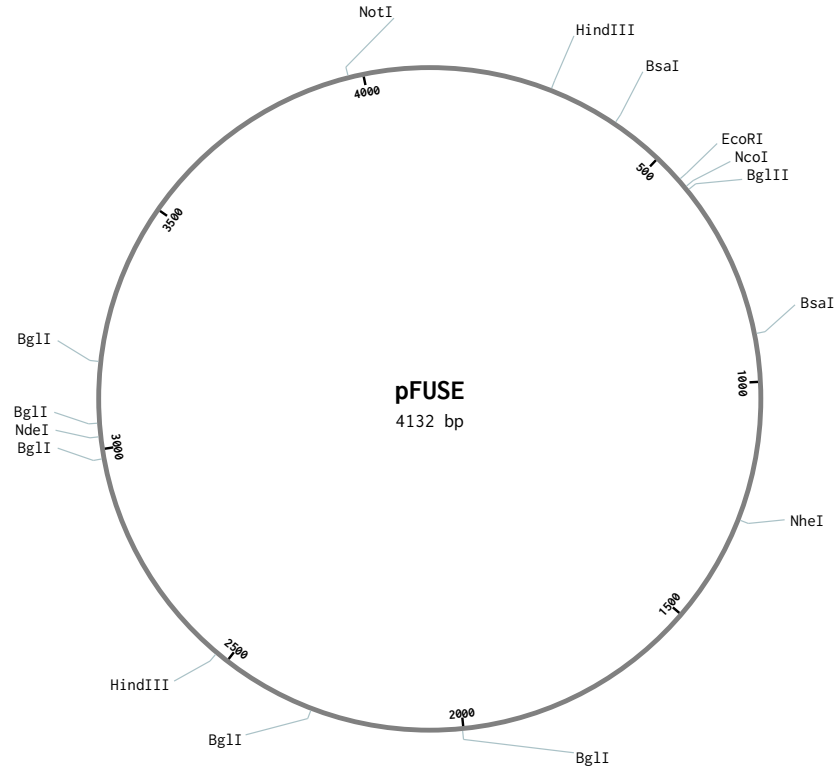

3.1 Calculation for MIA coverage of MNP

For 30 nm MNPs: V = 2.7 x10^{-17} cm^{-3}; ρ = 5 g cm^{-3}; so, m = 1.35 x 10^{-16} g; SA = 5.4 x 10^{3} nm^{2}

n[Fe] = 5 x10^{2} μmol/3

Fe_3O_4 = 231.5 g mol^{-1}; m = 3.8 x 10^{-2} g

Number of particles = 1.3 x 10^{-16} g/3.8 x 10^{-2} g = 2.85 x 10^{14}

[Fe_3O_4] = 0.47 nM

SA_{MIA} = 3.2 nm x 2.1 nm = 6.7 nm^{2}

Therefore MIA^{-1} particle = 5.4 nm^{2} x 10^{3}/6.7 nm^{2} = 803

38 mg of magnetite requires 58 μg MIA

4.1 MIA_{AVI} oligonucleotide primer sequences

Construct	Forward oligonucleotide primer	Reverse oligonucleotide primer
MIA_{AVI} insert	GCGCTGCTAGCGCAACCGCAACCGGTG	GCTACGCCGGCGACGTAGTG

4.2 QuikChange™ site directed mutagenesis oligonucleotide primer sequences for terminal Cys

Construct	Forward oligonucleotide primer	Reverse oligonucleotide primer
Cys-tagged CC	ATGGTAGGTCTCAAATGGGTAGTCATCATCAC CACCATCA	ATGGTAGGTCTCAGCGCTTTAGGCCTGCAATTTC TTTTTT

4.3 Oligonucleotide primer sequences for ScFv construct

Construct	Forward oligonucleotide primer	Reverse oligonucleotide primer
UCL-GFP	ATGGTAGGTCTCAAATGAAATACCTGCTGCCG ACCGCTG	ATGGTAGGTCTCAGCGCTTTTATGCTTTTTGCTTT TATG
UCL-ScFv	GCCGCTAGCATGGCTCAGGTGAAGCTGG	GGCGCGGCCGCTTTGATCTCCAGCTTGGTGG
UCL-13CC	GTTACAGGCACCGGCGGCCGCAGGCGGTGG	CCACCGCCTGCGGCCGCCGGTGCCTGTAAC
UCL-ScFv QC	GGTTAAGCCTGGCGCGAGCGTGAAACTCTC	GAGAGTTTCACGCTCGCGCCAGGCTTAACC

4.4 Oligonucleotide primer sequences for synthesis of the MmsFCC mutants

Construct	Forward oligonucleotide primer	Reverse oligonucleotide primer
MmsFCC(D1S)	GCTGCAGGCGTCTCGTGACGATG	CATCGTCACGAGACGCCTGCAGC
MmsFCC(F6Y)	CGTGACGATGAATATGTGTATTTCCAC	GTGGAAATACACACATATTCATCGTCACG
MmsFCC(F9Q)	GAATTTGTGTATCAGCACGCAAAGC	GCTTTGCGTGCTGATACACAAATTC
MmsFCC(F6Y, F9Q)	GAAACTGCAGGCGGACAAAGACGATGAAT AC	GTATTGATCGTCTTTGTCGCGCTGCAGTTC

5.1 AcrBCC MS

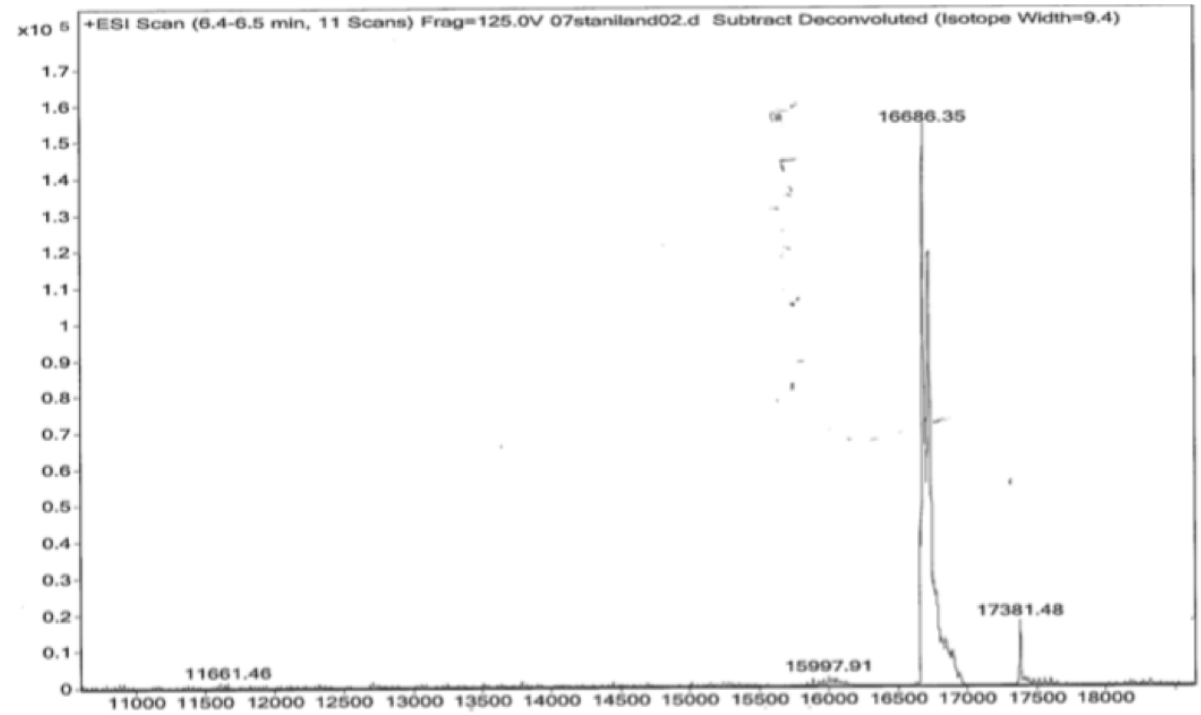

5.2 Mms13CC MS

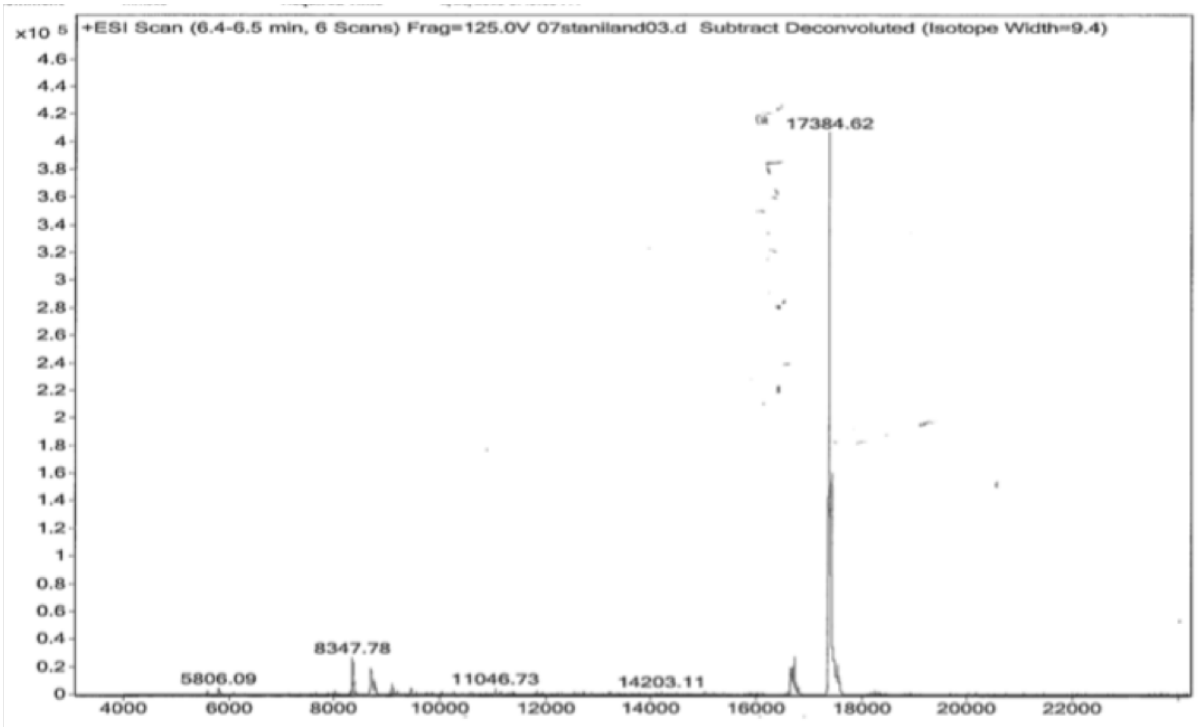

5.3 Data analysis of MmFCC, MmxFCC, MamFCC

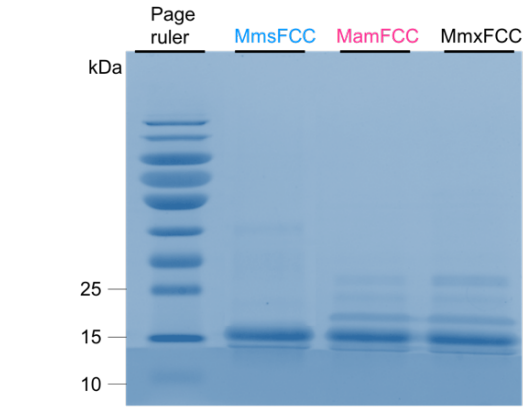

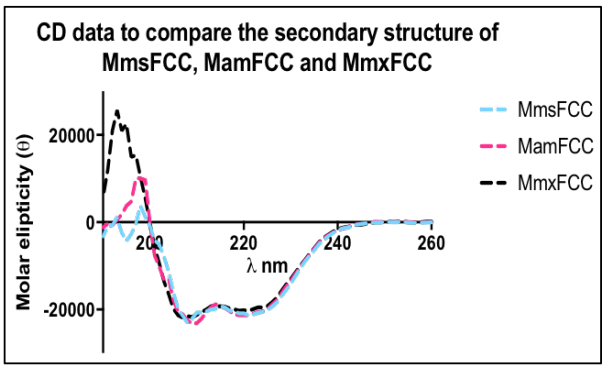

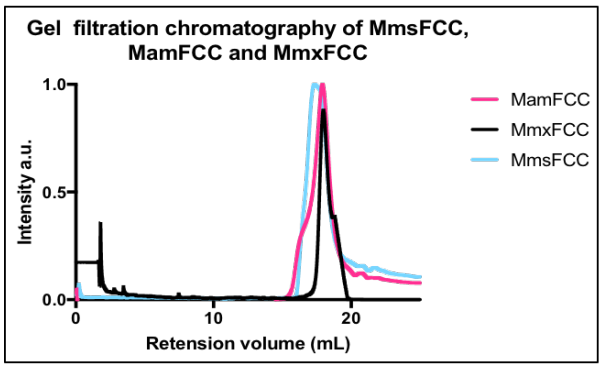

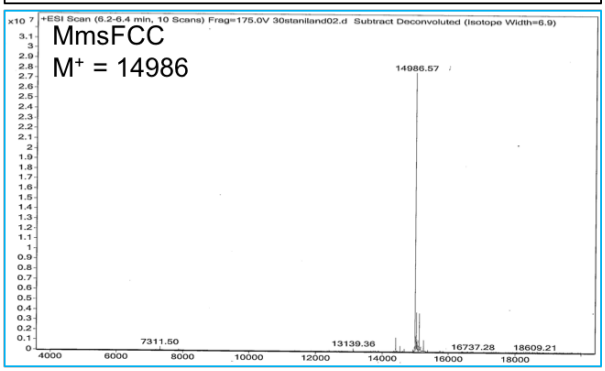

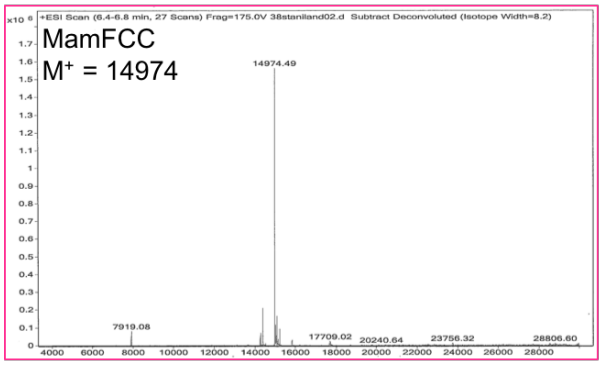

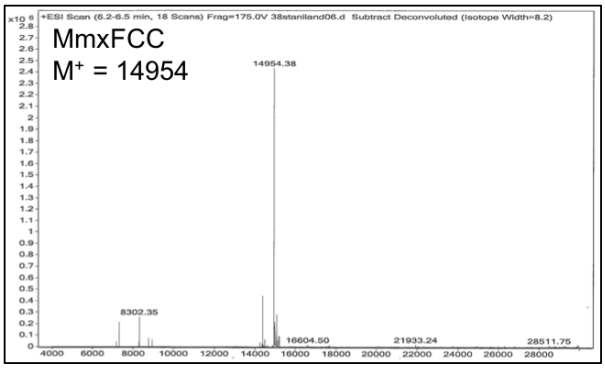

Protein	Predicted M^+ peak position	Observed M^+ Peak position	Predicted retention Vol (mL)	Observed retention Vol (mL)
MmsFCC	14986	14986	17.5	17.4
MamFCC	14974	14974	17.5	17.6
MmxFCC	14954	14954	17.5	17.6

Data analysis of the MmsFCC homologs: MamFCC and MmxXFCC. The analysis includes SDS-PAGE; room temperatire CD (in water); gel filtration using a superdex 200 10/30 GL column and MS for each of the three proteins. The table presents the predicted and obserevd peak positions for gel filtration and MS.